J. Hydrol. Hydromech., 66, 2018, 1, 1–11
DOI: 10.1515/johh-2017-0037

The significance of soil moisture in forecasting characteristics of flood events. A statistical analysis in two nested catchments.

Peter Chifflard[1*], Julius Kranl[2], Georg zur Strassen[3], Harald Zepp[2]

[1] Department of Geography, Philipps-University Marburg, Deutschhausstr. 10, 35032 Marburg, Germany.
[2] Department of Geography, Ruhr- University Bochum, Universitätsstr. 150, Building NA, 44780 Bochum, Germany.
[3] Ruhrverband, Kronprinzenstr. 37, 45128 Essen, Germany.
[*] Corresponding author. Tel.: +49(0)6421 28-24155. Fax: +49(0)6421 28-28950. E-mail: peter.chifflard@geo.uni-marburg.de

Abstract: We examine the feasibility and added value of upscaling point data of soil moisture from a small- to a meso-scale catchment for the purpose of single-event flood prediction. We test the hypothesis that in a given catchment, the present soil moisture status is a key factor governing peak discharge, flow volume and flood duration. Multiple regression analyses of rainfall, pre-event discharge, single point soil moisture profiles from representative locations and peak discharge, discharge duration, discharge volume are discussed. The soil moisture profiles are selected along a convergent slope connected to the groundwater in flood plain within the small-scale catchment Husten (2.6 km²), which is a headwater catchment of the larger Hüppcherhammer catchment (47.2 km², Germany). Results show that the number of explanatory variables in the regression models is higher in summer (up to 8 variables) than in winter (up to 3 variables) and higher in the meso-scale catchment than in the small-scale catchment (up to 2 variables). Soil moisture data from selected key locations in the small catchment improves the quality of regression models established for the meso-scale catchment. For the different target variables peak discharge, discharge duration and discharge volume the adding of the soil moisture from the flood plain and the lower slope as explanatory variable improves the quality of the regression model by 15%, 20% and 10%, respectively, especially during the summer season. In the winter season the improvement is smaller (up to 6%) and the regression models mainly include rainfall characteristics as explanatory variables. The appearance of the soil moisture variables in the stepwise regression indicates their varying importance, depending on which characteristics of the discharge are focused on. Thus, we conclude that point data for soil moisture in functional landscape elements describe the catchments' initial conditions very well and may yield valuable information for flood prediction and warning systems.

Keywords: Soil moisture; Runoff prediction; Catchment hydrology; Spatial-temporal variability; Multivariate statistics.

INTRODUCTION

Accurate runoff prediction is of vital interest for any integrated management of water resources and for controlling reservoirs. This calls for reliable functions describing how rainfall is transformed into creek and river discharge depending on the properties of the catchment. The prediction is aggravated by the fact that runoff generation is a highly nonlinear process and threshold processes are observed in many catchments due to the initial conditions (Ali et al., 2015; Chifflard and Zepp, 2008; Chifflard et al., 2004; Penna et al., 2015; Tromp-van Meerveld and McDonnell, 2006a, b; Zehe and Blöschl, 2004). Thus, information describing the wetness of a catchment prior to a flood event is increasingly being introduced into flood warning tools (e.g. Brocca et al., 2009; Bronstert et al., 2012; Graeff et al., 2012). One hydrological variable frequently found to be non-linearly related to runoff is soil moisture, which impacts the catchment runoff response at the field and headwater scale (Ali et al., 2010; Brocca et al., 2010; Zehe et al., 2010). Typically referred to as antecedent soil moisture, pre-event soil moisture or antecedent wetness condition, the spatiotemporal dynamics of the soil moisture are commonly used to describe the internal state of a catchment which expresses the sensitivity of the catchment to generating surface flow, subsurface flow and to triggering base flow (Bronstert et al., 2012; Casper et al., 2007). The internal status of a catchment can be also expressed easily by e.g. pre-event discharge or antecedent precipitation indices as proxies for the soil moisture. However, these indices do not meet the requirements of a distributed modelling approach (Graeff et al., 2009; Longobardi et al., 2003). In fact, the application of spatial soil moisture patterns are potentially valuable for calibrating and validating models (Parajka et al., 2006; Rinderer et al., 2012) and the inclusion of locally measured soil moisture data in a conceptual rainfall-runoff model greatly improves flood forecasting, especially during high flow conditions (Aubert et al., 2003; Bronstert et al., 2012). The high spatiotemporal variability of soil moisture monitoring for large areas is not an easy task and hinders the general application of soil moisture assimilation in rainfall-runoff models (Brocca et al., 2009; Bronstert et al., 2012; Chen et al., 2014). Attempts are being made to gather spatially distributed information on the soil moisture status of entire catchments by means of regionalization and remote sensing (Alvarez-Garreton et al., 2014; Massari et al., 2014). The current microwave remote sensing techniques provide the opportunity to measure soil moisture of large areas, but the spatial and temporal resolutions of the observations is too coarse for hydrological applications in small catchments (Alvarez-Garreton et al., 2014; Brocca et al., 2010; Lakshmi, 2013; Wagner et al., 2007). To improve the spatial resolution up to 1 km, different soil moisture disaggregation algorithms have been formulated (e.g. Fang and Lakshmi, 2014; Pellenq et al., 2003), as for which in situ measurements of soil moisture are required for validation. This is extremely ambitious and thus restricted to complex measurement operations. On the other hand, the approaches favoring regionalization are based on the installation of numerous spatially distributed soil moisture sensors (Bogena et al., 2010; Brocca et al., 2009; Bronstert et al., 2012; Casper et al., 2007; Engels et

al., 2012; Zehe et al., 2010) or on repeated measurement efforts to obtain an adequate number of sampling points (Chifflard et al., 2013; Petrone et al., 2004; Western et al., 2004). Nevertheless, regardless of the method chosen (e.g. time domain reflectometry, ground penetrating radar) these measurements are expensive, time-consuming or both. Thus, major efforts still have to be made to optimize soil moisture networks (Vereecken et al., 2014).

In this context, various attempts have been made to determine both the number of samples needed to predict mean soil moisture content and the optimal placement of soil moisture sensors (Vereecken et al., 2014). A wide range of suggestions exists, anywhere from 3–32 samples (Jacobs et al., 2004) through 15–35 samples (Brocca et al., 2007) and more than 15 samples (Tague et al., 2010), which indicates that these values are site-specific and cannot be regionalized (Vereecken et al., 2014). Brocca et al. (2007) emphasizes that the number of samples required is highly dependent upon topography and increases with complex topographic structures. Zehe et al. (2010) assessed spatial patterns by the definition of soil moisture ensemble units, which are defined as areas that are uniform with respect to soil type, terrain properties, vegetation class as well as rainfall and radiation forcing. They showed that the average antecedent soil moisture of a forested soil moisture ensemble, measured by up to 39 TDR probes within a spatial extent of 100 m², explained up to 92% of the observed runoff coefficients at the outlet of a 16 km² catchment. Therefore, Zehe et al. (2010) conclude that the spatiotemporal highly resolved soil moisture sampling in key landscape units is a valuable opportunity to predict runoff. However, every attempt to forecast and monitor flooding faces the problem of upscaling, be it of the parameters or processes (Ojha et al., 2014). Thus, for enhanced flood warning the challenge in optimizing soil moisture sampling is to place the least number of sensors to retrieve sufficient data, while simultaneously expanding the runoff prediction to a larger spatial scale where additional spatially variable factors, such as rainfall or radiation, impact the spatial soil moisture variability. The principle question in this study is if the soil moisture status of a catchment derived from measurements on the point scale can be upscaled to model the larger catchments. Considering the constraints in retrieving spatially distributed soil moisture data and the necessity of assimilating the originally measured data instead of implementing them directly into deterministic models, we will assess the value of single point soil moisture profiles from representative locations in a catchment to explore soil moisture control on the runoff generation across spatial scales. Therefore we will use multiple linear regression models by using different response variables and predictor variables describing the runoff generation and among others the antecedent moisture conditions, respectively. Aware of the nonlinearity of hydrological processes and the threshold behavior of the rainfall-runoff-relationships the application of linear models to predict catchment's response is an auspicious approach to identify significant predictor variables (e.g., Graeff et al., 2012; Hrnčíř et al., 2010). Blume et al. (2007) emphasize the surprisingly good results by using simple linear interrelationships to predict runoff coefficients, however, they point out that the derived model should not applied outside the range of the predictor variables. In the context of the principle question of this study, the derived multiple linear regression models will show that the integration of a selected number of single point soil moisture profiles located at hydrologically relevant plots will improve the quality of the regression model. Thus, to cover a wide range of aspects determining the catchment's wetness or sensitivity, we selected soils in the floodplain near the creek and at the lower, middle, and upper slope. Whereas the floodplain soil is influenced by the fluctuating groundwater table, the lower slope location is connected to the intermittent subsurface flow through the cover beds of the slope. The middle slope position represents a soil with a high water storage capacity in the fine-textured slope sediments (colluvial beds) and the upper slope is characterized by a shallow soil with bedrock contact. Thus, these soils should have the strongest moisture contrasts between humid and dry periods and cover a typical landscape unit within this catchment as postulated by Zehe et al. (2010). The overall shape of the slope is convergent (Fig. 1), creating flow concentration in the subsoil. We argue that vertical soil moisture profiles at selected locations represent the main features of the spatial variation of the catchment's wetness. Thus depicting the strongest moisture contrasts, we escape the uncertainties of small scale spatial variability in soil moisture. Furthermore, the sequence of locations along the convergent slope connected to the groundwater in the floodplain is an intelligent, process-motivated set-up with a convincing cost-benefit ratio as opposed to complex measurement installations.

We hypothesize that 1) the significance of measurement sites within the discharge generating catchment is more important than the absolute number of measurement sites, 2) under the condition of both rainfall and meso-scale physiographic homogeneity in terms of relief, soils and land use, it is possible to upscale the functional relationships between rainfall and discharge elaborated in a small catchment without loss of predictive reliability and 3) the influence of antecedent soil moisture is greater during the summer than in the humid winter, because spatial patterns are more pronounced during the season with high evapotranspiration than in the winter. On the other hand, spatial rainfall variations are larger in summer, counterbalancing the quality of any prediction model. The question thus arises as to whether the likelihood of predicting discharge characteristics in summer are smaller than in winter.

RESEARCH AREA

In this study, we apply a nested catchment approach. The catchment Husten (2.6 km^2) is a headwater catchment of the larger catchment Hüppcherhammer (47.2 km^2) located in the Rhenish Massif (Germany, Province of North Rhine-Westphalia) between 50°58' 50.000'' and 51°03'26'' northern latitude and 07°44'15.500'' and 07°49'49'' eastern longitude (Fig. 1). The gauging station at Hüpcherhammer lies at 313 m a.s.l., whereas the highest elevation reaches 514 m a.s.l. The Hüppcherhammer catchment consists of two main channels, the Rose and the Brachtpe, which jointly contribute to the Biggetal reservoir operated by the local water board Ruhrverband. Land use in both catchments is dominated by pasture land and spruce stands and mixed forests. Some arable land and settlements characterize the remaining part of the catchments. Mean annual temperature is approximately 9.1°C and mean annual rainfall is approximately 1227 mm, while 15-20% of the annual precipitation comes in the form of snow (Deutscher Wetterdienst, 2004). Water levels have been observed at the gauging station Hüppcherhammer since 1967 and since 1999 at the gauging station Husten as well, which are both operated by the Ruhrverband. The mean discharge (MQ) is about 1.24 m^3/s or 828 mm/year (Hüppcherhammer; 1967–2014) and about 0.078 m^3/s or 965 mm/year (Husten: 2001–2009; Ruhrverband 2014). The HQ5 reaches 29.6 m^3/s at the gauge Hüppcherhammer and 2.56 m^3/s at the gauge Husten. The geology is characterized by sandy-silty clay shale from the Lower and Middle Devonian (Grabert and Hilden, 1972). Loamy Cambisols derived of periglacial

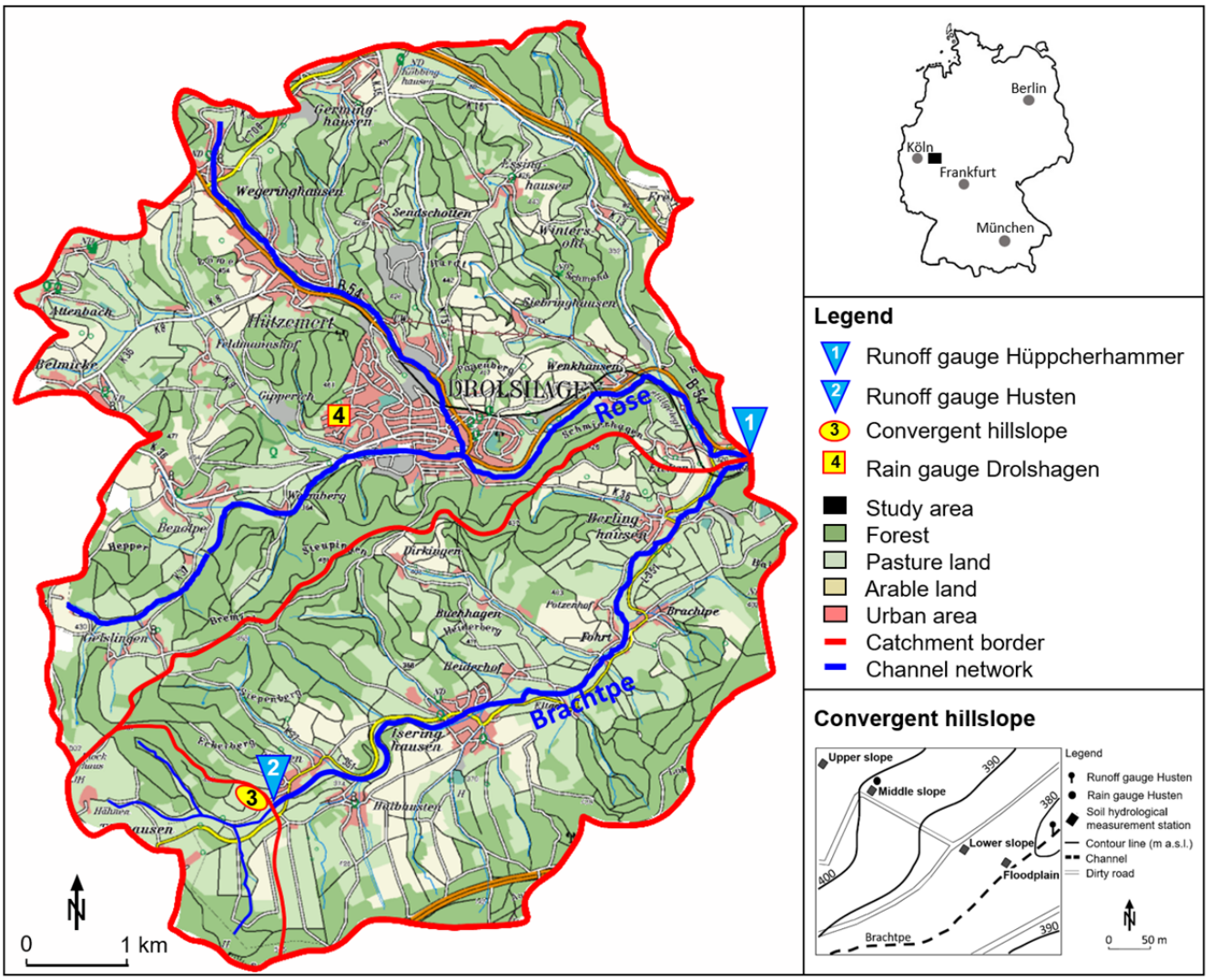

Fig. 1. Nested catchments Husten and Hüppcherhammer with locations of gauging, meteorological and soil moisture stations. (Base map: Bezirksregierung Köln, 2015).

slope deposits complemented by Leptosols and Stagnosols are the most prominent soils in the catchment (Chifflard et al., 2008).

METHODS

Measurements

Rainfall was measured in the small catchment Husten using a tipping bucket and recorded every 10 minutes (Fig. 1). Additionally, information on rainfall in the meso-scale catchment was supplemented by daily rainfall data from Drolshagen where no further temporal resolution is available. Snowfall and periods with snow cover are excluded from the data set. These periods were determined by using the meteorological dataset of the station Drolshagen where information about the daily snow depth are available.

Water level at the gauging stations Hüppcherhammer (15 min-interval) and Husten (10 min-interval) was observed by a bubble gauge and an H-flume, respectively. Discharge was calculated by the application of a water level-discharge relationship.

To monitor the soil moisture status, a convergent hillslope under grass cover (70 m in height, inclination of 8° and a mean altitude of 411 m a.s.l.) was equipped with tensiometers in 2 replicates per depth (20 cm up to 200 cm) following a hypothesized moisture gradient from upper slope to lower slope (for position and denomination of the tensiometer station cf. Fig. 1). The lowermost tensiometers were installed in floodplain sediments frequently saturated by groundwater from the nearby Brachtpe creek. Soil moisture was measured with pressure-transducer tensiometers, retrieved and logged every 10 minutes. The measurement unit was hPa. High positive values stand for dry soils, negative values stand for saturation below the groundwater or stagnant water table. Compared to measurement techniques for soil water content, tensiometers provide the advantage that they allow the hydraulic pressure within the aquifer to be quantified as well.

The following measurement depths for the soil water potential (S) are available at the different plots. The second letter in the abbreviation designates the slope position and the subscript stands for depth in cm:

Floodplain	SF_{20}, SF_{50}, SF_{80}, SF_{120}, SF_{150}
Lower slope	SL_{20}, SL_{50}, SL_{80}, SL_{120}, SL_{150}, SL_{190}
Middle slope	SM_{20}, SM_{50}, SM_{80}, SM_{120}, SM_{150}, SM_{180}, SM_{200}
Upper slope	SU_{20}, SU_{50}, SU_{80}, SU_{120}

For the further study the dataset from 2002 till 2003 was used. The observation period of the different variables (rainfall,

runoff, soil water potential) extends over the duration of about 10 years starting in 1999.

Definition and delineation of rainfall and discharge events

We used a pragmatic delineation to define single rainfall events, such as those introduced by Dikau (1986) and Baade (1994). According to our definition, a rainfall event starts with the first recording period and has ended when the following six hours stay dry. The additional rainfall data from Drolshagen was used to generate additional variables for the stepwise regression analysis. The primary purpose of this was to examine, if or how this additional information can improve the quality of the regression models. But the rainfall data from Drolshagen was not used for the assignment of rainfall and runoff events due to the daily sampling interval. The following variables attributed to each rainfall event:

[P_{t1}] Rainfall (mm) at catchment Husten
[P_d] Duration of rainfall event (min) at catchment Husten
[P_{int}] Intensity of rainfall (mm/min) at catchment Husten
[P_{int10}] Maximum 10 min-rainfall intensity at catchment Husten
[P_{t2}] Daily rainfall (mm) at Drolshagen (meso-scale catchment)
[P_{t3}] Daily rainfall (mm) at catchment Husten
[ΔP] Absolute difference between [P_{t2}] and [P_{t3}]

A discharge event starts once the discharge rate increases by 0.001 m³/s. This threshold factors in the precision of the gauging station and excludes discharge fluctuations not caused by rainfall. A discharge event is considered over at the first interval in which the slope of the hydrograph falls below that of the dry weather base flow recession curve. The variable discharge volume summarizes all runoff components during an event including baseflow, surface and subsurface runoff. The following variables are attributed to each rainfall event:

[Q_{i-1}] Discharge prior to the event (pre-event discharge) [m³/s]
[Q_{max}] Maximum discharge [m³/s] (peak flow)
[Q_d] Duration of discharge event [min]
[Q_V] Discharge volume [m³]

Assigning discharge events to rainfall events

Every runoff event measured at the gauging station Hüppcherhammer or Husten is assigned a triggering rainfall event identified at the meteorological station in the small catchment Husten (cf. Fig. 1). This event-based assignment is easily performed for the small catchment Husten, which is characterized by a short runoff response. This assignment is more complicated for the meso-scale catchment Hüppcherhammer due to its size, the distance between the meteorological station and the catchment outlet (about 9 km) as well as the fact that the catchment mainly consists of two sub-basins.

To decide, if a runoff event identified at the gauging station Hüppcherhammer could have been triggered by a rainfall event measured at the meteorological station Husten, a specific maximum time interval was defined for every runoff event. This specific time interval represents the maximum possible duration between the end of a local rainfall event in Husten and the starting point of the resulting discharge increase at the gauging station Hüppcherhammer given the prevalent discharge conditions (Table 1). If the time difference between a discharge event and the previous rainfall event exceeds this time interval, another event must have triggered the discharge at the gauging station Hüppcherhammer. In this case, the discharge event is discarded. Those discharge events could result from faulty rainfall measurement or rainfall events restricted to the sub-basin of the Rose creek. Furthermore, increased discharge could be the result of anthropogenic influence due to the village Drolshagen and the industry located there. The intervals are derived from flow velocity data measured by Schendzielorz (2004) on the 9 km stretch between the gauging station Hüppcherhammer and Husten. This data was linked to discharge classes that cover the span of the mean discharge of all runoff events at the gauging station Hüppcherhammer (Table 1). In the event a specific discharge event covers several rainfall events, these rainfall events will be connected and attributed to the first triggering rainfall event.

Table 1. Assignment of rainfall and runoff events on the basis of mean discharge of a runoff event.

Category	Upper limit of mean discharge [m³/s] of the runoff event	Lower limit of velocity [m/s]	Upper limit of duration for the assignment [min]
1	2.43	0.045	2741
2	4.83	0.282	438
3	7.24	0.518	238
4	9.65	0.755	163
5	12.06	0.991	124

Antecedent soil moisture

Antecedent soil moisture at 20 cm depth at all stations (SF_{20}, SL_{20}, SM_{20}, SU_{20}) measured 10 minutes before the onset of rainfall is assigned to the combined rainfall-runoff-event.

Statistics

As the multicollinearity of predictor variables can be problematic (Hedderich and Sachs, 2016), the variance inflation factor (VIF) of all potential predictors was calculated (Table 2). Since only the variable SL_{80} and SL_{120} show a VIF of about 25 due to a high correlation coefficient of 0.98, these parameters where separated and assigned into different subsets, one including SL_{80} and one including SL_{120}. Stepwise regression analyses were based on the latter subset and performed using SPSS Software Package, Version 17. The analyses included [Q_{max}], [Q_d], [Q_V] as dependent variables and [P_{t1}], [P_{t2}], [P_d], [P_{int}], [P_{int10}], [Q_{i-1}], [ΔP] and SF (soil moisture floodplain), SL (soil moisture lower slope), SM (soil moisture middle slope) SU (soil moisture upper slope) as independent variables. Independent variables are introduced one after another into the regression model, starting with variables that show the smallest F-probabilities. The software's default options were applied. The routine tracks the individual steps of the fitting procedures until the thresholds for inclusion and exclusion of variables are reached.

RESULTS

In the observation period (2002 and 2003) 30 events for the small-scale and 100 events for the meso-scale catchment were successfully isolated. Table 3 contains the main characteristics of the measured rainfall and runoff events in both catchments.

The majority (n = 71) of the events measured at the gauging station Hüppcherhammer was recorded during the summer. The duration (P_d) and the amount (P_t) of the winter rainfall events are noticeably higher than of the summer events, whereas

Table 2. Variance inflation factors (VIF) of all potential predictors.

	P_{t1}	Q_{i-1}	P_{int}	SF_{20}	SF_{50}	SF_{80}	SF_{120}	SF_{150}	SL_{20}	SL_{50}	SL_{80}	SL_{120}	SL_{150}	SL_{200}	P_d	P_{int10}
P_{t1}		1.16	1.03	1.00	1.00	1.00	1.00	1.00	1.01	1.03	1.03	1.02	1.00	1.01	2.58	1.12
Q_{i-1}	1.16		1.01	1.04	1.24	1.30	1.37	1.41	1.02	1.01	1.02	1.02	1.07	1.18	1.12	1.00
P_{int}	1.03	1.01		1.02	1.03	1.04	1.02	1.04	1.00	1.02	1.03	1.03	1.03	1.00	1.07	1.38
SF_{20}	1.00	1.04	1.02		3.85	1.67	2.16	2.03	2.01	1.68	2.05	1.96	1.16	1.10	1.01	1.02
SF_{50}	1.00	1.24	1.03	3.85		3.92	6.96	8.11	1.88	1.55	1.81	1.80	1.20	1.32	1.02	1.06
SF_{80}	1.00	1.30	1.04	1.67	3.92		2.52	5.49	1.47	1.23	1.28	1.34	1.13	1.28	1.04	1.11
SF_{120}	1.00	1.37	1.02	2.16	6.96	2.52		7.36	1.55	1.39	1.56	1.52	1.22	1.34	1.02	1.04
SF_{150}	1.00	1.41	1.04	2.03	8.11	5.49	7.36		1.57	1.34	1.47	1.49	1.19	1.36	1.03	1.12
SL_{20}	1.01	1.02	1.00	2.01	1.88	1.47	1.55	1.57		2.62	1.75	1.62	1.05	1.04	1.00	1.00
SL_{50}	1.03	1.01	1.02	1.68	1.55	1.23	1.39	1.34	2.62		5.67	5.14	1.46	1.10	1.00	1.00
SL_{80}	1.03	1.02	1.03	2.05	1.81	1.28	1.56	1.47	1.75	5.67		25.71	1.68	1.15	1.00	1.01
SL_{120}	1.02	1.02	1.03	1.96	1.80	1.34	1.52	1.49	1.62	5.14	25.71		2.01	1.21	1.00	1.01
SL_{150}	1.00	1.07	1.03	1.16	1.20	1.13	1.22	1.19	1.05	1.46	1.68	2.01		1.90	1.03	1.00
SL_{200}	1.01	1.18	1.00	1.10	1.32	1.28	1.34	1.36	1.04	1.10	1.15	1.21	1.90		1.03	1.01
P_d	2.58	1.12	1.07	1.01	1.02	1.04	1.02	1.03	1.00	1.00	1.00	1.00	1.03	1.03		1.00
P_{int10}	1.12	1.00	1.38	1.02	1.06	1.11	1.04	1.12	1.00	1.00	1.01	1.01	1.00	1.01	1.00	

Table 3. Characteristics of the rainfall and discharge events in the catchments Husten and Hüppcherhammer.

	Hüppcherhammer		Husten	
	Winter: Average; min - max	Summer: Average; min – max	Winter: Average; min – max	Summer: Average; min – max
$[Q_{i-1}]$	0.95 m³/s; 0.17–6.73 m³/s	0.35 m³/s; 0.10–1.34 m³/s	0.09 m³/s; 0.01–0.31 m³/s	0.02 m³/s; 0.01–0.09 m³/s
$[Q_{max}]$	13.7 m³/s	1.19 m³/s	0.2 m³/s; 0.02–0.69 m³/s	0.07 m³/s; 0.01–0.32 m³/s
$[Q_d]$	1,902 min; 45–6,825 min	1,272 min; 15–11,490 min	597 min; 120–1,290 min	721 min; 405–1,500 min
$[Q_V]$	245,000 m³; 2,365–3,374,300 m³	82,900 m³; 224–2,542,400 min	5,936 m³; 212–22,378m³	2,115 m³; 297–8,651 m³
$[P_{t1}]$			14.1 mm; 0.2–66 mm	10.7 mm; 0.2–79.4 mm
$[P_d]$			1,196 min; 10–3,890 min	675 min; 10–5,000 min
$[P_{int}]$			0.014 mm/min; 0.004–0.067 mm/min	0.023 mm/min; 0.001–0.093 mm/min
$[P_{int10}]$			1.3 mm/10min; 0.2–3.8 mm/10min	1.7 mm/10min; 0.2–6.4 mm/10min
$[P_{t2}]$	14.9 mm/d; 0–76.8 mm/d	10.8 mm/d; 0–75.2 mm/d		
$[P_{t3}]$			14.3 mm/d; 0–72.6 mm/d	11.2 mm/d; 0–79.8 mm/d
MQ	1.24 m³/s (48 years)		0.078 m³/s (8 years)	
HQ	37.3 m³/s (48 years)		3.16 m³/s (8 years)	

the rainfall intensity (P_{int}) of the events in summer is higher than in winter (Table 3). Spatially, merely a small difference was detected in daily rainfall measured at the station Drolshagen (P_{t2}) and Husten (P_{t3}) during summer and winter. At the gauging station Hüppcherhammer, the duration of the runoff events (Q_d) is, on average, 1902 minutes during the summer and 1272 minute during the winter. Also the total runoff amount (Qv) of an event is higher in winter (Ø 245.000 m³) than in the summer (Ø 82.900 m³). The pre-event discharge (Q_{i-1}) is lower in summer (0.35 m³/s) than in winter (0.95 m³/s).

Relations between soil water potential and discharge in the catchment Husten

The relationship between soil water potential (SF, SL, SM, SU) and discharge in the small-scale catchment Husten for the observation period 2001 underlines the influence of wetness conditions on discharge (Fig. 2). The scattering of the soil water tensions and the discharge values based on a 30 min-interval clearly shows that runoff increases if and only if the soil water potential in the upper soil (20 cm) reaches a specific threshold (60 hPa) which is similar to the upper, middle and lower slope. The threshold at the floodplain position is approximately 0 hPa. These thresholds describe the alternation between unsaturated and saturated conditions, which are combined with different flow velocities of the subsurface soil water and impacted by topographic features. Thus, for a higher discharge both the saturation of the upper and the lower soil is necessary. Additionally, the locations upper (SU), middle slope (SM) and lower slope (SL) show a similar scattering of the measured soil water potential and similar thresholds, which indicates that these two locations are characterized by a comparable soil hydrological behavior. Thus, these locations can be described as a hillslope hydrological system in comparison to the location at the floodplain (SF) which represents the riparian zone.

Regression model for the small-scale catchment Husten

In 2002 and 2003, 30 events could be isolated for the small-scale catchment. Due to the limited number of observations, separate calculations and statistical analyses were not performed for winter and summer seasons. The regression models show that, besides rainfall, soil water potential at the lower slope (SL_{200}) and floodplain (SF_{20}, SF_{80}) sites are highly relevant for peak discharge and discharge volume (Tables 4 and 5).

In the floodplain, soil moisture in the topsoil (20 cm) was detected as a significant variable for peak discharge, and soil moisture in the subsoil (80 cm) of the lower slope is part of the regression for discharge volume. Total rainfall is also significant for peak discharge and discharge volume in the models.

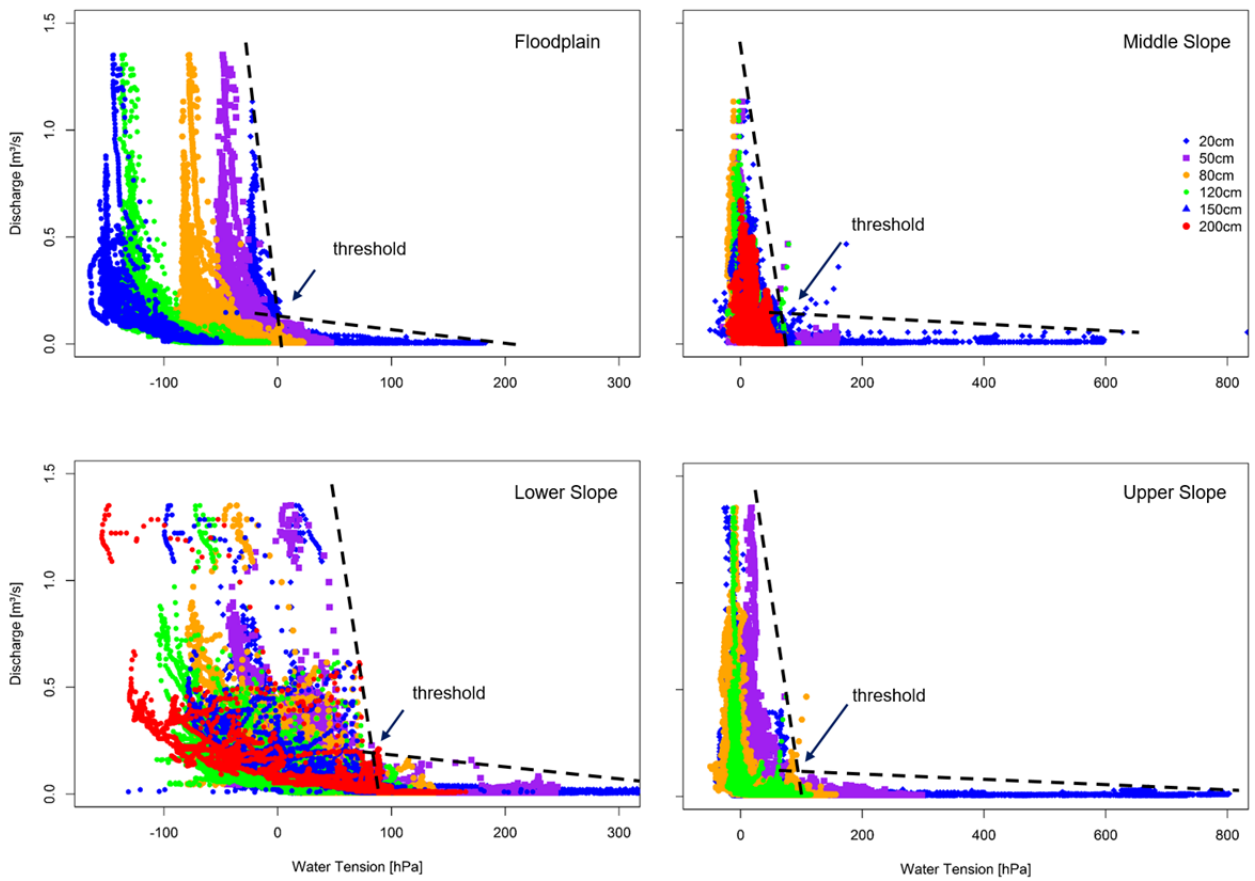

Fig. 2. Relationship between soil water potential at SF, SL, SM, SU and discharge in the catchment Husten for 2001 (30 min-interval; crossing points of the dashed lines indicate the thresholds).

Discharge duration, however, cannot be explained by any combination of variables in the catchment Husten. Only the soil water potential at the lower slope (SL_{200}) can explain about 14% of the scattering. Soil moisture of the middle and upper slope sites are not included in the regression model, which indicates that during the hydrological conditions of the observation period these sites are not sensitive for the prediction of peak discharge and discharge volume in the small catchment Husten. On the whole, the adding of the soil moisture potential from the flood plain and the lower slope improves considerably the quality of the regression models for the target variables peak discharge, discharge duration and discharge volume by approximately 10%, 14% and 21% at the small-scale catchment.

Results for the meso-scale catchment Hüppcherhammer

For 2002 and 2003, 100 events could be isolated for the meso-scale catchment Hüppcherhammer. Due to the large number of observations, separate calculations and statistical analyses for the hydrological winter and summer seasons could be performed. The regression models show that different independent variables are necessary for the prediction of the different discharge variables during the winter and summer seasons (Table 6 and 7). Additionally, the characteristics of rainfall events and soil moisture often show greater spatiotemporal variance during summer. Thus, more variables are stepwise included in the model to depict the more complex situation. Comparing the coefficients of determination of the different regression models it is noteworthy that the coefficients for the winter are nearly always higher than for the summer or for both periods combined. On the whole, for the different target variables peak discharge, discharge duration and discharge volume the adding of the soil moisture from the flood plain and the lower slope as explanatory variable improves the quality of the regression model for the meso-scale catchment by 15%, 20% and 10%, respectively, especially during the summer season. In the winter season the improvement is smaller (up to 6%) and the regression models mainly include rainfall characteristics as explanatory variables.

The most important explanatory variables for **peak flow** (Q_{max}) are rainfall variables (Table 7); this is daily rainfall in winter and event rainfall in summer. The different rainfall variables can be interpreted as to the dominance of short and localized rain storms during summer, whereas more evenly distributed rainfall is common in winter. Aside from rainfall, the pre-event discharge is significant for the peak discharge in winter.

Soil moisture at a depth of 50 cm at the floodplain site increases the model quality for both the total period and for the summer.

Unsurprisingly, rainfall duration best explains the **duration of a discharge** (Q_d) event, particularly in winter, when soil moisture is less variable (Table 8). Aside from rainfall duration, maximum 10-minute rainfall intensity is the sole additional variable in the final model for the winter season. Soil moisture at the lower slope position increases the quality of the model for the summer. In the stepwise search for the variables that

Table 4. Small-scale catchment Husten: Coefficient of determination of the regression models and independent variables with algebraic sign.

	Husten, all events (n = 30)
[Q_{max}]	0.777 ([$+P_{t1}$],[$-SF_{20}$])
[Q_d]	0.144 ([$-SL_{200}$])
[Q_V]	0.892 ([$+P_{t1}$],[$-SF_{80}$])

Table 5. Stepwise regression analyses for Q_{max} Q_d and Q_v with the coefficients of determination (Husten).

	Q_{max}			Q_d		Q_V		
Model no.	adj. R^2	P_{t1}	SF_{20}	adj. R^2	SL_{200}	adj. R^2	P_{t1}	SF_{80}
1	0.686	x		0.144	x	0.682	x	
2	0.777	x	x			0.892	x	x

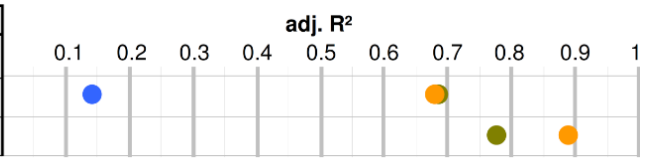

● = Q_{max}; ● = Q_d; ● = Q_V

Table 6. Meso-scale catchment Hüppcherhammer: Coefficient of determination of the regression models and independent variables with algebraic sign.

	All events (n = 100)	Winter events (n = 29)	Summer events (n = 71)
[Q_{max}]	0.833 ([+P_{t1}], [+Q_{i-1}], [+P_d], [–SF_{50}], [+P_{t2}])	0.920 ([+P_{t2}], [+Q_{i-1}]	0.762 ([P_{t1}], [–SF_{50}], [+P_d], [–ΔP])
[Q_d]	0.672 ([+P_d], [–SL_{120}], [+P_{int}], [–P_{t2}], [+P_{t1}])	0.791 ([+P_d], [–P_{int10}])	0.711 ([+P_d], [+P_{t1}], [–SL_{120}], [–P_{t2}], [–SF_{150}], [–SF_{120}], [+P_{int}],], [–ΔP])
[Q_V]	0.819 ([+Q_{i-1}], [+P_{t1}], [–SL_{120}], [–SF_{120}], [–P_{int10}])	0.925 ([+Q_{i-1}], [+SF_{120}], [+P_d])	0.659 ([+P_{t1}], [–SL_{120}],], [–P_{int10}])

Table 7. Stepwise regression analyses for Q_{max} with the coefficients of determination (Hüppcherhammer).

Model no.	adjusted R^2			P_{t1}	P_d	P_{t2}	ΔP	Q_{i-1}	SF_{50}
1	0.641	0.612	0.823	◆ ■		▲			
2	0.794	0.673	0.920	◆ ■		▲		◆ ▲	■
3	0.813	0.729		◆ ■	◆ ■			◆	■
4	0.823	0.762		◆ ■	◆ ■		■	◆	◆ ■
5	0.833			◆	◆	◆		◆	◆

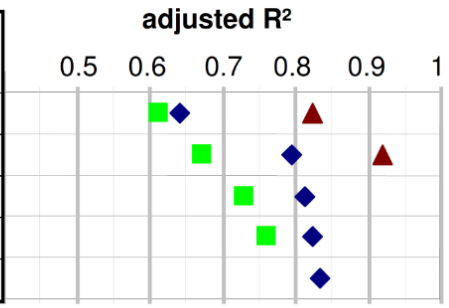

◆ = 12-month period; ■ = summer season (May 1 - October 31); ▲ = winter season (November 1 – April 30)

Table 8. Stepwise regression analyses for Q_d with the coefficients of determination (Hüppcherhammer).

Model no.	adjusted R^2			P_{t1}	P_d	P_{int}	P_{int10}	ΔP	P_{t2}	SF_{120}	SF_{150}	SL_{20}	SL_{120}
1	0.515	0.444	0.674		◆ ■ ▲								
2	0.559	0.509	0.791		◆ ■ ▲			▲				■	◆
3	0.607	0.562		■	◆ ■	◆						■	◆
4	0.620	0.598		■	◆ ■	◆			◆			■	◆ ■
5	0.672	0.596		◆ ■	◆ ■	◆			◆				◆ ■
6		0.631		■	■				■				■
7		0.656		■	■				■	■			■
8		0.678		■	■				■	■	■		■
9		0.694		■	■	■			■	■	■		■
10		0.711		■	■	■		■	■	■	■		■

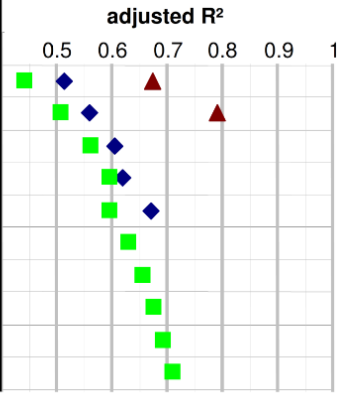

◆ = 12-month period; ■ = summer season (May 1 - October 31); ▲ = winter season (November 1 – April 30)

Table 9. Stepwise regression analyses for Q_v with the coefficients of determination (Hüppcherhammer).

Model no.	adjusted R^2			P_{t1}	P_d	P_{int10}	Q_{i-1}	SF_{120}	SL_{120}
1	0.557	0.543	0.801	■			◆ ▲		
2	0.768	0.639	0.869	◆ ■			◆ ▲	▲	■
3	0.783	0.659	0.925	◆ ■	▲	■	◆ ▲	▲	◆ ■
4	0.809			◆			◆	◆	◆
5	0.819			◆		◆	◆	◆	◆

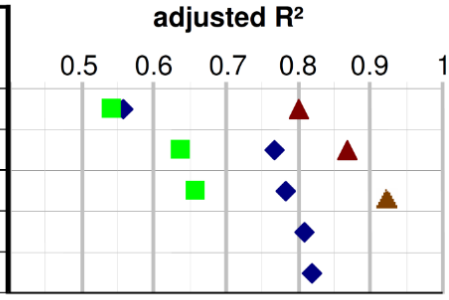

◆ = 12-month period; ■ = summer season (May 1 - October 31); ▲ = winter season (November 1 – April 30)

best explain the variance, soil moisture at a depth of 20 cm, introduced in step 2, is replaced by soil moisture at a depth of 120 cm in step 5. The daily rainfall measured at the additional gauging station (P_{t2}) in the meso-scale catchment is included in the models for the summer season and the 12-month period to depict the spatially more complex rainfall pattern in the summer. Furthermore, with the last step of the regression analysis the difference (ΔP) between the daily rainfall in Drolshagen (P_{t2}) and Husten (P_{t3}) becomes part of the final model for summer. Discharge prior to the event and the rainfall [P_{t1}] are by far the most important variables, resulting in a R^2 of 0.768 (Table 9) for the total **discharge volume** (Q_v) in the 12-month period. The addition of three more independent variables only slightly improves the quality of the model to 0.819. During the winter period, the pre-event discharge appears to be most significant. This variable alone statistically explains 80% of the variance, however this high value is likely attributable to one extreme discharge event. Therefore, the hydrological relevance of the pre-event discharge must be discussed. Once again, soil moisture in 120 cm at the lower slope ranks second in importance behind rainfall in summer. Concerning flow volume in winter, soil moisture in the flood plain at a depth of 120 cm is more important than during summer, when soil moisture variability is high.

DISCUSSION

Controlling factors for discharge at the small-scale catchment Husten

At this spatial scale the results of the regression analyses clearly show that the event-based rainfall amount (P_{t1}) is the most important independent variable for predicting peak discharge and discharge volume, as it explains nearly 69% of their variability. The soil water potentials at depths of 20 cm and 80 cm (SF_{20} and SF_{80}) at the floodplain site and of 200 cm at the lower slope site (SL_{200}) markedly improve the performance of these regression models up to coefficients of determination of 0.78 and 0.89, respectively. For a small mountain catchment (22 km²) Kostka and Holko (2003) also showed that the runoff volume is mainly controlled by the rainfall amount. Nevertheless, the observation of the soil moisture dynamics at the point scale arranged at different slope positions (upper, middle, lower slope and floodplain) and covering different soil depths are a good estimator for the average soil moisture dynamics at the small-scale catchment. Furthermore, the inclusion of the variables SF_{20}, SF_{80} and SL_{200} in the regression models indicates the importance that the adjacent floodplain and the lower hillslope wetness have for the runoff response in this small-scale catchment, especially for the prediction of the discharge volume (Qv). This is consistent with studies that show the wetness at the lower hillslope sector (Zehe et al., 2010) or the soil moisture at 30 cm soil depth (Aubert et al., 2003) has great explanatory power for event discharge. The pre-event discharge, which is often used for the antecedent wetness of a catchment (e.g. Graeff et al., 2009), has no statistical effect on the prediction of the mentioned runoff parameters in the small-scale catchment Husten. This underlines the importance of direct soil moisture measurements to estimate antecedent wetness as shown in e.g. Blume et al. (2009), Schädel (2006), Zehe and Blöschl (2004) or Zehe et al. (2010). Thus, a set of distributed point measurements of soil water potential may yield representative information on temporal soil moisture dynamics at the headwater scale. Additionally, this information on temporal soil water potential dynamics can be used and may even be advantageous for flood warning purposes, as shown by Aubert et al. (2003) and Anctil et al. (2008).

Controlling factors for discharge at the meso-scale catchment Hüppcherhammer

The results of the regression analyses show that the number of explanatory variables for the prediction of the runoff parameters (peak discharge, discharge volume and duration of discharge event) at the meso-scale catchment Hüppcherhammer (47.2 km²) are higher in the meso-scale catchment than in the small-scale catchment and additionally, are higher in summer than in winter. This indicates the greater complexity of the larger drainage basin. Small-scale temporal and spatial variability of processes that eventually generate creek and river discharge superimpose each other and smoothen the hydrograph. To achieve a reasonable statistical description for peak flow (Q_{max}), at least one or more precipitation variables must be included in the model. One precipitation variable is sufficient for the winter model, whereas three precipitation variables are necessary to capture the effects of the temporally and spatially more complex precipitation situation in summer. For the latter, the combination of rainfall event sum and duration describe the rainfall intensity, which shows a much larger span in summer than in winter. To aid in describing the larger spatial variability of precipitation during summer, the difference in daily rainfall between the two measurement sites is included as a third precipitation variable as well. For both the summer and the total period, soil moisture at a depth of 50 cm at the floodplain site increases the model quality. Similar to the small-scale catchment and in accordance with the findings of Kostka and Holko (2003), this indicates the importance of the riparian zone in the headwater of a catchment in peak discharge prediction. Besides rainfall characteristics, the regression models for prediction of summer discharge duration also includes the lower slope soil moisture at a depth of 120 cm, which depicts the connectivity between the slope hydrological system and the adjacent floodplain best. Blume and van Meerveld (2015) underline the importance of antecedent wetness conditions for the subsurface connectivity. In our study, the tensiometers were installed in the Sw-horizon of a soil with a transient perched aquifer that developed within the lower slope sediments. Thus, the water table gradient is steep and hydraulic conductivity is highest, which means a great deal of water is transferred towards the floodplain as subsurface runoff and eventually into the creek. Subsurface runoff is reported to be the dominant runoff process in many other studies of low mountain ranges in temperate climates (Bachmair and Weiler, 2011; Blume and van Meerveld, 2015; Moldenhauer et al., 2013). Indeed, the functional relationship to discharge is effective only when rainfall is incorporated in the model, but in this context the role of stratified soils has to be noticed. The soil moisture dynamic at the lower slope is influenced both by groundwater in the lower horizons (SL_{150} & SL_{190}) and by soil water in the upper horizons (SL_{20} & SL_{50}). Thus, a high correlation of the temporal variability of the soil water measurements in these depths maybe expected, but the low VIF of these depths don`t confirm this assumption (Table 2). It is assumed, that the low VIF for the soil moisture variables are caused by the specific soil structure at this location, which is very heterogeneous. Stratified soils consist of different soil hydraulic properties in the different layers and horizons, which can cause different soil moisture dynamics within the same time period. Thus, the soil moisture dynamic on the different depths can be temporally decoupled more often than in homogenous soils and integrated separately into the developed regression models. The fact that during winter maximum 10-minute rainfall intensity is included as a second independent variable in the Q_d model can be interpreted to represent the fast runoff

components. The variable has a negative coefficient, which means that especially high rainfall intensities are connected to relatively short events. The highly significant statistical relationship between pre-event discharge and flow volume (Q_V) in winter was affected by a single, extreme event. If this is excluded from the dataset, R^2 drops to 0.11, whereas rainfall [P_{tl}] explains 38% of the variance. To conclude, the lower the base flow, the more important rainfall is for a high flow volume. This is in accordance with Zillgens et al. (2007), who analyzed 201 rainfall runoff events in three nested catchments (0.07 km², 15.5 km² and 150 km²; Saalach, Austrian Alps) and found that the characteristics of runoff events clearly depend on rainfall characteristics and initial base flow level.

In general, it has to be noticed that the adding of the soil water potential at the meso-scale catchment improves the predictive performance of the regression models relatively small by 15% (peak discharge), 20% (discharge duration) and 10% (discharge volume). This may be due to differences in hillslope geomorphology and correspondingly in soil hydrological responses to rainfall. Proceeding from the headwaters downstream, relatively large areas are more distant from the river and valley slopes steepen. This changes hydrological connectivity and soil hydrological reaction patterns. These effects might not have been covered by our experimental slope. Moreover, there is still a great need for research since the impact of the width of riparian areas on the hydrological subsurface connectivity between hillslope and stream is still not yet investigated sufficiently (Grabs et al., 2012; Jencso et al., 2010; Uchida et al., 2005). Especially for the shift from small-scale to meso-scale catchments the widths between hillslope and stream are increasing considerably. Additionally, the spatial variability of the rainfall within the meso-scale catchment could be a reason for the relatively small improvement of the regression models taking the soil water potential into account. However, the correlation of the daily rainfall of the station Drolshagen and Husten show a correlation coefficient of r = 0.95 which underlines the assumption, that in this study the spatial variability of the rainfall events at the meso-scale catchment is negligible and emphasizes the importance of the hillslope geomorphology.

Detecting the optimal placement of soil moisture sensors

The significance of single point soil moisture measurements essentially depends on the identification of a suitable location due to a catchment's spatial heterogeneity. Here, the riparian zone and the lower hillslope locations (Kostka and Holko 2003; Zehe et al., 2010), which are included in nearly all regression models (except for Q_{max} and Q_d in winter) at both scales, play an important role. This indicates that the soil moisture measured at and near the base of a valley appears more important than the soil moisture conditions at the upper and the middle hillslope. This is consistent with results published by Sidle et al. (2000), McGlynn and McDonnell (2003), McGlynn and Seibert (2003) and Klaus et al. (2015), who also emphasize the importance of the riparian zone for the runoff response of a catchment. Woods et al. (1997) additionally indicate the relevance of riparian zones in the forefront of convergent hillslopes. Such topographic features foster the concentration of surface and subsurface runoff in the center of the hillslope and benefits saturated areas downwards as a result of lateral water flow and decreasing hillslope inclination. The soil moisture measurement sites lower hillslope (SL) and floodplain (SF) represent such areas forefront of convergent hillslopes and are included in regression models at both spatial scales. Thus, these findings suggest that convergent hillslopes are key landscape units for runoff generation in this catchment, which is typical for low mountain ranges in Central Europe. The single point measurement of the soil moisture in this functional unit and in the detected depths may be optimal for estimating the antecedent wetness of the small- and meso-scale catchments and may thus yield valuable information for flood warning.

CONCLUSIONS

The most important finding is that soil moisture appears significant in every regression model. The influence of soil moisture as a determinant is generally higher for summer events than in winter. Soil moisture, as an indicator of the catchment's wetness or sensitivity to generate discharge, modulates the discharge triggered by rainfall. The appearance of the soil moisture variables in the stepwise regression indicates their varying importance, depending on which characteristics of the discharge are of interest. Floodplain soil moisture is important in the models for flow volume (winter season) and peak flow (summer season) in both catchments. As the soil water potential from this site reflects the groundwater level, it not only represents the wetness caused by prior weather conditions (e.g. rainfall and evapotranspiration) but it also indicates the hydraulic status of the aquifer near the creek. Thus, it carries dual information and correlates with pre-event discharge.

On the other hand, soil moisture at the lower slope is of great significance for both flow volume and flow duration. Both models of the meso-scale catchment include the soil moisture at a depth of 120 cm. As expected, lower slopes function as connective elements between the hydrological subsystem of the slope and that of the floodplain. Especially in the case of convergent slopes, subsurface flow is either quickly routed through the lower slope to the aquifer or it transmits a pressure pulse downslope towards the aquifer, where water eventually escapes to the receiving creeks. This is a strong argument for our hypothesis that using point data of soil moisture to forecast discharge characteristics for fairly large catchments is justified, as long as the measurement sites are carefully selected. Another prerequisite is that the entire moisture depth profile should be examined before defining the measurement depth with the highest significance.

Rainfall from two stations is incorporated in two of the three models for the meso-scale catchment. This is consistent with the practice (e.g. Pluntke et al., 2010) that spatial variations of precipitation cannot be neglected in scale transitions. In this respect, upscaling the most important input variable does not seem to be justified. We can assume that rainfall from the gauging station Drolshagen in the meso-scale catchment does not show up in the model for flow volume because it is substituted by the antecedent discharge which – standing alone or in combination with other variables – is indeed a highly significant determinant for peak flow and flow volume.

All in all, the number of independent variables is greater in the case of the meso-scale catchment than in the small scale catchment. For example, for Q_D and Q_V these are 5 and 2 variables, respectively. This reflects the greater complexity of the larger drainage basin, in which the runoff generating processes at the small scale are blurred. Small-scale spatiotemporal variability of processes that eventually generate creek and river discharge superimpose each other and smoothen the hydrograph. Consequently, characteristics of a discharge event cannot be assigned to data from single points that merely depict subordinate and local processes. We suspect that in general, discharge fluctuates considerably in small catchments, making flood forecasts extremely difficult at this scale. Also, the num-

ber of explanatory variables is higher in summer (up to 10) than in winter (3 or less). This can be explained by the higher temporal and spatial variability of soil moisture in summer as well as the fact that localized rainfall events occur more often, many of which with high intensity.

Our study underpins the expedience of using tensiometers in place of TDR probes, which are commonly used (Brocca et al., 2007; Penna et al., 2011; Zehe et al., 2010) to assimilate soil moisture into rainfall-runoff modeling. Our analysis shows that further studies on flood forecasting should concentrate on carefully selecting representative measurement sites to improve the quality of forecasts instead of labor-intensive and costly attempts to monitor the soil moisture of an entire catchment. We value extensive soil moisture monitoring for its function in, for instance, precision farming and risk analysis concerning the fate of agrochemicals, however not in its use in operational flood warning systems.

REFERENCES

Ali, G., Tetzlaff, D., McDonnell, J.J., Soulsby, C., Carey, S., Laudon, H., McGuire, K., Buttle, J., Seibert, J., Shanley, J., 2015. Comparison of threshold hydrologic response across northern catchments. Hydrol. Process., 29, 16, 3575–3591.

Ali, G.A., Roy, A.G., Legendre, P., 2010. Spatial relationships between soil moisture patterns and topographic variables at multiple scales in a humid temperate forested catchment. Water Resour. Res., 46, W10526. DOI: 10.1029/2009wr008804.

Alvarez-Garreton, C., Ryu, D., Western, A.W., Crow, W.T., Robertson, D.E., 2014. The impacts of assimilating satellite soil moisture into a rainfall–runoff model in a semi-arid catchment. J. Hydrol., 519, 2763–2774.

Anctil, F., Lauzon, L., Filion, M., 2008. Added gains of soil moisture content observations for streamflow predictions using neural networks. J. Hydrol., 359, 3–4, 225–234.

Aubert, D., Loumagne, C., Oudin, L., 2003. Sequential assimilation of soil moisture and streamflow data in a conceptual rainfall-runoff model. J. Hydrol., 280,145–161.

Baade, J., 1994. Geländeexperimente zur Verminderung des Schwebstoffaufkommens in landwirtschaftlichen Einzugsgebieten. Heidelberger Geographische Arbeiten 96, 215 p.

Bachmair, S., Weiler, M., 2011. New dimensions of hillslope hydrology. In: Levia, D.F., Carlyle-Moses, D., Tanaka, T. (Eds.): Forest Hydrology and Biogeochemistry: Synthesis of Past Research and Future Directions. Ecological Studies 216, pp. 455–481.

Bezirksregierung Köln, 2015. TIM-Online; http://www.tim-online.nrw.de. Accessed 10 September 2015.

Blume, T., van Meerveld, H.J.I., 2015. From hillslope to stream: methods to investigate subsurface connectivity. Wiley Interdisciplinary Reviews: Water, 2, 3, 177–198.

Blume, T., Zehe, E., Bronstert, A., 2007. Rainfall-runoff response, event-based runoff coefficients and hydrograph separation. Hydrological Sciences Journal, 52, 5, 843–862.

Blume, T., Zehe, E., Bronstert, A., 2009. Use of soil moisture dynamics and patterns at different spatio-temporal scales for the investigation of subsurface flow processes. Hydrol. Earth Syst. Sci., 13, 1215–1233. DOI: 10.5194/hess-13-1215-2009.

Bogena, H.R., Herbst, M., Huisman, J.A., Rosenbaum, U., Weuthen, A., Vereecken, H., 2010. Potential of wireless sensor networks for measuring soil water content variability. Vadose Zone Journal, 9, 4, 1002–1013.

Brocca, L., Morbidelli, R., Melone, F., Moramarco, T., 2007. Soil moisture spatial variability in experimental areas of central Italy. J. Hydrol., 333, 356–373.

Brocca, L., Melone, F., Moramarco, T., Singh, V.P., 2009. Assimilation of observed soil moisture data in storm rainfall-runoff modelling. J. Hydrol. Eng., 14, 2, 153–165.

Brocca, L., Melone, F., Moramarco, T., Morbidelli, R., 2010. Spatial-temporal variability of soil moisture and its estimation across scales. Water Resour. Res., 46, W02516. DOI: 10.1029/2009WR008016.

Bronstert, A., Creutzfeldt, B., Graeff, T., Hajnsek, I., Heistermann, M., Itzerott, S., Jagdhuber, T., Kneis, D., Lück, E., Reusser, D., Zehe, E., 2012. Potentials and constraints of different types of soil moisture observations for flood simulations in headwater catchments. Nat. Hazards, 60, 879–914.

Casper, M., Gemmar, P., Gronz, O., Johst, M., Stüber, M., 2007. Fuzzy logic-based rainfall-runoff modelling using soil moisture measurements to represent system state. Hydrol. Sci. J., 52, 3, 478–490.

Chen, F., Chrow, W.T., Ryu, D., 2014. Dual forcing and state correction via soil moisture assimilation for improved rainfall-runoff modeling. J. Hydrometeor., 15, 1832–1848. DOI: http://dx.doi.org/10.1175/JHM-D-14-0002.1.

Chifflard, P., Zepp, H., 2008. Erfassung der zeitlichen Variabilität der Abflussbereitschaft eines Einzugsgebietes auf Grundlage von Bodenfeuchtemessungen. HyWa, 52, 3, 98–109.

Chifflard, P., Zepp, H., Schumann, A., 2004. Untersuchungen zum Einfluss der Vorfeuchte und des Reliefs auf die Abflussbildung. Forum für Hydrologie und Wasserbewirtschaftung, 05.04(2), 69–73.

Chifflard, P., Didszun, J., Zepp, H., 2008. Skalenübergreifende Prozess-studien zur Abflussbildung in Gebieten mit periglazialen Deckschichten (Sauerland, Deutschland). Grundwasser, 13, 1, 27–41.

Chifflard, P., Gall, S., Zepp, H., 2013. Regionalisierung der Oberbodenfeuchte im Südsauerländer Bergland (Deutschland, Nordrhein-Westfalen). Jahrbuch der Marburger Geographischen Gesellschaft 2013, pp. 146–165.

Deutscher Wetterdienst, 2004. Langjährige Klimadaten der Stationen Reichshof-Eckenhagen, Bergneustadt-Hüngrighausen und Attendorn-Listertalsperre. Offenbach.

Dikau, R., 1986. Experimentelle Untersuchungen zu Oberflächenabfluss und Bodenabtrag von Messparzellen und landwirtschaftlichen Nutzflächen. Heidelberger Geographische Arbeiten, 81, 195 p.

Engels, S., Marschner, B., Zepp, H., 2012. Analysing soil moisture reactions to precipitation for soil moisture regionalization. Geophys. Res. Abstr., 14, EGU2012-8472.

Fang, B., Lakshmi, V., 2014. Soil moisture at watershed scale: Remote sensing techniques. J. Hydrol., 516, 258–271.

Grabert, H., Hilden, H.D., 1972. Geologische Karte von Nordrhein-Westfalen 1:25000, Blatt 5012 Eckenhagen mit Erläuterungen. Geologisches Landesamt Nordrhein-Westfalen, Krefeld.

Grabs, T., Bishop, K., Laudon, H., Lyon, S.W., Seibert, J., 2012. Riparian zone hydrology and soil water total organic carbon (TOC): implications for spatial variability and upscaling of lateral riparian TOC exports. Biogeosciences, 9, 3901–3916.

Graeff, T., Zehe, E., Reusser, D., Luck, E., Schroder, B., Wenk, G., John, H., Bronstert, A., 2009. Process identification through rejection of model structures in a mid-mountainous rural catchment: observations of rainfall-runoff response, geophysical conditions and model inter-comparison. Hydrol. Process., 23, 5, 702–718. DOI: 10.1002/hyp.7171.

Graeff, T., Zehe, E., Blume, T., Francke, T., Schröder, B., 2012. Predicting event response in a nested catchment with generalized linear models and a distributed watershed model. Hydrol. Process., 26, 3749–3769.

Hedderich, J., Sachs, L., 2016. Angewandte Statistik. Methoden-

sammlung mit R. Revised 14th printing. Springer, Berlin, Heidelberg, 969 p. DOI: 10.1007/978-3-662-45691-0.

Hrnčíř, M., Šanda, M., Kulasová, A., Císlerová, M., 2010. Runoff formation in a small catchment at hillslope and catchment scales. Hydrol. Process., 24, 2248–2256, DOI: 10.1002/hyp.7614.

Jacobs, J.M., Mohanty, B.P., Hsu, E.C., Miller, D., 2004. SMEX02: Field scale variability, time stability and similarity of soil moisture. Remote Sens. Environ., 92, 4, 436–446.

Jencso, K.G., McGlynn, B.L., Gooseff, M.N., Bencala, K.E., Wondzell, S.M., 2010. Hillslope hydrologic connectivity controls riparian groundwater turnover: Implications of catchment structure for riparian buffering and stream water sources. Water Resour. Res., 46, W10524.

Klaus, J., McDonnell, J.J., Jackson, C.R., Du, E., Griffiths, N.A., 2015. Where does streamwater come from in low-relief forested watersheds? A dual-isotope approach. Hydrol. Earth Syst. Sci., 19, 125–135.

Kostka, Z., Holko, L., 2003. Analysis of rainfall-runoff events in a mountain catchment. In: Holko, L., Miklanek, P. (Eds.): Interdisciplinary Approaches in Small Catchment Hydrology: Monitoring and Research. IHP-VI Technical Documents in Hydrology No. 67, UNESCO, Paris, pp. 19–25.

Lakshmi, V., 2013. Remote sensing of soil moisture. ISRN Soil Science, 2013, Article ID 424178, 33 p. DOI: 10.1155/2013/424178.

Longobardi, A., Villani, P., Grayson, R.B., Western, A.W., 2003. On the relationship between runoff coefficient and catchment initial conditions. In: Proceedings of MODSIM 2003, pp. 867–872.

Massari, C., Brocca, L., Moramarco, T., Tramblay, Y., Lescot, J.F.D., 2014. Potential of soil moisture observations in flood modelling: Estimating initial conditions and correcting rainfall. Adv. Water Resour., 74, 44–53.

McGlynn, B.L., McDonnell, J.J. 2003. Quantifying the relative contributions of riparian and hillslope zones to catchment runoff. Water Resour. Res., 39, 11, 1310. DOI: 10.1029/2003WR002091.

McGlynn, B.L., Seibert, J., 2003. Distributed assessment of contributing area and riparian buffering along stream networks. Water Resour. Res., 39, 4, 1082. DOI: 10.1029/2002WR001521.

Moldenhauer, K.M., Heller, K., Chifflard, P., Hübner, R., Kleber, A., 2013. Influence of cover beds on slope hydrology. In: Kleber, A., Terhorst, B. (Eds.): Mid-Latitude Slope Deposits (Cover Beds). Elsevier, Amsterdam, 302 p.

Ojha, R., Morbidelli, R., Saltalippi, C., Flammini, A., Govindaraju, R.S., 2014. Scaling of surface soil moisture over heterogeneous fields subjected to a single rainfall event. J. Hydrol., 516, 21–36.

Parajka, J., Naemi, V., Blöschl, G., Wagner, W., Merz, R., Scipal, K., 2006. Assimilating scatterometer soil moisture data into conceptual hydrologic models at coarse scales. Hydrol. Earth Syst. Sci., 10, 353–368.

Pellenq, J., Kalma, J., Boulet, G., Saulnier, G.M., Wooldridge, S., Kerr, Y., Chehbouni, A., 2003. A disaggregation scheme for soil moisture based on topography and soil depth. J. Hydrol., 276, 112–127.

Penna, D., Tromp-van Meerveld, H.J.I., Gobbi, A., Borga, M., Dalla Fontana, G., 2011. The influence of soil moisture on threshold runoff generation processes in an alpine headwater catchment. Hydrol. Earth Syst. Sci., 15, 689–702.

Penna, D., Mantese, N., Hopp, L., Dalla Fontana, G., Borga, M., 2015. Spatio-temporal variability of piezometric response on two steep alpine hillslopes. Hydrol. Process., 29, 198–211.

Petrone, R.M., Price, J.S., Carey, S.K., Waddington, J.M., 2004. Statistical characterization of the spatial variability of soil moisture in a cutover peatland. Hydrol. Process., 18, 1, 41–52.

Pluntke, T., Jatho, N., Kurbjuhn, C., Dietrich, J., Bernhofer, C., 2010. Use of past precipitation data for regionalisation of hourly rainfall in the low mountain ranges of Saxony, Germany. Nat. Hazards Earth Syst. Sci., 10, 353–370.

Rinderer, M., Kollegger, A., Fischer, B.M.C., Stähli, M., Seibert, J., 2012. Sensing with boots and trousers - qualitative field observations of shallow soil moisture patterns. Hydrol. Process., 26, 26,4112–4120.

Schädel, W., 2006. Schritte zur Verbesserung der Hochwasserfrühwarnung mittels Online-Bodenfeuchtemessungen. Mitteilungen des Institutes für Wasser und Gewässerentwicklung, Bereich Wasserwirtschaft und Kulturtechnik der Universität Karlsruhe, Band 234, 186 p.

Schendzielorz, E., 2004. Channel morphology of the stream Brachtpe. Internal dynamic, human-caused impacts on the flood generation and requirements for renaturation. Unpublished Master Thesis. Ruhr-University of Bochum, Germany. (In German.)

Sidle, R.C., Tsuboyama, Y., Noguchi, S., Hosoda, I., Fujieda, M., Shimizu, T., 2000. Stormflow generation in steep forested headwaters: a linked hydrogeomorphic paradigm. Hydrol. Process., 14, 369–385.

Tague, C., Band, L., Kenworthy, S., Tenebaum, D., 2010. Plot- and watershed-scale soil moisture variability in a humid Piedmont watershed. Water Resour. Res., 46, W12541. DOI: 10.1029/2009WR008078.

Tromp-Van Meerveld, I., McDonnell, J.J., 2006a. Threshold relations in subsurface stormflow: 1. A 147-storm analysis of the Panola hillslope. Water Resour. Res., 42, W02410. DOI: 10.1029/2004WR003778.

Tromp-Van Meerveld, I., McDonnell, J.J., 2006b. Threshold relations in subsurface stormflow: 2. The fill and spill hypothesis. Water Resour. Res., 42, W02411, DOI: 10.1029/2004WR003800.

Uchida, T., Asano, Y., Onda, Y., Mjyata, S., 2005. Are headwaters just a sum of hillslopes? Hydrol. Process., 19, 3251–3261.

Vereecken, H., Huisman, J.A., Pachepsky, Y., Montzka, C., van der Kruk, J., Bogena, H., Weihermüller, L., Herbst, M., Martinez, G., Vanderborght, J., 2014. On the spatio-temporal dynamics of soil moisture at the field scale. J. Hydrol., 516, 76–96.

Wagner, W., Blöschl, G., Pampaloni, P., Calvet, J.C., Bizzarri, B., Wigneron, J.P., Kerr, Y., 2007. Operational readiness of microwave remote sensing of soil moisture for hydrologic applications. Nord Hydrol., 38, 1, 1–20.

Western, A., Zhou, S.L., Grayson, R.B., McMahon, T.A., Blöschl, G., Wilson, D.J., 2004. Spatial correlation of soil moisture in small catchments and its relationship to dominant spatial hydrological processes. J. Hydrol., 286, 1–4, 113–134.

Woods, R.A., Sivapalan, M., Robinson, J.S., 1997. Modeling the spatial variability of subsurface runoff using the topographic index. Water Resour. Res., 33, 5, 1061–1073.

Zehe, E., Blöschl, G., 2004. Predictability of hydrologic response at the plot and catchment scales: Role of initial conditions. Water Resour. Res., 40, W10202, DOI: 10.1029/2003WR002869.

Zehe, E., Graeff, T., Morgner, M., Bauer, A., Bronstert, A., 2010. Plot and field scale soil moisture dynamics and subsurface wetness control on runoff generation in a headwater in the Ore Mountains. Hydrol. Earth Syst. Sci., 14, 873–889.

Zillgens, B., Merz, B., Kirnbauer, R., Tilch, N., 2007. Analysis of the runoff response of an alpine catchment at different scales. Hydrol. Earth Syst. Sci., 11, 1441–1454.

Received 8 December 2016
Accepted 16 May 2017

J. Hydrol. Hydromech., 66, 2018, 1, 12–22
DOI: 10.1515/johh-2017-0044

Influence of discharge on fish habitat suitability curves in mountain watercourses in IFIM methodology

Viliam Macura[1], Zuzana Štefunková[2], Martina Majorošová[1], Peter Halaj[3], Andrej Škrinár[1*]

[1] Department of Land and Water Resources Management, Faculty of Civil Engineering, Slovak University of Technology in Bratislava, Bratislava, Slovakia.
[2] Department of Hydraulic Engineering, Faculty of Civil Engineering, Slovak University of Technology in Bratislava, Bratislava, Slovakia.
[3] Department of Landscape Engineering, Faculty of Horticulture and Landscape Engineering, Slovak University of Agriculture in Nitra, Nitra, Slovakia.
[*] Corresponding author. E-mail: andrej.skrinar@stuba.sk

Abstract: In this study, the quality of the aquatic habitats of mountain and piedmont streams was evaluated using the 'Instream Flow Incremental Methodology (IFIM)' decision-making tool. The quality of habitats was interpreted from the behaviour of bioindicators in the form of habitat suitability curves (HSCs). From 1995 until the present, 59 different reaches of 43 mountain streams in Slovakia and 3 validation reaches were evaluated, and the results analysed. The aim of this study was to generalize the parameters of the HSCs for the brown trout. The generalized curves will be useful for water management planning. It is difficult and time-consuming to take hydrometrical and ichthyological measurements at different water levels. Therefore, we developed a methodology for modifying suitability curves based on an ichthyological survey during a low flow and a flow at which fish lose the ability to resist the flow velocity. The study provides the information how such curves can be modified for a wider flow range. In summary, this study shows that generalized HSCs provide representative data that can be used to support both the design of river restoration and the assessment of the impacts of the water use or of climate change on stream habitat quality.

Keywords: Instream Flow Incremental Methodology (IFIM); Weighted Usable Area (WUA); Habitat suitability curves (HSCs); Brown trout.

INTRODUCTION

River regulation changes the basic morphology and flow characteristics of a river by, for example, removing the alternating of riffle zones with calm pool areas, as well as destroying the variable riparian borders and a wide range of cover places for fish. This type of activity has a negative impact on the biota of rivers, and typically results in decreased biodiversity (Cianfrani et al., 2009; Palmer et al., 2010). The negative impacts are further exacerbated by intense climate change (Van Loon et al., 2015), mainly by intense droughts during the summer seasons (Macura et al., 2016).

Modifications that result from river regulation are very noticeable in assessments of the availability of specific habitats that are needed for river restoration (Sullivan et al., 2006). It has been shown that the negative impacts of river regulation are mainly restricted to the upper reaches or *rhithral* of streams. The variability of the riverbed morphology decreases in the upper part of a stream, which has a significant impact on the ichthyofauna. Hence, any morphological changes are reflected by fish (Macura et al., 2012). The Water Framework Directive 2000/60/EU (2000) requires information about morphological changes and other quality characteristics of a stream that influence the presence of bioindicators including fish, diatoms, macrophytes, macroinvertebrates and similar organisms (Artemiadou and Lazaridou, 2005; Friberg et al., 2005).

A river restoration scheme that preserves the high variability of a riverbed does not have a negative impact on the overall ecosystem. The design parameters of covers, pools, and other structures that create a variable morphology in a regulated channel are therefore an important component of river restoration proposals (Pekárik et al., 2012). Biological and hydrological relationships have been studied in many streams, and authors have drawn attention to specific flow patterns that are particular to individual regions. These relationships, however, are better described by biological responses to alterations in flow regimes (Kändler and Seidler, 2013; Snelder and Lamouroux, 2010).

Lengthy discussions are ongoing among water managers, ichthyologists, and hydrobiologists (Lichner et al., 2014). At present, these specialists believe that the success or failure of any restoration project will depend on ongoing stream monitoring. Therefore, the aim of current research is to quantify the design characteristics of suitable habitats for river restoration (Döll and Zhang, 2010; Hatten et al., 2013; Pastuchová et al., 2010).

Considerable attention has been paid to the impact of climate on flow regimes (Filipe et al., 2013) and aquatic ecosystems (Fung et al., 2013), and on the protraction of dry seasons (Krysanova et al., 2010). IFIM, which is based on bioindicators, can be used to model the quality of a habitat in such studies.

When we initiated this stage of our research, we studied macrozoobenthos along with the ichthyofauna. Invertebrates respond to changes in flow and hydraulic changes (Mérigoux et al., 2009) but are less sensitive to morphological changes in regulated mountain streams (Holčík and Macura, 2001). Fish, however, are sensitive to morphological changes (Aparicio et al., 2011; Slavík et al., 2005). Furthermore, fish along with invertebrates are also sensitive to changes in water temperature, discharge (Lamouroux et al., 2006), and the quality of riparian vegetation (Džubáková et al., 2015).

MATERIALS AND METHODS

The quality of the aquatic habitats of mountain and piedmont streams was evaluated using the 'Instream Flow Incremental Methodology (IFIM)' decision-making tool. IFIM is based on

the knowledge that most fish species prefer certain combinations of water depths, flow velocities (Ayllón et al., 2010), availability of cover, and bed materials (Parasiewicz and Walker, 2007). IFIM can provide robust assessments of the quality of a river when sufficient data are available (Casper et al., 2011). One of the greatest advantages of IFIM over alternative methods (CCA, RDA, GLM and related-analyses) is the fact that it incorporates spatially distributed model in any desired detail. In the IFIM methodology the relationship between abiotic and biotic characteristics is represented by the HSCs of various species, which are multiparametric. The curves for flow velocity and water depth are the most widely used expressions of habitat preferences by particular fish species. The preferred technique of determining values on the vertical axis between 0.0 (avoided habitat) and 1.0 (most preferred habitat) is to fit a curve to a frequency distribution of empirically-derived data.

The summer period is confining for ichthyofauna because of the low water depths, limited refuge possibilities, and low oxygen content of overheated water. The main purpose of this study was to establish the standard HSCs ranging from low flows to flows at which the fish were washed out from preferred microhabitats. These curves give better picture of the real fish habitat preference and are more suitable for designing a river restoration scheme or to support a minimum flow assessment (Harby et al., 2007). The methodology for creating HSCs that represent a wider range of flow rates is presented in this contribution.

An understanding of the influence of various parameters on the shape of the HSCs was essential, so that this information could be applied to other similar flows. The process for developing the curves involved the following steps:

- reference reaches of the streams were selected;
- an ichthyological survey and hydrometric measurements were carried out;
- topographical measurements were made of the reference reaches;
- the probability distribution functions and return period curves of flows in the reference reaches of the streams were evaluated;
- the impact of velocity and water depths on the suitability rating of a habitat were evaluated;
- the HSCs were generalized, and
- the weighted usable area (WUA) was evaluated.

These steps are further described in following section:

Selection of the reference reaches of streams

From 1995 until the present, 59 different reaches of 43 mountain streams in Slovakia and 3 validation reaches have been evaluated. In this study, we focused on smaller mountain and piedmont streams (Fig. 1) for the following reasons:

- Mountain streams have more characteristics in common, and they have been badly managed in many areas. Because of the common characteristics of mountain streams, we can expect that the results from different streams will be similar.
- Mountain streams are found in the upper reaches of a river basin. They are generally difficult to access and therefore the pollution is uncommon. The water quality therefore generally reflects the impacts of the restoration on the flow and its surroundings.
- River regulation mainly affects the morphology of the riverbed. In order to distinguish the impact of the river morphology on the quality of the aquatic habitat, only streams with good water quality have been selected. In case of poor water quality it is difficult to distinguish the impact of morphology on habitat.
- The study was focused on the upper reaches of a stream (rhithral) mainly due to the following reasons: The regulation of mountain streams aimed to flood protection significantly changes the topography of the riverbed. Regulated channels are wide and there are small water depths during low flows. This is not a suitable habitat for fish. Furthermore, mountain streams have smaller basins and are mostly not affected by pollution, thus having a good water quality. The upper reaches are therefore more sensitive to changes in flow and morphology. In this study we determined the composition of the biotic trophic groups and their production.
- When using bioindicators and IFIM to research the quality of an aquatic habitat, we assume that extreme loads of river biota also affect its overall condition. Summer low flows are considered as an extreme period. Fish are the most sensitive bioindicator of morphological changes. The responses of the bioindicators are demonstrated through the suitability curves in IFIM. The specification of the HSCs, which represent the biota of the river, is therefore an important factor in IFIM.
- The correlation between the suitability curve parameters for the depths and the hydraulic characteristics of a river has been confirmed in our previous studies (Macura et al., 2016). Therefore, we assume that the HSCs can be generalized for certain areas with different flow depths.
- Evaluations of the impact of riverbed morphology on individual fish species show that the brown trout (*Salmo trutta* m. *fario*) is the most sensitive bioindicator of mountain streams (Macura et al., 2012). The trout is the only useful indicator in small Slovak streams and is therefore the primary target species; it was also the target species in studies of Danish streams according to Friberg et al. (2005). Therefore, we decided to focus on generalizing the HSCs for the brown trout.

Ichthyological survey and hydrometric measurements

This study was undertaken with the approval of the Ministry of Environment of the Slovak Republic. All the fish samples collected by electrofishing were immediately counted, weighted, measured and returned unharmed back to original locality in the riverbed. Authors declare that all customary standards concerning handling the live material applicable in the EU were complied.

Our ichthyological survey of selected reaches focused on determining the HSCs of individual fish species. It is important to remember that the HSCs were derived for an adult trout, because the juvenile species prefer other habitats, and would have influenced the shape of the curves (Ayllón et al., 2012). There is a similar effect from the body size of a brown trout (Ayllón et al., 2009; Parra et al., 2011). Data were obtained by electro fishing, as in Lamouroux et al. (1998). The fish were collected by an electrical aggregate with a continuous choice of electrical parameters (Hans Grassl-ELT62IIHI). The parameters of the electrical current of the aggregate were determined by the water conductivity and were also based on the fish species and their sensitivity to an electrical current, as reported in (Scholten, 2003). The flow depth, the characteristics of the microhabitat, and the velocity were surveyed at the sites where the fish were captured. The velocity was measured by a set of three hydrometric rod-mounted propellers at standard water depths (D) of 0.2 D, 0.4 D, and 0.8 D. The mean velocity in vertical derived from these measurements was used to evaluate the HSC for the velocity.

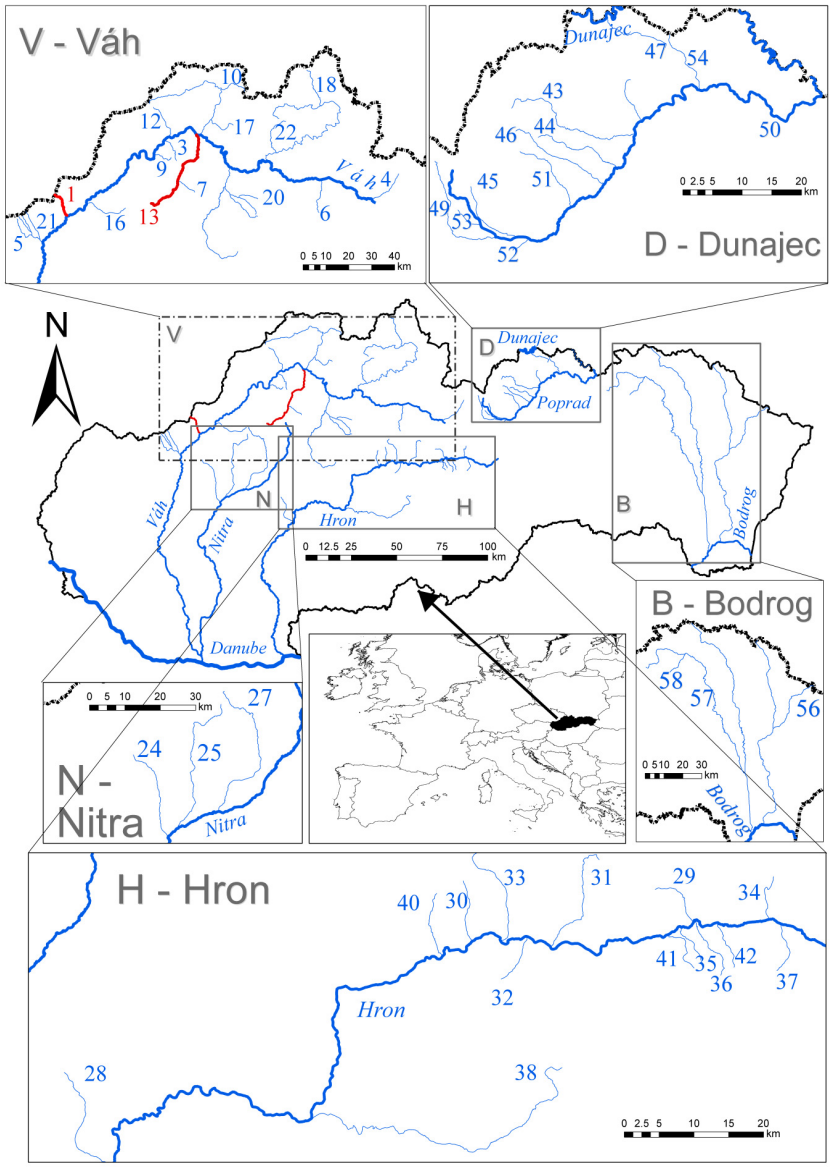

Fig. 1. Mountain and piedmont streams selected in Slovakia.

Topographical measurements of the reference reaches

The accuracy of the topographical survey of the reaches was adapted to the requirements of the hydraulic modelling. The river channel morphology was measured by cross-sections using levelling (Leica Sprinter 200M automatic level with height accuracy of 1.5 mm/1000m). Cross-sections locations were set by the Leica FlexLine TS02 Total Station (positional accuracy 1.5 mm + 2 ppm). Transformation to a national coordinate system S-JTSK was provided by the Leica GS15 GNSS measurements in the permanent SmartNet network.

Evaluation of the probability distribution functions and return period curves in the reference reaches of the streams

The quality of the habitat was assessed at different flow rates, and the M-day flow rates, determined in cooperation with the Slovak Hydrometeorological Institute, were used in the reference reaches. M-day flow is the average daily flow rate reached or exceeded by M days a year. The evaluation followed the interpolation method outlined in the national standard STN 75 1410-1:2008-01 (2008). The characteristics of the reference reaches and their M-day flows are presented in Table 1.

RESULTS

Generalization of the suitability curves

Suitability curves are time-consuming to develop because they are derived from an ichthyological survey using an electrical aggregate. If at all possible, therefore HSCs should be generalized.

As previously noted, the adult brown trout is the most sensitive bioindicator; therefore, we have generalized the characteristics of this fish in this study. A more detailed analysis and evaluation of the correlation between the abiotic and biotic characteristics is given in Macura et al. (2012).

The set of curves derived from the reference reaches of the streams (Table 1) was divided into several intervals depending on the average maximum water depths in the reach, i.e., <0.20 m, 0.21–0.30 m, 0.31–0.40 m, and 0.41–0.50 m. The average maximum water depth represents the average value of the maximum depths at the reference reaches. Each water depth interval was assigned to the corresponding HSCs, which were plotted together.

Table 1. The characteristics of the reference reaches.

Stream	Catchment	Stream character	Catchment area	M-day flow			Brown trout abundance
				Q_{30}	Q_{270}	Q_{364}	
			(km^2)	($m^3.s^{-1}$)	($m^3.s^{-1}$)	($m^3.s^{-1}$)	($pcs.ha^{-1}$)
Drietomica 1	Váh	Regulated	90.3	2.319	0.24	0.037	109
Drietomica 2	Váh	Natural	82.5	2.136	0.221	0.034	364
Hradnianka	Váh	Natural	32.1	0.675	0.133	0.025	1 081
Hybica 1	Váh	Natural	44.8	1.108	0.239	0.03	624
Kamečnica	Váh	Natural	12.8	0.366	0.038	0.006	2 267
Klačianka	Váh	Natural	27.2	0.76	0.137	0.02	1 374
Lesnianka 1	Váh	Regulated	25.3	1.179	0.169	0.058	1 131
Lesnianka 2	Váh	Natural	20.9	1.052	0.151	0.052	745
Manínsky stream	Váh	Natural	9.6	0.295	0.06	0.015	900
Osčadničanka	Váh	Regulated	52	2.613	0.27	0.05	35
Osčadničanka	Váh	Natural	52	2.613	0.27	0.05	560
Petrovička 2	Váh	Regulated	33.5	1.414	0.126	0.016	745
Rajčianka 1	Váh	Natural	12	0.457	0.073	0.012	1 326
Rajčianka 2	Váh	Regul. - old	11	0.457	0.073	0.012	1 680
Rajčianka 3	Váh	Regul. - new	8.7	0.457	0.073	0.012	519
Teplička 2	Váh	Natural	51.1	1.474	0.253	0.052	288
Vadičovsky stream	Váh	Natural	39.4	1.66	0.17	0.05	318
Veselianka 1	Váh	Natural	85.9	3.665	0.489	0.127	306
Veselianka 2	Váh	Natural	69.1	3.274	0.381	0.104	346
Vôdky	Váh	Natural	15.8	0.4	0.115	0.045	1 007
Vrzavka	Váh	Natural	10	0.535	0.055	0.008	1 802
Zázrivka 1	Váh	Natural	76.5	4.269	0.817	0.258	325
Zázrivka 2	Váh	Natural	96.1	5.219	0.999	0.315	216
Chotina	Nitra	Natural	82	1.843	0.15	0.008	242
Bebrava 1	Nitra	Regulated	71.2	1.939	0.376	0.124	111
Bebrava 2	Nitra	Natural	43.4	1.819	0.353	0.116	154
Nitrica 1	Nitra	Regulated	188.4	6.169	0.737	0.211	110
Nitrica 2	Nitra	Natural	202.5	6.233	0.744	0.213	188
Kľak	Hron	Natural	54.6	2.342	0.266	0.076	591
Bacúšsky s.	Hron	Natural	24.2	0.876	0.223	0.118	329
Bukovec	Hron	Natural	16.8	0.785	0.126	0.065	470
Bystrianska	Hron	Natural	90.9	4.927	0.802	0.35	103
Čelno	Hron	Natural	10	0.326	0.064	0.022	1 074
Jaseniansky stream	Hron	Natural	56.9	3.463	0.702	0.21	509
Krivuľa	Hron	Natural	5.1	0.421	0.074	0.035	505
Malý Zelený s.	Hron	Natural	6.5	0.212	0.047	0.02	614
Petríkovo	Hron	Natural	17	0.58	0.128	0.055	267
Rácov	Hron	Natural	19.8	0.569	0.126	0.054	932
Slatina 1	Hron	Regulated	400.1	8.318	1.148	0.384	–
Slatina 2	Hron	Natural	383.4	8.047	1.11	0.372	–
Vážna	Hron	Natural	15.4	0.612	0.136	0.058	298
V. Zelený stream	Hron	Natural	11.8	0.356	0.079	0.034	169
Volchovo	Hron	Natural	10	0.295	0.065	0.028	1 003
Biela	Dunajec	Natural	91.2	4.063	0.421	0.095	217
Čierna voda	Dunajec	Natural	35.5	0.598	0.113	0.021	613
Hagánsky stream	Dunajec	Natural	10.5	0.44	0.115	0.042	843
Kežmar. B. Voda	Dunajec	Natural	27.3	0.44	0.098	0.003	938
Lipník 1	Dunajec	Natural	76.1	2.485	0.391	0.077	441
Lipník 2	Dunajec	Natural	37	1.491	0.235	0.046	570
Mlynica	Dunajec	Natural	39.8	0.44	0.145	0.049	2 939
Poprad	Dunajec	Regulated	45.7	2.81	0.566	0.188	318
Skalnatý stream	Dunajec	Natural	33.7	1.346	0.312	0.085	395
Teplica	Dunajec	Natural	3.5	0.057	0.014	0.001	8 824
Vesník	Dunajec	Natural	4	0.06	0.018	0.004	1 520
Kamienka 1	Dunajec	Regulated	34.4	1.01	0.116	0.006	626
Kamienka 2	Dunajec	Natural	19.5	0.563	0.065	0.003	1 376
Udava	Bodrog	Natural	59.3	2.467	0.19	0.025	1 456
Topľa	Bodrog	Natural	131.5	2.288	0.443	0.129	380
Šibská voda	Bodrog	Natural	54.9	0.711	0.141	0.024	5 429

The suitability curves for the 21–30 cm water depth interval are shown in Fig. 2; similarly, the HSCs for all the other depth intervals mentioned above are shown in Fig. 3. These curves were derived from ichthyological measurements during low flows and so they do not represent the state during higher flow rates.

The main result of the study was to develop the HSC modification methodology based on the optimal range of flow velocities for the brown trout.

The preference of the trout habitats in relation to the discharge was examined on the Drietomica River. The results show a good consistency between the HSC derived from an

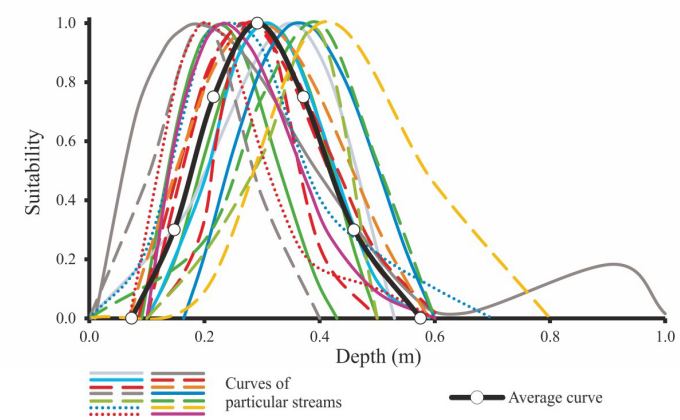

Fig. 2. Representative averaged suitability curves for flows with average water depths from 21 to 30 cm (solid black line) derived from the set of HSCs obtained by direct measurements of the mountain streams in Slovakia (colour lines).

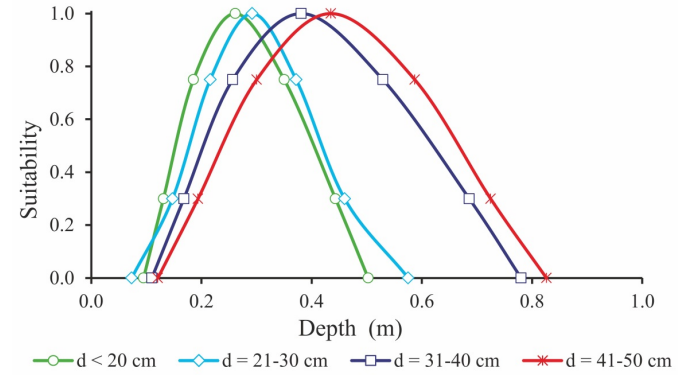

Fig. 3. Average water depth suitability curves for the brown trout (*Salmo trutta* m. *fario*) divided into intervals of the mean maximum water depth.

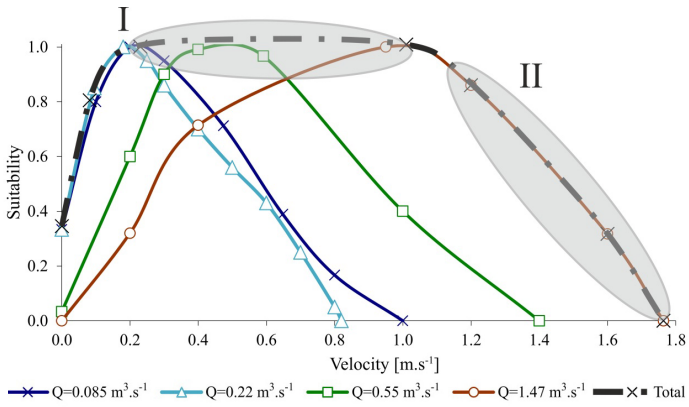

Fig. 4. Generalized suitability curve for the flow velocity for brown trout (*Salmo trutta* m. *fario*) in the Drietomica River, areas I. – II.

optimal range of flow velocities and the HSC determined from direct survey at individual flows. An example of the shape of the curves created by both methods is given in Fig. 8.

Impact of the flow velocity on the habitat quality

In general, it can be stated that there is a significant reduction of flow velocity in large bed scours, which cause the changes in the character of the substrate, from gravel-sand to silt-clay material. There were only few such bed scours within our reaches. However, there was low trout abundance in all cases.

The second factor that limits the rate of suitability of a habitat is the flow velocity at which the fish are washed away into other habitats. Therefore, a habitat that is suitable at a low flow rate is not necessarily suitable at higher flow rates, and this has a direct influence on the shape of the HSC. The limiting factor is the ability of the fish to resist the flow velocity. Hooper (1973) reported that the most suitable flow velocity for the brown trout was between 0.40 and 0.52 m.s^{-1}. According to Shirvell and Dungey (1983), the trout mostly prefers flow velocities close to 0.40 m.s^{-1}. Reiser and Wechse (1976) also identified a range of critical flow velocities for the brown trout. Their minimum flow velocity (v_{min}) was below 0.15 m.s^{-1}, while the maximum flow velocity (v_{max}) that the brown trout would resist in preferred microhabitats for a long time was 0.90 m.s^{-1}. The optimal range of flow velocities for the brown trout was between 0.40 m.s^{-1}and 0.70 m.s^{-1}. Similar velocities were present also in the reference reach of the Drietomica River.

In this study, we assumed a mean velocity in vertical that was determined from three values, i.e., three propellers on a hydrometric rod. A decrease in preference occurred at a velocity of 1.0 m.s^{-1} (Fig. 4). This value is consistent with the maximum flow velocity v_{max} = 0.9 m.s^{-1} stated by Reiser and Wechse (1976) that the brown trout would resist in the preferred microhabitats for a long time.

Based on previous statements, we can conclude that the flow rate mainly affects the shape of a HSC during higher flow rates, which leads to washing out the fish from the preferred habitat. We used the HSCs that were determined from the ichthyological survey of the Drietomica River at different flow rates to derive a HSC that characterized the quality of the habitat in a wider flow range, i.e., from the low flow up to the flow at which the fish were washed out from their preferred habitats.

Description of the suitability curve areas for the velocity

The HSC for the velocity, i.e., the line of the HSC for different flow rates (labelled by different line types and colours), can be divided into different characteristic areas as follows (Fig. 4):

I. The optimal level of fitness, area I.

At a low flow rate the brown trout chooses a habitat according to its depth. Fig. 5 shows an evaluation of the rate of suitability of the reference reach of the Drietomica River at the lowest measured flow rate (Q) of 0.085 m^3.s^{-1} (Q_{355} = 0.077 m^3.s^{-1}). The cover areas, where the depths are larger and the velocities are smaller (Fig. 5) have the highest suitability rate. A flow rate of 0.55 m^3.s^{-1} (Q_{180} = 0.43 m^3.s^{-1}) still corresponds to the optimum conditions for the brown trout; therefore, the habitat quality is the same as for the Q_{355} flow.

II. Declining rate of suitability, area II.

When the flow increases, the velocity also increases. When the velocity exceeds the threshold that the brown trout is usually able to resist, the rate of suitability is significantly reduced, and is represented by Region II in Fig. 4. The rate of suitability for the velocity at a flow rate of 1.50 m^3.s^{-1} (Q_{60}) is evaluated in Fig. 6. The areas with lower rates of suitability at higher flow rates start to occur in the areas that were the most suitable at lower flow rates.

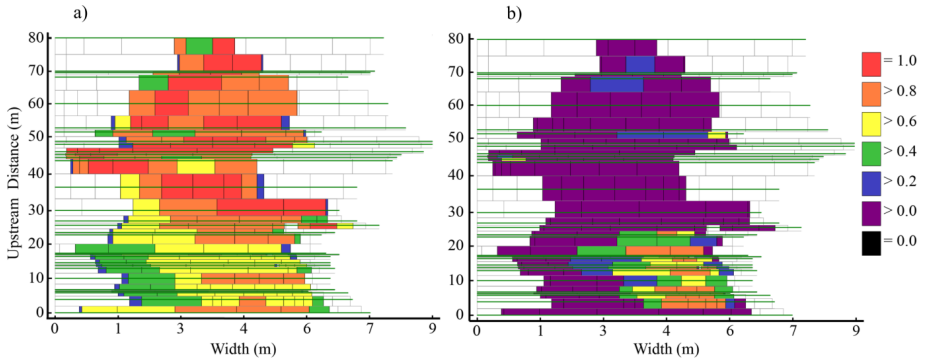

Fig. 5. Plan view of suitability rate of the Drietomica River for the brown trout (*Salmo trutta* m. *fario*) for Q = 0.085 $m^3.s^{-1}$ (a) for the velocity, and (b) for the depth. Width (m) is the channel width in the water level and upstream distance (m) is a relative river station (distance between cross-sections).

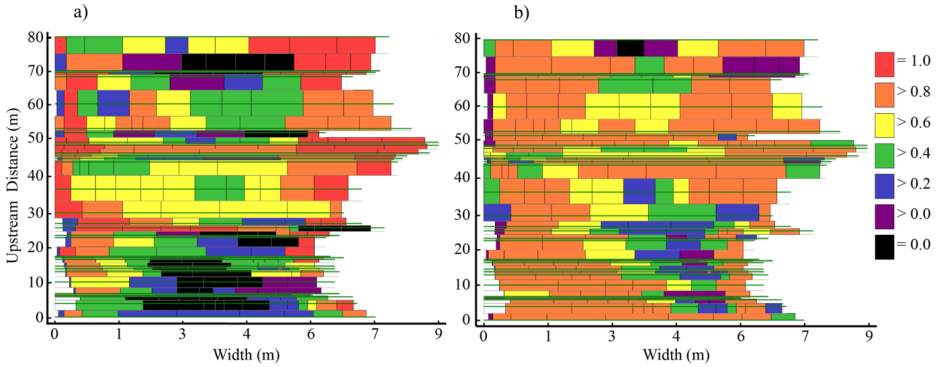

Fig. 6. Plan view of suitability rate of the Drietomica River for the brown trout (*Salmo trutta* m. *fario*) for Q = 1.50 $m^3.s^{-1}$ (a) for the depth, and (b) for the velocity. Width (m) is the channel width in the water level and upstream distance (m) is a relative river station (distance between cross-sections).

Table 2. The results of the ichthyological survey for the Drietomica River in 2012 and 2013. species: CS – Carpathian sculpin (*Cottus poecilopus*), BT - brown trout (*Salmo trutta* m. *fario*), Ch – chub (*Leuciscus cephalus*), M – Eurasian minnow (*Phoxinus phoxinus*), S – stone loach (*Barbatula barbatula*).

Cross section		1	2	3	4	5	6	7	8	9	10	11	12	13	14	15	16	17	18	19
Species	CS	1/0	3/2	2/0	10/3	0/2	0/0	3/0	1/2	2/2	0/0	0/0	0/0	2/0	5/0	0/0	3/2	2/2	1/0	1/2
	BT	1/2	3/2	4/0	0/0	2/1	5/1	2/0	2/1	4/3	1/0	3/0	2/0	1/2	4/2	9/2	1/0	2/0	2/1	1/2
	Ch	0/0	0/0	0/0	0/0	1/0	0/0	0/0	0/0	0/0	0/0	0/0	0/0	0/0	0/0	0/0	0/0	0/0	0/0	0/0
	M	0/0	0/0	0/0	0/0	0/0	0/11	0/0	0/0	0/0	0/0	0/0	0/0	0/0	0/2	0/0	0/0	0/0	0/0	0/0
	SL	0/0	0/0	0/0	0/0	0/0	0/0	0/0	0/0	0/0	0/0	0/0	0/0	1/0	0/0	0/0	0/0	0/0	0/0	0/0
	Total	86/50																		

Legend for Table 2: x/y – x is the amount of the specific fish species during the measurement on the 8.7.2012
y is the amount of the specific fish species during the measurement on the 8.7.2013

The ichthyological and hydrometrical measurements on the reference reach of the Drietomica River demonstrate that, at a flow rate of 1.47 $m^3.s^{-1}$, areas with velocities higher than 1.20 $m.s^{-1}$, that the trout cannot permanently resist, were created.

For a flow rate of 1.47 $m^3.s^{-1}$, the number of brown trout in their preferred areas decreased significantly. In 19 microhabitats, there were 32 adult trout when the flow rate was 0.55 $m^3.s^{-1}$, but only 15 trout when the flow rate was 1.47 $m^3.s^{-1}$ (Table 2). The fish started to move into the slower areas (cover places, flow obstacles and the like) for 1.47 $m^3.s^{-1}$. These results are similar to those from other locations. For example, at locations 6, 14, and 15, the number of fish decreased from 5 pc to 1 pc, from 4 to 2, and from 9 to 2, respectively (Table 2). These results also correspond with the previously described literature parameters for the maximum flow velocity v_{max} = 0.9 $m.s^{-1}$. At a flow velocity of 1.2 $m.s^{-1}$, there was a significant decrease in the fish quantity.

Effect of the depth on the quality of an aquatic habitat

Evaluation of the measurements from 59 representative reaches in 43 mountain streams showed that the depth and hydraulic characteristics of the flow were strongly correlated in natural watercourses (Macura et al., 2012).

Trout prefer habitats with a sufficient depth until higher velocities start to flush the fish out of these habitats. This fact is documented by the set of HSCs that were derived from four measurements during four various flow rates (Fig. 7). The curves have similar shapes and only shift when the depth increased at a higher flow rate. As the depth increases, the suitable habitat area increases as well, and improved quality of the habitat is still maintained. The upper area of the HSC is therefore determined by the shape of the curve at the low flow rate; the rate of suitability is constant and has a maximum value (Fig. 7; bold red dashed line). The course of the HSC for trout or salmon populations at a depth is provided, for example, by

Booker and Acreman (2007), Mäki-Petäys et al. (2002), or Freeman et al. (1999). A constant maximum suitability rate can be regarded as a hypothetical assumption, because a HSC represents the frequency of the occurrence of fish. In the clean main channel, the velocities are typically higher at higher depths, and the fish are washed out of the preferred areas; this occurred at a flow rate of 1.47 $m^3.s^{-1}$ in the Drietomica River.

This analysis shows that the suitability of the habitat was limited by the water depth when the flow was low (Fig. 7). At higher flow rates the velocity had a strong influence. At a flow rate of 1.47 $m^3.s^{-1}$, there was a significant increase in flow velocities, and a decrease of fish abundance in their preferred habitats. This flow rate can therefore be considered marginal, and the declining area of the HSCs for velocity and depth was represented by the HSCs for a flow of 1.47 $m^3.s^{-1}$ (brown curve in Fig. 7). In Figs. 4 and 7 the suitability curve is shown by a bold dashed black line labelled by crosses that represents the actual habitat preference of brown trout.

In Fig. 7, there are HSCs which were derived from direct measurements at four various water stages. In Fig. 8, the resulting curve from Fig. 7 is compared with a curve that was derived from the generalized HSC in Fig. 3. The Drietomica River belongs to the depth category d = 0.41–50 cm (marked with a red line). In the Drietomica hydraulic model, a flow rate, at which the average velocity at maximum depths reached 0.9 $m.s^{-1}$, was determined. This value was reached at a flow rate of 1.25 $m^3.s^{-1}$ and the mean water level difference compared to the one at Q_{365} was 24 cm. The peak of the curve was moved by this value (24 cm), as shown in Fig. 8. Comparing both curves, it can be concluded that there is a good match between the two.

The HSCs plotted for the velocity (Fig. 4) and depth (Fig. 7) indicated that changes in habitat preference followed the same trends as changes in the water surface. Specifically, the shelter depths ranged from 0.15 m (d_{min}) to 0.60 m (d_{max}) at a flow rate of Q = 0.085 $m^3.s^{-1}$, and the maximum fitness was at a depth of 0.5 m (Fig. 7; dark blue curve labelled by crosses). At the highest measured flow rate (Q = 1.47 $m^3.s^{-1}$), the shelter depths ranged from 0.45 m (d_{min}) to 0.88 m (d_{max}). The longitudinal profiles show that the water level varied from 0.2 to 0.3 m for flow rates of 0.085 $m^3.s^{-1}$and 1.47 $m^3.s^{-1}$ in the various cross sections. According to Table 3, the difference of d_{max} was 28 cm. The changes in the water surface level and in the maximum rate of suitability were therefore practically identical in this case. Similar results have been obtained when the changes in suitability for velocity were compared at flow rates of 0.085 $m^3.s^{-1}$ and 1.47 $m^3.s^{-1}$. The difference in v_{max} for these two flow rates was 0.51 $m.s^{-1}$ (Table 3).

From previous statements, it follows that the shape of the HSC at the low flow determines the upward part of the HSC. It is not necessary to derive the downward part of the HSC from direct measurements as presented on the example of Drietomica. This part can be constructed by moving a curve to an area where the fish would resist the higher velocities in the shelter for a longer time. Specifically, in Drietomica that occurs for a flow of 1.47 $m^3.s^{-1}$, with maximum velocities of 0.95 $m.s^{-1}$ (Tab. 3). The water level difference between flows 0.085 and 1.47 $m^3.s^{-1}$ was 43 cm ($d_{max} - d_{min}$ from Tab. 3). The HSC can be shifted by this value from a low flow. The shape of the HSC thus constructed is similar to the curve resulting from the direct measurements in Fig. 7. This technique can be universally applied including use of the generalized HSCs in Fig. 3.

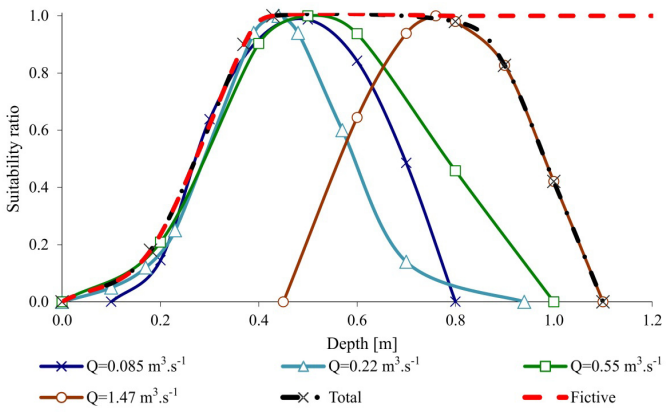

Fig. 7. Depth suitability curves for the brown trout at Drietomica River derived for Q = 0.085, 0.22, 0.55, and 1.47 $m^3.s^{-1}$.

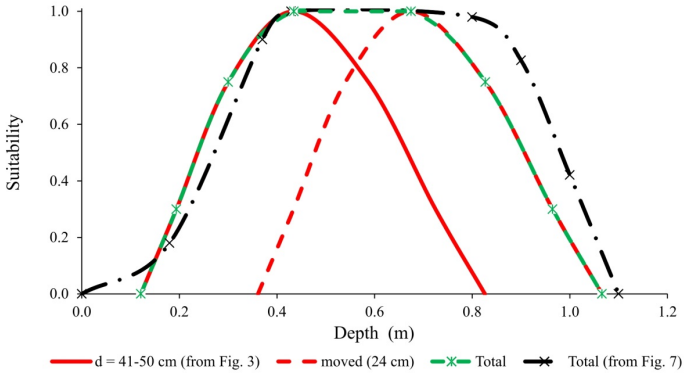

Fig. 8. Comparison of depth suitability curves for the brown trout at Drietomica River determined by field survey (from Fig. 7) and derived from average curve (from Fig. 3).

Table 3. Comparison of the depth and velocity range in the cover places.

	$d_{avg.}$ (m)	$d_{min.}$ (m)	$d_{max.}$ (m)	$v_{avg.}$ ($m.s^{-1}$)	$v_{min.}$ ($m.s^{-1}$)	$v_{max.}$ ($m.s^{-1}$)
Q = 0.085 $m^3.s^{-1}$	0.38	0.15	0.6	0.15	0.05	0.44
Q = 1.47 $m^3.s^{-1}$	0.67	0.45	0.88	0.65	0.45	0.95

DISCUSSION

The essential parameters of an instream habitat are divided into abiotic and biotic within IFIM. Data for the abiotic parameters are needed to support the hydraulic flow modelling of the area of interest. Fish, as elements of biotic quality, are bioindicators of a stream habitat. The relationship between the abiotic and biotic characteristics is represented by the HSCs of the individual species, as previously described by Macura et al. (2012). IFIM mostly uses the depth and velocity suitability curves, because they are important characteristics of a mesohabitat (Cluer and Thorne, 2014; Harby et al., 2007; Vezza et al., 2012).

Wilding et al. (2014) noted that, for several years, ecohydraulics research focused on the effects of velocity and depth on the channel habitats of fish and other aquatic species. Applications of numerous models such as IFIM have demonstrated that a stream can provide a range of velocity-depth combinations that support a wide range of species throughout their life stages (Shirvell and Dungey, 1983; Slavík et al., 2005). Previous studies have confirmed the correlation between the suitability curves characteristics and flow hydraulics, especially in relation to water depth and velocity (Davey

et al., 2011; Macura et al., 2012). Therefore,the study is focused on the transformation of the HSCs for depth. The idea of transforming the HSCs is not new. In the studies of Ayllón et al. (2012) or Valentin et al. (1996) the authors point out that the HSC derived from one flow does not represent the behaviour of the ichthyofauna in the broader flow range. Therefore, they proposed a simple HSC transformation. The top of the curve continues by line with the maximum rate of suitability. This means that any higher flow rate has the maximum suitability rate. On the contrary, the method of the HSC creation introduced in this study describes the real behaviour of ichthyofauna in the whole flow spectrum.

The influence of HSCs on the evaluation of WUA is shown on the example of the Slatina River. For practical purposes, it is very difficult to determine the shape of a HSC using a set of measurements from different flow rates, as has been demonstrated by the example of the Drietomica River. It is advisable to use a technique to modify the HSC derived from the low flow that has been described on the example of Drietomica at the end of the previous chapter. We provide an example from the reference reach of the Slatina River to show how the HSCs for velocity and depth can be modified. The Slatina River is located in central Slovakia and belongs to the Hron River basin; i.e., the left tributary of the Danube River in the Slovak Republic. The Slatina River is surrounded by foothills and is one of the last remaining naturally meandering streams in Slovakia; together with its river bank vegetation, it represents a biocorridor of regional significance.

Table 4. Fish species and amount of fish caught in the 351 m reference reach of the Slatina River (area of the village of Slatinka).

Name of species	number
Roach (*Rutilus rutilus*)	178
Gudgeon (*Gobio gobio*)	166
Schneider (*Alburnoides bipunctatus*)	139
Chub (*Leuciscus cephalus*)	77
Freshwater bream (*Abramis brama*)	44
Stone loach (*Barbatula barbatula*)	19
Common nase (*Chondrostoma nasus*)	17
Common dace (*Leuciscus leuciscus*)	11
European perch (*Perca fluviatilis*)	7
Eurasian minnow (*Phoxinus phoxinus*)	7
Barbel (*Barbus barbus*)	4
Grayling (*Thymallus thymallus*)	3
Peloponnese barbel (*Barbus peloponnesius*)	2
Total	**674**

Table 5. Fish species and amount of fish caught in the 377 m reference reach of the Slatina River (below the village of Zvolenská Slatina).

Name of species	number
Gudgeon (*Gobio gobio*)	419
Stone loach (*Barbatula barbatula*)	154
Schneider (*Alburnoides bipunctatus*)	145
Roach (*Rutilus rutilus*)	116
Chub (*Leuciscus cephalus*)	92
Bleak (*alburnus alburnus*)	15
Freshwater bream (*Abramis brama*)	14
Eurasian minnow (*Phoxinus phoxinus*)	12
Common dace (*Leuciscus leuciscus*)	11
Brown trout (*Salmo trutta m. fario*)	9
Common nase (*Chondrostoma nasus*)	3
European perch (*Perca fluviatilis*)	2
Barbel (*Barbus barbus*)	1
Grayling (*Thymallus thymallus*)	1
Total	**994**

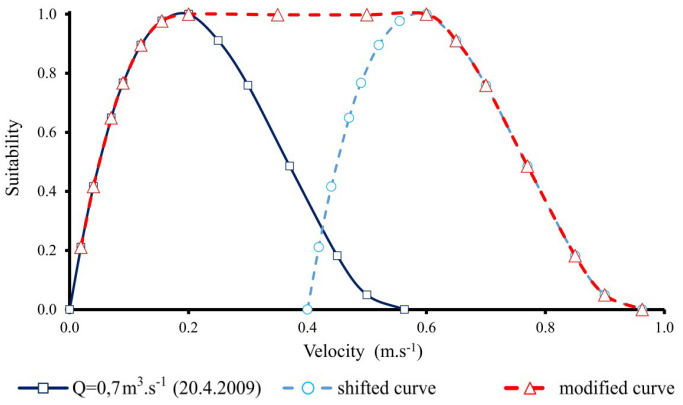

Fig. 9. Derivation of the brown trout velocity suitability curve from the values obtained for $Q = 0.7$ m^{3}s^{-1}, for the Slatina River.

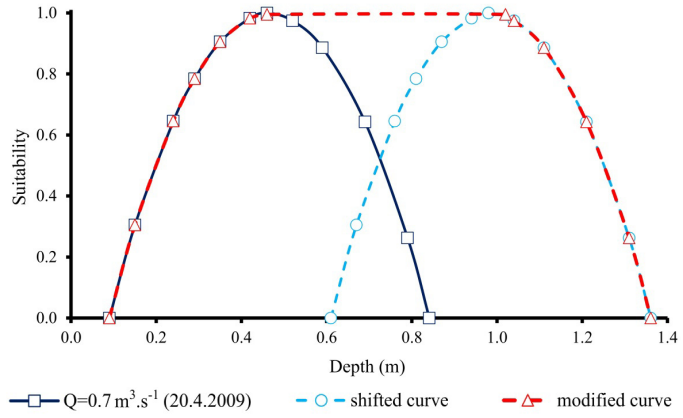

Fig. 10. Derivation of the brown trout depth suitability curve from the values obtained for $Q = 0.7$ m^{3}s^{-1}, for the Slatina River.

Two reference reaches with lengths of 351 and 377 m were selected in the Slatina River. These reaches were characterized by 21 and 15 cross sections, respectively, which are an essential input for the hydraulic model of the reach. The M-day flows for the area of the reference reaches are provided in Table 1.

An ichthyological survey was carried out in 2012. A total of 674 fish were caught in the 351-m reference reach, and 994 fish were caught in the 377-m reference reach (Tab. 4 and 5).

We used the chub to evaluate the impact of the flow rate and channel morphology, because, out of all the fish that are sensitive to the morphology of a riverbed, the chub was the most abundant. The HSCs for velocity and depth were derived from the ichthyological survey (Figs. 9 and 10). The measurements were taken at a flow rate of 0.643 m^3.s^{-1}, which is about Q_{330} (Table 1). The habitat for the maximum preferences of the chub is at a velocity of 0.20 m.s^{-1} (Fig. 9). However, the chub can withstand a velocity of 0.60 m.s^{-1} for an extended period, so the peak of the HSC for the velocity moved to an area of 0.60 m.s^{-1} (Fig. 9). The hydraulic model shows that this velocity occurred at a rate of 8.10 m^3.s^{-1} in the maximum depths where the chub was hiding. The average mean velocity in vertical in the covers at this flow rate was 0.64 m.s^{-1}. An increase in the flow rate from 0.643 to 8.10 m^3.s^{-1} resulted in an increase of 0.57 m in the average water level in the individual cross sections. The HSC for the depth was shifted with this value (Fig. 10). The resulting line from these curves represents the actual shape of the HSC that can be applied to the low flow rates as well as to flow rates of up to 8.0 m^3.s^{-1}, which spans a range from Q_{365} to Q_{30}.

Evaluation of the weighted usable area (WUA)

This section comprises a documentation and evaluation of the differences in the WUA of a curve derived from a single measurement and of a curve modified for a velocity that the chub can resist for a longer time. Fig. 11 compares the course of the WUA that was derived from the HSC at a low flow rate (dark blue line) and the course of the WUA that was derived from the modified curve shown in Figs. 9 and 10 (in Fig. 11, the line is indicated by a light blue colour). The initial course of the WUA was the same for both methods. The WUA derived from the curve at the low flow rate started to decline at a rate of 1.40 $m^3.s^{-1}$ (Fig. 11). This trend is apparent from the shape of the HSCs at a flow rate of 0.70 $m^3.s^{-1}$ (Figs. 9 and 10). The course of the WUA derived from the modified curve has a real shape. The value of the WUA increased until the flow rate reached a value of 4.20 $m^3.s^{-1}$. The WUA decreased slightly when the flow rate increased further (Fig. 11). The shape of the decreasing part of the WUA curve was not as significant as that of the HSC, because, by increasing the flow rate, the water surface area also increases. In particular, the rate of suitability in the areas with low depths increased when the flow rates were low, meaning that the rate of suitability was small.

When we evaluated the quality of the habitat in the individual cells in the footprint, an even more significant difference was apparent. The quality of the habitat based on the HSC derived at the low flow rate (Figs. 9 and 10 at Q = 0.70 $m^3.s^{-1}$) is evaluated in Fig. 12. At a flow rate of 8.10 $m^3.s^{-1}$ (Q_{30}), the rate of suitability was favourable for the depth, which is logical, because the depth in the shallow

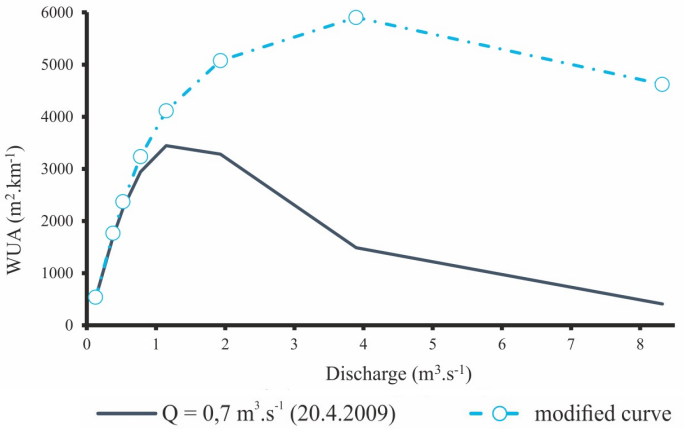

Fig. 11. Comparison of the WUA on the Slatina River. The light blue line was derived from the modified HSCs in Figs. 9 and 10. The dark blue line was derived from the HSC measured at the low flow rate.

areas increases when the flow rate increases (Fig. 12 a). This means that the conditions for the rheophilous species (Brown trout, European grayling) improve when the flow is increased (Harby et al., 2007). A different outcome occurs when the rate of suitability is examined according to the velocity. A significant part of the reach had a higher velocity than the range of the HSCs derived from the minimum flow rate. Therefore, a significant part had zero rate of suitability (Fig. 12 b); moreover, the combined rate of suitability was inappropriate (Fig. 12 c), as confirmed by the low value of the WUA (500 m^2) (Fig. 11).

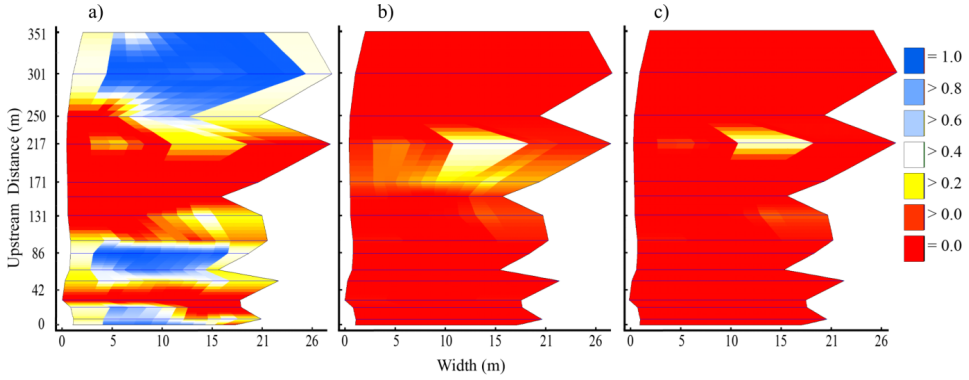

Fig. 12. Rate of suitability for the chub in the Slatina River at a flow rate of Q_{30} = 8.10 $m^3.s^{-1}$. A HSC modified according to the low flow rates was used. (a) the rate of suitability according to depth, (b) the rate of suitability according to velocity, (c) the combined rate of suitability.

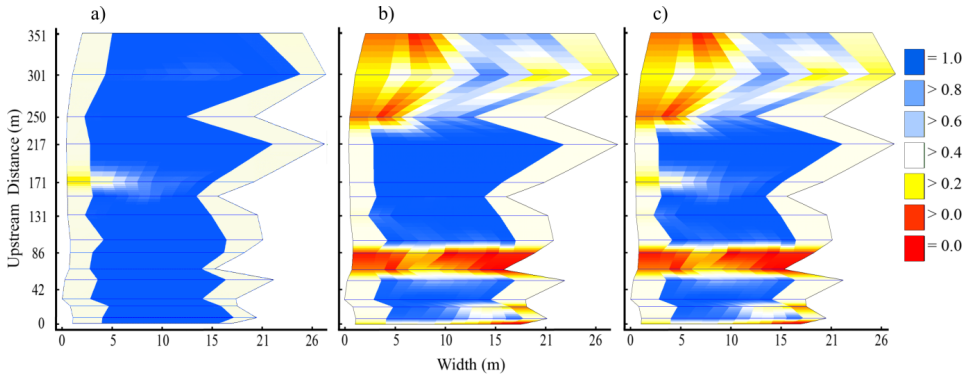

Fig. 13. Rate of suitability for the chub in the Slatina River at a flow rate of Q_{30} = 8.10 $m^3.s^{-1}$. A HSC modified for a wider range of flow rates was used; (a) the rate of suitability according to depth, (b) the rate of suitability according to velocity, (c) combined rate of suitability.

The same reach was evaluated with modified HSCs (Figs. 9 and 10). Fig. 13 shows that a substantial part of the reach had the highest quality level. This is the actual condition, because the velocities and depths of the flow provide an optimal area for the ichthyofauna. It can be stated that HSCs derived from a particular measurement can be applied only for the discharge at which they were derived. The tests show that the modified HSC represented fish behaviour across a wider flow range.

Acknowledgements. We thank staff from the Slovak Hydrometeorological Institute for cooperation on the M-day flow rates determination and Jaroslav Andreji from Slovak University of Agriculture in Nitra for cooperation on the ichthyological surveys. This study has been supported by the Scientific Grant Agency under Contracts Nos. VEGA 1/0625/15 and VEGA 1/0665/15.

REFERENCES

Aparicio, E., Carmona-Catot, G., Moyle, P.B., García-Berthou, E., 2011. Development and evaluation of a fish-based index to assess biological integrity of Mediterranean streams. Aquatic Conserv: Mar. Freshw. Ecosyst., 21, 324–337, DOI: 10.1002/aqc.1197.

Artemiadou, V., Lazaridou, M., 2005. Evaluation score and interpretation index for the ecological quality of running waters in Central and Northern Hellas. Environ. Monit. Assess., 110, 1–40. DOI: 10.1007/s10661-005-6289-7.

Ayllón, D., Almodóvar, A., Nicola, G.G., Elvira, B., 2009. Interactive effects of cover and hydraulics on brown trout habitat selection patterns. River Res. Applic., 25, 1051–1065. DOI: 10.1002/rra.1215.

Ayllón, D., Almodóvar, A., Nicola, G.G., Elvira, B., 2010. Modelling brown trout spatial requirements through physical habitat simulations. River Res. Applic., 26, 1090–1102. DOI: 10.1002/rra.1315.

Ayllón, D., Almodóvar, A., Nicola, G.G., Elvira, B., 2012. The influence of variable habitat suitability criteria on PHABSIM habitat index results. River Res. Applic., 28, 1179–1188. DOI: 10.1002/rra.1496.

Booker, D.J., Acreman, M.C., 2007. Generalisation of physical habitat-discharge relationships. Hydrol. Earth Syst. Sci., 11, 141–157. DOI: 0.5194/hess-11-141-2007, 2007.

Casper, A. F., Dixon, B., Earls, J., Gore, J. A., 2011. Linking a spatially explicit watershed model (SWAT) with an in-stream fish habitat model (PHABSIM): A case study of setting minimum flows and levels in a low gradient, subtropical river. River Res. Applic., 27, 269–282. DOI: 10.1002/rra.1355.

Cianfrani, C.M., Sullivan, S.M.P, Hession, W.C, Watzin, M.C., 2009. Mixed stream channel morphologies: implications for fish community diversity. Aquatic Conservation: Marine and Freshwater Ecosystems, 19, 147–156.

Cluer, B., Thorne, C., 2014. A stream evolution model integrating habitat and ecosystem benefits. River Res. Applic., 30, 135–154. DOI: 10.1002/rra.2631.

Davey, A.J.H., Booker, D.J., Kelly, D.J., 2011. Diel variation in stream fish habitat suitability criteria: implications for in-stream flow assessment. Aquatic Conserv: Mar. Freshw. Ecosyst., 21, 132–145. DOI: 10.1002/aqc.1166.

Döll, P., Zhang, J., 2010. Impact of climate change on freshwater ecosystems: a global-scale analysis of ecologically relevant river flow alterations. Hydrol. Earth Syst. Sci., 14, 783–799. DOI: 10.5194/hess-14-783-2010.

Džubáková, K., Molnar, P., Schindler, K., Trizna, M., 2015. Monitoring of riparian vegetation response to flood disturbances using terrestrial photography. Hydrol. Earth Syst. Sci., 19, 195–208. DOI: 10.5194/hess-19-195-2015.

Filipe, A.F., Markovic, D., Pletterbauer, F., Tisseuil, C., De Wever, A., Schmutz, S., Bonada, N., Freyhof, J., 2013. Forecasting fish distribution along stream networks: brown trout (*Salmo trutta*) in Europe. Diversity Distrib., 19, 1059–1071. DOI: 10.1111/ddi.12086.

Freeman, M.C., Bowen, Z.H., Bovee, K.D., 1999. Transferability of habitat suitability criteria: response to comment. North American Journal of Fisheries Management, 19, 626–628, DOI: 10.1577/1548-8675(1999)019<0626:TOHSCR>.

Friberg, N., Baartrup-Pedersen, A., Pedersen, M.L., Skriver, J., 2005. The new Danish stream monitoring programme (NOVANA) - preparing monitoring activities for the Water Framework Directive era. Environ. Monit. Assess., 111, 27–42. DOI: 10.1007/s10661-005-8038-3.

Fung, F., Watts, G., Lopez, A., Orr, H.G., New, M., Extence, C., 2013. Using large climate ensembles to plan for the hydrological impact of climate change in the freshwater environment. Water Resour. Manage., 27, 1063–1084. DOI: 10.1007/s11269-012-0080-7.

Harby, A., Olivier, J.-M., Merigoux, S., Malet, E., 2007. A mesohabitat method used to assess minimum flow changes and impacts on the invertebrate and fish fauna in the Rhône River, France. River Res. Applic., 23, 525–543, DOI: 10.1002/rra.997.

Hatten, J.R., Batt, T.R., Scoppettone, G.G., Dixon, C.J., 2013. An ecohydraulic model to identify and monitor moapa dace habitat. PLoS ONE, 8: e55551. DOI: 10.1371/journal.pone.0055551.

Holčík, J., Macura, V., 2001. Some problems with the interpretation of the impact of stream regulations upon the fish communities. Ecology, 20, 423–434.

Hooper, D., 1973. Evaluation of the effects of flows on trout stream ecology. Pacific Gas and Electric Company, Dept. of Engineering Research, Emeryville, California, 97 p.

Kändler, M., Seidler, C., 2013. Influence of hydrological situations on benthic organisms in a small river in Saxony (Germany). J. Hydrol. Hydromech., 61, 188–194. DOI: 10.2478/johh-2013-0024.

Krysanova, V., Dickens, C., Timmerman, J., Varela-Ortega, C., Schlüter, M., Roest, K., Huntjens, P., Jaspers, F., Buiteveld, H., Moreno, E., de Pedraza Carrera, J., Slámová, R., Martínková, M., Blanco, I., Esteve, P., Pringle, K., Pahl-Wostl, C., Kabat, P., 2010. Cross-comparison of climate change adaptation strategies across large river basins in Europe, Africa and Asia. Water Resour. Manage., 24, 4121–4160. DOI: 10.1007/s11269-010-9650-8.

Lamouroux, N., Capra, H., Pouilly, M., 1998. Predicting habitat suitability for lotic fish: linking statistical hydraulic models with multivariate habitat use models. Regul. Rivers: Res. Mgmt., 14, 1–11, DOI: 10.1002/(SICI)1099-1646(199801/02)14:1<1::AID-RRR472>3.0.CO;2-D.

Lamouroux, N., Oliver, J.M., Capra, H., Zylberblat, M., Chandesris, A., Roger, P., 2006. Fish community change after minimum flow increase: testing quantitative predictions in the Rhône River at Pierre-Bénite, France. Freshwater Biology, 51, 1730–1743, DOI: 10.1111/j.1365-2427.2006.01602.x.

Lichner, L.U., Cerdà, A., Rajkai, K., Tesař, M., 2014. Biohydrology research after Landau 2013 conference. J. Hydrol. Hydromech., 62, 253–257. DOI: 10.2478/johh-2014-0041.

Macura, V., Škrinár, A., Kalúz, K., Jalčovíková, M., Škrovinová, M., 2012. Influence of the morphological and hydraulic characteristics of mountain streams on fish habitat suitability curves. River Res. Applic., 28, 1161–1178. DOI: 10.1002/rra.1518.

Macura, V., Štefunková, Z., Škrinár, A., 2016. Determination of the effect of water depth and flow velocity on the quality of an in-stream habitat in terms of climate change. Advances in Meteorology, Article ID 4560378, 17 p. DOI: 10.1155/2016/456037.

Mäki-Petäys, A., Huusko, A., Erkinaro, J., Muotka, T., 2002. Transferability of habitat suitability criteria of juvenile Atlantic salmon (*Salmo salar*). Canadian Journal of Fisheries and Aquatic Sciences, 59, 2, 218–228. DOI: 10.1139/F01-209.

Mérigoux, S., Lamouroux, N., Olivier, J.-M., Dolédec, S., 2009. Invertebrate hydraulic preferences and predicted impacts of changes in discharge in a large river. Freshwater Biology, 54, 1343–1356, DOI: 10.1111/j.1365-2427.2008.02160.x.

Palmer, M.A., Menninger, H.L., Bernhardt, E., 2010. River restoration, habitat heterogeneity and biodiversity: a failure of theory or practice? Freshwater Biology, 55, 205–222.

Parasiewicz, P., Walker, J.D., 2007. Comparison of Meso-HABSIM with two microhabitat models (PHABSIM and HARPHA). River Res. Applic., 23, 904–923. DOI: 10.1002/rra.1043.

Parra, I., Almodóvar, A., Ayllón, D., Nicola, G.G., Elvira, B., 2011. Ontogenetic variation in density-dependent growth of brown trout through habitat competition. Freshwater Biology, 56, 530–540. DOI: 10.1111/j.1365-2427.2010.02520.x.

Pastuchová, Z., Grešková, A., Lehotský, M., 2010. Spatial distribution pattern of macroinvertebrates in relation to morphohydraulic habitat structure: perspectives for ecological stream assessment. Polish Journal of Ecology, 58, 347–360.

Pekárik, L., Koščo, J., Švátora, M., 2012. Reference conditions for fish microhabitat use in foothill streams: A case study on undisrupted carpathian streams. River Res. Applic., 28, 369–376. DOI: 10.1002/rra.1462.

Reiser, D.W., Wesche, T.A., 1976. Determination of physical and hydraulic preferences of brown and brook trout in the selection of spawning locations. University of Wyoming, Water Resources Research Institute, Water Resources Series 64, 224 p.

Scholten, M., 2003. Efficiency of point abundance sampling by electro-fishing modified for short fishes. Journal of Applied Ichthyology, 19, 265–277, DOI: 10.1046/j.1439-0426.2003.00505.x.

Shirvell, C.S., Dungey, R.G., 1983. Microhabitats chosen by brown trout for feeding and spawning in rivers. Transactions of the American Fisheries Society, 112, 3, 355–367.

Slavík, O., Bartoš, L., Mattas, D., 2005. Does stream morphology predict the home range size in burbot? Environ. Biol. Fish., 74, 89–98. DOI: 10.1007/s10641-005-3998-2.

Snelder, T.H., Lamouroux, N., 2010. Co-variation of fish assemblages, flow regimes and other habitat factors in French rivers. Freshwater Biology. 55, 881–892. DOI: 10.1111/j.1365-2427.2009.02320.x.

Sullivan, S.M.P., Watzin, M.C., Hession, W.C., 2006. Influence of stream geomorphic condition on fish communities in Vermont, U.S.A. Freshwater Biology, 51, 1811–1826. DOI: 10.1111/j.1365-2427.2006.01616.x.

Valentin, S., Lauters, F., Sabaton, C., Breil, P., Souchon, Y., 1996. Modelling temporal variations of physical habitat for brown trout (*Salmo trutta*) in hydropeaking conditions. Regulated Rivers: Research & Management, 12, 2–3, 317–330.

Van Loon, A.F., Ploum, S.W., Parajka, J., Kleig, A.K., Garnier, E., Laaha, G., Van Lanen, H.A.J., 2015. Hydrological drought types in cold climates: quantitative analysis of causing factors and qualitative survey of impacts. Hydrology and Earth System Sciences, 19, 1993–2016. DOI: 10.5194/hess-19-1993-2015.

Vezza, P., Parasiewicz, P., Rosso, M., Comoglio, C., 2012. Defining minimum environmental flows at regional scale: Application of mesoscale habitat models and catchments classification. River Res. Applic., 28, 717–730, DOI: 10.1002/rra.1571.

Wilding, T.K., Bledsoe, B., Poff, N.L., Sanderson, J., 2014. Predicting habitat response to flow using generalized habitat models for trout in Rocky Mountain streams. River Res. Applic., 30, 805–824. DOI: 10.1002/rra.2678.

Standards and directives

Slovak national standard STN 75 1410-1:2008-01, 2008. Hydrology (In Slovak: Hydrológia).

European Union, 2000. Directive 2000/60/EC of the European Parliament and of the Council of 23 October 2000 establishing a framework for Community action in the field of water policy.

Received 17 February 2017
Accepted 17 July 2017

J. Hydrol. Hydromech., 66, 2018, 1, 23–31
DOI: 10.1515/johh-2017-0032

Laboratory studies on bedload transport under unsteady flow conditions

Magdalena M. Mrokowska[1*], Paweł M. Rowiński[1], Leszek Książek[2], Andrzej Strużyński[2], Maciej Wyrębek[2], Artur Radecki-Pawlik[2, 3]

[1] Institute of Geophysics, Polish Academy of Sciences, ul. Ks. Janusza 64, 01-452 Warsaw, Poland.
[2] University of Agriculture in Krakow, Faculty of Environmental Engineering and Land Surveying, Department of Hydraulic Engineering and Geotechnics, Al. Mickiewicza 24/28, 30-059 Kraków, Poland.
[3] Institute of Structural Mechanics, Cracow University of Technology, ul. Warszawska 24, 31-155 Kraków, Poland.
[*] Corresponding author. Tel.: +48 22 69 15 849. Fax: +48 22 87 76 722. E-mail: m.mrokowska@igf.edu.pl

Abstract: Two sets of triangular hydrographs were generated in a 12-m-long laboratory flume for two sets of initial bed conditions: intact and water-worked gravel bed. Flowrate ranging from 0.0013 $m^3 s^{-1}$ to 0.0456 $m^3 s^{-1}$, water level ranging from 0.02 m to 0.11 m, and cumulative mass of transported sediment ranging from 4.5 kg to 14.2 kg were measured. Then, bedload transport rate, water surface slope, bed shear stress, and stream power were evaluated. The results indicated the impact of initial bed conditions and flow unsteadiness on bedload transport rate and total sediment yield. Difference in ratio between the amount of supplied sediment and total sediment yield for tests with different initial conditions was observed. Bedload rate, bed shear stress, and stream power demonstrated clock-wise hysteretic relation with flowrate. The study revealed practical aspects of experimental design, performance, and data analysis. Water surface slope evaluation based on spatial water depth data was discussed. It was shown that for certain conditions stream power was more adequate for the analysis of sediment transport dynamics than the bed shear stress. The relations between bedload transport dynamics, and flow and sediment parameters obtained by dimensional and multiple regression analysis were presented.

Keywords: Bedload; Bed shear stress; Dimensional analysis; Hysteresis; Stream power; Unsteady flow.

INTRODUCTION

Unsteadiness of water flow in rivers may be caused by both natural and accidental events, namely by heavy rainfall in a catchment, snow melt, breaking of log or ice-jams, operation of control gates, tides in estuaries or tidal rivers causing backwater effects. Flow unsteadiness intensifies transport processes, causes morphological changes in rivers, and affects water quality (De Sutter et al., 2001; Galia and Hradecky, 2011; Gharbi et al., 2016; Julien et al., 2002; Mao, 2012; Michalik and Książek, 2009). However, our knowledge on how matter, particularly sediment, is transported under unsteady flow conditions is still insufficient. This situation triggered a good deal of experimental, theoretical and computational efforts exploring how it works (Bombar, 2016; De Sutter et al., 2001; Julien et al., 2002; Lee et al., 2004; Mao, 2012; Mrokowska et al., 2016; Phillips and Sutherland, 1990; Wang et al., 2015). Nevertheless, the problem of bedload transport is still open for systematic research.

The processes involved in bedload transport are complex and case specific, which makes bedload transport difficult to express in general mathematical relations (Cao et al., 2016). Although there are multiple numerical models allowing for the predictions of bedload transport under unsteady flow conditions, such models seem not reliable and useful for the prediction purposes and not validated against sufficient amount of reliable datasets.

Laboratory experiments and field observations have revealed a variety of bedload transport patterns during the passage of flood waves. These patterns are due to the mutual effect of the water flow conditions and bed composition. Bedload transport rate – flowrate relationship under unsteady flow usually takes the form of clockwise or anti-clockwise hysteresis (Humphries et al., 2012; Mao, 2012; Moog and Whiting, 1998). It is hardly surprising that unsteady flows are intertwined with hysteretic behaviour as observed with respect to many variables (see e.g. O'Kane, 2005; Rajwa-Kuligiewicz et al., 2015; Rowiński et al., 2000).

Mao (2012) reported a clockwise hysteresis in experimental tests and attributed this type of relation to changes in organization of bed surface grains, which caused smaller bedload transport along the falling limb. Kuhnle (1992) observed a clockwise hysteresis in natural streams and attributed this pattern of transport to the formation and destruction of roughness elements. Bombar et al. (2011) reported an anti-clockwise hysteresis in experiments with a static armour layer, where the maximum bedload transport was possible only after the peak flowrate, when the armour layer was destroyed by a high flow. When sediment is heterogeneous, sediment transport is affected by grain arrangement (Ockelford and Haynes, 2013): microforms (clusters) are formed (Mao, 2012), static or mobile armour layer appears (Guney et al., 2013), and partial transport may take place (Sun et al., 2015). To make things more complicated, bedload transport is additionally controlled by the availability of upstream sediment in supply-limited rivers (Mao et al., 2011).

Contrary to the unsteady flow, a large number of bedload transport relations have been derived for steady flow conditions (Dey, 2014; Haddadchi et al., 2013; Talukdar et al., 2012; Yalin, 1972). Under unsteady flow, bedload transport is claimed to be more intensive than under corresponding steady flow. Similarly, total sediment yield is larger than evaluated for corresponding steady flow conditions (Tabarestani and Zarrati, 2015). Therefore, more and more researchers strive to develop methods dedicated to the unsteady flow, and cease to approximate it by step-wise steady flow conditions (Tabarestani and Zarrati, 2015).

A number of laboratory cases were studied experimentally with respect to bedload transport under unsteady flow. They varied in terms of various factors, such as the shape of unsteady

flow hydrograph, e.g., triangular (Lee et al., 2004), trapezoidal (Bombar et al., 2011), step-wise (Mao, 2012), naturally shaped (Humphries et al., 2012); bed composition – uni-modal or bimodal (Wang et al., 2015); supply of sediment from upstream (Mao, 2012); initial bed conditions – armoured bed (Bombar et al., 2011) and not armoured bed (Humphries et al., 2012), or duration of flow from a few minutes (Guney et al., 2013) to a few hours (Mao, 2012). Some studies took into account or commented on scaling from natural to laboratory conditions, e.g., (Cooper and Tait, 2009; Wang et al., 2015).

In this paper, experimental data on gravel bedload transport are analysed. Preliminary results limited to just a few experimental sets and a detailed description of the experiments were published by Mrokowska et al. (2016). Herein, new experimental tests with water-worked initial bed conditions are reported. The aim of this paper is to assess the extent to which initial bed conditions and unsteadiness of flow affect bedload transport intensity and total sediment yield. The paper focuses on the impact of flowrate, bed shear stress and stream power on bedload transport dynamics and on the relations between parameters governing transport processes.

MATERIAL AND METHODS

Experimental set-up

The experiment on bedload transport under unsteady flow was performed in a 12-m-long, 0.485-m-wide and 0.60-m-deep flow-recirculating tilting flume with glass side walls in the laboratory of Faculty of Environmental Engineering and Land Surveying, Agricultural University in Kraków, Poland (Fig. 1). Detailed description of the experimental settings were given by Mrokowska et al. (2016), so we just provide a brief summary with indication of aspects not mentioned in the previous paper.

A total of 10 experimental tests were carried out under unsteady flow conditions. The tests were classified according to the characteristics of flow and initial bed conditions. For each test, the channel bottom was covered with 12-cm-thick gravel layer that was well-mixed and screeded. Initial bed was composed of uniformly graded fine gravel with mean grain size d_m = 4.93 mm and maximum grain size d_{max} = 18 mm. These initial bed conditions were denoted by '-'. In some experimental tests, the bed was additionally water-worked by sub-threshold steady flow for about one hour and such initial conditions were denoted by '+'. During all tests, sediment was supplied manually from upstream to prevent excess scouring and deposition. Bed slope was constant for all tests I = 0.0083.

Two sets of unsteady flow, namely Hyd1 and Hyd2, in the form of triangular hydrographs were generated by manual stepwise changing of valve opening. Both hydrographs were generated for two sets of initial bed conditions '-' and '+', a few times for each condition. Experimental tests were denoted

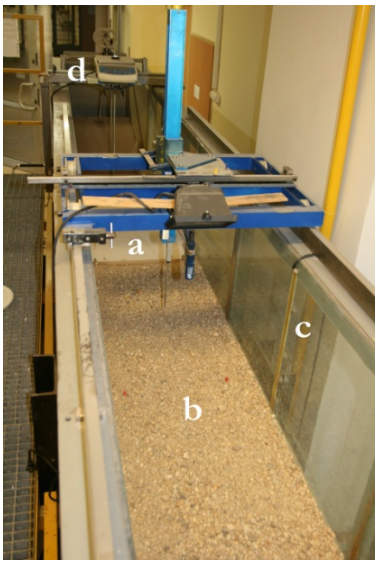

Fig. 1. Experimental channel - the closing section: a) non movable bed, b) movable bed, c) resistive water level sensor, d) bedload trap element - weighing scale.

Table 1. Classification of the experimental tests.

	Hyd1			Hyd2		
Bed-	Hyd1-1	Hyd1-2	Hyd1-3	Hyd2-1	Hyd2-2	
Bed+	Hyd1+1	Hyd1+2		Hyd2+1	Hyd2+2	Hyd2+3

by Hyd(no)_(-or+)_(test no), where the first term stands for the type of hydrograph, the second for the initial bed conditions, and the third one for the number of experimental tests with conditions described by preceding terms. The tests are listed in Table 1.

The following variables were measured: flowrate in delivery inlet pipe by ultrasonic flow meter, water level in 5 profiles along the flume x = 2.6 m, x = 3.6 m, x = 4.6 m, x = 5.6 m, x = 6.6 m with spatial step Δx = 1 m by resistive sensors, and cumulative mass of sediment measured in the outlet of the flume. Relevant hydrographs and cumulative sediment mass data are depicted in Fig. 2.

The characteristics of the unsteady flow experiments are listed in Table 2. The unsteady flow conditions are characterized by base flow (Q_b), peak flow (Q_{max}), base water depth (h_b), peak water depth (h_{max}), and duration of the rising limb (t_r). Also, Froude number for peak flow (Fr_{max}) was evaluated. Subscript $_b$ stands for base flow, $_{max}$ for the maximum value of a variable, $_r$ for the rising limb of a wave, and $_f$ for the falling limb of a wave. Figure 3 presents definitions of terms used to describe the flow characteristics. The two sets of unsteady flow differed in steepness of their limbs expressed as dQ/dt

Table 2. Characteristics of the experimental tests.

Run	t_r (s)	$\alpha_r \times 10^{-3}$ (–)	$\alpha_f \times 10^{-3}$ (–)	P_{gt} (–)	Q_b (m^3 s^{-1})	Q_{max} (m^3 s^{-1})	h_b (m)	h_{max} (m)	U_b (m s^{-1})	U_{max} (m s^{-1})	τ_b (N m^2)	τ_{max} (N m^2)	Fr_{max} (–)
Hyd1-1	406	0.10	–0.11	0.0081	0.0013	0.0414	0.02	0.10	0.20	0.92	1.13	6.69	0.98
Hyd1-2	407	0.10	–0.10	0.0081	0.0022	0.0435	0.02	0.10	0.25	0.87	1.40	8.12	0.94
Hyd1-3	404	0.09	–0.09	0.0081	0.0020	0.0387	0.02	0.10	0.23	0.81	1.49	7.72	0.87
Hyd1+1	277	0.12	–0.11	0.0082	0.0123	0.0456	0.05	0.11	0.52	0.89	3.67	7.10	0.92
Hyd1+2	267	0.12	–0.11	0.0082	0.0114	0.0429	0.05	0.10	0.53	0.86	3.48	7.38	0.89
Hyd2-1	262	0.15	–0.15	0.0081	0.0030	0.0405	0.02	0.10	0.33	0.90	1.47	7.05	0.99
Hyd2-2	257	0.16	–0.16	0.0081	0.0035	0.0429	0.02	0.10	0.29	0.85	2.00	7.69	0.89
Hyd2+1	170	0.18	–0.16	0.0081	0.0131	0.0419	0.05	0.10	0.54	0.867	3.80	7.40	0.87
Hyd2+2	168	0.17	–0.16	0.0081	0.0122	0.0420	0.05	0.10	0.53	0.86	3.83	7.67	0.86
Hyd2+3	176	0.18	–0.16	0.0081	0.0129	0.0432	0.05	0.10	0.57	0.88	3.51	7.21	0.88

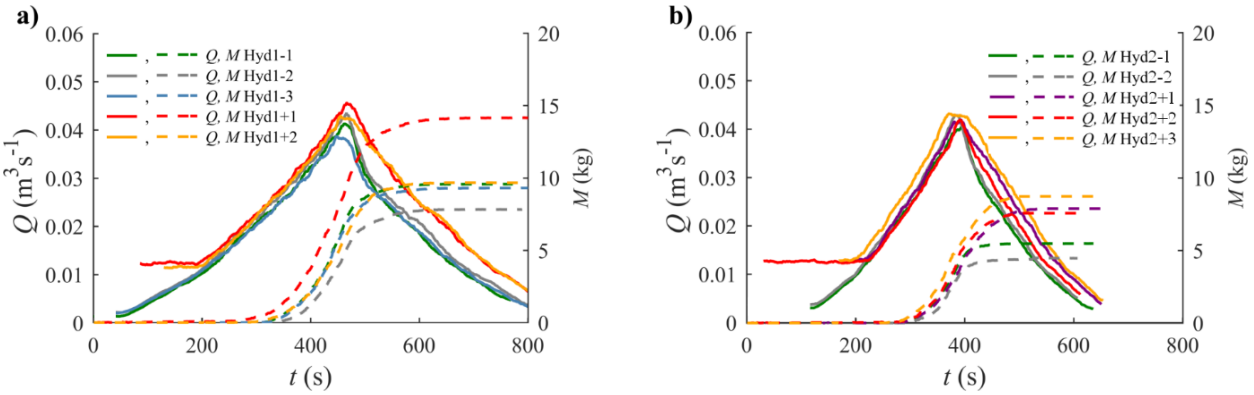

Fig. 2. Flowrate (Q) and cumulative sediment mass (M) measured during the experimental tests; a) Hyd1, b) Hyd2. Only a fraction of steady sub-threshold flow from one-hour flow is depicted for water-worked bed tests Hyd+.

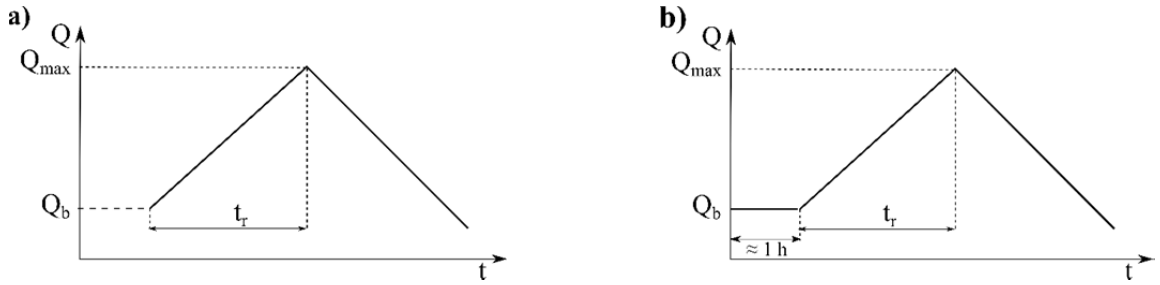

Fig. 3. Definition sketch of the terms used to characterize unsteady flow experiments; a) intact bed ('–'), b) water-worked bed ('+').

(Wang et al., 2015), denoted by α_r and α_f for the rising and the falling limb, respectively. Parameter α is referred to as the rate of unsteadiness in this study. Additionally, unsteadiness parameter introduced by (Bombar et al., 2011) was evaluated:

$$P_{gt} = \frac{\left| gI - \frac{U_{max} - U_b}{t_r} \right|}{g} \tag{1}$$

where g – gravitational acceleration (m s^{-2}), I – bed slope (–), U – mean flow velocity (m s^{-1}).

Data processing and analysis

Evaluation of bedload transport rate

Bedload transport may be expressed by cumulative mass, bedload transport rate, i.e., solid volume/weight/submerged weight of sediment transported per unit time, or by bedload transport intensity in non-dimensional form (Dey, 2014). In this study, weight of the sediment transported per unit time (q) was evaluated from cumulative sediment mass data (M) collected during the experimental tests.

Savitzky-Golay filter (Savitzky and Golay, 1964) was applied to smooth the raw cumulative transport data and to evaluate the bedload rate. Suitability of this method was demonstrated by Mrokowska et al. (2016) in selected experimental datasets.

This paper confirmed that the results of Savitzky-Golay filter were compatible with those obtained by approximating the data with a difference quotient and then by Fourier Transform filtering that is very popular in unsteady flow data smoothing (Bagherimiyab and Lemmin, 2013; Rowiński and Czernuszenko, 1998; Song and Graf, 1996). Nonetheless, in this case, Savitzky-Golay filter appeared to be superior to the other one thanks to its straightforward application; it also produced much fewer oscillations.

Evaluation of water surface slope

Water surface slope (S_w) reflects the pattern of flow but it is also used as an approximation of energy slope when applicable, i.e., under equilibrium steady flow and unsteady diffusive flow. S_w may be evaluated as a difference quotient, provided spatial measurements of water level in several locations along the channel are available (Mrokowska et al., 2015b).

It is more difficult to control and evaluate water surface slope than the flowrate in unsteady flow, which has been broadly discussed in the literature (Dottori et al., 2009; Mrokowska et al., 2015b; Perumal et al., 2004). Moreover, water surface slope results are very sensitive to the fluctuations of water level data. Minor spatial fluctuations of water level (H) may cause water slope evaluated from water level data to vary in unexpected way. For this reason, the application of various difference quotients was compared in this study. Water surface slope was evaluated in the central measuring profile x = 4.6 m as a central difference quotient, Eq. (2), and a five point quotient, Eq. (3).

$$S_w \approx \frac{H(x+\Delta x) - H(x-\Delta x)}{2\Delta x}, \tag{2}$$

$$S_w \approx \frac{-H(x+2\Delta x) + 8H(x+\Delta x) - 8H(x-\Delta x) + H(x-2\Delta x)}{12\Delta x} \tag{3}$$

The results were then filtered using Fourier Transform. Thanks to this low-pass filter, data fluctuations of undesired frequencies were removed. Satisfactory results were obtained for threshold frequency 0.03 Hz. A time series of water surface slope was transformed into the frequency domain and only components lower than the threshold frequency were taken.

Then, filtered data were transformed back to time domain. More details on Fourier Transform application may be found in (Bendat and Piersol, 2010; Mrokowska et al., 2015b; Song and Graf, 1996).

Evaluation of bed shear stress and stream power

Analysis of the relations between bed shear stress and bedload transport rate during flood wave propagation may provide important information on the relations between water flow and bedload transport. It is, in fact, a subject of ongoing debate and multiple interpretations (Guney et al., 2013; Mao et al., 2011; Mrokowska et al., 2016).

Under unsteady mobile bed conditions, measurement of bed shear stress is subject to high degree of uncertainty. A definition of bed shear stress under mobile bed conditions is not straightforward (Ferreira et al., 2012; Nikora et al., 2007), and for this reason the measurements of bed shear stress require cautious interpretation. Moreover, it should be noted that methods that may be applied under unsteady flow are scarce, mainly due to theoretical assumptions (Mrokowska et al., 2015a). Formulae derived from Saint-Venant model have become popular in unsteady flow experiments (Bombar, 2016; Song and Graf, 1996; Mrokowska et al., 2015b). However, the question about their applicability in evaluating bed shear stress under mobile bed conditions remains unanswered. Saint-Venant model was derived for fixed beds and its results applied to mobile bed conditions may be burdened with possible significant errors. The same applies to other methods of anticipation.

In this study, bed shear stress τ_b (N m^{-2}) was evaluated using the formula that may be derived from the Saint-Venant model for a diffusive wave:

$$\tau_b = \rho g h S_w \tag{4}$$

where ρ – density of water (kg m^{-3}), h – water depth (m). Next, bed shear stress was corrected for side-wall effects using the procedure proposed by Guo (2015).

Another widely used concept for bedload transport is stream power (ω) characteristic for Bagnold approach. While bed shear stress refers to forces exerted on a channel bed, stream power refers to the rate of energy necessary to transport sediment. It is applied as an indicator of channel sensitivity to deposition and erosion (Bizzi and Lerner, 2015), and to predict bed form type (Dey, 2014). In this study, stream power was evaluated using the following formula:

$$\omega = \tau_b U. \tag{5}$$

Dimensional and multiple regression analysis

Dimensional analysis provides methods for reducing the number of phenomena describing variables by classifying them into dimensionless groups (Dey, 2014; Ettema, 2000). This classical method was applied to find the relationships for bedload transport in other studies as well (Ahanger et al., 2008; Sinnakaudan et al., 2006).

Bedload transport is controlled by a number of variables: M – cumulative mass, U – mean flow velocity, h – flow depth, ρ – water mass density, ρ_s – mass density of sediment particles, $\Delta g = (\rho_s - \rho)g/\rho$ – reduced gravity, g – gravitational acceleration, ν – kinematic viscosity of water, d – sediment particle diameter, t – time elapsed from beginning of transport. The variables are of the following dimensions (M – mass, L – length, T - time): M [M]; d [L]; ν [L^{2}T^{-1}]; Δg [LT^{-2}]; U [LT^{-1}]; h [L]; ρ [ML^{-3}]. The functional relationship between cumulative mass as a dependent variable and other variables is as follows:

$$f(M, d, \nu, \Delta g, t, \rho, h, U) = 0. \tag{6}$$

Buckingham π-theorem was applied to identify dimensionless parameters. M, h, and Δg were taken as the repeating variables. Having three dimensions, 8 variables reduced to 5 non-dimensional parameters:

$$\pi_1 = \Delta g^{-0.5} h^{-0.5} U \tag{7}$$

$$\pi_2 = \Delta g^{-0.5} h^{-1.5} \nu \tag{8}$$

$$\pi_3 = h^{-1} d \tag{9}$$

$$\pi_4 = \Delta g^{0.5} t h^{-0.5} \tag{10}$$

$$\pi_5 = M^{-1} h^3 \rho \tag{11}$$

The set of dimensionless parameters formed the following relation:

$$f\left(h^{-1}d, \Delta g^{-0.5}h^{-1.5}\nu, \Delta g^{0.5}th^{-0.5}, \Delta g^{-0.5}h^{-0.5}U, M^{-1}h^3\rho\right) = 0. \tag{12}$$

This is obviously not a unique procedure and is a matter of subjective choice of dimensionless parameters. Multiple regression analysis was applied to find out the relationships between dimensionless parameters (Sinnakaudan et al., 2006). Nonlinear least-squares data fitting by Gauss-Newton method was applied.

DISCUSSION OF RESULTS

Relation between supplied sediment mass and total sediment yield

Data analysis has revealed a specific pattern of relationships between the amount of supplied sediment and total sediment yield. Figure 4 shows that more sediment was supplied than transported in the tests with intact initial bed, and larger or equal amount of sediment was transported than supplied in the tests with water-worked bed. In the tests with intact initial bed ('-'), more sediment was supplied compared with corresponding tests for water-worked bed ('+'). This pattern was due to the fact that a criterion for the supply rate was to prevent the bed from excessive erosion or deposition. In the tests with water-worked bed, the bed was not as prone to erosion as in '-' tests, at least in the initial flow phase, and consequently less sediment was required to supply.

Grain size distribution of bed surface material was measured after each experimental test but no significant variation was observed (Mrokowska et al., 2016).

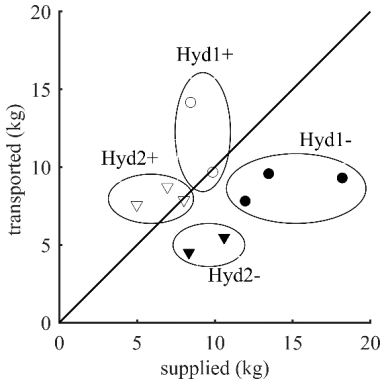

Fig. 4. Supplied and transported mass of the sediment for the experimental tests with intact ('-') and water-worked ('+') bed.

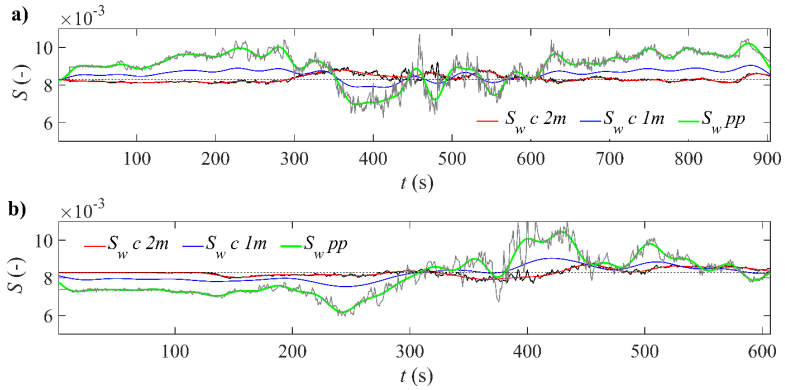

Fig. 5. Temporal variation of water surface slope; a) Hyd1-1, b) Hyd2-1.

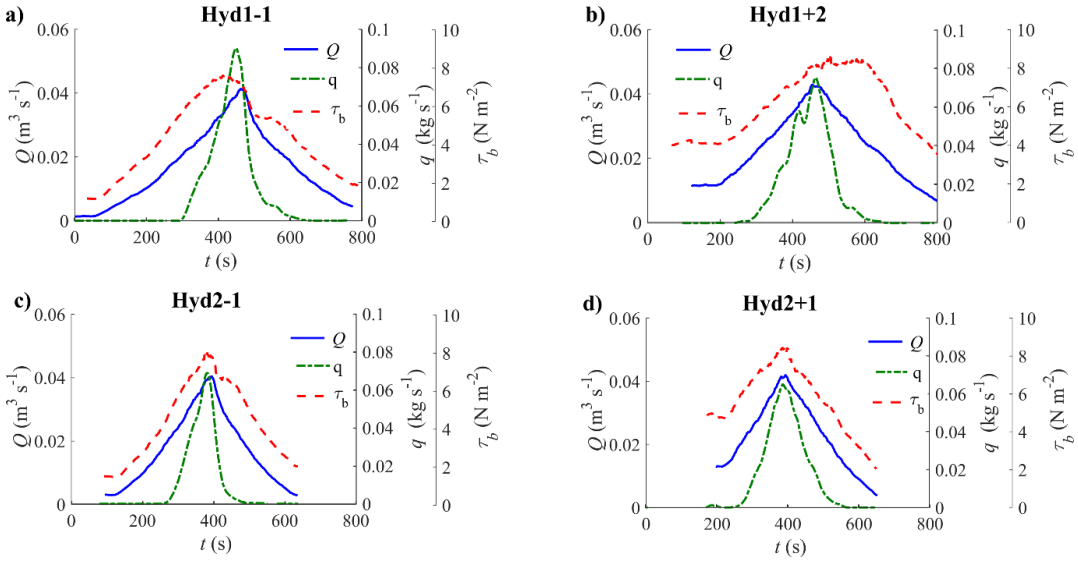

Fig. 6. Temporal variation of flowrate (Q) bedload transport rate (q) bed shear stress (τ_b) during experimental tests.

Evaluation of water surface slope

Figure 5 presents a comparison of water surface slope (S_w) results obtained by five point difference quotient, S_w *pp*, Eq. (3) for Δx = 1 m and central difference quotient, Eq. (2) for Δx = 2m and Δx = 1 m denoted by S_w *c 2m* and S_w *c 1m*, respectively. Black and grey lines represent the results before and colour lines after filtering with Fourier Transform. S_w *c 2m* proved to be the most reliable evaluation, since its values were closest to bed slope I = 0.0083 highlighted in Fig. 5 by a dotted line. The results of water surface slope close to bed slope were expected because spatial variability of water depth along the channel was small (less than 1 cm).

The figure clearly shows that for five point difference quotient the results were much more noisy than for central difference quotient. This was due to minor spatial water depth fluctuations. They are more likely under mobile bed conditions where erosion and deposition occur than under fixed bed conditions. Moreover, shallow water as in this study (ranging from 2 cm to 11 cm, see Table 2) also induced these fluctuations. To prevent the formation of eroded and deposited regions inducing fluctuations of water surface slope, sediment was supplied manually to control the supply rate.

A number of similar problems were also pointed out in other studies. Qu (2002) stressed that it was difficult to control water surface slope in laboratory channels. We found that water surface slope was better controlled in the tests with higher rate of unsteadiness, i.e., Hyd2.

Relation between bedload rate and flowrate

Figure 6 shows a temporal variation of bedload rate (q), flowrate (Q), and bed shear stress (τ_b) for selected experimental tests. A time lag between the peak flowrate and the peak bedload rate is visible, i.e., in general, the bedload rate attained its peak slightly before the maximum flowrate. The time lag varied between 5 and 13 seconds, except for Hyd1+2 where the maximum bedload rate was observed after the peak flowrate. These results were consistent with the findings of the studies on bedload transport in unsteady flow with unarmoured bed (Humphries et al., 2012; Mao, 2012). Bombar et al. (2011) showed that the time lag directly correlated with the unsteadiness of the hydrograph evaluated from Eq. (1). In this study, no significant differences in time lags between the experimental tests were observed. In fact, both hydrographs had the same value of P_{gt} (Table 2).

The relationship between Q and q under unsteady flow had a form of a clock-wise hysteresis (Fig. 7) indicating that the bedload rate was larger for specific flowrate along the rising limb than along the falling limb of a wave. There is no particular pattern in hysteresis shape that may indicate any impact of flow unsteadiness (difference between Hyd1 and Hyd2 tests) or initial bed condition (difference between '-' and '+' tests) on the bedload transport. This is due to the fact that the sediment was supplied during the experimental tests at a variable rate. Higher bedload rate along the rising limb may be triggered by unlimited sediment supply, mobile bed and higher values of bed

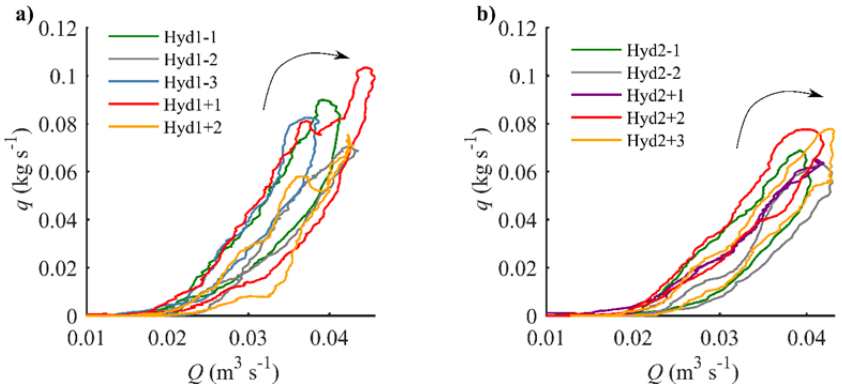

Fig. 7. Relationship between bedload rate (q) and flowrate (Q) for the experimental tests.

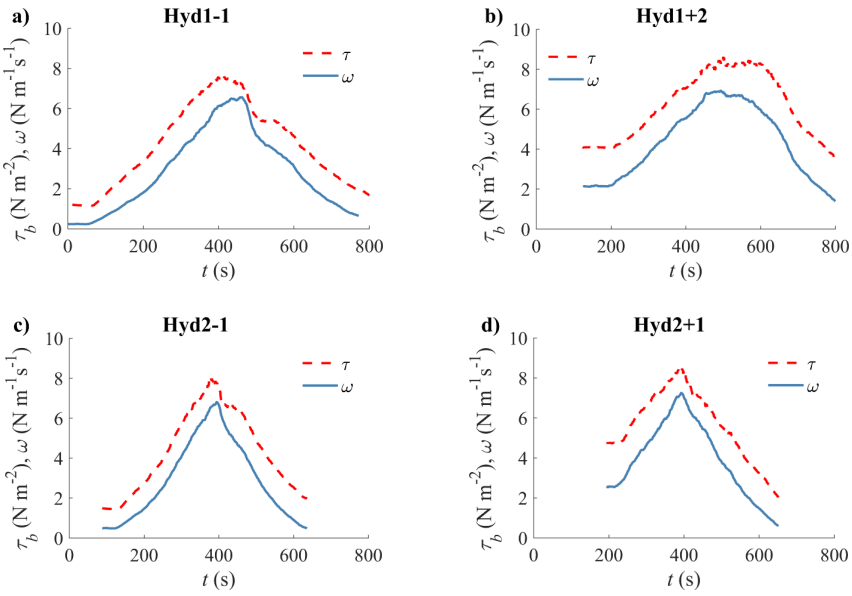

Fig. 8. Temporal variation of bed shear stress (τ_b) and stream power (ω) during experimental tests.

shear stress and stream power along the rising limb. The last scenario is discussed in the proceeding section.

Relation between bedload rate, bed shear stress, and stream power

In general, it is expected that the peak of bed shear stress triggers the peak of the bedload transport in unarmoured beds (Song and Graf, 1996). However, when bed shear stress results are subject to high uncertainty, unexpected variation of this variable may occur. This was the case of Hyd1+2 (Fig. 6b) where the peak bed shear stress occurred along the rising limb as expected but, additionally, unexpectedly high values were observed along the falling limb of the wave. This could be explained by the variation of water surface slope which is significant variable in the bed shear stress formula.

As discussed in the previous sections, input variables for Eq. (4) - water depth (h) and water surface slope (S_w) were problematic to control and evaluate, which was a source of uncertainty in bed shear stress assessment. Mean water depth is usually evaluated based on temporal variation of water level and mean bed level measured after the experimental test. When water depth is shallow, as in our experiment (Table 2), uncertainty of water depth evaluation based on water level and bed topography increases.

Alternatively, the effect of stream power on bedload rate was analysed. The shape of temporal variation of the stream power corresponded to the variation of bed shear stress (Fig. 8) but the impact of water surface slope on the result was suppressed due to multiplication by mean velocity. These results show that stream power may be a good alternative for bed shear stress in the analyses of factors affecting bedload rate, especially when bed shear stress is evaluated from bulk variables and water slope data are of high uncertainty.

The results for stream power were more homogenous than the results for bed shear stress in terms of time lags between peak values. Figure 9 shows a comparison between time lags, Δt, between the peaks of bedload rate and stream power, and bedload rate and bed shear stress. Peak bedload transport occurred from $\Delta t = -29$ s to $\Delta t = -5$ s after the peak stream power. The variability of lag between the bedload rate and bed shear stress was larger and ranged from $\Delta t = -132$ s and $\Delta t = 39$ s. The fact that peak bedload rate occurred before the peak of stream power might be attributed to the uncertainty of stream power results.

Despite identified sources of uncertainty, the results show general patterns - both bed shear stress and the stream power were greater along the rising limb resulting in a clock-wise hysteresis (Fig. 10). This is, along with the sediment supply, the explanation for higher bedload rate along rising limbs discussed in the previous section.

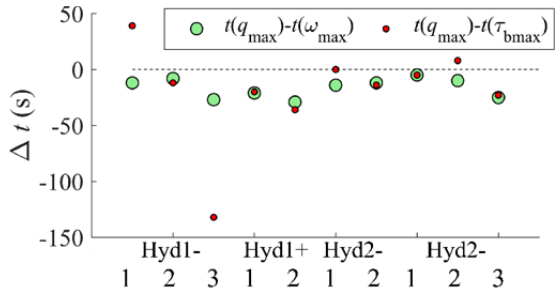

Fig. 9. Time lags, Δt, between the peaks of bedload rate (q_{max}) and stream power (ω_{max}) and the peaks of bedload rate and bed shear stress (τ_{bmax}).

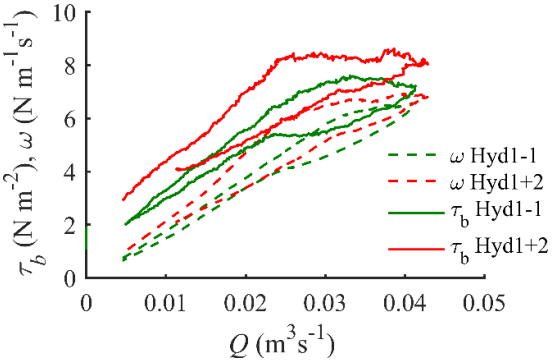

Fig. 10. Relationship between bed shear stress (τ_b) and flowrate (Q) and stream power (ω) and flowrate (Q) for sample experimental tests.

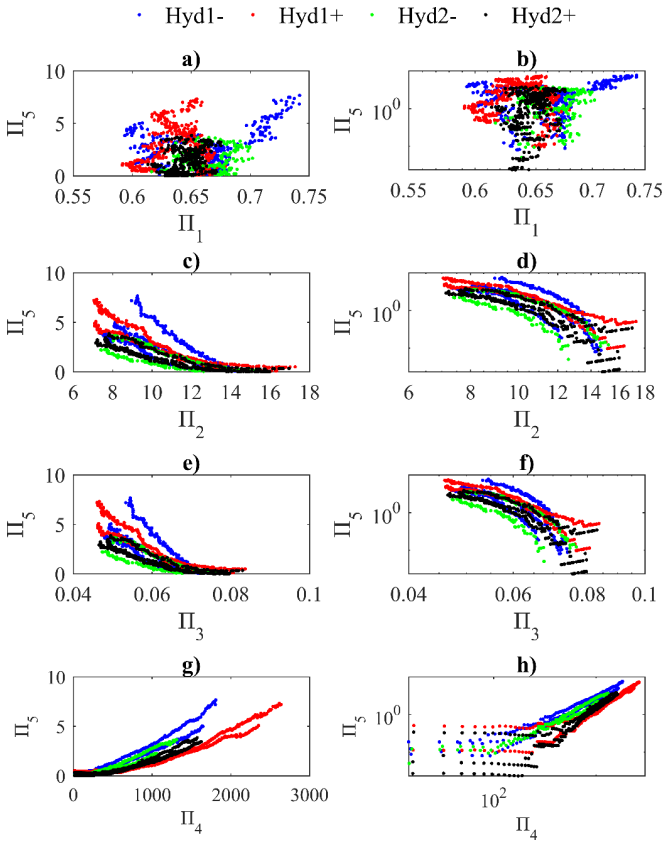

Fig. 11. Relations between independent and dependent dimensionless parameters.

Multiple regression analysis

Parameter $\pi_5 = M^{-1}h^3\rho$ expressing dimensional cumulative mass was chosen as a dependent parameter. A correlation between the dependent parameter π_5, and independent parameters, $\pi_1, \pi_2, \pi_3, \pi_4$ was tested for the rising limbs of the hydrographs.

Figure 11 shows the relation between dimensionless parameters on normal and log-log scales. The graphs reveals a linear relation between π_5 and π_2, π_3, and a power relation between π_5 and π_4. There was no correlation between π_5 and π_1, and consequently π_1 was not taken into account in the model development. Three independent dimensionless variables, π_2, π_3, π_4, were selected to find relevant expressions for the dependent variable π_5:

$$M^{-1}h^3\rho = f\left(h^{-1}d, \Delta g^{-0.5}h^{-1.5}\nu, \Delta g^{0.5}th^{-0.5}\right). \tag{13}$$

A general form of the model indicates that bedload transport does not directly depend on mean velocity, U. Performance of various models was tested and assessed based on the coefficient of determination and Nash-Sutcliff coefficient. The best fit model was as follows:

$$\pi_5 = b_1 + b_2\pi_2 + b_3\pi_3 + b_4\pi_4^{b_5}. \tag{14}$$

This model fitted independently four groups of data: Hyd1-, Hyd1+, Hyd2-, Hyd2+ for which the regression parameters $b_1, \ldots, b_5$ were identified. The resulting models for Hyd1-, Hyd1+, Hyd2-, Hyd2+ are presented below:

$$M^{-1}h^3\rho = -16.684 - 1.832\left(\frac{\nu}{\Delta g^{0.5}h^{1.5}}\right) + 594.222\left(\frac{d}{h}\right) + \\ +192*10^{-6}*\left(\frac{\Delta g^{0.5}t}{h^{-0.5}}\right)^{1.426} \tag{15}$$

$$M^{-1}h^3\rho = -24.828 - 2.424\left(\frac{\nu}{\Delta g^{0.5}h^{1.5}}\right) + 803.105\left(\frac{d}{h}\right) + \\ +24*10^{-6}*\left(\frac{\Delta g^{0.5}t}{h^{-0.5}}\right)^{1.672} \tag{16}$$

$$M^{-1}h^3\rho = -15.045 - 2.380\left(\frac{\nu}{\Delta g^{0.5}h^{1.5}}\right) + 667.100\left(\frac{d}{h}\right) + \\ +21*10^{-6}*\left(\frac{\Delta g^{0.5}t}{h^{-0.5}}\right)^{1.709} \tag{17}$$

$$M^{-1}h^3\rho = -12.967 - 1.187\left(\frac{\nu}{\Delta g^{0.5}h^{1.5}}\right) + 401.719\left(\frac{d}{h}\right) + \\ +44*10^{-6}*\left(\frac{\Delta g^{0.5}t}{h^{-0.5}}\right)^{1.609} \tag{18}$$

Figure 12 presents a comparison between cumulative mass data and the results from the models. Results for cumulative mass obtained from the models fitted the data very accurately – both coefficients, the coefficient of determination and Nash-Sutcliff coefficient, were about 0.99.

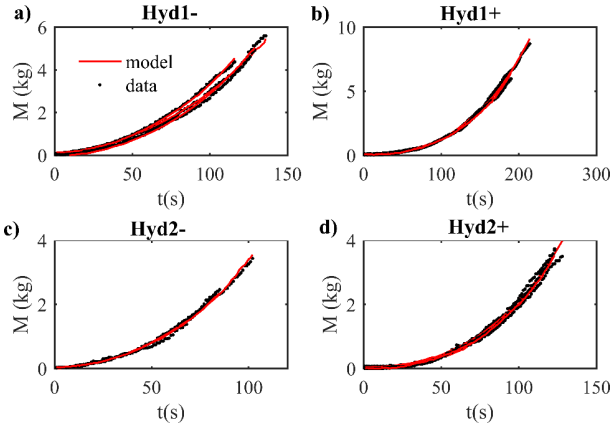

Fig. 12. Comparison of data and regression models for cumulative mass transport.

The above regression models were valid only for the experimental conditions presented in this study. Applicability to other conditions needs to be verified. The models may be used during further experimental tests in similar conditions.

CONCLUDING REMARKS

In this study, we demonstrated the impact of initial bed conditions and flow unsteadiness on total sediment yield and bedload transport rate. The effect of initial bed conditions was particularly visible in the analysis of total supplied and transported sediment mass. Different proportions between the amount of supplied and transported sediment for the sets of initial conditions revealed a significant role of bed material sorting and bed roughness in the sediment transport during a flood wave propagation.

The study showed that unsteadiness of flow triggered variable bed shear stress and stream power that consequently affected bedload transport rate. It was indicated by the fact that the bedload rate, bed shear stress and stream power were in clockwise hysteretic relationship with the flowrate.

A number of questions have arisen regarding data interpretation and definitions. Bed shear stress definition and measurement methods induce high uncertainty and difficulty in data interpretation. As each method of evaluation of the bed shear stress is uncertain to some extent, a comparison of a few methods may be helpful in interpreting the results as shown in other studies (Bombar, 2016; Qu, 2002).

The study showed that when bed shear stress is evaluated from bulk variables the results may be highly affected by the uncertainty of input variables, especially water surface slope. In such cases, stream power turns out to be less sensitive to the uncertainty of water surface slope and therefore may be more adequate than the bed shear stress in the analyses of factors affecting bedload rate. In other words computations of stream power led to more homogenous results.

The study revealed some problems regarding the experimental design and performance. The most serious one was to avoid water surface slope fluctuations in a flume for the mobile bed and shallow flow. We noticed smaller fluctuations for the tests with higher rate of unsteadiness. For such cases, evaluation of the variables based on water depth and water surface slope such as bed shear stress and stream power is more reliable.

It is crucial to control the impact of physical variables on the experimental results. Classical physical methods, such as dimensional analysis may help to understand relations between the bedload transport and the parameters governing its dynamics. In this study, a set of five dimensionless parameters and multiple regression model for dimensional cumulative mass were identified. The best fit model was as follows: $\pi_5 = b_1 + b_2\pi_2 + b_3\pi_3 + b_4\pi_4^{b_5}$.

The regression parameters $b_1,\ldots,b_5$ were identified for experimental data. These results may be used in future design of similar experiments.

Acknowledgements. This study has been partially financed by National Science Centre. Grant No. DEC-2011/01/N/ST10/07395 and partially within statutory activities No. 3841/E-41/S/2016 and 202961/E-377/S/2016 assigned by the Ministry of Science and Higher Education of Poland.

REFERENCES

Ahanger, M.A., Asawa, G.L., Lone, M.A., 2008. Experimental study of sediment transport hysteresis. Journal of Hydraulic Research, 46, 5, 628–635. DOI:10.3826/jhr.2008.3185.

Bagherimiyab, F., Lemmin, U., 2013. Shear velocity estimates in rough-bed open-channel flow. Earth Surface Processes and Landforms, 38, 14, 1714–1724. DOI: 10.1002/esp.3421.

Bendat, J., Piersol, A.G., 2010. Random Data: Analysis and Measurement Procedures. Wiley, Hoboken, NJ.

Bizzi, S., Lerner, D.N., 2015. The use of stream power as an indicator of channel sensitivity to erosion and deposition processes. River Research and Applications, 31, 1, 16–27. DOI: 10.1002/rra.2717.

Bombar, G., 2016. Hysteresis and Shear Velocity in Unsteady Flows. Journal of Applied Fluid Mechanics, 9, 2, 839–853.

Bombar, G., Elci, S., Tayfur, G., Guney, S., Bor, A., 2011. Experimental and numerical investigation of bed-load transport under unsteady flows. Journal of Hydraulic Engineering-ASCE, 137, 10, 1276–1282. DOI: 10.1061/(asce)hy.1943-7900.0000412.

Cao, D.P., Chiew, Y.M., Yang, S.Q., 2016. Injection effects on sediment transport in closed-conduit flows. Acta Geophysica, 64, 1, 125–148. DOI: 10.1515/acgeo-2015-0064.

Cooper, J.R., Tait, S.J., 2009. Water-worked gravel beds in laboratory flumes - a natural analogue? Earth Surface Processes and Landforms, 34, 3, 384–397. DOI: 10.1002/esp.1743.

De Sutter, R., Verhoeven, R., Krein, A., 2001. Simulation of sediment transport during flood events: laboratory work and field experiments. Hydrological Sciences Journal-Journal Des Sciences Hydrologiques, 46, 4, 599–610. DOI: 10.1080/02626660109492853.

Dey, S., 2014. Fluvial Hydrodynamics: Hydrodynamic and Sediment Transport Phenomena, Fluvial Hydrodynamics: Hydrodynamic and Sediment Transport Phenomena. GeoPlanet-Earth and Planetary Sciences. Springer, 687 p. DOI: 10.1007/978-3-642-19062-9.

Dottori, F., Martina, M.L.V., Todini, E., 2009. A dynamic rating curve approach to indirect discharge measurement. Hydrology and Earth System Sciences, 13, 6, 847–863.

Ettema, R., 2000. Hydraulic modelling: concepts and practice, ASCE manuals and reports on engineering practice no. 97. American Society of Civil Engineers, Reston, VA, USA.

Ferreira, R.M.L., Franca, M.J., Leal, J.G.A.B., Cardoso, A.H., 2012. Flow over rough mobile beds: Friction factor and vertical distribution of the longitudinal mean velocity. Water Resources Research, 48. DOI: 10.1029/2011wr011126.

Galia, T., Hradecky, J., 2011. Bedload transport and morphological effects of high-magnitude floods in small headwater streams - Moravskoslezske Beskydy Mts. (Czech Republic). Journal of Hydrology and Hydromechanics, 59, 4, 238–250. DOI: 10.2478/v10098-011-0020-x.

Gharbi, M., Soualmia, A., Dartus, D., Masbernat, L., 2016. Floods effects on rivers morphological changes application to the Medjerda River in Tunisia. Journal of Hydrology and Hydromechanics, 64, 1, 56–66. DOI: 10.1515/johh-2016-0004.

Guney, M.S., Bombar, G., Aksoy, A.O., 2013. Experimental study of the coarse surface development effect on the bimodal bed-load transport under unsteady flow conditions. Journal of Hydraulic Engineering-ASCE, 139, 1, 12–21. DOI: 10.1061/(asce)hy.1943-7900.0000640.

Guo, J., 2015. Sidewall and non-uniformity corrections for flume experiments. Journal of Hydraulic Research, 53, 2, 218–229. DOI: 10.1080/00221686.2014.971449.

Haddadchi, A., Omid, M.H., Dehghani, A.A., 2013. Bedload equation analysis using bed load-material grain size. Journal of Hydrology and Hydromechanics, 61, 3, 241–249. DOI: 10.2478/johh-2013-0031.

Humphries, R., Venditti, J.G., Sklar, L.S., Wooster, J.K., 2012. Experimental evidence for the effect of hydrographs on sediment pulse dynamics in gravel-bedded rivers. Water Resources Research, 48. DOI: 10.1029/2011wr010419.

Julien, P.Y., Klaassen, G.J., Ten Brinke, W.B.M., Wilbers, A.W.E., 2002. Case study: Bed resistance of Rhine River during 1998 flood. Journal of Hydraulic Engineering-ASCE, 128, 12, 1042–1050. DOI: 10.1061/(asce)0733-9429(2002)128:12(1042).

Kuhnle, R.A., 1992. Bed-load transport during rising and falling stages on 2 small streams. Earth Surface Processes and Landforms, 17, 2, 191–197. DOI: 10.1002/esp.3290170206.

Lee, K.T., Liu, Y.L., Cheng, K.H., 2004. Experimental investigation of bedload transport processes under unsteady flow conditions. Hydrological Processes, 18, 13, 2439–2454. DOI: 10.1002/hyp.1473.

Mao, L., 2012. The effect of hydrographs on bed load transport and bed sediment spatial arrangement. Journal of Geophysical Research-Earth Surface, 117. DOI: 10.1029/2012jf002428.

Mao, L., Cooper, J.R., Frostick, L.E., 2011. Grain size and topographical differences between static and mobile armour layers. Earth Surface Processes and Landforms, 36, 10, 1321–1334. DOI: 10.1002/esp.2156.

Michalik, A., Książek L., 2009. Dynamics of water flow on degraded sectors of Polish mountain stream channels. Polish Journal of Environmental Studies, 18, 4, 665–672.

Moog, D.B., Whiting, P.J., 1998. Annual hysteresis in bed load rating curves. Water Resources Research, 34, 9, 2393–2399. DOI: 10.1029/98wr01658.

Mrokowska, M.M., Rowiński, P.M., Kalinowska, M.B., 2015a. A methodological approach of estimating resistance to flow under unsteady flow conditions. Hydrology and Earth System Sciences, 19, 10, 4041–4053. DOI: 10.5194/hess-19-4041-2015.

Mrokowska, M.M., Rowiński, P.M., Kalinowska, M.B., 2015b. Evaluation of friction velocity in unsteady flow experiments. Journal of Hydraulic Research, 53, 5, 659–669. DOI: 10.1080/00221686.2015.1072853.

Mrokowska, M., Rowiński, P., Książek, L., Strużyński, A., Wyrębek, M., Radecki-Pawlik, A., 2016. Flume experiments on gravel bed load transport in unsteady flow – preliminary results. In: Rowiński, P., Marion, A. (Ed.): Hydrodynamic and Mass Transport at Freshwater Aquatic Interfaces. Geoplanet: Earth and Planetary Sciences. Springer International Publishing Switzerland, Berlin, Heidelberg, pp. 221–233. DOI: 10.1007/978-319-27750-9_18.

Nikora, V., McEwan, I., McLean, S., Coleman, S., Pokrajac; D., Walters, R., 2007. Double-averaging concept for rough-bed open-channel and overland flows: Theoretical background. Journal of Hydraulic Engineering-ASCE, 133, 8, 873–883. DOI: 10.1061/(asce)0733-9429(2007)133:8(873).

Ockelford, A.-M., Haynes, H., 2013. The impact of stress history on bed structure. Earth Surface Processes and Landforms, 38, 7, 717–727. DOI: 10.1002/esp.3348.

O'Kane, J.P., 2005. Hysteresis in hydrology. Acta Geophysica Polonica, 53, 4, 373–283.

Perumal, M., Shrestha, K.B., Chaube, U.C., 2004. Reproduction of hysteresis in rating curves. Journal of Hydraulic Engineering-ASCE, 130, 9, 870–878. DOI: 10.1061/(asce)0733-9429(2004)130:9(870).

Phillips, B.C., Sutherland, A.J., 1990. Temporal lag effect in bed-load sediment transport. Journal of Hydraulic Research, 28, 1, 5–23.

Qu, Z., 2002. Unsteady open-channel flow over a mobile bed. Ecole Polytechnique Federale de Lausanne, Lausanne, Switzerland.

Rajwa-Kuligiewicz, A., Bialik, R.J., Rowiński, P.M., 2015. Dissolved oxygen and water temperature dynamics in lowland rivers over various timescales. Journal of Hydrology and Hydromechanics, 63, 4, 353–363. DOI: 10.1515/johh-2015-0041.

Rowiński, P.M., Czernuszenko, W., Pretre, J.M., 2000. Time-dependent shear velocities in channel routing. Hydrological Sciences Journal-Journal Des Sciences Hydrologiques, 45, 6, 881–895. DOI: 10.1080/02626660009492390.

Rowiński, P.M., Czernuszenko, W., 1998. Experimental study of river turbulence under unsteady conditions. Acta Geophysica Polonica, 46, 4, 461–480.

Savitzky, A., Golay, M., 1964. Smoothing and differentiation of data by simplified least squares procedures. Analytical Chemistry, 36, 1627–1639. DOI: 10.1021/ac60214a047.

Sinnakaudan, S.K., Ab Ghani, A., Ahmad, M.S.S., Zakaria, N.A., 2006. Multiple linear regression model for total bed material load prediction. Journal of Hydraulic Engineering-ASCE, 132, 5, 521–528. DOI: 10.1061/(asce)0733-9429(2006)132:5(521).

Song, T., Graf, W.H., 1996. Velocity and turbulence distribution in unsteady open-channel flows. Journal of Hydraulic Engineering-ASCE, 122, 3, 141–154. DOI: 10.1061/(asce)0733-9429(1996)122:3(141).

Sun, H., Chen, D., Zhang, Y., Chen, L., 2015. Understanding partial bed-load transport: Experiments and stochastic model analysis. Journal of Hydrology, 521, 196–204. DOI: 10.1016/j.jhydrol.2014.11.064.

Tabarestani, M.K., Zarrati, A.R., 2015. Sediment transport during flood event: a review. International Journal of Environmental Science and Technology, 12, 2, 775–788. DOI: 10.1007/s13762-014-0689-6.

Talukdar, S., Kumar, B., Dutta, S., 2012. Predictive capability of bedload equations using flume data. Journal of Hydrology and Hydromechanics, 60, 1, 45–56. DOI: 10.2478/v10098-012-0004-5.

Wang, L., Cuthbertson, A.J.S., Pender, G., Cao, Z., 2015. Experimental investigations of graded sediment transport under unsteady flow hydrographs. International Journal of Sediment Research, 30, 4, 306–320. DOI: 10.1016/j.ijsrc.2015.03.010.

Yalin, M.S., 1972. Mechanics of Sediment Transport. Pergamon Press, Oxford, UK, 288 p.

Received 29 September 2016
Accepted 20 March 2017

J. Hydrol. Hydromech., 66, 2018, 1, 32–42
DOI: 10.1515/johh-2017-0041

An unusual kind of diurnal streamflow variation

Jaime G. Cuevas[1, 2, 3*], José L. Arumí[4], Alejandra Zúñiga-Feest[3, 5], Christian Little[6, 7]

[1] Centro de Estudios Avanzados en Zonas Áridas (CEAZA), Av. Raúl Bitrán 1305, La Serena, Chile.
[2] Instituto de Ingeniería Agraria y Suelos, Universidad Austral de Chile, Valdivia, Chile.
[3] Centro de Investigaciones en Suelos Volcánicos (CISVo), Universidad Austral de Chile, Valdivia, Chile.
[4] Facultad de Ingeniería Agrícola, Departamento de Recursos Hídricos, Centro CRHIAM, Universidad de Concepción, Chillán, Chile.
[5] Laboratorio de Biología Vegetal, Instituto de Ciencias Ambientales y Evolutivas, Facultad de Ciencias, Universidad Austral de Chile, Valdivia, Chile.
[6] Instituto Forestal (INFOR), Sede Los Ríos, Fundo Teja Norte s/n, Valdivia, Chile.
[7] Center For Climate and Resilience Research (CR)[2], Chile.
[*] Corresponding author. Tel.: +56 51 2204378. E-mail: jxcuevas@ceaza.cl.

Abstract: During hydrological research in a Chilean swamp forest, we noted a pattern of higher streamflows close to midday and lower ones close to midnight, the opposite of an evapotranspiration (Et)-driven cycle. We analyzed this diurnal streamflow signal (DSS), which appeared mid-spring (in the growing season). The end of this DSS coincided with a sustained rain event in autumn, which deeply affected stream and meteorological variables. A survey along the stream revealed that the DSS maximum and minimum values appeared 6 and 4 hours earlier, respectively, at headwaters located in the mountain forests/ plantations than at the control point in the swamp forest. Et in the swamp forest was higher in the morning and in the late afternoon, but this process could not influence the groundwater stage. Trees in the mountain headwaters reached their maximum Ets in the early morning and/or close to midday. Our results suggest that the DSS is a wave that moves from forests high in the mountains towards lowland areas, where Et is decoupled from the DSS. This signal delay seems to convert the link between streamflow and Et in an apparent, but spurious positive relationship. It also highlights the role of landscape heterogeneity in shaping hydrological processes.

Keywords: Evapotranspiration; Groundwater; Riparian zones; Streamflow; Swamp forests.

INTRODUCTION

The pattern of higher streamflow at dawn and lower streamflow during the afternoon has been identified for the past 80 years (Gribovszki et al., 2010). According to Graham et al. (2013), the source of these signals and the way in which they are propagated to stream gauging sites are poorly understood. The traditional concept establishes that groundwater is the link between the plant cover and the stream (Gribovszki et al., 2008; Szilágyi et al., 2008). When the groundwater level decreases at times of high evapotranspiration (Et), this decreases the stream recharge (Hughes, 2010), which lowers its stage. Conversely, when Et is low, water can be replenished in sites with depressed levels (including the stream) from groundwater coming from the uplands, from areas where phreatic water was not affected by an Et cycle (grasslands for example). However, other evidence suggests that the link might also be mediated by water found in the vadose zone (Bond et al., 2002; Bren, 1997; Burt, 1979; Graham et al., 2013). For example, Barnard et al. (2010), Moore et al. (2011) and Puchi (2013) found correlations between soil moisture, streamflow and evapotranspiration. Conversely, Brooks et al. (2010), based on a study with stable isotopes, demonstrated that water used by trees and that which feeds streams have different origins, where the latter is "mobile water", and the former is more tied to the soil. At present, it is not completely clear whether vadose zone moisture is a cause of diurnal streamflow variations or a correlate of groundwater fluctuations. Therefore, more research is necessary in this regard.

In spite of the fact that diurnal streamflow fluctuations have been studied for a long time, this topic has been comparatively little analyzed with respect to other hydrological characteristics. However, it has received renewed interest in recent years (Carlson Mazur et al., 2014; Graham et al., 2013; Mutzner et al., 2015). Some studies have even tested the possibility of artifacts caused by modern pressure transducers (Cuevas et al., 2010; Gribovszki et al., 2013; McLaughlin and Cohen, 2011). Even though some instruments can overestimate diurnal fluctuations, the consensus is that they are real.

Over the course of our hydrological research in a swamp forest in southern Chile, we noted an unusual pattern expressed as a higher streamflow close to midday, while the lowest streamflow was detected close to midnight. This is exactly the opposite pattern of an evapotranspiration-driven cycle. The studied catchment was not affected by snow melting or by soil freezing and thawing (Caine, 1992; Jordon, 1983), nor by water diversion for human use, nor does it experience heavy afternoon rains as occur in the tropics (Wain, 1994), which could all be evident explanations for the phenomenon. Long time lags, such as those found in this study, have scarcely been reported in the literature (Wondzell et al., 2007). When they have been detected, they have been explained in the context of water signals travelling through the catchments. Thus, the present finding motivated a detailed analysis of the variation. Therefore, this study's objective was to provide an explanation for this peculiar pattern, which challenges our present knowledge on the topic. Possible drivers were investigated, namely stream variables, groundwater, biological factors, meteorology, geomorphology, and land cover.

MATERIALS AND METHODS

Study site

The work was conducted at the Austral Experimental Livestock and Agriculture Station, located in the Los Ríos Region in southern Chile (39° 46' 55" S, 73° 13' 24" W), 4 km north of the city of Valdivia, and 15 km from the Pacific Ocean (Fig. 1a).

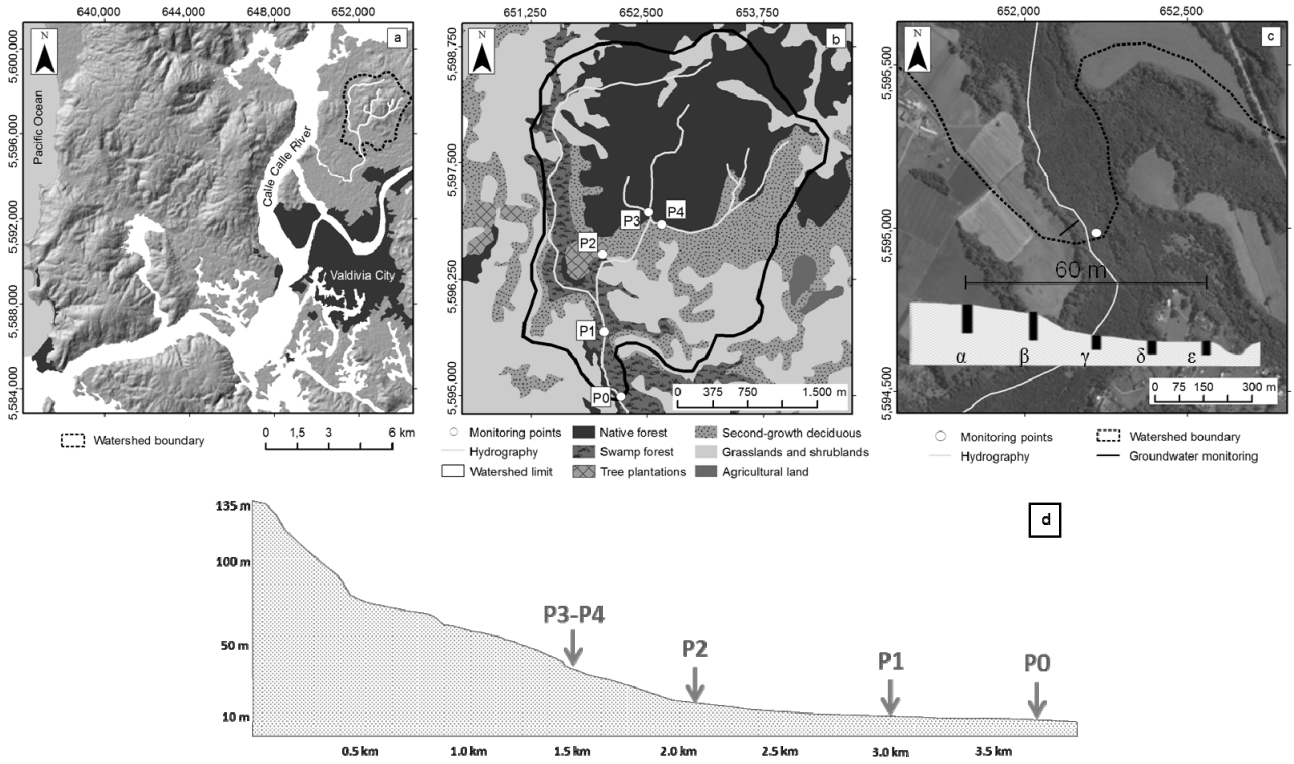

Fig. 1. a) Location of the study site in southern Chile. b) Delimitation of the Santa Rosa watershed. c) Detail of the main studied site (P0), showing the transect for groundwater evaluation (black line), and the position of boreholes along the slope. d) Longitudinal profile of the studied stream, with the monitoring points for stream stage (P0 to P4). Evapotranspiration rates were monitored for the trees *Blepharocalyx cruckshanksii* (at the site P1), *Eucalyptus nitens* and *Nothofagus dombeyi* (both at the site P3).

The climate is humid temperate (Amigo and Ramírez, 1998), with an average annual temperature of 12°C. Annual rainfall is 2,500 mm; most of the rain is concentrated in the winter season (June – August).

We studied the Santa Rosa watershed, whose creek is 5–6 m wide with a discharge of 45–1,107 L s^{-1} (in the summer and winter, respectively). The creek forms part of a watershed whose approximate area is 9.29 km^2 (Fig. 1b), flowing through the middle of a 250 m-wide native forest.

The geomorphology is mainly composed of alluvial terraces, with the uplands (0.5–3° slope) covered by grasslands of *Lolium perenne* L. (perennial ryegrass). A forested slope (25 m wide, 35° inclination) then connects with the floodplain (4° slope), which is also covered by native forest. The grasslands are located about 17 m a.s.l., while the Santa Rosa Creek is located at 4 m a.s.l. The stream begins to rise up to 140 m a.s.l. between 1.8 and 4.3 km upstream of the main studied site (named control point, P0), where second-growth, evergreen native forests and exotic tree plantations are found in the mountain headwaters (Figs. 1b, d).

The forested slope and the foothills below the mountain headwaters are dominated by second-growth deciduous forests of *Nothofagus obliqua* var. *obliqua* trees, *Chusquea quila* bamboo, and *Hedera helix*, an exotic vine. *N. obliqua* corresponds mainly to the indigenous vegetation that dominated the grassland area before its utilization for livestock breeding. The riparian vegetation found in the floodplain is characterized principally by native trees including *Blepharocalyx cruckshanksii*, *Myrceugenia exsucca*, and *Drimys winteri* var. *chilensis*, with few individuals of *N. obliqua*. The second-growth evergreen native forest found in the mountainous headwaters is mainly made up of arboreal individuals of *Aextoxicon punctatum*, *Amomyrtus luma*, *Luma apiculata*, *Lomatia hirsuta*, and *Nothofagus dombeyi*; vines of *Cissus striata* and *Boquila trifoliolata*, and bamboo thickets of *Chusquea quila*. Finally, exotic species include *Eucalyptus* spp., *Pseudotsuga mensiezii* and *Pinus radiata.* With the exception of *N. obliqua*, all of the flora is evergreen. In terms of land cover, grasslands account for 22% of the watershed, swamp forests 16%, exotic tree plantations 0.74%, second-growth evergreen forests 38%, and the second-growth deciduous forests on the foothills and on the slope adjacent to the swamp forests the remaining 23.26% of the area (Fig. 1b).

All of the soils are volcanic, but they belong to different orders. In the alluvial terraces adjacent to the control point, the soil corresponds to an Andisol, Valdivia series (Duric Hapludand or a Petroduri-Silandic Andosol; WRB, 2006). This soil is characterized by a low bulk density (< 0.9 Mg m^{-3}, Dörner et al., 2010) and a well-defined inter- and intra-aggregate pore system (Dörner et al., 2010), which allows for a large porosity and water holding capacity with a high saturated hydraulic conductivity, and thus a high water infiltration rate (Dörner et al., 2009). In the mountain headwaters, on the other hand, the soils belong to the order Acrisol (WRB, 2006) (also termed as Ultisols; Soil Survey Staff, 1999). This soil has a red clay aspect, and the corresponding series is Los Ulmos. Bulk density is 1.0 Mg m^{-3} (CIREN, 2001). In general, Ultisols are less porous than Andisols, and are more prone to overland flow.

General approach

Our study's overall method consisted of: i) documenting the diurnal streamflow signal (DSS) as detected by pressure loggers submerged in the stream. ii) Then, we confirmed whether the pattern was real by visually inspecting the stream during 24 h-cycles. iii) We also examined the full hydrological and rainfall series to detect when the DSS appeared and disappeared. iv) The stream temperature, which is a variable influenced by both

meteorological and hydrological factors, was also seasonally monitored. v) The influence of groundwater from adjacent floodplains was studied as well, since this has been documented in previous studies as a source of water for DSS. vi) We determined the signal timing in order to assess the precise moment when maxima and minima occurred, in addition to their variations throughout the season. vii) A more detailed study was carried out along a transect encompassing a longer extension of the Santa Rosa Creek, to assess the evolution of the DSS on both a temporal and spatial scale. viii) The influence of evapotranspiration was measured in representative trees in order to establish a link between plant Et, ground- and surface water. ix) The analysis of meteorological variables allowed for a longer time record of variables influencing potential Et (Et_0). x) Watershed geomorphology was considered due to the differences between the mountain headwaters and lowland areas' slopes, aspects, and altitudes. xi) Finally, the contribution of different land cover was assessed, since the studied watershed has multiple uses (mainly forestry, livestock and agriculture). Considering all of the aforementioned elements, we proposed an explanation for the observed DSS.

Streamflow variations

A HOBO U20-001-01 pressure logger (Onset Computer Corporation, Bourne, USA) was placed in the middle of the Santa Rosa Stream from May 2014 to November 2015 (the "control point, P0", Figs. 1b, c). This equipment, which measures pressure and temperature, was hung from a steel chain connected to the top cap of a PVC tube. The barometric pressure compensation logger was also placed in the stream, but within a PVC tube that was closed at the bottom to prevent water from entering. The top end of the PVC tube was left open, but was isolated from rain with a non-hermetic plastic "hat". The same barometer was used for the compensation of all the loggers installed in surface and groundwaters (see the following sections), making only some corrections necessary due to differences in altitude between the sampled wells and the stream (12 Pa m^{-1}). The interval of measurement was every 15 min.

The stream gauge was also visually inspected during two 24 h-surveys of water stage, in order to validate the logger's measurements. With this purpose, we installed a stake into the streambed with a tape measure glued to it. This tape was calibrated in millimeters and was carefully inspected from the same point of view, to avoid parallax errors, and using a flashlight at night.

The stream stages were converted into streamflow by using direct measurements with a Seba F1 current meter (Eijkelkamp, The Netherlands) at the studied stream reach P0, 100 m upstream and 100 m downstream; these measurements were then averaged to give a unique value. The stream's velocities were measured at 20 and 80% of the stream depth, in several sections of each of the three studied transects. Discharges were measured 11 times from December 2012 to August 2015 and were related to water stage by means of a power function.

Well assessment

Five wells were installed in a line from the upland area to the floodplain, perpendicular to the stream (P0 point, Fig. 1c). The positions were α (upland), the upland-slope border (β), 15 m from the border on the slope (γ), and 30 (δ) and 45 m (ε) from the same border, corresponding to the floodplain. The ε wells were adjacent to the stream. Wells were cased with 7.5 cm-diameter PVC tubes, and were screened with 2 mm openings. The screened sections were covered by a thin fabric (openings 200 μm) to prevent blockage by incoming sediment. The boreholes were then sealed with a mixture of gravel and sand. Finally, the top 25 cm were sealed with swelling bentonite mixed with soil.

The groundwater level was studied by placing HOBO U20-001-01 pressure loggers inside the five monitoring wells; these were the only loggers available in 2015. A small hole was perforated on the sidewall of each PVC well, to equalize internal and external barometric pressures, which is necessary for true barometric compensation. The interval of measurement was also 15 min.

Stream stage variation along the stream

A more detailed survey was undertaken between December 2016 and March 2017, when four additional loggers were placed 622 (P1), 1759 (P2), 2608 (P3) and 2639 m (P4) upstream of P0, following the main reach. Two of these loggers were located in the swamp forest, at about the same altitude, while the two farthest points were 40 m a.s.l. in the mountainous forest, where two tributaries converged to form part of the main reach (Fig. 1b). Thus, P3 and P4 belonged to the sequence P0- P1- P2- P3 (or P4), but the latter two did not form part of the same drainage area.

Due to the availability of equipment, a Levelogger Junior sensor (model 3001, Solinst, Ontario, Canada) had to be used in P1, while in the other stations we employed HOBO dataloggers. All time is referred to in UTC minus 5 hours, according to the time zone where Chile is located (meridian 71° W).

Sensor accuracy

According to the manufacturer, the HOBO logger's operation range is 0 to 207 kPa (approx. 0–9 m water depth at sea level), and from –20 to 50 °C. The typically reported error is 0.5 cm for water level and 0.37°C (at 20°C) for temperature, with a resolution of < 0.02 kPa (0.21 cm water) and 0.1°C (at 20°C) (Onset Computer Corporation, 2005, 2006). Cuevas et al. (2010) experimentally determined that the error for the model used in this study is equivalent to 0.4 cm. On the other hand, the corresponding values for the Levelogger consist of a 10 m range, 0.9 cm error, and 0.27 cm resolution (Solinst, 2011).

Tree evapotranspiration

To investigate one of the possible drivers of the diurnal streamflow pattern, the following species were studied: *Blepharocalyx cruckshanksii*, the most common tree in the swamp forest adjacent to the P1 site (March 24th, 2017); *Eucalyptus nitens*, a common exotic species planted in this area and in southern Chile in general; and *Nothofagus dombeyi*, which is representative of the mountain forest. The two latter species were studied close to the P3 site (March 29th, 2017; Fig. 1b). Three to five healthy leaves were randomly selected from a height of about 1.7 m above the ground from 2–5 individuals per species. We measured the transpiration rate using an Infrared Gas Analyzer (model ADC-LCA4, Analytical Development Co., Hoddesdon, UK). This variable was measured 10-15 times throughout the day, with a phase difference of 10 min from tree to tree. The time lapse was from 7:30 to 17:20 h (UTC–5), given that evapotranspiration is expected to be negligible during night hours (Puchi, 2013). The results were expressed on a leaf area basis and per unit of time, determined by the size of the measurement chamber.

Meteorological variables

A longer meteorological record was obtained for precipitation, air temperature and solar radiation, which were measured every 30 min using a Davis Vantage Pro 2 weather station (Hayward, CA, USA), installed 6 km from the study site in the city of Valdivia (Miraflores; https://centroccbb.cl). Valdivia's potential evapotranspiration (Et_0) was estimated according to the Penman-Monteith equation at an hourly resolution. Relative air humidity was obtained hourly from the Las Lomas (Máfil) station (Campbell Scientific CR 1000, Logan, UT, USA, available from http://agromet.inia.cl), 30 km from the study site, since the other station was unequipped to measure this variable.

Data analyses

Times for maximum and minimum values of the variables of interest were calculated through macros designed with Excel ® software (Microsoft Corporation, Redmond, WA, USA). Times were reported only for those days when the DSS was present. For comparisons of diurnal cycles along the stream we only selected those days that met the following criteria: i) DSS was perceptible through visual inspection of the datalogger records; ii) the amplitude of the signal for both the rising and falling limb of the diurnal hydrogram was above the instrumental error; iii) no rainfall above 1.8 mm fell that day, since this was the threshold that was unable to hide or distort the diurnal signal.

RESULTS

Signal detection

The stream showed clear diurnal fluctuations in water stage, where maximum levels were observed around midday and minimum levels close to midnight (Fig. 2a). The forested slope's groundwater also demonstrated a diurnal fluctuation, although it was slightly more buffered at the rising limb (5 mm) than the stream stage (10 mm), but the converse was observed at the falling limb (19 mm on the slope vs. 11 mm in the stream) (Fig. 2a). Since the stage diminutions were more marked for groundwater, this explains why the stream level was more stable during the analyzed period. Contrary to the aforementioned trends, neither the floodplain (Fig. 2a) nor the upland groundwater (data not shown) showed a discernible diurnal fluctuation.

Visual characterization of the pattern

The visual inspection on January 28th and 29th 2015 revealed that stream level did not fluctuate between 7:30 and 15:30, but did decrease from then onwards (Fig. 3). The minimum level was reached at 1:30 a.m., equivalent to 1 cm less than at the beginning of the inspection. Stream stage recovered 7 mm by 11:00 h, showing lower levels later on. The maximum on January 29th could not be precisely determined because hourly observations were not conducted as they were on the previous day. However, with the help of data logger records it could be determined that this curve followed approximately the direct inspection curve (with the exception of the morning and early afternoon of January 28th). The data logger record peaked between 13:00 and 14:15 on January 29th. The noise in this curve may be associated with instrumental error (0.5 cm) and the disturbance of water flow caused by submerged and emergent woody stems. Observations on February 10th and 11th 2016 showed a smooth pattern, with a minimum level at 7:30 a.m., and a maximum level between 11:30 and 13:30 on February

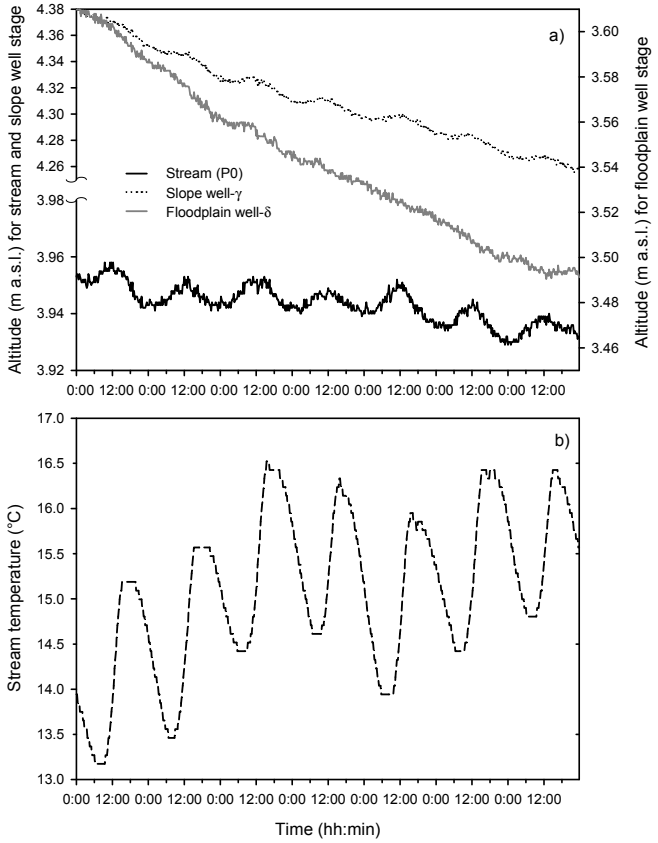

Fig. 2. a) Diurnal stream level variation for a representative week beginning on January 15th 2015. The slope and floodplain groundwater table altitudes are also shown. Ground level is 9.13 m a.s.l. for the slope and 4.83 m for the floodplain. b) Diurnal stream temperature variation for the same week. The upland groundwater (α, β wells) did not show a discernible diurnal level fluctuation and thus data are not shown.

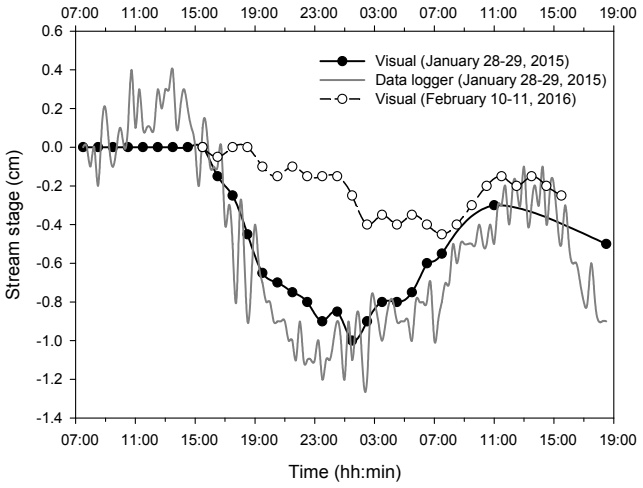

Fig. 3. Diurnal stream stage variation for two dates through visual inspection, contrasted with the data logger record. The water level at the start of the measurements was arbitrarily considered as 0.

11th (Fig. 3). No datalogger records were available for these dates. Generally, the maximum of any given day is lower than the maximum of the previous day. In other words, the decreasing stage trend throughout the night cannot be compensated for by an equivalent rise the next day.

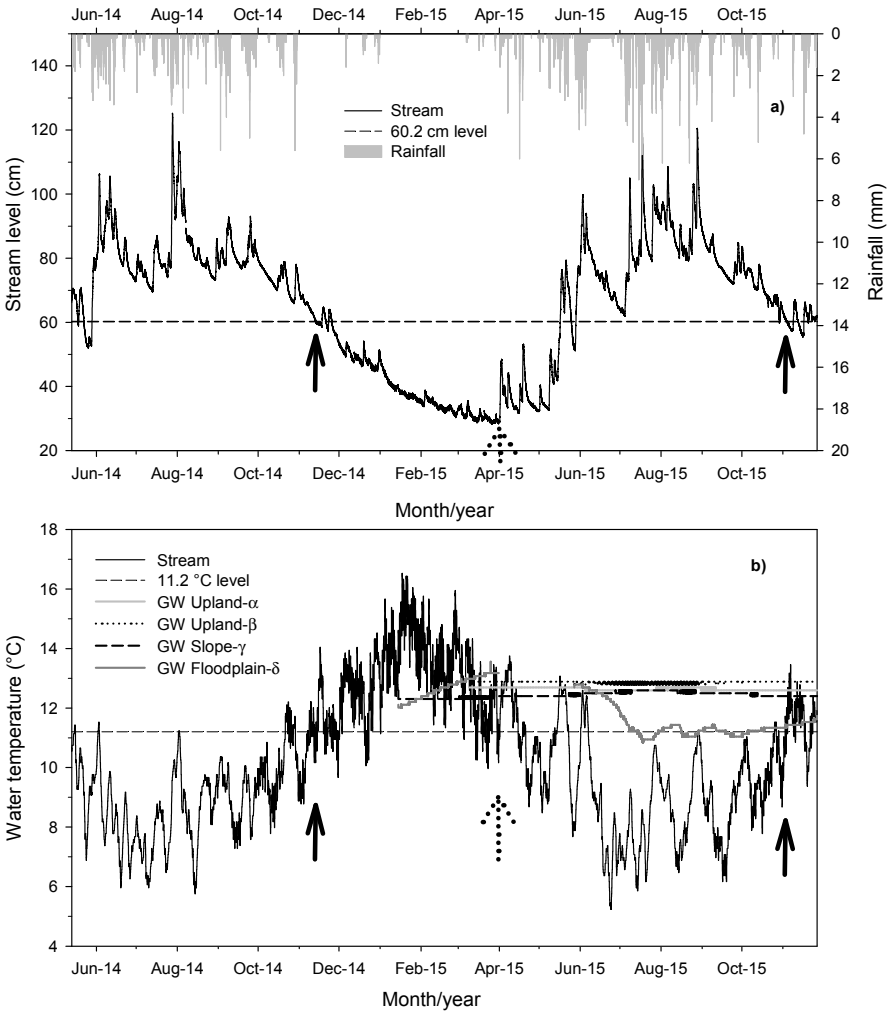

Fig. 4. Temporal fluctuations in stream water level (a), and stream and groundwater (GW) temperature (b). The black arrows indicate the start of the diurnal fluctuation in stream level, while the dotted arrow is the end. The reference lines indicate the values for the appearance or disappearance of this signal.

Signal onset and extinction

The stream level demonstrated large fluctuations throughout the autumn, winter and beginning of spring, due to rainfall events (Fig. 4a). The DSS was first detected on November 14th, 2014 when the stream water stage was 59.6 cm above the streambed. This date corresponds to mid-spring in the Southern Hemisphere, when the growing season is well advanced. The signal remained while the streamflow decreased, even though some sporadic rain events hid the diurnal variation. The signal disappeared on April 1st, 2015 (autumn) when the stream level was 29.2 cm, due to a rain event of 30 mm in 29 hours. No evident signal was detected from April until the beginning of November 2015 (the 3rd day). This time, the stream water stage was 60.9 cm. In general, the DSS was present throughout most of the spring and summer, with a slight trend to decrease in amplitude throughout the season (Fig. 5).

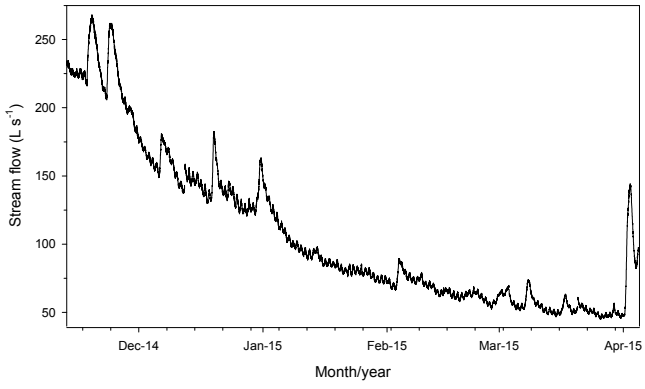

Fig. 5. Seasonal dynamics of the diurnal streamflow variation.

Ground- and surface water temperature

When the DSS appeared in November 2014, the stream temperature was 11.3°C (Fig. 4b). The signal disappeared on April 1st when it was 11.1°C. In the following months, the stream temperature only sporadically surpassed this value. When the signal reappeared on November 3rd, 2015 it was 11.0°C.

Stream temperature experienced repetitive fluctuations throughout the duration of the DSS, from 1.5–2°C each day (Figs. 2b, 4b). These fluctuations are shown in Fig. 4b as more intense and frequent than those corresponding to the rainy season, when the daily temperature fluctuations are not so regular.

Groundwater experienced no temperature fluctuations in upland-α (12.6°C), upland-β (12.9°C), and slope-γ (12.4°C) (Fig. 4b).

Conversely, floodplain-δ groundwater fluctuated between 10.8 and 13.6°C during the first seven months of 2015, and then remained fairly stable towards the end of this year. A diurnal cycle was not detected in any of the studied groundwater.

Signal timing

In November 2014, the maximum stream stage was recorded at 11:00 a.m., on average, with a range covering the entire morning and early afternoon (Table 1). Throughout the season, the maximum water stage became further delayed, reaching 13:00 in March 2015. The minimum water stages were registered late at night, with a progressive temporal shift as the summer season advanced (Table 1).

From January to March, the time of the recorded maximum levels for the forested slope's groundwater varied from 11:42 to 13:22 on average, while the time of the minimum levels ranged from 4:07 to 6:12 (Table 1). The time at which the maximum slope's groundwater table was recorded did not greatly differ from that of the maximum streamflow; however, the time at which the minimum slope's groundwater table was recorded showed a clear delay compared to minimum streamflow.

Stream stage variation along the stream

The P4 station showed stream stage diurnal cycles that, on average, peaked at 6:14 h in the summer (Table 2). P2 reached its maximum at 8:08 h, while the two downstream stations showed maximum stream levels about midday, supporting the previous year's findings for P0. On the other hand, P3, which is located in a different tributary than P4, but which both drain into the Santa Rosa Creek, was rather atypical because its maximum stream stage occurred at 9:25 h (see Discussion). Thus, there was a lag of about 6 h between the highest and lowest stations.

Regarding the minima, the pattern was less distinct than in the previous analysis because P4 showed the lowest stream stages at 19:39 h (summer average), which was very similar to P3 (Table 2). P2, on the other hand, reached the lowest stream levels at 17:27 h, and finally P1 and P0 at 23:39 and 23:48, respectively. When considering all of the studied cases, a lag of 4 h was found between the opposite extremes of the studied stream segment.

Fig. 6 shows the hydrograms for three representative days in the middle of the 2017 summer. For example, on February 2nd P0 was the last to reach its maximum stage at 13:45 h, while P4 was the first at 7:00 h, followed by P3 at 10:45 h, P2 at 11:45 h, and then P1 at 12:30 h.

Once again, the times for the lowest stages had a lower discriminating power for these cycles (Fig. 6). From P4 to P0, the sequence was 20:15, 18:15, 15:45, 20:15, and 20:00–20:15 (P0). For the other days, in general the trend found at the highland stations anticipated that of the lowland sites, for both the maxima and the minima.

Table 1. Time for minimum and maximum stream and slope groundwater stage.

	P2											
Month/year	Stream level maxima			Stream level minima			Slope groundwater maxima			Slope groundwater minima		
	Mean	Min	Max	Mean	Min	Max	Mean	Min	Max	Mean	Min	Max
Nov-2014	11:00	8:30	14:30	0:09	20:45	3:30	nd[a]	nd	nd	nd	nd	nd
Dec-2014	10:55	6:30	13:30	0:34	22:00	4:00	nd	nd	nd	nd	nd	nd
Jan-2015	12:09	9:00	15:00	1:52	23:00	6:00	11:42	9:30	14:30	4:07	0:45	7:15
Feb-2015	12:51	10:45	15:15	1:53	19:45	7:15	12:17	9:00	15:30	3:39	22:15	11:45
Mar-2015	12:59	10:00	15:15	2:28	18:45	7:00	13:22	10:15	15:15	6:12	21:00	11:15

[a]nd: no data since the sensor was installed on site in January 2015.

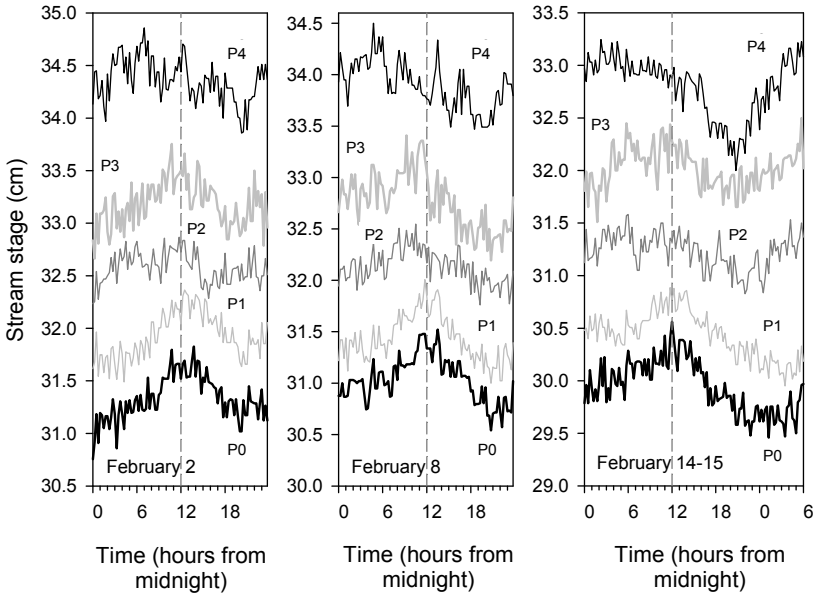

Fig. 6. Variations of stream stage at different stations located in the Santa Rosa Creek, at 0 m (P0, lowest curve), 622 m (P1), 1759 m (P2), 2608 m (P3), and 2639 m (P4, highest curve), upstream of P0. Stage offsets were applied to each curve to decrease the vertical separation among curves, allowing for a simplified comparison of cycles. The vertical dashed line represents midday.

Table 2. Times for maximum and minimum stream stages for points located along the Santa Rosa Creek, at 0 m (P0), 622 m (P1), 1759 m (P2), 2608 m (P3), and 2639 m (P4), upstream of P0. N = sample size for the period December 14th, 2016 to March 9th, 2017.

Station	Time for maximum stream stage				Time for minimum stream stage			
	Mean	Min	Max	N	Mean	Min	Max	N
P0	11:51	7:15	14:45	37	23:48	17:15	9:00	39
P1	12:06	8:45	14:45	12	23:39	19:30	7:30	25
P2	08:08	3:00	14:15	29	17:27	12:30	0:00	27
P3	9:25	3:45	15:30	50	19:23	9:45	23:45	54
P4	6:14	2:15	10:30	26	19:39	14:45	23:00	28

Tree evapotranspiration

Blepharocalyx cruckshanksii showed transpiration rates of 30–750 µmol H_2O m^{-2} s^{-1}, depending on the individual tested and the time of day (Fig. 7a). Maximum values were observed during the morning (8:00 a.m.), while the lowest values were observed at midday. The Et intensified towards the last time analyzed (16:20 h).

On the other hand, *Eucalyptus nitens* (Fig. 7b) showed a clear pattern, where maximum Et occurred around midday, while lower values were observed at earlier and later hours. However, Fig. 7b suggests that there is a secondary peak at 8:00 a.m. Finally, *Nothofagus dombeyi* exhibited a pattern that may be considered a mixture of the other two species' behaviors (Fig. 7c). Et was very high in the early morning (> 2 mmol H_2O m^{-2} s^{-1}), followed by a decrease, and then a recovery after midday. However, Et started to decrease again in the afternoon. Interestingly, the Et experienced diminutions in the middle of the high Et period for both *Eucalyptus* and *Nothofagus*.

Meteorological variables

Fig. 8a shows that air temperature was the highest during the first hours of the afternoon, with its lowest values around 6:00 a.m. The solar radiation cycle anticipated that of the air temperature, which reached its maximum values close to midday, and minimal values (0 W m^{-2}) from 18:00 to 6:00 h, at the end of March 2015 (Fig. 8a). The relative humidity reached values close to 100% even in the summer, peaking before dawn and dropping to its lowest values during the first hours of the afternoon (Fig. 8b). However, since this variable was measured 30 km from our study site, we cannot be sure that the relative humidity was the same in both sites. Potential evapotranspiration (Et_0) also reached its maximum values close to midday, while its minimum or null values were estimated at night (Fig. 8b).

These variables demonstrated no special change in their patterns before the beginning of the DSS in November 2014; their magnitudes simply increased or decreased progressively with the advance of the season (data not shown).

Conversely, at the end of the DSS, April 1st and 2nd, rain profoundly affected all of these variables (Fig. 8). This is apparent when the buffered fluctuations are compared to the period when the DSS was active.

Regarding maximum air temperature, little seasonal temporal shifting was observed (the timing was about 13:00 h, Table 3). Minimum temperatures were registered between 4:07 and 5:14 a.m., on average, when the season progressed.

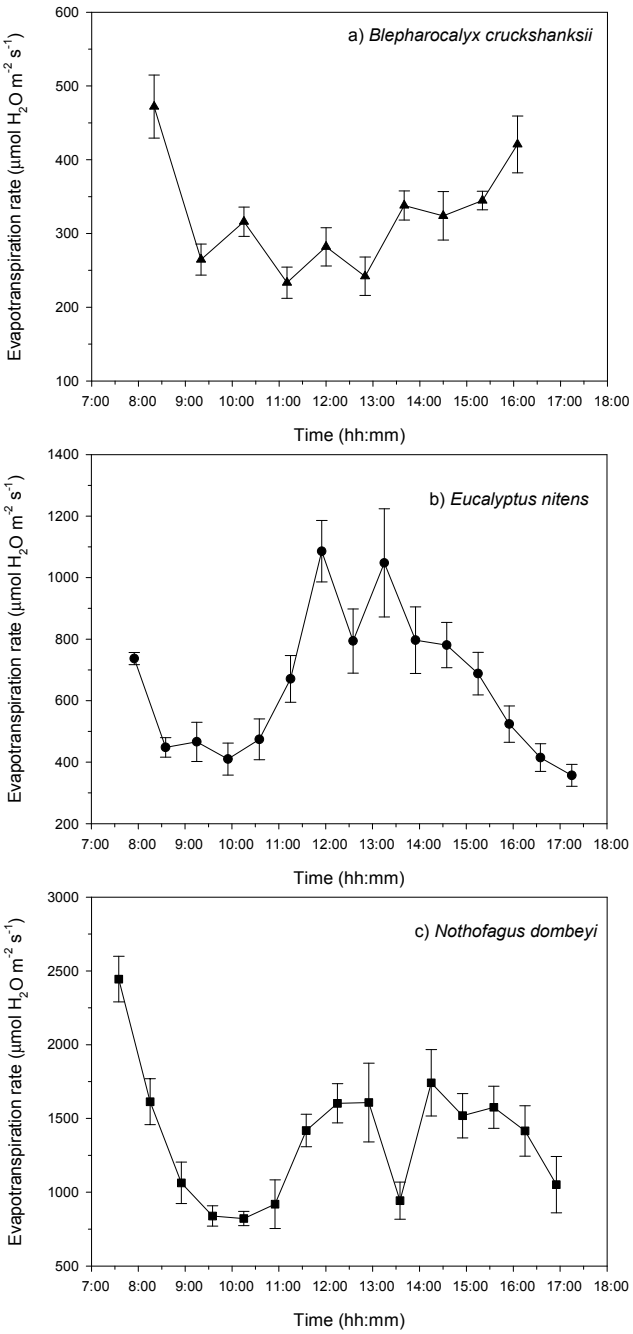

Fig. 7. Evapotranspiration rates for the trees *Blepharocalyx cruckshanksii* (site P1), *Eucalyptus nitens* and *Nothofagus dombeyi* (both at the site P3) throughout the daylight hours. Values are averages ± standard error of 2–5 trees per species, with 3–5 leaves as replicates per tree and per sampling time.

DISCUSSION

Stream and meteorological variables

The visual inspection of the Santa Rosa Creek revealed that the DSS is real. The amplitude of the signal was small, typically 1.0 cm, but higher than the sensor accuracy. Since the noise of most water sensors available in the market is rarely under 0.5 cm, the DSS pattern poses challenges for the detection of small

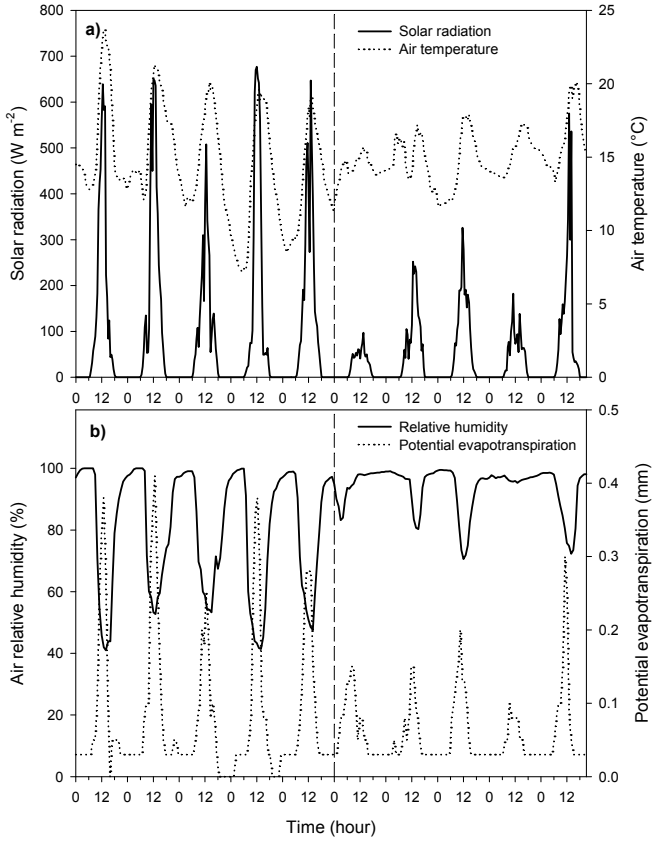

Fig. 8. Variables recorded at the Valdivia (Miraflores) or Máfil (Las Lomas, only relative humidity) meteorological stations at the end of March 2015. a) Air temperature and solar radiation; b) Air relative humidity and potential evapotranspiration. The vertical dashed line corresponds to the end of the diurnal streamflow signal and to the start of the sustained rain (April 1st).

Table 3. Time for minimum and maximum air temperature.

Month/year	Air temperature maxima			Air temperature minima		
	Mean	Min	Max	Mean	Min	Max
Nov-2014	nd[a]	nd	nd	nd	nd	nd
Dec-2014	13:06	10:00	16:00	4:07	21:30	5:30
Jan-2015	13:47	10:00	15:30	4:13	21:30	5:30
Feb-2015	nd	nd	nd	nd	nd	nd
Mar-2015	13:17	12:00	16:00	5:14	21:30	7:30

[a]nd: no data because the meteorological station was out of service.

signals. Thus, the most sensitive and accurate dataloggers should be used for this kind of studies. The DSS appearance when a certain stream stage is reached suggests hydraulic control, while the associated stream temperature at the phenomenon's onset is most likely related to a meteorological effect. The former association is consistent with generalizations about an increase in stream-groundwater exchanges when streamflows and stream stage are lowest (Valett et al., 1997; Voltz, 2011; Wroblicky et al., 1998). On the other hand, the regular pattern in stream temperature variation for the duration of the DSS is most likely related to the regular and intense variations in air temperature (Mohseni and Stefan, 1999) typical of sunny days in the summer. This is fundamentally different from other seasons, when stream temperature is more directly driven by the influx of water during storms (sparse curve patterns). The influence of the aforementioned increase in stream-groundwater exchanges on stream temperature was expected to be smaller than that of the air temperature, because groundwater temperature was nearly constant and did not exhibit a diurnal temperature cycle. This pattern also discards recent causes used to explain the present DSS, such as water viscosity fluctuations (Schwab et al., 2016).

The DSS has also been found to begin when monthly Et_0 surpasses monthly rain in November and ends when this pattern reverses (April; Huertas et al., 2016). Meteorological variables such as air temperature, solar radiation, and Et_0 are well known to progressively increase from winter to summer (Cruz and Calderón, 2008; Sánchez, 2016). The upward crossings of certain levels for these variables (in addition to stream temperature) or downward crossing for air relative humidity, and stream stage, seem to be the indicators related to the onset of the DSS. Thus, the DSS becomes visible at a relatively low stream stage, low air relative humidity, in addition to high air and stream temperatures, and high radiation and Et_0, compared to the weeks prior to the appearance of the DSS. This generalization was fairly coherent for the two spring seasons analyzed.

The end of the DSS was also found to be related to several of the analyzed variables, which either increased or decreased almost suddenly and simultaneously, or demonstrated a lower diurnal fluctuation (Fig. 8). The DSS vanished even though the stream stage was within the range that should have demonstrated a DSS, because the stream flow recovery required a sustained rate of rainfall that hid the DSS. Bond et al. (2002) and Graham et al. (2013) have also pointed out that diurnal streamflow signals are interrupted by rain events and cloud-covered days. Overall, most variables continuously rose or declined from spring to summer, with no abrupt changes that could have triggered the DSS.

Moreover, soil moisture has been found to decrease below a certain threshold value at the DSS start, and recover concomitantly to the DSS extinction (data not shown). This background highlights the importance of catchment storage for DSS appearance, which deserves further research.

Evapotranspiration

If Et is the direct cause of the DSS, corresponding time lags with respect to the streamflow response should occur within a few hours, as has already been reported by Constantz (1998), Bond et al. (2002), Szilágyi et al. (2008), among others. However, in our study, the lag between the maximum expected evaporative demand and the lowest streamflow was about 12 h; the lag between the lowest Et_0 and the highest stream level was up to 8 h.

The time difference may not correspond to our expectations because the temporal cycle of Et_0 is not necessarily the same as that of tree Et. In fact, the analyzed species showed main or secondary maximum rates in the morning (before 8:00 a.m.) and in the late afternoon (after 16:00 h for *B. cruckshanksii*). We have no data for earlier and later hours; thus, the exact moment of maxima throughout the 24 h-cycle is unknown. However, it is expected that Et be very low at night, as shown by other research (Puchi, 2013). Moreover, Zúñiga-Feest et al. (2017) found that two of the main species of the studied swamp forest (*L. apiculata* and *M. exsucca*) have higher stomatal conductance (a proxy of the transpiration rate) early in the morning (8:00–9:00 a.m., UTC − 5) as compared to that which occurs in the afternoon. The probable cause is that stomatal conductance in these seedlings is more responsive to changes in air humidity than to light availability during the day. These greenhouse studies also showed that two other riparian species (*D. winteri* and *B. cruckshanksii*) showed no significant variations in relation to this physiological characteristic throughout the course of

the day. The pattern found for *B. cruckshanksii* in the field should generate a lower streamflow during the first morning hours than that expected for a common Et-driven DSS, and viceversa in the case of the Et minima at midday. However, the floodplain groundwater showed no diurnal signal, probably because water is not a limiting resource in this environment, as tree roots are extensively submerged. Furthermore, during the course of slug tests Huertas et al. (2016) observed a very fast recovery of the floodplain's water table, in the order of minutes, compared to slope wells (30 min) and upland wells (more than 1 h). The slope's groundwater could be difficult to relate to the local Et because its diurnal fluctuations were also very out-of-time with respect to common Et-cycles. Thus, the diurnal signal found under the slope-γ could reflect a dragging, delayed effect from the stream, rather than the cause of the DSS.

The signal has been found to vanish under the uplands where grassland roots cannot influence the groundwater table 7–8 m belowground (Cuevas et al., 2014). This is coherent with a study in headwater catchments in Oregon, USA, where Voltz (2011) also found that the amplitude of the diurnal groundwater table variation is maximal at intermediate distances from the stream.

The two species belonging to the mountain forest had Et cycles similar to that expected for typical forest species, with some important diminutions at the peak of the evaporative demand, probably related to the decrease of stomatal conductance that we measured in parallel (data not shown). This indicates that these species can restrict their water loss and do not simply behave as a passive water reservoir. Puchi (2013) also found that *Eucalyptus globulus* has Et cycles with maximum transpiration rates close to midday, with very low values at night.

Interpretation of the diurnal signal

Our results show that the DSS reached maximum values early in the morning for the stations located in the headwater mountain forest areas, coherent with a typical Et control. The maximum appeared progressively later downstream. P3 did not demonstrate the exact same timing as P4. If we consider that they belong to different tributaries, it is not surprising that they have a different DSS. No data is available for explaining this discrepancy, but perhaps some heterogeneity in apparently homogeneous watersheds exists, given the differences in vegetation cover, slopes, aspects, drainage area, etc.

The minimum values of DSS also occurred earlier in the mountainous area, but later than the expected time (19:30 h). Usually, the lowest streamflows occur during the first hours of the afternoon (13:30–16:30 h; Wondzell et al., 2007; Gribovszki et al., 2008; Cuevas et al., 2010). In addition to a delay between maximum Et and the previously reported stream response (Bond et al., 2002; Constantz, 1998; Szilágyi et al., 2008), we must consider that the watershed begins 1.5–2.0 km upstream of our highest monitoring points (P3 and P4), which may explain the relatively late time for the stream minima, if the DSS does indeed originate upstream.

In fact, the present evidence suggests that the DSS is a wave that originates in the mountainous forests and travels through the tributaries that drain to the Santa Rosa Creek. We recorded a short lag between the timing for the observed Et cycles, which would reach their minimum values at night, and the corresponding maximum streamflows. However, when the streamflow enters the swamp forest, we found this vegetation cover (and the adjacent deciduous forest) unable to generate an Et cycle that could impact ground- and surface waters. Thus, the signal appeared to be progressively decoupled from the vegetation cycles. Finally, when the DSS reached P0 it was fully reversed with respect to the expected timing.

The origin of the Et-driven DSS in the mountains located in the headwaters may have to do with the second-growth evergreen forests and exotic tree plantations (less than 20 years old) found there, which are in an active period of growth, with comparatively high Et rates. Exotic *Eucalyptus* trees are especially well known for their high Et (Fetene and Beck, 2004; Scott and Prinsloo, 2008). However, the cover of this species alone (0.74% in the Santa Rosa catchment) may not be the only factor controlling stream levels. Cuevas et al. (2010), working in the Coastal Mountain Range of southern Chile, found a clear DSS. Its watershed had a 69% cover of *Eucalyptus*, but even in those areas covered entirely by native forest the pattern was still clear. Thus, native species also have the potential to influence the stream stage, despite their lower Et rates compared to *Eucalyptus* trees (Jiménez-Castillo et al., 2011; Puchi, 2013).

Moreover, different soil orders may also be involved in the diverse responses of streams to Et cycles. Andisols, which have a large water holding capacity (Dörner et al., 2009), are typical of the swamp forest, while Ultisols dominate the mountain headwaters. Given that Cuevas et al. (2010) also detected a clear DSS on Ultisols, further research should clarify how the different hydraulic properties of these soils modulate the transmission of Et signals towards the stream.

In small headwater catchments, the DSS would most likely propagate very quickly as found by Cuevas et al. (2010), but in those with an important flat zone, such as the studied swamp forest, the time lag could be much longer. Long time lags, such as those found in this study, have scarcely been reported in the literature (Wondzell et al., 2007), and when they were established they were analyzed in a different context than our research. For instance, Voltz (2011) showed that the DSS minimum ranged from 15:00 to 1:00 h, while the DSS maximum varied from 2:00 to 10:00 h, suffering a progressive delay with the advance of the season. Graham et al. (2013) found lags of up to 9 hours between the sap flow and the DSS. These patterns have been explained based on Wondzell et al. (2007), who considered Et to be a signal generated over an entire catchment, where at low flows the reduced stream velocity could (conceptually) produce a destructive interference of down-network traveling signals, masking some or all of the upstream signals. This hypothesis received support from Graham et al. (2013), but in our study the net result was the DSS delay due to the long travel time from the mountains.

Our interpretation of the DSS lag is a little different from Wondzell et al. (2007), Voltz (2011) and Graham et al. (2013) given that their watersheds were relatively homogeneous in their riparian vegetation, soil, and slope along the same stream channel. In our case, these factors change along the altitudinal gradient, and thus highlight the role of landscape heterogeneity in shaping hydrological processes. It would be interesting to determine if the DSS lag still persists in watersheds with old-growth forests in the uplands, vegetation which was never replaced by grasslands.

CONCLUSIONS

The diurnal streamflow pattern examined in this paper shows the complex interrelationship between atmospheric variables (air temperature, solar radiation, air relative humidity), plant cover (Et), geomorphology, land cover, and stream and groundwater stage. Meteorological variables showed no special consistent changes during the onset of the DSS, instead the crossing of environmental values appears to activate this

stream signal. This is most likely caused by intensified evapotranspiration cycles from late spring onwards, when water becomes a limiting resource. Conversely, the end of the signal was profoundly influenced by rain, which strongly affects the meteorological, plant, soil, and water variables. We propose that stream stage delays with respect to a typical Et cycle are due to the great distance between source areas high in the mountains (covered by second-growth evergreen native forests and exotic tree plantations) and the lowland zones covered by swamp forest, under a scenario of null influence of local Et on stream stage. These long lags make the cause-and-effect relationship of local Et and stream stage seem non-apparent or even positively and spuriously related. Diurnal fluctuations in streamflow are more complex than presently considered by accepted models, and we concur with Gribovski et al. (2010) that this topic deserves further study.

Acknowledgements. Funding was provided by Fondecyt grant 1110156. INIA hosted the first author during the phase of data collection. We would like to thank the Santa Rosa Experimental Station staff for their help, especially the Administrator Carlos Villagra. JC also thanks his deceased colleague Miguel Ángel López (INIA Quilamapu) for designing the macro used in this paper Felipe Labra (INFOR) drew the Fig. 1. Logistical support was provided by Mr. César Lemus, Mlle. Mélanie Krauth, and especially Rodrigo Bravo. Dr. José Dörner provided some helpful ideas for earlier versions of this paper. Additional acknowledgements go to Dr. Carlos Oyarzún (Universidad Austral de Chile), who supported this research, Dr. Antonio Lara and Mr. David Lobos from CR^2 (Center for Climate and Resilience Research) for lending us part of the equipment used in this study, and to the Water Center CRHIAM Conicyt/Fondap/15130015 for supporting part of the data analysis and the English edition of the document. Finally, two anonymous reviewers contributed with helpful suggestions.

REFERENCES

Amigo, J., Ramírez, C., 1998. A bioclimatic classification of Chile: woodland communities in the temperate zone. Plant Ecol., 136, 1, 9–26.

Barnard, H., Graham, C., Van Verseveld, W., Brooks, J., Bond, B., McDonnell, J., 2010. Mechanistic assessment of hillslope transpiration control of diel subsurface flow: a steady-state irrigation approach. Ecohydrology, 3, 2, 133–142.

Bond, B.J., Jones, J.A., Moore, G., Phillips, N., Post, D., McDonnell, J.J., 2002. The zone of vegetation influence on baseflow revealed by diurnal patterns of streamflow and vegetation water use in a headwater basin. Hydrol. Process., 16, 8, 1671–1677.

Bren, L.J., 1997. Effects of slope vegetation removal on the diurnal variation of a small mountain stream. Water Resour. Res., 33, 2, 321–331.

Brooks, J., Barnard, H., Coulombe, R., McDonnell, J., 2010. Ecohydrologic separation of water between trees and streams in Mediterranean climate. Nat. Geosci., 3, 2, 100–104.

Burt, T.P., 1979. Diurnal variations in stream discharge and throughflow during a period of low flow. J. Hydrol., 41, 3–4, 291–301.

Caine, N., 1992. Modulation of the diurnal streamflow response by the seasonal snowcover of an alpine basin. J. Hydrol., 137, 1, 245–260.

Carlson Mazur, M.L., Wiley, M.J., Wilcox, D.A., 2014. Estimating evapotranspiration and groundwater flow from water-table fluctuations for a general wetland scenario. Ecohydrology, 7, 2, 378–390. DOI:10.1002/eco.1356.

CIREN (Centro de Información de Recursos Naturales), 2001. Estudio Agrológico X Región, Tomo I. CIREN, Santiago, Chile.

Constantz, J., 1998. Interaction between stream temperature, streamflow, and groundwater exchanges in alpine streams. Water Resour. Res., 34, 7, 1609–1615.

Cruz, C., Calderón, J., 2008. Guía climática práctica. [online] Dirección Meteorológica de Chile, p.117. Available at: http://164.77.222.61/climatologia/publicaciones/climatica_practica.pdf [Accessed 26 Jul. 2016].

Cuevas, J.G., Calvo, M., Little, C., Pino, M., Dassori, P., 2010. Are diurnal fluctuations in streamflow real? J. Hydrol. Hydromech., 58, 3, 149–162.

Cuevas, J.G., Huertas, J., Leiva, C., Paulino, L., Dörner, J., Arumí, J.L., 2014. Nutrient retention in a microwatershed with low levels of anthropogenic pollution. Bosque, 35, 1, 75–88.

Dörner, J., Dec, D., Peng, X., Horn, R., 2009. Change of shrinkage behavior of an Andisol in southern Chile: Effects of land use and wetting/drying cycles. Soil Till. Res., 106, 1, 45–53.

Dörner, J., Dec, D., Peng, X., Horn, R., 2010. Effect of land use change on the dynamic behaviour of structural properties of an Andisol in southern Chile under saturated and unsaturated hydraulic conditions. Geoderma 159, 1–2, 189–197.

Fetene, M., Beck, E., 2004. Water relations of indigenous versus exotic trees species, growing at the same site in a tropical montane forest in southern Ethiopia. Trees, 18, 4, 428–435.

Graham, C.B., Barnard, H.R., Kavanagh, K.L., McNamara, J.P., 2013. Catchment scale controls the temporal connection of transpiration and diel fluctuations in streamflow. Hydrol. Process., 27, 18, 2541–2556.

Gribovszki, Z., Kalicz, P., Szilágyi, J., Kucsara, M., 2008. Riparian zone evapotranspiration from diurnal groundwater level fluctuations. J. Hydrol., 349, 1, 6–17.

Gribovszki, Z., Szilágyi, J., Kalicz, P., 2010. Diurnal fluctuations in shallow groundwater levels and streamflow rates and their interpretation – A review. J. Hydrol., 385, 1–4, 371–383.

Gribovszki, Z., Kalicz, P., Szilágyi, J., 2013. Does the accuracy of fine-scale water level measurements by vented pressure transducers permit for diurnal evapotranspiration estimation? J. Hydrol., 488, 166–169.

Huertas, J., Cuevas, J.G., Paulino, L., Salazar, F., Arumí, J.L., Dörner, J., 2016. Dairy slurry application to grasslands and groundwater quality in a volcanic soil. J. Soil Sci. Plant Nutrit., 16, 3, 745–762.

Hughes, D.A., 2010. Unsaturated zone fracture flow contributions to stream flow: evidence for the process in South Africa and its importance. Hydrol. Process., 24, 6, 767–774.

Jiménez-Castillo, M., Lobos-Catalán, P., Aguilera-Betti, I., Rivera, R., 2011. Daily transpiration rates and hydraulic relationships in tree species with different shade-tolerance level in a Chilean temperate forest. Gayana Bot., 68, 2, 155–162. (In Spanish.)

Jordon, P., 1983. Meltwater movement in a deep snowpack. 1. Field observations. Water Resour. Res., 19, 4, 971–978.

McLaughlin, D.L., Cohen, M.J., 2011. Thermal artifacts in measurements of fine-scale water level variation. Water Resour. Res., 47, W09601.

Mohseni, O., Stefan, H.G., 1999. Stream temperature/air temperature relationship: a physical interpretation. J. Hydrol., 218, 3–4, 128–141.

Moore, G., Jones, J., Bond, B.J., 2011. How soil moisture mediates the influence of transpiration on streamflow at hourly

to interannual scales in a forested catchment. Hydrol. Process., 25, 24, 3701–3710.

Mutzner, R., Weijs, S.V., Tarolli, P., Calaf, M., Oldroyd, H.J., Parlange, M.B., 2015. Controls on the diurnal streamflow cycles in two subbasins of an alpine headwater catchment. Water Resour. Res., 51, 5, 3403–3418. DOI: 10.1002/2014WR016581.

Onset Computer Corporation, 2005, 2006. HOBO® U20 Water Level Logger (Part # U20-001-01). Doc # 8976-G, MAN-U20-001-01. Bourne, Massachusetts, USA.

Puchi, P.F., 2013. Influencia de la transpiración sobre la variación del caudal a escala horaria en una microcuenca cubierta con *Eucalyptus globulus* Labill. Master thesis, Faculty of Sciences, Universidad Austral de Chile, Valdivia, Chile. 56 p + xiv.

Sánchez, S., 2016. Comportamiento de la radiación ultravioleta (UV-B) en Chile. Dirección Meteorológica de Chile. Available at: http://164.77.222.61/climatologia/publicaciones/Comportamiento_radiacion_UV-B.pdf [Accessed 26 Jul. 2016].

Schwab, M., Klaus, J., Pfister, L., Weiler, M., 2016. Diel discharge cycles explained through viscosity fluctuations in riparian inflow. Water Resour. Res., 52, 11, 8744–8755. DOI: 10.1002/2016WR018626.

Scott, D., Prinsloo, F., 2008. Longer-term effects of pine and eucalypt plantations on streamflow. Water Resour. Res., 44, 7, W00A08.

Soil Survey Staff, 1999. Soil taxonomy: A basic system of soil classification for making and interpreting soil surveys. 2nd Ed. Natural Resources Conservation Service, U.S. Department of Agriculture Handbook 436, Washington D.C., USA.

Solinst, 2011. User Guide Levelogger Series Software Version 4. Solinst Canada Ltd., 35 Todd Road, Georgetown, ON, L7G 4R8st Canada.

Szilágyi, J., Gribovszki, Z., Kalicz, P., Kucsara, M., 2008. On diurnal riparian zone groundwater-level and streamflow fluctuations. J. Hydrol., 349, 1–2, 1–5.

Valett, H.C., Dahm, C.N., Campana, M.E., Morrice, J.A., Baker, M.A., Fellows, C.S., 1997. Hydrologic influences on groundwater-surface water ecotones: heterogeneity in nutrient composition and retention. J. N. Am. Benthol. Soc., 16, 1, 239–247.

Voltz, T.J., 2011. Riparian hydraulic gradient and water table dynamics in two steep headwater streams. Thesis in Ms Civil Engineering. The Pennsylvania State University, USA, 150 p.

Wain, A.S., 1994. Diurnal river flow variations and development planning in the tropics. Geogr. J., 160, 3, 295–306.

Wondzell, S.M., Gooseff, M.N., McGlynn, B.L., 2007. Flow velocity and the hydrologic behavior of streams during baseflow. Geophysical Research Letters 34, L24404. DOI: 10.1029/2007GL031256.

WRB (World Reference Base for Soil Resources), 2006. World reference base for soil resources. A framework for international classification, correlation and communication. 2nd Ed. FAO, World Soil Resources Reports No. 103, Rome, Italy.

Wroblicky, G.J., Campana, M.E., Valett, H.M., Dahm, C.N., 1998. Seasonal variation in surface-subsurface water exchange and lateral hyporheic area of two stream-aquifer systems. Water Resour. Res., 34, 3, 317–328.

Zúñiga-Feest, A., Bustos-Salazar, A., Alves, F., Martínez, V., Smith-Ramírez, C., 2017. Physiological and morphological responses to permanent and intermittent waterlogging in seedlings of four evergreen trees of temperate swamp forests. Tree Physiol., 37, 6, 776–789. DOI: 10.1093/treephys/tpx023.

Received 2 May 2017
Accepted 24 July 2017

J. Hydrol. Hydromech., 66, 2018, 1, 43–54
DOI: 10.1515/johh-2017-0027

Canopy structure and topography effects on snow distribution at a catchment scale: Application of multivariate approaches

Michal Jenicek*, Hana Pevna, Ondrej Matejka

Department of Physical Geography and Geoecology, Faculty of Science, Charles University, Albertov 6, 128 43 Prague, Czech Republic.
* Corresponding author. E-mail: michal.jenicek@natur.cuni.cz

Abstract: The knowledge of snowpack distribution at a catchment scale is important to predict the snowmelt runoff. The objective of this study is to select and quantify the most important factors governing the snowpack distribution, with special interest in the role of different canopy structure. We applied a simple distributed sampling design with measurement of snow depth and snow water equivalent (SWE) at a catchment scale. We selected eleven predictors related to character of specific localities (such as elevation, slope orientation and leaf area index) and to winter meteorological conditions (such as irradiance, sum of positive air temperature and sum of new snow depth). The forest canopy structure was described using parameters calculated from hemispherical photographs. A degree-day approach was used to calculate melt factors. Principal component analysis, cluster analysis and Spearman rank correlation were applied to reduce the number of predictors and to analyze measured data. The SWE in forest sites was by 40% lower than in open areas, but this value depended on the canopy structure. The snow ablation in large openings was on average almost two times faster compared to forest sites. The snow ablation in the forest was by 18% faster after forest defoliation (due to the bark beetle). The results from multivariate analyses showed that the leaf area index was a better predictor to explain the SWE distribution during accumulation period, while irradiance was better predictor during snowmelt period. Despite some uncertainty, parameters derived from hemispherical photographs may replace measured incoming solar radiation if this meteorological variable is not available.

Keywords: Snowpack distribution; Canopy structure; Leaf area index; Degree-day; Bark beetle.

INTRODUCTION

Snow is an important component of hydrological cycle in many world's catchments. A significant quantity of water is stored in the form of snow during cold period causing higher runoff during spring. This higher runoff may cause floods and thus it forms a potential danger for people living near the rivers. Therefore, the knowledge of water volume stored in the snowpack and its spatial distribution represents the basic information for hydrological forecasting.

The snow storage is determined by the spatial distribution of snow water equivalent (SWE), which is mostly controlled by the spatial distribution of snow depth (Seibert et al., 2014). Large-scale variations of snow storage are controlled by air temperature, which is related to elevation and latitude (Kucerova and Jenicek, 2014; Molotch and Meromy, 2014). However, at smaller scales, the snow accumulation and snowmelt are more driven by topography and vegetation (Grünewald et al., 2013; Jenicek et al., 2012, 2017; Šípek and Tesař, 2014). Stähli and Gustafsson (2006) found that, over a long-term period, the annual SWE maximum is by up to 50% higher in open areas than in the forest. However, this effect decreases with increasing snow accumulations. The differences between snow storages accumulated in open areas and in forests with different structure were reported from many other world's areas (Lundquist et al., 2013; Revuelto et al., 2016).

The forest influences snow storage on canopy (snow interception), snow redistribution due to wind and the density of snowpack during snow accumulation, depending mainly on forest type (coniferous, deciduous) and on structure influencing canopy leaf area index (LAI). The snow interception affects snow accumulation under treetops (Garvelmann et al., 2013; Holko et al., 2009; Stähli et al., 2009; Strasser et al., 2011). Additionally, the forest influences turbulent fluxes (Pohl et al., 2006) and reduces the amount of short-wave solar radiation and thus snowmelt rates (Pomeroy et al., 2012; Schnorbus and Alila, 2013). The proportion of longwave and shortwave radiation varies depending on yearly climatic conditions and thermal regime of the study site (Lundquist et al., 2013). The longwave radiation under forest canopy is relatively more important than incoming shortwave radiation especially in mid-winter because it causes faster snowmelt compared to adjacent open area. This occurs because the efficiency of forest to reduce incoming shortwave radiation is most important during spring when the shortwave radiation is high enough (Lundquist et al., 2013; Schnorbus and Alila, 2013).

Although the effect of forest on the snowmelt volume is more driven by the energy budget of snowpack, the effect on runoff is more complex and it is strongly influenced, among others, by meteorological conditions at the beginning and during the snowmelt. As documented by Pomeroy et al. (2012), who performed a wide range of different hypothetical scenarios at Marmot Creek in Canada, the total spring and summer runoff volume increases by less than 10% in case of forest burning and logging, however, the snowmelt volume increases by 45%. The mentioned study also showed that burning and pine beetle impacts affect more peak flows than seasonal runoff volumes (by up to 25%). The effect of clear-cutting is documented by Schelker et al. (2013) for a catchment in northern Sweden. They observed that the SWE increased after clear-cutting by 30%, snowmelt occurred earlier and spring flood runoff increased significantly in some years.

The bark beetle (*Ips typographus*) outbreak occurs in the Sumava Mountains (Bohemian Forest) and the Bavarian Forest national parks in the Czech Republic, Germany and Austria. It is a natural disaster affecting large areas of Norway spruce forest (*Picea abies*). Both windstorms and the bark beetle are the main factors causing land cover changes in the Sumava

Mountains, which have an effect on interception, evaporation and consequently runoff (Kliment et al., 2011; Langhammer et al., 2015a; Vlcek et al., 2012). The bark beetle causes tree defoliation. Therefore, snow interception becomes less important which results in snow storages increase. However, the difference between snow stored under healthy and disturbed forest become less important in snow-rich years because the large snowfalls exceed the interception capacity of the canopy (Boon, 2012).

On the contrary, snow melts faster due to the decreasing canopy shading effect and thus the increasing solar radiation. Additionally, ongoing climate changes and consequent changes of winter and spring runoff represent positive feedback and might further underline the impact of land cover changes on runoff (Blahušiaková and Matoušková, 2015; Langhammer et al., 2015b).

The assessment of the effect of different forest structures and forest disturbances on snow accumulation and snowmelt is often done using suitable modelling approaches, as it is usually less time and costly demanding than field observations (Essery et al., 2009, 2013; Jost et al., 2012; Kutlakova and Jenicek, 2012; Pomeroy et al., 2012). However, field data bridge the gap between the real physical process and its conceptualization using suitable equation and parameters. Based on measured or simulated data, it is possible to estimate the effect of forest disturbances on snowmelt dynamics, such as windstorms, fires and insect attacks (Burles and Boon, 2011; Pomeroy et al., 2012; Pugh and Small, 2013; Winkler et al., 2015).

The objective of our study was to quantify the role of main factors governing the snowpack distribution at a catchment scale during snow accumulation and snow ablation periods. More specifically, we tested different bivariate and multivariate statistical approaches to select key controls influencing snow characteristics using meteorological, topography and vegetation data which are relatively easy to derive from climate observations, digital terrain model and land cover data. Although, we are aware that snow ablation is driven by the complex energy balance, our aim was to apply simple procedures to enable easier application in areas without detailed meteorological monitoring. This is not a new topic, but our study focuses more on the effect of different canopy structure (including disturbed forest due to the bark beetle) during both snow accumulation and snow ablation period. We chose a simple distributed sampling design and we benefit from a large data set sampled at 16 localities for five years covering a wide range of snow conditions.

MATERIAL AND METHODS

Study area and data monitoring

We performed detailed field survey of snow depth, snow density and SWE in small mountain catchment of Ptaci Brook (4 km^2), which is an experimental catchment of the Charles University (Fig. 1). The Ptaci Brook catchment is located in the Sumava Mountains (Bavarian forest) in the southwest part of the Czech Republic. The catchment is located from 1130 to 1330 m a.s.l. with prevailing west, north and east oriented slopes with mean slope gradient 6° (with maximum up to 30°). The dominant tree species is Norway spruce (*Picea abies*), although large parts of forests were damaged by the bark beetle (*Ips typographus*). Vegetation changes are still largely occurring until now.

Data from three meteorological stations were used in this study. First two of them (Ptaci Brook and Breznik) are operated by the Charles University using the same instrumentation as deployed by the national observation network of the Czech Hydrometeorological Institute. The Ptaci Brook station is located directly in the study area (sampling site "15, 16", see Fig. 1) and the Breznik station is located 1.5 km W from the study area at the same elevation as sampling sites. The third station is operated by German Weather Service (DWD) and it is located 28 km NW from the study area 100–250 m higher than sampling sites. The air temperature, global radiation and snow depth (using ultrasonic sensor) measured every 10 minutes were adjusted to daily resolution and used to calculate predictor variables (see the part "Predictors and response variables"). Data from several stations were used because of gaps in time series of the Ptaci Brook station which would otherwise be most appropriate to calculate all predictors.

Sampling strategy

We chose simple distributed sampling design with location placed uniformly in the catchment and covering major topography and vegetation characteristics typical for the study area.

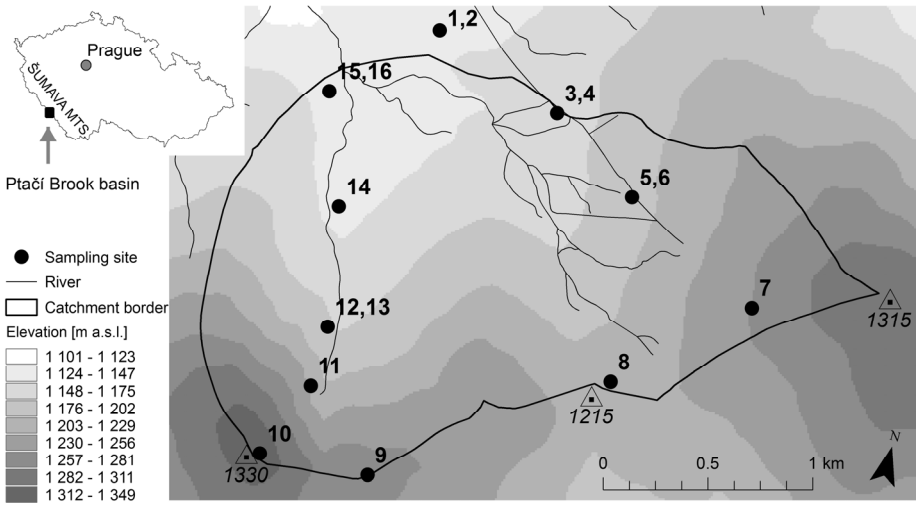

Fig. 1. Geographical location of the Ptaci Brook basin. Black dots indicate sampling sites. Two numbers at one location indicate paired measuring of snow depth and SWE in open area/clearing and in forest. The position of Ptačí Brook meteorological station corresponds with location "15, 16".

The snow depth and SWE were sampled at 16 sites either in forest or in open area/clearing (Fig. 1). In total, we used data from 6 forest sites (including 3 forested sites affected by the bark beetle), 5 clearings (small open areas protected from solar radiation and wind by surrounding trees in maximum distance up to triple of the trees height) and 5 large open areas. At each sampling site, the snow depth was measured 5 times along 50 m long transect in regular step. Each from the five snow depth values was calculated as an average from 10 individual measurements with a probe to avoid possible errors due to small scale topography, stones and ground vegetation. The SWE was measured 2 times along the same transect using a snow tube. Basic characteristics of all 16 sampling sites are displayed in Fig. 2, individual characteristics are explained in the section "Predictors and response variables".

Manual field surveys of snow depth and SWE were carried out fourteen times during five winter seasons from 2011 to 2015 (Table 1). Different climatic conditions in each winter enable us to measure the data during different snow conditions, such as early winter snow accumulations with low snow densities, mid-winter accumulations with or without partial melting caused by rain-on-snow events and high snow densities during snowmelt periods. The evolution of snow depth in all winter seasons is displayed in Fig. 3.

Predictors and response variables

We selected eleven predictors related to sampling site characteristics and to winter and spring meteorological conditions (Table 2). These predictors were used to explain the variability of snow accumulation and ablation in the study area.

Elevation and slope were expressed as real values (in m a.s.l., respectively in decimal degrees) calculated from digital terrain model. The slope orientation (aspect) was recalculated as transformed aspect (Eq. 1).

$$\text{Transformed\_aspect} = (\sin(\text{aspect}_{\text{rad}} - (\pi/2)) + 1) / 2 \qquad (1)$$

Equation 1 transforms aspects into values ranging from 0 to 1. Value 1 represents south orientation, value 0 represents north orientation and 0.5 represents both east and west orientations. A similar approach was used by Jost et al. (2007).

The influence of vegetation on the snowpack distribution was described using parameters derived from hemispherical images of the sky and canopy: i) LAI (often known as LAI4 which considers 60° wide sector from zenith), ii) percentage rate of pixels representing canopy to pixels representing sky (canopy openness) and iii) the potential amount of shortwave radiation calculated as a sum from November 1 to April 30 (potential irradiance). Overall, 32 hemispherical images were taken in the study area (two at each site). All images were taken during one day. The images were taken using camera with fish-eye lens (Sigma Circular Fisheye with focal length 4.5 mm) and analyzed using Gap Light Analyzer software (Frazer et al., 1999). Geographical coordinates, elevation and digital terrain model (used for shading effect calculation) were used as input data for each locality. All variables needed for calculations were set up as shown in Table 3. We tested different values of cloudiness index and found no impact on resulting correlations since we analyzed relative differences of potential irradiance between individual sampling sites/dates. Frazer et al. (1999) provide more information regarding the above variables.

The use of only two hemispherical images per one locality may produce a random error in calculation of the specific parameter. Therefore, we chose three sites in different land covers where we took 25 images in regular grid 25 x 25 m (with 5 m step) and assessed their variability using coefficient of variation C_v.

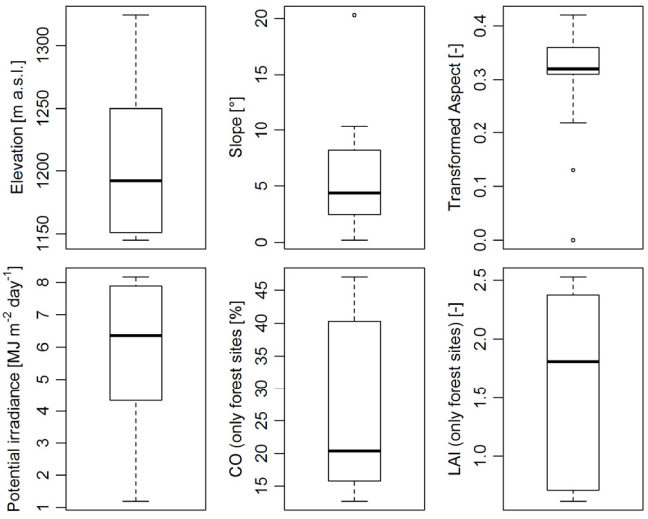

Fig. 2. Basic characteristics of 16 sampling sites. CO is the canopy openness; LAI is the Leaf area index. Individual characteristics are explained in the text.

Table 1. Dates of data sampling and related characteristics. Column "Snowmelt" indicates snow accumulation or snowmelt conditions during data sampling. The total irradiance represents the irradiance for open areas (without shading effect of vegetation). Individual characteristics are explained in the text.

Date	Snowmelt	Mean SWE [mm]	Range [mm]	Mean snow depth [cm]	Mean snow density [–]	Sum of T^+ [°C]	Sum of new SD [cm]	Total irradiance [MJ m^{-2} d^{-1}]
19 Mar 2011	No	177	11–307	49	0.36	99.4	253	846
26 Mar 2011	Yes	152	69–266	39	0.39	120.4	253	987
29 Feb 2012	No	487	283–730	139	0.35	28.7	324	539
16 Mar 2012	No	457	215–696	117	0.39	62.6	328	774
24 Mar 2012	Yes	425	217–635	100	0.42	101.9	328	935
7 Apr 2012	Yes	305	19–499	76	0.40	144.5	328	1170
6 Mar 2013	No	296	97–467	93	0.31	38.3	375	517
16 Mar 2013	No	286	112–484	80	0.35	56.2	384	646
13 Apr 2013	No	302	110–503	82	0.37	65.2	451	1002
23 Apr 2013	Yes	137	0–374	35	0.39	137.3	451	1215
10 Mar 2014	Yes	112	0–238	34	0.34	167.6	178	731
18 Mar 2014	Yes	80	0–209	22	0.36	203.8	193	848
12 Mar 2015	No	169	40–257	59	0.28	73.9	150	645
23 Mar 2015	Yes	153	0–257	48	0.32	93.7	153	823

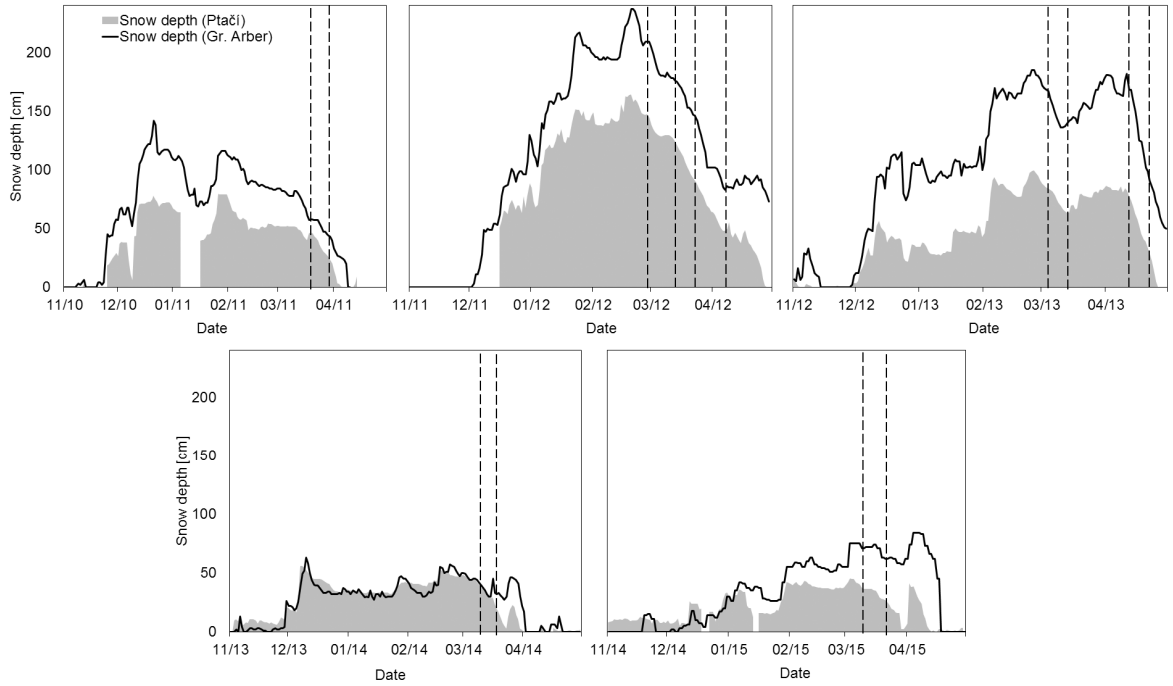

Fig. 3. The snow depth in winter seasons 2011–2015 measured in the Ptaci Brook meteorological station (grey areal plot, gaps indicate missing data) and Grosser Arber (Bavarian forest, solid line). Dashed vertical lines represent sampling dates. Data: Charles University and German Weather Service (DWD).

Table 2. Predictors and response variables used in analyses.

Predictor variable	Response variable
Elevation	Snow water equivalent (SWE)
Slope	Snow depth (SD)
Slope orientation (expressed as transformed aspect)	Snow density
Leaf Area Index (LAI)	Melt factor m_f calculated using the degree-day approach
Canopy Openness	
Potential amount of shortwave radiation at the site from November 1 to April 30 (Potential irradiance)	
Irradiance at the site from start of snow accumulation to sampling date (Total irradiance)	
Mean daily irradiance from preceding sampling date to sampling date (Partial irradiance)	
Sum of new snow depth from start of accumulation to sampling date (Sum of new SD)	
Sum of positive air temperature from start of accumulation to sampling date (Sum of T^+)	
Day of year of data sampling (DOY)	

Table 3. User input variables set up in the GLA software for hemispherical photos analysis.

User input variables	Value
Cloudiness index	0.5
Spectral fraction (0.25–25 mm)	1
Beam fraction	0.5
Clear-sky transmission coefficient	0.6
Solar constant [W m^{-2}]	1367

Resulting C_v showed that the variability does not significantly changed among individual land cover types for canopy openness and potential radiation in selected sites, although some variability of LAI within the plot scale increased for disturbed forest and for clearings.

The irradiance at the site from the start of snow accumulation to the sampling date (Total irradiance) represents the sum of incoming solar radiation (in MJ m^{-2} d^{-1}) measured at the Breznik meteorological station. The total irradiance at the specific site was adjusted to represent conditions below forest canopy. To do this, the canopy openness calculated from respective hemispherical image was used as a multiplicative factor.

The mean daily irradiance from the preceding sampling date to the sampling date (Partial irradiance) represents mean daily sum of incoming solar radiation for each period of two succeeding surveys. This predictor was calculated from total irradiance and used for snowmelt assessment.

The sum of new snow depth (Sum of new SD) and the sum of positive air temperatures (Sum of T^+) were used as parameters to describe the evolution of meteorological conditions

during specific winter season. Both parameters were calculated from the beginning of snow accumulation to the day of field measurement as specified in Table 1. Both variables were calculated using snow depth and air temperature from Grosser Arber meteorological station, where complete observations were available. Air temperature was adjusted to the sampling sites elevation using a lapse rate 0.6°C/100 m. The day of year of data sampling (DOY) was used to describe whether the response variable (especially snow density) changed during winter season.

The above described predictors were tested to explain the variability of four response variables describing snow conditions: i) SWE [mm], ii) snow depth [cm], iii) snow density [–] and iv) melt factor m_f (also known as degree-day factor) calculated from measured data according to the degree-day approach (Hock, 2003).

The degree-day approach represents the simplified energy balance of the snowpack, which is described using the air temperature and melt factor (Eq. 2).

$$M = m_f (T_a - T_c), \quad (2)$$

where m_f [mm °C^{-1} d^{-1}] is the melt or degree-day factor representing the SWE decrease in a day caused by the air temperature change T_a of 1°C compared to the critical air temperature T_c in which the melting process begins.

The melt factors for different types of vegetation were calculated based on measured SWE decreases between two sampling dates. Only periods with zero or very small influence of precipitation were taken into account (the maximum daily precipitation between sampling dates was less than 2 mm/day, but typically near zero). In total, 78 m_f values were analyzed from 2011 to 2015. Air temperature from two meteorological stations was used to calculate the melt factors. Lapse rates accounting for temperature change with elevation were calculated for each day and each sampling site. Critical temperature T_c was set up to 0°C in this study.

Bivariate and multivariate statistical analyses

The correlation analysis between snowpack properties and site characteristics was based on the assumption that the snowpack distribution depends on preceding meteorological conditions and site properties connected to vegetation structure and topography.

First, the correlation was assessed using Spearman rank correlation coefficients between predictors and response variables and displayed as correlation heat maps.

Second, the importance of both vegetation and topography parameters was additionally tested using Cluster Analysis. The whole dataset from all sampling campaigns was assessed either as a one set or divided into several subsets according to the vegetation classes. Each subset was put into hierarchical cluster analysis using the Euclidean distance as a measure of similarity. A similar procedure was used to evaluate similarity of individual sampling locations based on site characteristics related to topography (elevation, slope, slope orientation), vegetation (canopy openness, potential irradiance) and snowmelt dynamics (melt factor m_f).

Finally, the relation between snow conditions and site characteristics was examined with Principal Component Analysis (PCA). The PCA is an explorative analysis which enables to reduce number of predictors and to classify them among principal components which capture the much of the variance of the original dataset (Fischer et al., 2015; López-Moreno and Latron, 2008; Revuelto et al., 2016). A set of mutually correlated variables are transformed into a set of uncorrelated variables (principal components, PC) which are ordered by reducing variability. The PCs are linear combinations of the original variables. The PCs which explain a little variance can be removed with minimum loss of explanatory power of the original dataset. The transformed data are rotated such that maximum variability is projected onto the PCA axes using a biplot.

All predictors were expressed as normalized values using z-score (the mean is 0, standard deviation is 1). The mutual independency of predictors was tested using Pearson correlation coefficient at 0.05 significance level. The R software (R Core Team, 2016) and Statistica software (http://www.statsoft.com/) were used for all calculations in this study.

RESULTS

Multivariate analysis of selected predictors and response variables

There are two groups of predictors used in this study which are necessary to be assessed separately. The first group is formed by predictors which are supposed to be time-invariant (such as topography and canopy structure). The second group of predictors is formed mostly by characteristics related to meteorological conditions and they are changing over the time both during one winter season and between seasons (sum of new SD, sum of T^+ and total irradiance). Therefore, Spearman rank correlation coefficients between predictors and response variables were calculated separately 1) for each sampling date and all sampling points using only time-invariant predictors (Fig. 4, left) and 2) for each locality using predictors which are changing in time (Fig. 4, right). The Spearman rank correlation coefficients were displayed as heat maps together with dendrograms showing clusters of similar predictors and response variables (Fig. 4).

The Spearman rank correlation coefficients calculated separately for individual sampling dates (Fig. 4, left) indicated high correlations of melt factors m_f with variables related to canopy structure as well as with partial irradiance calculated from previous sampling date. The correlation of m_f and partial irradiance was relatively high not only when comparing specific localities to each other for specific sampling date (Fig. 4, left), but also when comparing inter-annual variations of m_f at the specific site (Fig. 4, right).

All parameters related to vegetation structure were significantly correlated with snow depth, SWE and snow density both for snow accumulation and snowmelt periods, although the correlations for snow accumulation periods were a bit higher (Fig. 4, left). The LAI was better predictor to explain the SWE distribution during accumulation period; the total irradiance and potential irradiance were slightly better during snowmelt period. However, the differences are rather minor.

Similar to canopy characteristics and irradiance, the explanatory power of elevation was higher for response variables measured during snow accumulation period than during snowmelt. However, elevation was not significantly correlated to m_f.

The slope orientation (expressed as transformed aspect) was not important to explain any of response variable. This is probably due to relatively low range of slope orientations with prevailing NW to NE slopes.

The sum of positive air temperatures (sum of T^+) is important especially for the SWE and snow depth measured during both the snow accumulation and snowmelt period (Fig. 4, right). Especially for the snow accumulation period, the sum of T^+ seems to be an interesting parameter to explain inter-annual

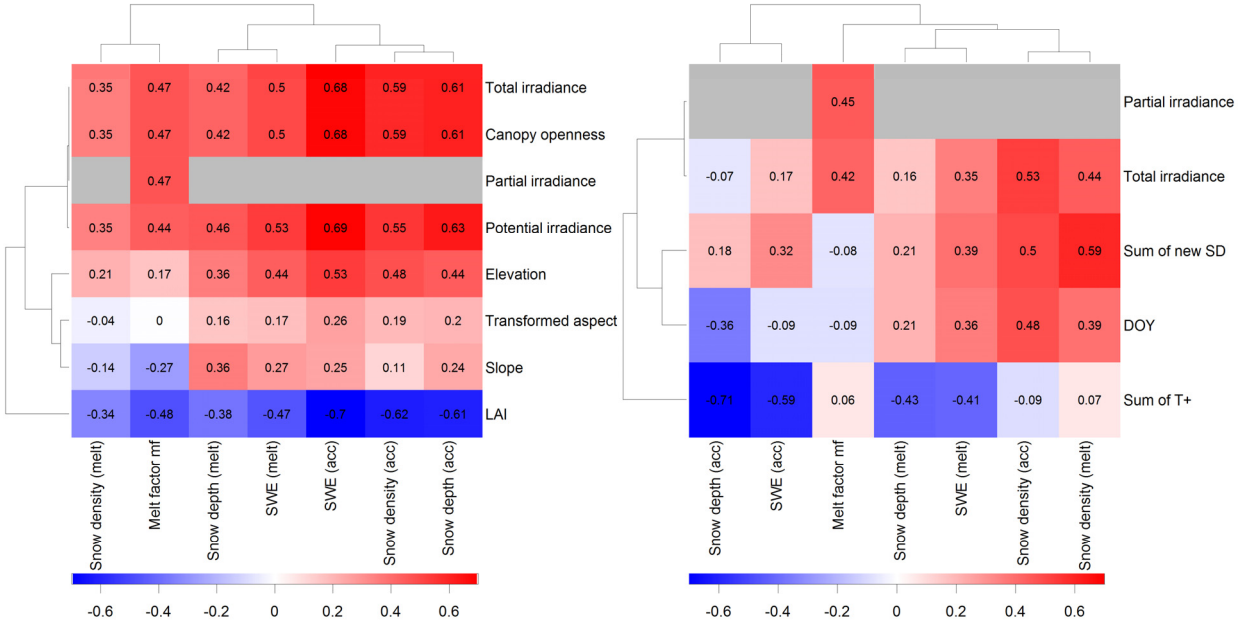

Fig. 4. Heat maps showing Spearman correlation coefficients for all predictors (row) and response variables (columns) for 1) date (left) and 2) locality (right). Colors and numbers represent mean value from all dates/localities. Hierarchical cluster analysis and Euclidean distance were used to show similarity of individual predictors and response variables. Grey color used for NA values.

variations in snow depth and SWE. This was expected since air temperature influences the precipitation phase and thus the snowfall fraction. Similarly, the snow density expectedly increased with DOY of data sampling.

However, the low Spearman correlation between the sum of new SD and snow depth/SWE is surprising (Fig. 4, right). The physical explanation of these low correlations is that the snow depth and SWE were influenced by several periods with air temperature above freezing point and thus partial thawing. Another reason might be the wind redistribution influencing the punctually measured snow depth. Additionally, the calculation of the sum of new SD did not account for canopy interception since data from an automatic snow depth sensor placed in open area were used to calculate this predictor. Moreover, the sum of new SD was calculated based on data from Grosser Arber meteorological station which is placed 100–250 m higher than our sampling sites (see methods section). Although this predictor describes general snow conditions in the winter period rather than the snow depth evolution in individual sampling site, the mention difference in elevation and geographical location could produce a considerable uncertainty for result interpretation.

Despite the significance of the correlations, their values are not high which indicates that snowpack distribution is influenced by more than a single variable (maximum explained variability was 71% for the relation between snow depth and sum of positive air temperature). Additionally, some of the predictors are not mutually independent. Since our focus was primarily on the role of vegetation, LAI and irradiance (both potential and total) seem to be the best parameters to predict the snow depth and SWE, although the differences between individual predictors are not large.

The major importance of canopy parameters followed by topography (elevation) is documented by results from cluster analysis (see the dendrogram in Fig. 4). Canopy parameters and total irradiance are major ones when grouping individual sites into clusters based on site characteristic. The elevation and slope have lower importance.

The sampled data containing time-variant information about meteorological and snow conditions and time-invariant site characteristics were further explored with PCA separately for each sampling date. The results from four sampling campaigns made in 2013 were selected as typical representatives and displayed in Fig. 5. Two components were sufficient to explain from 75.4% (23 Apr 2013) to 82.5% (6 Mar 2013) of the variance since the eigenvalues of third and other components were less than one. The different site characteristics (represented as arrows) are located in different quadrants and may be correlated to different sampling locations (represented as points). The LAI seems to be the most important factor for forest sites, while topography is more important for open areas and clearings. The LAI is strongly negatively correlated with canopy openness and irradiance since all of the factors were either derived from hemispherical images or these images were used for their calculation. The LAI and potential irradiance explained the majority of the variance of component 1 (Fig. 6). On the contrary, slope and aspect (mutually positively correlated; vectors are close to each other) remained uncorrelated with LAI and irradiance (their vectors are perpendicular to LAI and irradiances vectors) and thus they explained the majority of the variance of component 2. The melt factor (DDF) was strongly positively correlated with canopy openness and irradiance and negatively correlated with LAI (Fig. 5, sampling date 23 Apr 2013). This indicates that the mentioned factors are the most important factors to explain the melt factor variability.

Sampling points from healthy and disturbed forest sites are grouped in quadrants II and IV. Large open areas are mostly grouped in quadrants I and III as well as sampling locations in clearings. However, all vegetation categories form clearly separate groups. The mentioned distribution does not significantly change in time from snow accumulation (first two sampling dates) to snowmelt period (last two sampling dates). The points are almost uniformly distributed in the plot area especially along the x-axis representing the PC 1. This indicates that the PC 1 explained the majority of the variance of the original dataset.

The Fig. 6 shows the correlation of LAI (zenith angle 60°) and potential irradiance (both factors are mutually negatively correlated) to explain the variability of PC 1. Unlike to Fig. 5

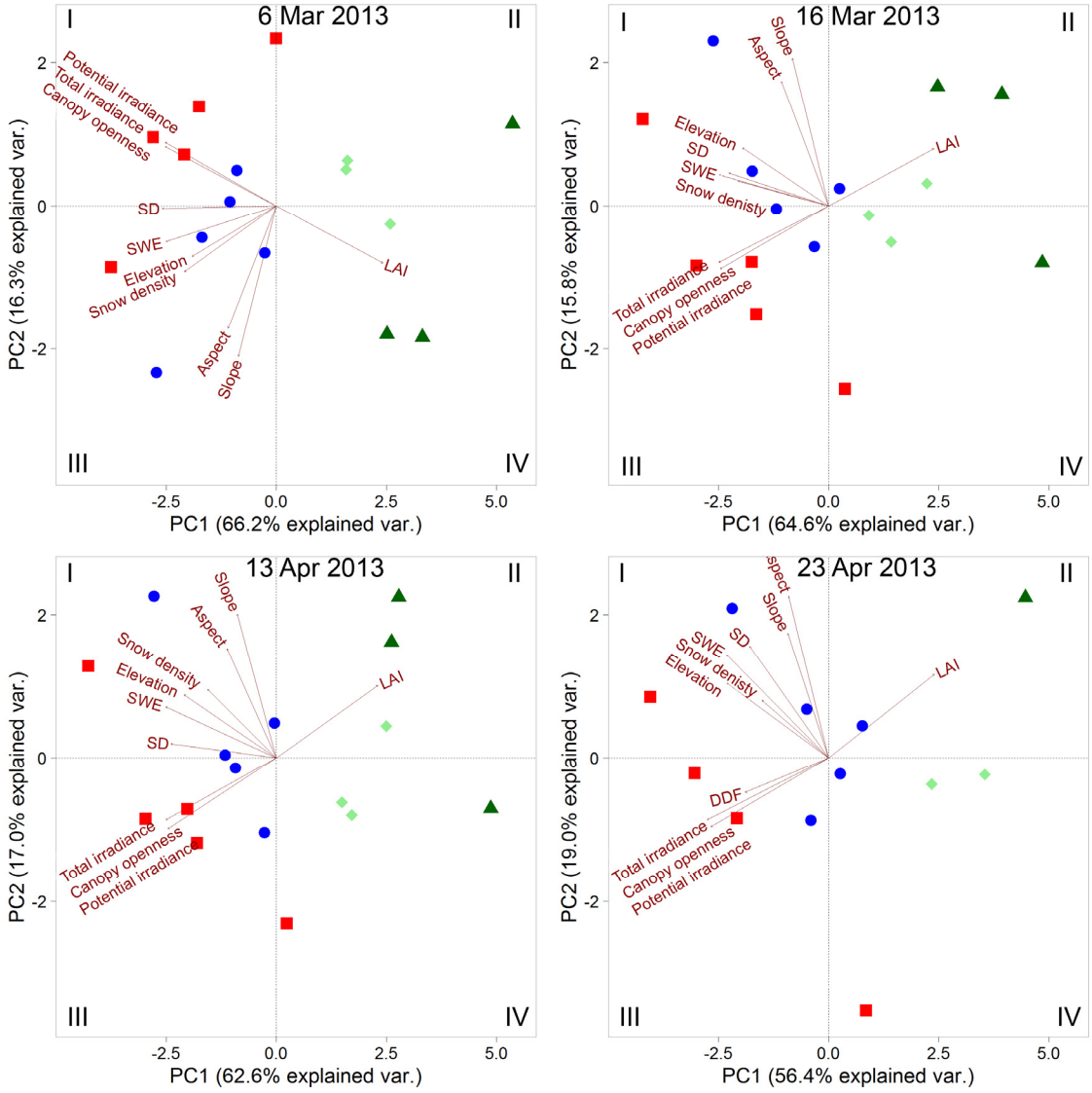

Fig. 5. PCA-biplot for four selected sampling campaigns. Points indicate individual sampling locations (open areas are in red, clearings in blue, healthy forests in dark green and disturbed forests in light green). Arrows indicate eigenvectors for individual site characteristics.

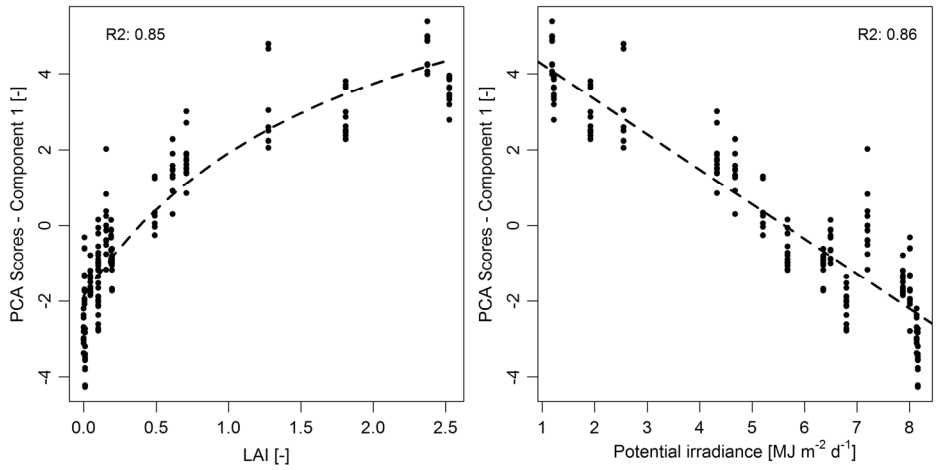

Fig. 6. Correlation between LAI and scores of PC 1 (left panel) and potential irradiance and scores of PC 1 (right panel). Dashed lines represent fitted functions.

which shows only selected sampling dates, Fig. 6 uses the PCA results from all sampling dates and all locations (note that PCA was applied separately for each sampling date). Both the potential irradiance and LAI showed very good fit with the scores of

PC 1 (R^2 equal 0.85 and 0.86, respectively). The non-linear relationship in case of LAI indicates a general good explanatory power in case of higher LAI values (typically forest sites) and lower explanatory power in case of LAI < 0.5 (typically clearings and open areas). Here, the irradiance seems to be better predictor.

The SWE and snow density variability in relation to vegetation

Several multivariate analyses showed in the previous chapter confirmed the crucial role of canopy structure on the snowpack distribution and snowmelt rates in the study area. Therefore, we performed a further separate analysis focused on canopy parameters and irradiance.

In order to establish a relation between the SWE in open area and forest we used only data from localities with paired measurement of SWE both from open areas/clearings and adjacent forest sites (for position of the paired sampling sites see Fig. 1). The derived prediction model using all pair measurements from 2011 to 2015 enables us to calculate the SWE for forest sites when only the SWE in the open area is measured (Fig. 7). As the dependence is almost linear, we conclude that the SWE in forest sites is on average by 40% lower than in open areas and clearings and this value does not vary significantly with increasing snow depth or SWE. This difference is almost the same for snow accumulation (40%) and snowmelt (39%). However, Fig. 7 shows a large data variability when 79% of this variability may be explained by vegetation during snow accumulation period and only 49% during snowmelt.

The same dataset as mentioned above was used to estimate the effect of forest disturbance caused by the bark beetle on snow accumulation in the Ptaci Brook basin. Our data from sites attacked by the bark beetle showed that the combined effect of snow interception and sublimation caused lower SWE differences between open areas and defoliated spruce forest with standing trees compared to the difference between open area and healthy forest (29.1% and 44.8%, respectively). It is expected that the interception effect is likely to decrease due to the gradual fall of branches and trunks, and thus snow accumulation increases in locations with disturbed forest.

The snow density is another important parameter which varies in different types of vegetation. Not surprisingly, there was lower snow density during accumulation period compared to ablation period in all vegetation categories (Fig. 8). The lowest snow density was usually in the forest during snow accumulation period, although the variability was relatively high. However, in forests disturbed by the bark beetle, the snow density in snow accumulation period slightly increased while the variability decreased. The highest snow density was mainly in large open areas, probably due to the combined effect of wind (affecting snow crystals structure) and higher incoming solar radiation which caused melt-freeze cycles, and thus the increase in snow density. Both effects causing the higher density in open area than in forest sites are probably more important than opposite effects of higher longwave radiation and canopy drip causing the increase in snow density in forest sites.

Melt factors variability related to different vegetation structure

The melt factor m_f as a key parameter in degree-day approach shows different snowmelt dynamics (regardless of air temperature) and enables to take into account specific vegetation structure of sampling sites (Fig. 9). Despite the large data

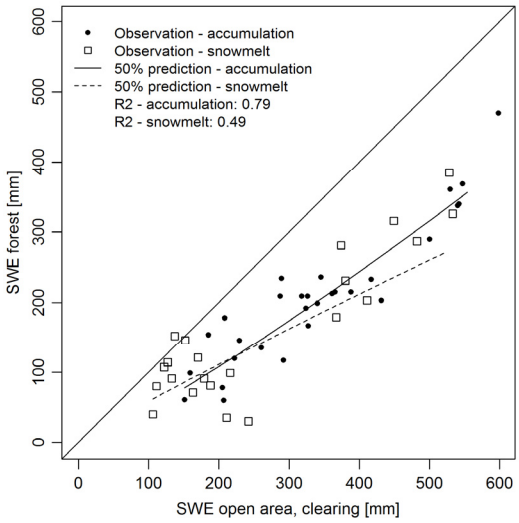

Fig. 7. The SWE in open areas and clearings (x-axis) compared to the SWE measured in the same time in the adjacent forest (y-axis) for all sampling dates. Lines represent 50% probability of prediction.

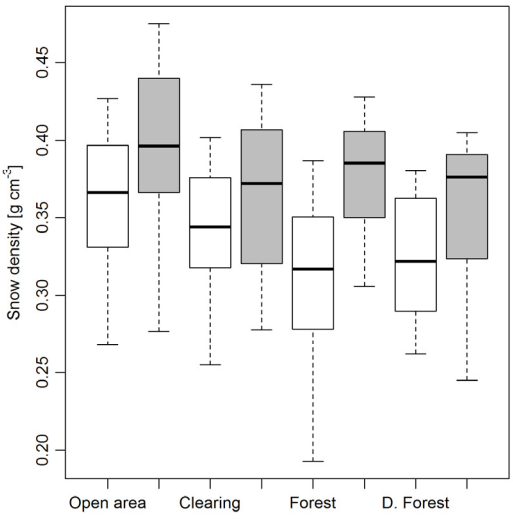

Fig. 8. The snow density in open areas, clearings, forests and disturbed forests. White box plots represent snow accumulation period; grey box plots represent snowmelt period. Boxes represent 25% and 75% percentile (with median as a thick line), whiskers represent 1.5 multiplier of interquartile range (IQR).

variability, it is clear that melt factors increased due to increase in incoming solar radiation (caused by sparser canopy cover) and thus a decrease of shading effects. The snow ablation in open areas was almost two times faster compared to forest sites (Table 4). On the contrary, the snow ablation in clearings partly protected against solar radiation was only by 27% faster than in neighboring forest.

There was lower interception (and thus higher snow accumulation) and faster snow ablation in the disturbed forest, compared to the healthy forest. The snow ablation was by 18% faster after forest defoliation and we expect an even faster ablation in case of complete forest decline due to further increase in solar radiation. However, the effect of faster snowmelt after forest decline is only temporary since one can expect increasing shading effects and thus decreasing melt factors during forest regeneration and growth. The relatively large variability of m_f values within each vegetation category indicates their limited applicability in other world's regions.

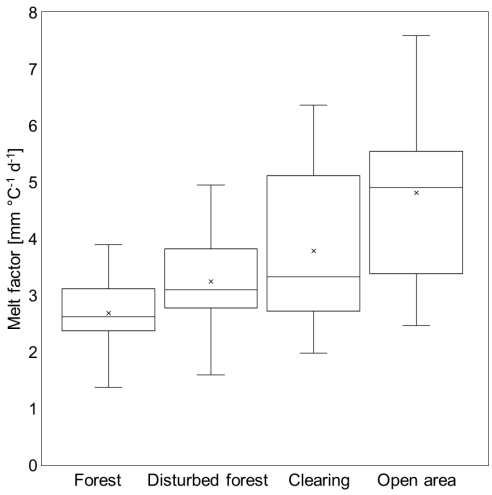

Fig. 9. Melt factors for different vegetation in the study area based on measured data from 2011 to 2015. Boxes represent 25% and 75% percentile (with median as a thick line), crosses represent mean values and whiskers represent minimum and maximum.

Table 4. Melt factors for different vegetation in the study area based on measured data from 2011 to 2015.

Vegetation	Median	Maximum	Minimum	Increase compared to the forest
Forest	2.6	3.9	1.4	0%
Disturbed forest	3.1	4.9	1.6	18%
Clearing	3.3	7.2	2.0	27%
Open Area	4.9	7.6	2.5	87%

The relation between melt factor m_f, LAI and sum of irradiance since the previous date of data sampling (partial irradiance) is shown in Fig. 10. Both LAI and partial irradiance expectedly showed a good relation to the respective melt factor, although there was some portion of variability which cannot be explained by these two predictors. This figure clearly shows that solar radiation is crucial for the variability of m_f and should not be neglected when using the degree day approach. This is especially important for regions where needle forest covers significant part of the study area. Additionally, the results showed that both irradiance and LAI are suitable parameters to estimate the m_f for different vegetation. However, it is important to mention that the irradiance was directly measured only in open area and it was adjusted using canopy openness for specific forest site. Thus both LAI and total irradiance are not mutually independent.

DISCUSSION

Snow sampling design

The snowpack variability is extremely large in mountainous conditions, even more than the variability of precipitation. This is caused by the simple fact, that after snow accumulation, there are a lot of subsequent processes influencing the snowpack variability, such as snow redistribution due to wind and avalanches, snow metamorphosis and snowmelt which is influenced by meteorological conditions and site characteristics. It is generally known that the snowpack distribution is difficult to describe by manual point measurements. For partly forested areas, the biggest differences were found when comparing snow amounts deposited in forests and in open areas as documented by this study and several other studies (see e.g. Holko et al., 2009; Jenicek et al., 2015; Jost et al., 2012; Pomeroy et al., 2012; Šípek and Tesař, 2014). Obviously, more sampling sites would lead to more reliable results. However, to increase their number is usually hardly possible due to time, financial demands a general accessibility of remote headwater areas, especially during snow season. Therefore, the use of methods applying one or more independent variables leads to applicable results as shown in our study.

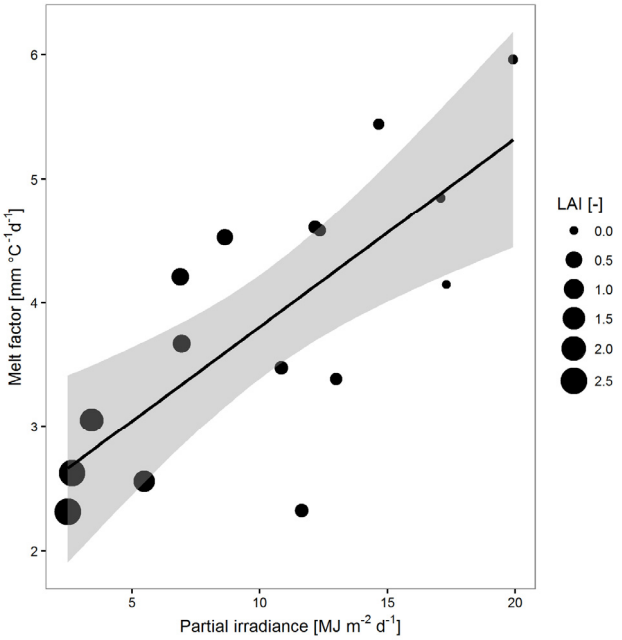

Fig. 10. The relation between melt factor and partial irradiance for sites with different LAI. Grey area represents the 95% confidence interval. Line represents linear regression with $R^2 = 0.51$.

Promising results have been also reported using remote sensing approaches such as the use of MODIS satellite data (Duchacek, 2014; He et al., 2014; Krajčí et al., 2016; Parajka et al., 2012), aerial or terrestrial laser scanning (Grünewald et al., 2013; López-Moreno et al., 2015) and unmanned aerial systems (UAV) (De Michele et al., 2016; Lendzioch et al., 2016). We are now testing camera placed on UAV to monitor the snow depth (Lendzioch et al., 2016). However, this approach is still hardly possible to use for distributed sampling design at a catchment scale as used in this study. Additionally, UAV-based sensing monitors snow depth, not snow density and SWE.

Results presented in our study may be influenced not only by selection of sampling points, but also by irregular distribution of sampling campaigns during winter and spring. On the contrary, our data were sampled in five consecutive winter seasons and we were often focused on relative differences of snowpack parameters between sampling dates (such as m_f). All these facts minimize the uncertainty arising from irregular sampling campaigns.

Most of the correlations found in our study are statistically significant at 0.05 level. However, there is still large variability which cannot be explained by the selected set of predictors. The uncertainty of derived regression models stems partly from imperfect sampling design. Therefore, testing of methods which might be able to measure at a plot or catchment scales such as laser scanning and UAV would be beneficial as documented for example in Lendzioch et al. (2016).

The use of only two hemispherical images per one locality may produce a random error in calculation of the specific parameter. Although we performed particular analysis showing the potential inaccuracies of such approach, Lendzioch et al.

(2016) tested several methods to derive LAI in the same study area (such as LAI derived from camera placed in UAV, ground-based measurement using Li-Cor plant canopy analyzer and hemispherical photography) and concluded that the hemispherical images provided generally good estimations of LAI at a plot scale. Additionally, different zenith angles used to calculate the LAI (60° in our case) could also influence the results. This issue was addressed e.g. by López-Moreno and Latron (2008) who concluded that optimal zenith angles are in the range 35–55° when analyzing the snowpack distribution in a temperate mountain range.

The influence of catchment characteristics on snowpack distribution

The differences in SWE in the forest and adjacent open area in our study catchment do not significantly vary for winters with high snow storages compared to winters with low snow storages. However, Stähli and Gustafsson (2006) reported decreasing effect of the forest with increasing snow storage in Alptal valley in Switzerland, especially in higher elevations. This contrast might be explained by the shorter observation period of our observations and by the fact that the SWE maximum in Alptal is usually higher than in our study area (600–800 mm in Alptal; up to 600 mm in Ptaci Brook catchment). It means we cannot exclude a decreasing effect of interception in Ptaci Brook catchment in case of even higher snow accumulations. However, the difference between the SWE deposited in open area and forest was lower for forest sites with lower LAI typically formed by defoliated forest affected by the bark beetle.

The air temperature used to calculate the melt factors was measured at two climatological stations and it was adjusted to specific sampling site using the site elevation and a lapse rate calculated for each day. Using these daily air temperatures cannot capture their small scale variations due to the small scale variability of topography. This effect might be important in spring especially in clear sky conditions at night and early morning. The minimum temperature strongly varies according to the site topography (frost pockets) which could affect the mean daily air temperature used to calculate melt factors. The above mentioned fact could partially explain a relatively high variability of melt factors within one vegetation category, especially in clearings and large open areas. Here, the melt factors are almost equally distributed within their range. Therefore, it is not fully possible to use derived melt factors as general values to calculate snowmelt in other world regions.

The results from multivariate analyses showed that the LAI was slightly better predictor to explain the SWE during accumulation period, while the total irradiance and potential irradiance were slightly better predictors during snowmelt period. However, the differences are rather minor. Applicable results both for LAI and partial irradiance were achieved with m_f as a response variable. However, it is important to mention that the total irradiance (which was also used to calculate partial irradiance) was directly measured at the meteorological station in the open area. The total irradiance at specific forest site was adjusted according to the canopy openness calculated from the respective hemispherical image. Thus both LAI and total irradiance are not mutually independent and their similarity is logical and expected. Despite the above mentioned uncertainties, we can conclude that parameter derived from hemispherical photography may replace measured incoming solar radiation if this meteorological parameter is not available.

The differences of snow ablation rates between open area and forest were caused mainly by the different amount of solar radiation at the specific site. Faster snowmelt in clearings than in the forest also pointed to the fact that the decrease in shortwave radiation in the forest is more important than the increase in longwave radiation (due to trees as longwave radiation emitters). On the contrary, these effects might change according to the day of year and site conditions, such as the clearing size, distance from surrounding trees or forest gaps (López-Moreno and Latron, 2008; Musselman et al., 2015).

The influence of slope orientation (using the transformed aspect) and slope angle on snowpack distribution and snowmelt dynamics was not proven in our study. The reason is probably the fact that most of the slope aspects in the study area are occurring in NW to NE sector and slope angle maximum is 10° (with one exception of 20°). Therefore, the explanatory power of this predictor is rather limited as also showed in PCA performed in our study. However, the increasing importance of slope orientation on the snowpack distribution especially during snowmelt is expected in case of prevailing E-S-W slopes as proved e.g. by Jenicek et al. (2015).

Despite various predictors used in our study, which describe vegetation, topography and meteorological conditions in the study area, there are some effects, which were not included in this study. One example of such effect is wind. We subjectively observe its impact on snow redistribution at some sampling sites. Therefore, the use a suitable parameter describing this effect (surface curvature or similar) might improve the results especially for open areas during snow accumulation period. However, it would require detailed digital terrain model (<1 m resolution) which was not available in the time of the study processing.

The wind has an impact on the small scale variations of turbulent fluxes during snowmelt. Pohl et al. (2006) explored the wind field variability due to topography and found that turbulent fluxes varied up to 20% from the mean within their research area resulting in relatively high differences in snowmelt by up to 70 mm over the entire melt period. The described effect is changing in different localities and it is also important for forested areas which markedly influence ground wind speed (Matejka and Jenicek, 2015).

Vegetation structure and its possible impact on runoff

Despite the relatively simple degree-day approach, our results based on field survey proved an important influence of defoliated forest disturbed by the bark beetle on snow ablation compared to the healthy spruce forest. Our results are in accord with Pomeroy et al. (2012) who used the CRHM model to simulate the impact of forest disturbed be the pine beetle on snow ablation. The decreasing importance of snow interception after spruce forest defoliation was proven in our study, which corresponds to results reported by Pugh and Small (2013) from the western United States. Our results also correspond to conclusions presented by Winkler et al. (2015) who used both measured shortwave radiation and hemispherical photographs to derive the canopy transmittance. However, the reliability of results from the Ptaci Brook catchment could be influenced by the fact that our sampling sites are mostly in disturbed forests with dense treetops, and thus there is still a relatively big amount of snow intercept by the canopy formed by small branches. However, it is expected that the interception effect is likely to decrease due to the gradual fall of branches and trunks. Moreover, we assume that the canopy characteristics of our sites did not change in the period of our sampling campaigns which might be a large simplification especially for sites formed by forests affected by the bark beetle.

Higher snow accumulations represent a bigger water volume further available for snowmelt and runoff, which does not necessarily mean that total runoff or possible flood peaks would be much higher. As documented by Pomeroy et al. (2012) in their study sites, the total spring and summer runoff volume increased by less than 10%, however, the snowmelt volume increased by 45% in case of forest burning and logging. Pomeroy et al. (2012) also showed that burning and pine beetle impacts affected more peak flows than seasonal runoff volumes (up to 25%). It strongly depended on climatological conditions during snowmelt, such as the air temperature, liquid precipitation (rain-on-snow) and wind. The important effect of needle forest on snowmelt dynamics and thus runoff generation was shown also in modelling experiments performed by Kutlakova and Jenicek (2012).

Practical use of the results

Although our study mainly confirmed generally known processes influencing snow distribution, the results showed a possible way to improve the estimation of both SWE and snowmelt rates using meteorological, topography and vegetation indices which are relatively simple to derive from basic climate observations and digital terrain model. Such a procedure may be used e.g. by meteorological services and water management to better calculate snow storages in remote mountain areas and it might support existing procedures used by these institutions. Furthermore, it could improve water balance models or enhance reservoirs manipulations.

The results showed that the SWE and snow depth distribution was influenced by several factors which varied in different land covers and changed in time. Therefore, creating groups based either on vegetation categories or dominating snow process (accumulation vs. melting) before creating of a regression model seems to be an effective way to assess the SWE/melt rates variability.

CONCLUSIONS

We analyzed the snowpack variability in a forested mountain catchment with special interest in the effect of forest structure on both snow accumulation and ablation. Our study was based on repeated distributed measurements of the snow depth and SWE at 16 localities from 2011 to 2015. Based on results, we draw up following conclusions:

- The LAI was slightly better predictor to explain the SWE distribution during accumulation period, while the total irradiance and potential irradiance were slightly better predictors during snowmelt period. However, the differences are rather minor.
- Applicable results both for the LAI and partial irradiance were achieved with the use of melt factor as a response variable. Despite mutual dependence of both parameters, we can conclude that parameters derived from hemispherical images may replace measured incoming solar radiation if this meteorological variable is not available.
- The SWE and snow depth distributions were influenced by several factors which varied in different land covers and which changed in time. Therefore, creating groups either based on vegetation categories or dominating snow process (accumulation vs. melting) seems to be an effective way before the calculation of snow storages in some study area is made. However, despite the significance of the correlations found, there was still large variability which was not explained by the selected set of predictors.
- The combined effect of snow interception and sublimation caused lower SWE difference between open areas and defoliated spruce forest with standing trees compared to the difference between open area and healthy forest (29% and 45%, respectively). The snow ablation was by 18% faster after forest defoliation and we expect even faster ablation in case of complete forest decline. The snow ablation in open areas was almost two times faster compared to forest sites.

Acknowledgement. Support from the Czech Science Foundation (project No. 13-32133S „Headwaters retention potential with respect to hydrological extremes") and European Union (project EU COST Action 1306, no. LD15130 "Impact of landscape disturbance on the stream and basin connectivity") is gratefully acknowledged.

REFERENCES

Blahušiaková, A., Matoušková, M., 2015. Rainfall and runoff regime trends in mountain catchments (Case study area: the upper Hron River basin, Slovakia). J. Hydrol. Hydromech., 63, 183–192.

Boon, S., 2012. Snow accumulation following forest disturbance. Ecohydrology, 5, 279–285.

Burles, K., Boon, S., 2011. Snowmelt energy balance in a burned forest plot, Crowsnest Pass, Alberta, Canada. Hydrol. Process., 25, 3012–3029.

De Michele, C., Avanzi, F., Passoni, D., Barzaghi, R., Pinto, L., Dosso, P., Ghezzi, A., Gianatti, R., Della Vedova, G., 2016. Using a fixed-wing UAS to map snow depth distribution: an evaluation at peak accumulation. Cryosph., 10, 511–522.

Duchacek, L., 2014. Vertical variability in the position of the zero isochion in geomorphologic regions of Czechia. Geografie, 119, 145–160.

Essery, R., Rutter, N., Pomeroy, J., Baxter, R., Stähli, M., Gustafsson, D., Barr, A., Bartlett, P., Elder, K., 2009. SNOWMIP2: An Evaluation of Forest Snow Process Simulations. Bull. Am. Meteorol. Soc., 90, 1120–1135.

Essery, R., Morin, S., Lejeune, Y., B Ménard, C., 2013. A comparison of 1701 snow models using observations from an alpine site. Adv. Water Resour., 55, 131–148.

Fischer, B.M.C., Rinderer, M., Schneider, P., Ewen, T., Seibert, J., 2015. Contributing sources to baseflow in pre-alpine headwaters using spatial snapshot sampling. Hydrol. Process., 29, 5321–5336.

Frazer, G.W., Canham, C.D., Lertzman, K.P., 1999. Gap Light Analyzer (GLA), Version 2.0: Imaging software to extract canopy structure and gap light transmission indices from true-colour fisheye photographs, users manual and program documentation. Simon Fraser University, Burnaby.

Garvelmann, J., Pohl, S., Weiler, M., 2013. From observation to the quantification of snow processes with a time-lapse camera network. Hydrol. Earth Syst. Sci., 17, 1415–1429.

Grünewald, T., Stötter, J., Pomeroy, J.W., Dadic, R., Moreno Baños, I., Marturià, J., Spross, M., Hopkinson, C., Burlando, P., Lehning, M., 2013. Statistical modelling of the snow depth distribution in open alpine terrain. Hydrol. Earth Syst. Sci., 17, 3005–3021.

He, Z.H., Parajka, J., Tian, F.Q., Blöschl, G., 2014. Estimating degree-day factors from MODIS for snowmelt runoff modeling. Hydrol. Earth Syst. Sci., 18, 4773–4789.

Hock, R., 2003. Temperature index melt modelling in mountain

areas. J. Hydrol., 282, 104–115.
Holko, L., Škvarenina, J., Kostka, Z., Frič, M., Staroň, J., 2009. Impact of spruce forest on rainfall interception and seasonal snow cover evolution in the Western Tatra Mountains, Slovakia. Biologia, 64, 594–599.
Jenicek, M., Beitlerova, H., Hasa, M., Kucerova, D., Pevna, H., Podzimek, S., 2012. Modeling snow accumulation and snowmelt runoff - present approaches and results. Acta Universitatis Carolinae Geographica, 47, 15–24.
Jenicek, M., Pevna, H., Matejka, O., 2015. Snow accumulation and ablation in three forested mountain catchments. Acta Hydrol. Slovaca, 16, 208–216.
Jenicek, M., Hotovy, O., Matejka, O., 2017. Snow accumulation and ablation in different canopy structures at a plot scale: using degree-day approach and measured shortwave radiation. Acta Universitatis Carolinae Geographica, 52, 1, 51–62.
Jost, G., Weiler, M., Gluns, D.R., Alila, Y., 2007. The influence of forest and topography on snow accumulation and melt at the watershed-scale. J. Hydrol., 347, 101–115.
Jost, G., Dan Moore, R., Smith, R., Gluns, D.R., 2012. Distributed temperature-index snowmelt modelling for forested catchments. J. Hydrol., 420, 87–101.
Kliment, Z., Matouskova, M., Ledvinka, O., Kralovec, V., 2011. Trend analysis of rainfall-runoff regimes in selected headwater areas of the Czech Republic. J. Hydrol. Hydromech., 59, 36–50.
Krajčí, P., Holko, L., Parajka, J., 2016. Variability of snow line elevation, snow cover area and depletion in the main Slovak basins in winters 2001–2014. J. Hydrol. Hydromech., 64, 12–22.
Kucerova, D., Jenicek, M., 2014. Comparison of selected methods used for the calculation of the snowpack spatial distribution, Bystřice River basin, Czechia. Geografie, 119, 199–217.
Kutlakova, L., Jenicek, M., 2012. Modelling snow accumulation and snowmelt in the Bystrice River basin. Geografie, 117, 110–125.
Langhammer, J., Hartvich, F., Kliment, Z., Jeníček, M., Bernsteinová, J., Vlček, L., Su, Y., Štych, P., Miřijovský, J., 2015a. The impact of disturbance on the dynamics of fluvial processes in mountain landscapes. Silva Gabreta, 21, 105–116.
Langhammer, J., Su, Y., Bernsteinová, J., 2015b. Runoff response to climate warming and forest disturbance in a mid-mountain basin. Water, 7, 3320–3342.
Lendzioch, T., Langhammer, J., Jenicek, M., 2016. Tracking forest and open area effects on snow accumulation by unmanned aerial vehicle photogrammetry. ISPRS - Int. Arch. Photogramm. Remote Sens. Spat. Inf. Sci. XLI-B1, 917–923. DOI: 10.5194/isprs-archives-XLI-B1-917-2016.
López-Moreno, J.I., Latron, J., 2008. Influence of canopy density on snow distribution in a temperate mountain range. Hydrol. Process., 22, 117–126.
López-Moreno, J.I., Revuelto, J., Fassnacht, S.R., Azorín-Molina, C., Vicente-Serrano, S.M., Morán-Tejeda, E., Sexstone, G.A., 2015. Snowpack variability across various spatio-temporal resolutions. Hydrol. Process., 29, 1213–1224.
Lundquist, J.D., Dickerson-Lange, S.E., Lutz, J.A., Cristea, N.C., 2013. Lower forest density enhances snow retention in regions with warmer winters: A global framework developed from plot-scale observations and modeling. Water Resour. Res., 49, 6356–6370.
Matejka, O., Jenicek, M., 2015. An energy-based model accounting for snow accumulation and snowmelt in a coniferous forest and in an open area. In: Voda a Krajina 2015, 1–14.
Molotch, N.P., Meromy, L., 2014. Physiographic and climatic controls on snow cover persistence in the Sierra Nevada Mountains. Hydrol. Process., 28, 4573–4586.
Musselman, K.N., Pomeroy, J.W., Link, T.E., 2015. Variability in shortwave irradiance caused by forest gaps: Measurements, modelling, and implications for snow energetics. Agric. For. Meteorol., 207, 69–82.
Parajka, J., Holko, L., Kostka, Z., Blöschl, G., 2012. MODIS snow cover mapping accuracy in a small mountain catchment – comparison between open and forest sites. Hydrol. Earth Syst. Sci., 16, 2365–2377.
Pohl, S., Marsh, P., Liston, G.E., 2006. Spatial-temporal variability in turbulent fluxes during spring snowmelt. Arct. Antarct. Alp. Res., 38, 136–146.
Pomeroy, J., Fang, X., Ellis, C., 2012. Sensitivity of snowmelt hydrology in Marmot Creek, Alberta, to forest cover disturbance. Hydrol. Process., 26, 1891–1904.
Pugh, E.T., Small, E.E., 2013. The impact of beetle-induced conifer death on stand-scale canopy snow interception. Hydrol. Res., 44, 644–657.
R Core Team, 2016. A language and environment for statistical computing. R Foundation for Statistical Computing, Vienna, Austria. URL https://www.r-project.org/ (accessed 8.1.16).
Revuelto, J., López-Moreno, J.-I., Azorin-Molina, C., Alonso-González, E., Sanmiguel-Vallelado, A., 2016. Small-scale effect of pine stand pruning on snowpack distribution in the Pyrenees observed with a terrestrial laser scanner. Forests, 7, 166.
Seibert, J., Jenicek, M., Huss, M., Ewen, T., 2014. Snow and ice in the hydrosphere. In: Haeberli, W., Whiteman, C. (Eds.): Snow and Ice-Related Hazards, Risks, and Disasters. Elsevier, Amsterdam, pp. 99–137.
Schelker, J., Kuglerová, L., Eklöf, K., Bishop, K., Laudon, H., 2013. Hydrological effects of clear-cutting in a boreal forest – Snowpack dynamics, snowmelt and streamflow responses. J. Hydrol., 484, 105–114.
Schnorbus, M., Alila, Y., 2013. Peak flow regime changes following forest harvesting in a snow-dominated basin: Effects of harvest area, elevation, and channel connectivity. Water Resour. Res., 49, 517–535.
Stähli, M., Gustafsson, D., 2006. Long-term investigations of the snow cover in a subalpine semi-forested catchment. Hydrol. Process., 20, 411–428.
Stähli, M., Jonas, T., Gustafsson, D., 2009. The role of snow interception in winter-time radiation processes of a coniferous sub-alpine forest. Hydrol. Process., 23, 2498–2512.
Strasser, U., Warscher, M., Liston, G.E., 2011. Modeling snow–canopy processes on an idealized mountain. J. Hydrometeorol., 12, 663–677.
Šípek, V., Tesař, M., 2014. Seasonal snow accumulation in the mid-latitude forested catchment. Biologia, 69, 1562–1569.
Vlcek, L., Kocum, J., Jansky, B., Sefrna, L., Kucerova, A., 2012. Retention potential and hydrological balance of a peat bog: case study of Rokytka Moors, Otava River headwaters, sw. Czechia. Geografie, 117, 395–414.
Winkler, R., Spittlehouse, D., Boon, S., Zimonick, B., 2015. Forest disturbance effects on snow and water yield in interior British Columbia. Hydrol. Res., 46, 521–532.

Received 10 August 2016
Accepted 27 February 2017

J. Hydrol. Hydromech., 66, 2018, 1, 55–64
DOI: 10.1515/johh-2017-0045

Detection of changes in flow regime of rivers in Poland

Dariusz Wrzesiński, Leszek Sobkowiak*

Adam Mickiewicz University, Institute of Physical Geography and Environmental Planning, Chair of Hydrology and Water Management, Bogumiła Krygowskiego 10 str., 61-680 Poznań, Poland.
* Corresponding author. E-mail: lesob@amu.edu.pl

Abstract: The aim of this study is to detect changes in flow regime of rivers in Poland. On the basis of daily discharges recorded in 1951–2010 at 159 gauging stations located on 94 rivers regularities in the variability of the river flow characteristics in the multi-year period and in the annual cycle were identified and also their spatial uniformity was examined. In order to identify changes in the characteristics of river regime, similarities of empirical distribution functions of the 5-day sets (pentads) of discharges were analyzed and the percent shares of similar and dissimilar distributions of the 5-day discharge frequencies in the successive 20-year sub-periods were compared with the average values of discharges recorded in 1951–2010. Three alternative methods of river classification were employed and in the classification procedure use was made of the Ward's hierarchical clustering method. This resulted in identification of groups of rivers different in terms of the degree of transformation of their hydrological regimes in the multi-year and annual patterns.

Keywords: Flow regime; Detection of changes; Empirical distribution function; Typological classification; Ward's hierarchical clustering method.

INTRODUCTION

Identification and understanding of the multi-year changeability (or stability) of river regime is a key issue due to the present changes of climate and an increasing human impact on the water environment. River regime is a significant indicator that can be applied to identify spatial and temporal changes of river flow, its structure and seasonality, and also to determine the present and prospective water deficits.

According to Gutry-Korycka (2001) hydrological regime is a pattern of changes of all phenomena occurring in a river. It determines the state and response of a river system in relation to the climatic conditions and physical-geographical characteristics of its basin. Rotnicka (1988) defines the river regime as a kind of river discharges and their temporal structure in an average annual cycle. That structure consists of so-called hydrological periods that can be used to examine river regime and thus constitute a basis for its description.

Under the influence of the changing climate and human activity river regime may be altered and ultimately changed into a different one, sometimes with a distinctively different pattern of seasonal flow. As a consequence, the previously established hydro-ecological conditions and the water use patterns in that river basin may be disturbed. Stream flow seasonality and variability and their characteristics at the global scale were investigated by Dettinger and Diaz (2000), while Stahl et al. (2010) investigated selected near-neutral catchments in Europe to predict the future streamflow trends. At regional scale Parajka et al. (2010) investigated flood regimes and their seasonal characteristics across the Alpine-Carpathian range. At country-level scale Merz et al. (1999) studied the problem of seasonality of floods in Austria, while Parajka et al. (2009) applied the comparative approach to analyze the seasonality of hydrological characteristics in Slovakia and Austria. Bezak et al. (2015, 2016) analyzed flood events in Slovenian streams and identified their statistical trends and seasonality, while Merz et al. (2016) attempted to separate flood-rich and flood-poor periods in 68 catchments across Germany. Gaál et al. (2012) through the comparative hydrology stressed the role of the flood timescales as an important parameter integrating a range of climate and catchment. In analyses of the effects of climate changes on the natural environment, including water resources, there is a growing number of studies on climatic factors influencing seasonal changes of flow and altering river regimes, including that by Krasovskaia and Gottschalk (1992), Krasovskaia (1995), Krasovskaia (1996), Krasovskaia and Sælthun (1997) and Wilson et al. (2012). Results of studies on the runoff changes in relation to the observed and predicted global warming were presented by Labat et al. (2004).

Due to the global warming periodic variations of river discharges are observed. This attracts attention of scholars involved in studies on changes of river regimes, as for example Westmacott and Burn (1997), Middelkoop et al. (2001), Krasovskaia and Gottschalk (2002). In this context new methodological approaches and regional syntheses deserve attention (Arnell, 1999; Gutry-Korycka and Rotnicka, 1998; Krasovskaia et al., 1999; Shorthouse and Arnell, 1999; Wrzesiński, 2008, 2010a). Arnell (1999) presented an assessment of the effects of climate change on the hydrological regime of European rivers, also Hall et al. (2014) pointed out potential drivers of flood regime changes and on that basis predicted future changes in floods in selected sub-regions of Europe. Bower et al. (2004) provided a critical analysis of methods used to establish the climatic determinants of changes of river regime, while Dynowska (1988, 1993) studied the anthropogenic determinants of such changes observed in rivers in Poland.

In order to identify changes in any regularity, including those in the hydrological regime (regardless of their causes), in the first stage a proper identification and description of the initial state is required. Only then, in relation to that initial state it is possible to define departures and deviations observed in a multi-year period. In defining river regime both the supervised (Dynowska, 1971; Lvovich, 1938; Pardé, 1957) and unsupervised (Gottschalk, 1985; Haines et al., 1988; Rotnicka, 1988) approaches are applied. In the supervised approach regularities in the multi-year hydrometric data series that are in accordance

with predefined indices are sought, while in the unsupervised approach classificatory procedures (usually grouping) are used (Krasovskaia and Gottschalk, 2002; Wrzesiński, 2010a).

In that context the method of analysis and description of river regime through an identification of the temporal structure of hydrological phenomena and their changes in the annual cycle proposed by Rotnicka (1988) should be pointed out. It has been employed both in theoretical and applicative studies, among others to identify prospective changes in the river regime patterns under different scenarios of the global climate changes (Gutry-Korycka and Rotnicka, 1998). Moreover, that method is a very useful tool in determining the stability of the river regime characteristics, which can be altered by changing climate or human activity. Wrzesiński (2005, 2008, 2011) applied that method to assess changes in flow regimes of rivers triggered by different intensity of the North Atlantic Oscillation (NAO) and also to detect transformations of flow regime of rivers in Poland (Wrzesiński, 2010b, 2013b).

The aim of this study is to determine changes in flow regime of rivers in Poland through identification of their variation patterns both in the multi-year and annual cycles. Changes in these river regimes were identified on the basis of analysis of similarities between the empirical distribution functions of the five-day sets of discharges (pentads) and the percent share of similar and dissimilar frequency distributions of discharges in 41 twenty-year sub-periods separated within the multi-year period 1951–2010.

STUDY AREA AND DATA

Poland with an area of 312,823 square km shows considerable differences of its environmental conditions, both climatic and hydrological, that are reflected in different river feeding conditions and in a distinctive seasonal changeability of river flow. Woś (2010) distinguished 28 climatic regions in Poland, while Dynowska and Pociask-Karteczka (1999) identified five major types of hydrological regimes of the Polish rivers, namely: nival poorly developed, nival medium developed, nival clearly developed, nival-pluvial and pluvial-nival. In addition, in Poland there is a regionally differentiated influence of the macro-scale climatic phenomena on the country's hydrometeorological elements. Therefore, rivers in Poland are exposed to different factors influencing (altering) their flow and destabilizing their regimes. These factors include natural changes, climatic variations and human activity.

The aim of this research is to detect changes in flow regime resulting not only from the natural variability of climate but also from human activity. Consequently, all the available hydrometric data were examined, regardless of their statistical homogeneity. In this study daily discharges recorded at 159 gauging stations located on 94 rivers in Poland in the multi-year period 1951–2010 were analyzed. The data were provided by the Institute of Meteorology and Water Management in Warsaw, Poland.

METHODOLOGIES

In this paper changes in river regime were determined by investigating similarities between distributions of the river discharge frequencies clustered in the 5-day sets (pentads) of each hydrological year in 41 consecutive twenty-year sub-periods and distributions of the river discharge frequencies in the whole multi-year period 1951–2010. Details of that method can be found in Wrzesiński (2010b, 2013b). The five-day period (pentad) was taken as an elementary time unit and the value of discharge was set as a grouping criterion. That criterion was described by variable x, defined as the frequency distribution of water discharges. The hydrological year consists of 73 pentads, each representing five values of daily discharges. The hydrological year in Poland lasts from 1st November to 31st October of the next year, and it is additionally divided into the winter (1st November-30th April) and summer (1st May-31st October) seasons.

In the first part of the analysis frequency distributions of discharges in the individual pentads in the multi-year period (1951–2010) and of 41 twenty-year sub-periods, each one shifted by one year (that is 1951–1970, then 1952–1971 and so on, until 1991–2010) were calculated. Therefore, for the whole 60-year long observation period a 300-element (5 days multiplied by 60 years) set of discharge values for each pentad was calculated. Similarly, for each 20-year interval a 100-element set was obtained. Next, the calculated discharge frequencies were cumulated in a descending order, from the highest to the lowest value intervals. On the basis of the cumulative discharge frequencies for each yearly set of pentads empirical distribution functions were computed.

For each of 73 pentads similarities between empirical distribution functions of river discharges in the multi-year 1951–2010 and the consecutive 20-year sub-sets were determined with the use of the non-parametric Kolmogorov-Smirnov test (Sobczyk, 2007). Results of previous studies of Wrzesiński (2013b) show that the next stage of the analysis should be modified in such a way that in order to obtain information on the tendency of changes (increase or decrease) of river flow for the compared distributions instead of calculating the absolute values of differences between the empirical distribution functions (F_{n_k}, F_{n_p}), the maximum (or minimum) differences D should be computed, as follows:

$$D = \max(\min)(F_{n_k}(x) - F_{n_p}(x))$$

where: $F_{n_k}(x)$ is empirical distribution function of the multi-year 1951–2010 set and $F_{n_p}(x)$ is empirical distribution function of the respective twenty-year subset.

The λ statistic is: $\lambda = D\sqrt{n}$, where

$n = \frac{n_k n_p}{n_k + n_p}$, n_k, n_p denote the size of samples on the basis of which the empirical distribution functions were calculated. It has a Kolmogorov distribution.

Hypothesis H_0 about the goodness-of-fit of a pair of distributions was tested at the $\alpha = 0.05$ and $\alpha = 0.01$ significance levels. For the 300-element and 100-element samples, respectively, hypothesis H_0 was not rejected when $\lambda < \lambda_\alpha$, i.e. when $D\sqrt{n} < \lambda_\alpha$ or $D < \frac{\lambda_\alpha}{\sqrt{n}}$.

By substituting the critical values for $\alpha = 0.05$ and $\alpha = 0.01$ from the Kolmogorov distribution, we obtain the maximum and minimum differences for D, respectively:

$$D_{\max} < \frac{\lambda_{0.05}}{\sqrt{n}} = \frac{1.36}{\sqrt{\frac{30000}{400}}} = 0.157,$$

$$D_{\min} > \frac{\lambda_{0.05}}{\sqrt{n}} = \frac{1.36}{\sqrt{\frac{30000}{400}}} = -0.157,$$

$$D_{\max} < \frac{\lambda_{0.01}}{\sqrt{n}} = \frac{1.63}{\sqrt{\frac{30000}{400}}} = 0.188,$$

$$D_{\min} > \frac{\lambda_{0.01}}{\sqrt{n}} = \frac{1.63}{\sqrt{\frac{30000}{400}}} = -0.188.$$

If $D_{\max} < 0.157$ or $D_{\min} > -0.157$, the difference between distributions is not significant, and hence the distributions are similar. When $0.157 \leq D_{\max} < 0.188$ or $-0.157 \geq D_{\min} > -0.188$, the difference between distributions is probably not significant, and when $D_{\max} \geq 0.188$ or $D_{\min} \leq -0.188$, the difference between distributions is significant, and the distributions are dissimilar. An example of calculations of the D characteristics for two 20-year intervals (1951–1970 and 1991–2010, respectively) is given in Table 1. $D_{\max}$ was obtained when river flow of the respective twenty-year sub-period was lower than river flow of the multi-year 1951–2010 period, while $D_{\min}$ was obtained when river flow of the respective twenty-year sub-period was higher than river flow of the multi-year 1951–2010 period.

The testing procedure allows an assessment of similarities of discharge distributions calculated for each pentad of the consecutive twenty-year sub-periods of the multi-year period 1951–2010. The lack of similarity mans a statistically significant difference between the structure of discharges of the compared pentads of a twenty-year period and that of the initial (whole) multi-year period. Consequently, that departure from the initial multi-year pattern of flow indicates a change and destabilization of the flow regime. Additionally, this method allows determining the percent share of similar, probably similar and also dissimilar distributions for each pentad of the year and for the successive 20-year sub-periods. As a result it is possible to determine the time when significant changes in the distribution of discharge frequencies (or disturbances of the river regime) took place, both seasonally and in the whole multi-year period. Information obtained in this way allowed classification (grouping) of the analyzed rivers in three variants, that is:

1. On the basis of the percent share of similar and dissimilar distributions in the successive 41 twenty-year periods in the multi-year 1951–2010,
2. On the basis of the percent share of similar and dissimilar distributions in the successive 73 pentads on the hydrological year, and
3. On the basis of the maximum differences in empirical distribution functions ($D_{\max}$ or $D_{\min}$).

In classification of the investigated rivers the Ward's method of hierarchical grouping was applied. The Ward's method is one of the most popular ways of deriving clusters of similar elements. Ward (1963) suggested that at each step of the analysis, the loss of information associated with merging objects was measured by the sum of squares of deviations of each object from the center of the cluster to which it belongs. At each step of grouping, the union of every possible cluster pair is considered and two clusters whose function results in the lowest increase in information loss are combined. The information loss in this method is referred to as the error sum of squares (E.S.S.), defined:

$$E.S.S. = \sum_{i-1}^{n} x_i^2 - \frac{1}{n}\left(\sum_{i-1}^{n} x_i\right)^2$$

where x_i is the score of the i-th object.

The number of typological classes was determined on the basis of the dendrogram geometry and the binding distance curve. In the statistical analyses the Excel (Microsoft) and Statistica (StatSoft) software were applied, while the graphics were drawn with the help of Surfer (Golden Software) and CorelDraw 12 (Corel) tools. The isoline diagrams were constructed using the kriging procedure.

Table 1. Example of calculation of the D statistics for selected two twenty-year periods 1951–1970 and 1991–2010 (river: Warta, gauge: Poznań).

Discharge intervals	Empirical distribution functions of water discharges for chosen pentads of the year									Values of D statistics					
	1951–2010			1951–1970			1991–2010			$F_{1951-2010} - F_{1951-1970}$			$F_{1951-2010} - F_{1991-2010}$		
	F_{n1}	F_{n2}	F_{n73}	F_{n1}	F_{n2}	F_{n73}	F_{n1}	F_{n2}	F_{n73}	F_{n1}	F_{n2}	F_{n73}	F_{n1}	F_{n2}	F_{n73}
12.0 – 12.49	–	–	–	–	–	–	–	–	–	–	–	–	–	–	–
…	…	…	…	…	…	…	…	…	…	…	…	…	…	…	…
4.5 – 4.99	0.003	–	–	–	–	–	–	–	–	0.003	–	–	0.003	–	–
4.0 – 4.49	0.017	–	0.003	–	–	–	–	–	–	0.017	–	0.003	0.017	–	0.003
3.5 – 3.99	0.017	0.017	0.007	–	–	–	–	–	–	0.017	0.017	0.007	0.017	0.017	0.007
3.0 – 3.49	0.017	0.017	0.007	–	–	–	–	–	–	0.017	0.017	0.007	0.017	0.017	0.007
2.5 – 2.99	0.017	0.017	0.010	–	–	–	–	–	–	0.017	0.017	0.010	0.017	0.017	0.010
2.0 – 2.49	0.017	0.017	0.013	–	–	–	–	–	–	0.017	0.017	0.013	0.017	0.017	0.013
1.5 – 1.99	0.017	0.033	0.017	–	–	–	–	–	–	0.017	0.033	0.017	0.017	0.033	0.017
1.0 – 1.49	0.033	0.033	0.020	–	–	–	–	–	–	0.033	0.033	0.020	0.033	0.033	0.020
0.50 – 0.99	0.100	0.103	0.080	0.020	0.020	–	0.080	0.100	0.050	0.080	0.083	0.080	0.020	0.003	0.030
0 – 0.49	0.217	0.223	0.227	0.100	0.100	0.080	0.250	0.250	0.300	0.117	0.123	0.147	–0.033	–0.027	–0.073
–0.50 – 0.0	0.543	0.620	0.540	0.380	0.470	0.350	0.630	0.680	0.620	**0.163**	**0.150**	**0.190**	**–0.087**	**–0.060**	**–0.080**
–1.0 – –0.5	0.950	0.950	0.950	0.850	0.850	0.850	1.000	1.000	1.000	0.100	0.100	0.100	–0.050	–0.050	–0.050
–1.5 – –1.0	1.000	1.000	1.000	1.000	1.000	1.000	1.000	1.000	1.000	0.000	0.000	0.000	0.000	0.000	0.000

Note: the maximum values (positive or negative) are in bold

RESULTS

Changes of river regime in the multi-year period

In order to detect spatial regularities in changes of flow regime in the multi-year period 1951–2010 the analyzed rivers were classified by the percent share of similar and dissimilar discharge distributions in the consecutive 41 twenty-year periods. In this variant of classification at the E.S.S. = 6.0 grouping level the investigated rivers were divided into eight groups (Figure 1).

The most stable flow regime in the investigated multi-year period, reflected in the largest share of similar discharge distributions in all the 20-year periods compared to the whole 60-year period (1951–2010), is represented by rivers of the 1st and 2nd group. In the case of the 1st group the share of similar distributions is usually relatively high (on average higher than 95%), while in the 2nd group it is only slightly lower (between 90 and 95%). The highest share of dissimilar distributions (up to 10%) is observed at the beginning of the investigated period, more precisely in 1951–1970, when the flow was lower than the multi-year average and also in the 1960s, when it was higher than the average.

In the analyzed multi-year period changes of flow regime of rivers classified in the 3rd group occurred in the early 1950s and also in the 1970s and 1980s. In the 1950s the share of similar distributions of discharges reached 60% and the river flow was lower than the average. In the 1970s and 1980s the percent share of similar distributions of discharges was about 70%, but these departures were higher than the average (Figure 2).

Rivers of the 4th and 5th group show the most prominent changes of flow in the investigated multi-year period. Those are streams with flow regimes most significantly changed by human activity. Rivers of the 4th group have the largest deviations of their flow and tendency of changes similar to that of the 3rd group. However, the scope of these changes is much broader, which is proved by very low share of similar discharge distributions. In the 1950s the flow was lower, while in the 1970s and 1980s higher than the average and the shares of similar discharge distributions were 20 and 10%, respectively.

Rivers of the 5th group, similarly to those of the 4th group, display relatively big changes of flow in the analyzed multi-year period. However, the direction of that tendency is opposite. In the first part of the investigated period, specifically in 1951–1965, their flows are higher than the multi-year average, while in the second part (after 1975) they are lower than the average. The share of similar distributions in the two periods is very low, ranging between 10 and 40%.

Rivers of the 6th group show the highest deviations from the average values in the 1960s. Their flow values are clearly higher than the multi-year average and the share of similar distributions is about 40%. In 1991–2010 there are smaller, negative deviations from the average values of flow. The share of similar distributions is relatively higher (about 80%).

Similar changes of flow, but on a smaller scale are observed in the case of rivers of the 7th group. In the 1960s and 1970s their flows were higher than the average and the share of similar distributions was about 75%. In the 1990s and 2000s the flow was lower than the multi-year average value.

The flow of rivers of the 8th group is higher than the average in 1951–1970 and lower after 1980. The share of similar distributions in the two periods varies from 70 to 90%.

Changes of river regime in the annual cycle

Spatial regularities in changes of flow regime in the annual cycle (seasonal changes) have been analyzed on the basis of classification of the investigated rivers. The percentage of similar and dissimilar discharge distributions in the 73 five-day periods (pentads) in the successive 41 twenty-year periods of the multi-year 1951–2010 was taken as the grouping criterion. In this classification the rivers were divided into 5 groups (E.S.S. = 8.0) (Figure 3).

While rivers of the 1st group have the most stable flow regime in the annual cycle, changes of flow regime of rivers classified in the 2nd group are relatively slight and occur in the autumn-winter season (no later than mid-February) and also in June and July (Figure 4).

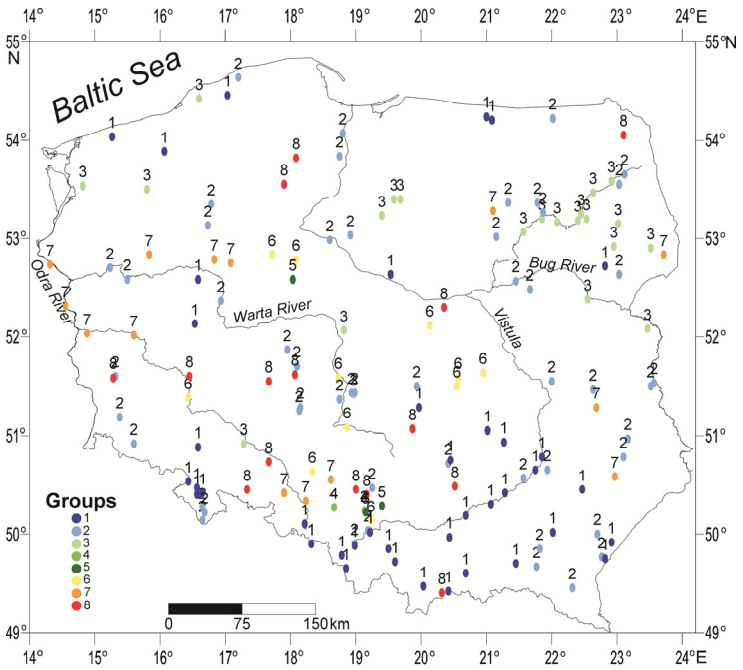

Fig. 1. Typology of rivers in Poland in terms of the proportion of similar discharge distributions in the successive 41 twenty-year intervals – the first grouping variant.

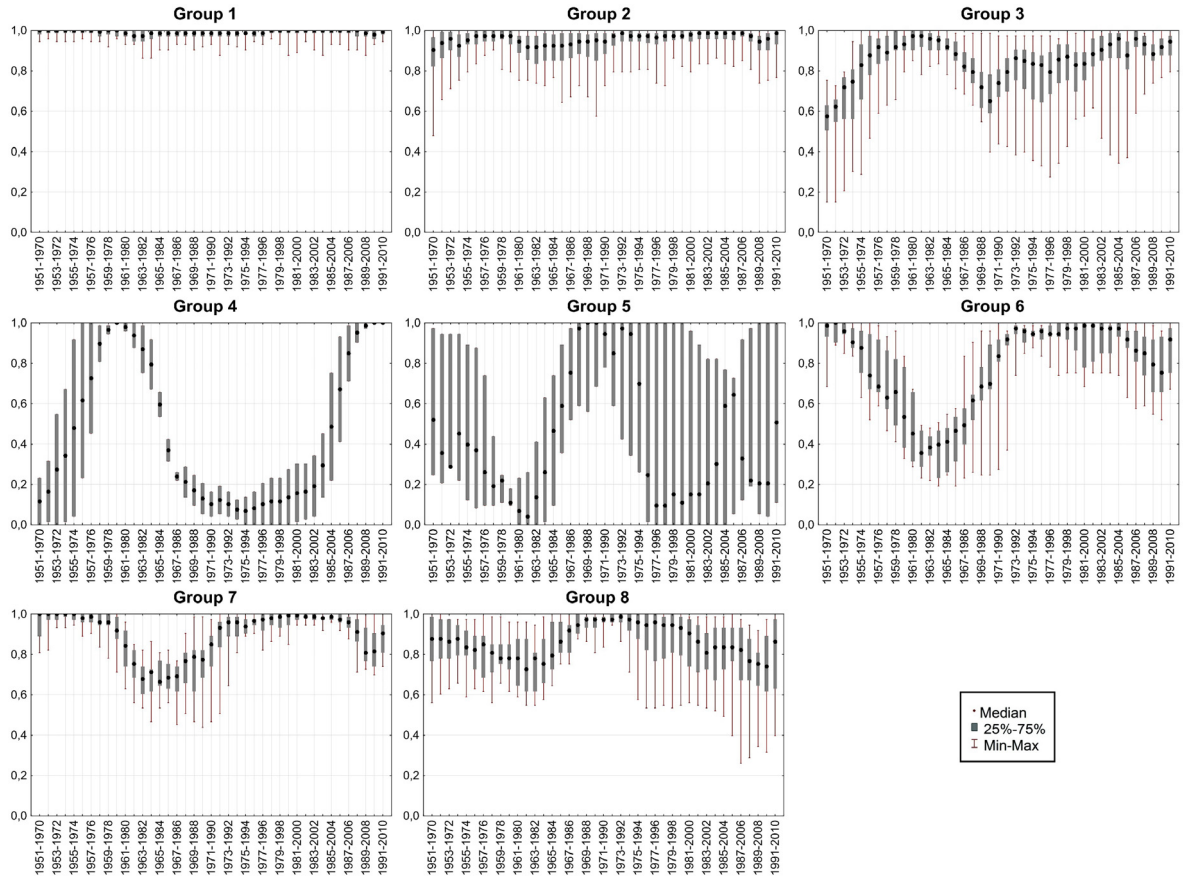

Fig. 2. Ranges of variability of the proportion of similar discharge distributions in the successive twenty-year intervals in the distinguished groups of rivers (1.0 = 100%).

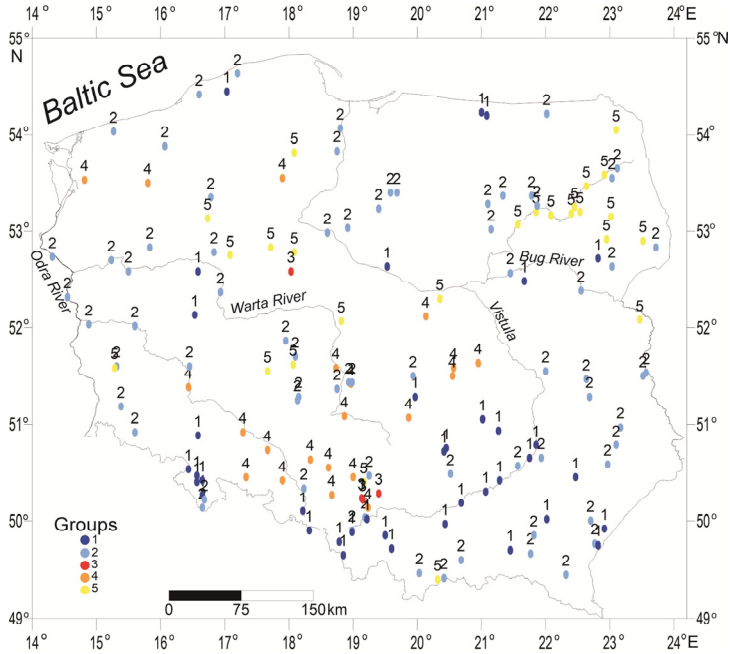

Fig. 3. Typology of rivers in Poland in terms of the proportion of similar discharge distributions in 73 pentads of the year – the second grouping variant.

The most prominent changes in the annual flow are observed in the case of rivers of the 3rd group. While the percent share of similar distributions in the successive pentads is small (between 30 and 60%), there is remarkably higher (about 30%) share of dissimilar distributions resulting from an increase of flow rather than from its decrease (up to 20%).

Rivers of the 4th and 5th group show more stable regimes in the annual cycle. Changes of flow of rivers belonging to the 4th group occur at the beginning of the hydrological year (i.e. in November and December) and also in the summer-autumn period. Rivers of the 5th group show the largest changes of flow in winter (January–February), when both its increase and de-

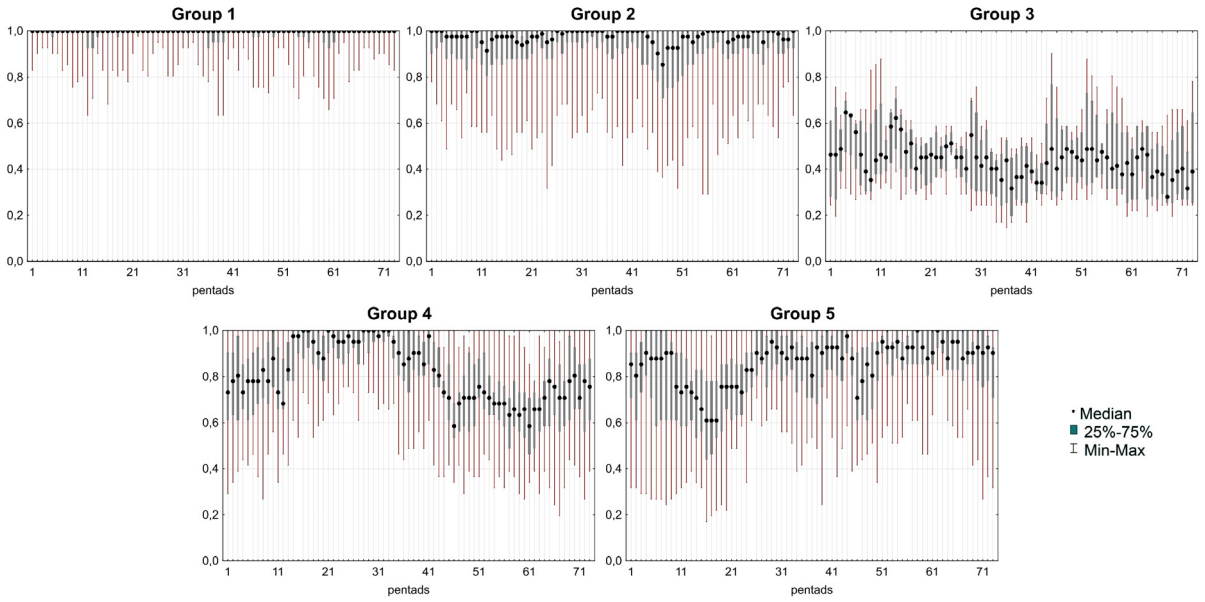

Fig. 4. Range of variability of the proportion of similar discharge distributions in 73 pentads of the year (1.0 = 100%).

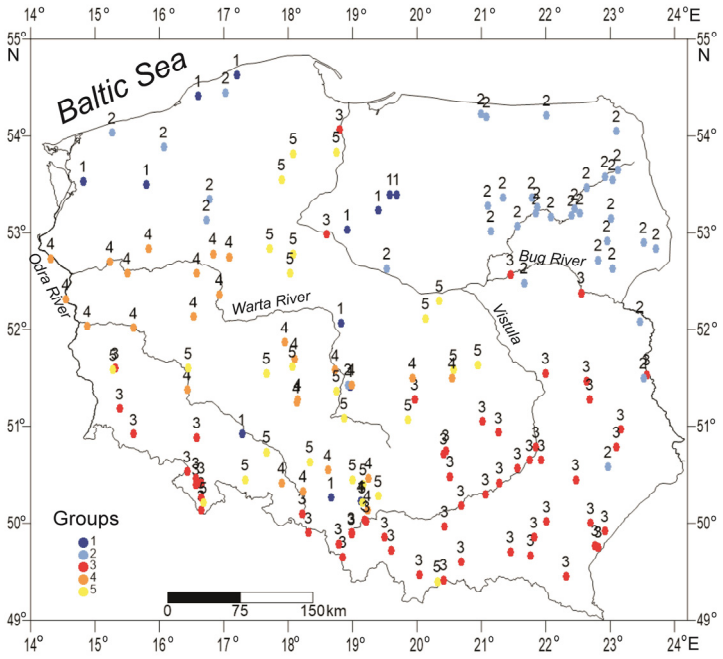

Fig. 5. Typology of rivers in Poland in terms of the similarity of the maximum differences in empirical distribution functions of the pentad sets of river flow – the third grouping variant.

crease can be observed, compared to the average flow conditions. During the other seasons, especially in summer (June–July) changes of their regime are influenced mainly by positive deviations of flow compared to the average values.

The third variant of grouping seems to be most optimal and universal. In that case a comparison between the empirical distribution functions of discharges of the separated pentads in the successive 20-year periods and the multi-year (60 years) period allowed distinguishing rivers with the most unstable and stable parameters of their flow regime, both in the annual cycle and in the analyzed multi-year period 1951–2010. In that grouping variant, on the basis of a set of characteristics D at the E.S.S. = 28 grouping level, the investigated rivers were divided into five groups, as shown in Figure 5.

Spatial distribution of the studied river gauges in the separated five groups is quite characteristic and regionally diversified (Figure 5). Rivers of the 1st group show the largest changes in their flow regimes, which are caused by human activity. They are located in different parts of Poland. In that group such rivers as the Kłodnica (at Gliwice gauge), Brynica (at Szabelnia gauge) and Czarna Przemsza in the Silesian region, the Oława in Lower Silesia, the Ner flowing through the Łódź agglomeration, the coastal rivers Wieprza and Łupawa and also rivers of the entire hydrographic systems of the Drwęca, Ina and Drawa in the Pomeranian Lakeland can be found. They all show a decreasing flow in 1951–1970, followed by an increase in 1971–1990 (Figure 6, Figure 7). The observed changes usually take place in winter (from mid-December to mid-February) and in the summer-autumn period (from mid-June to the end of October). In the summer-autumn season values of flow higher than the average are also observed in 1981–2000.

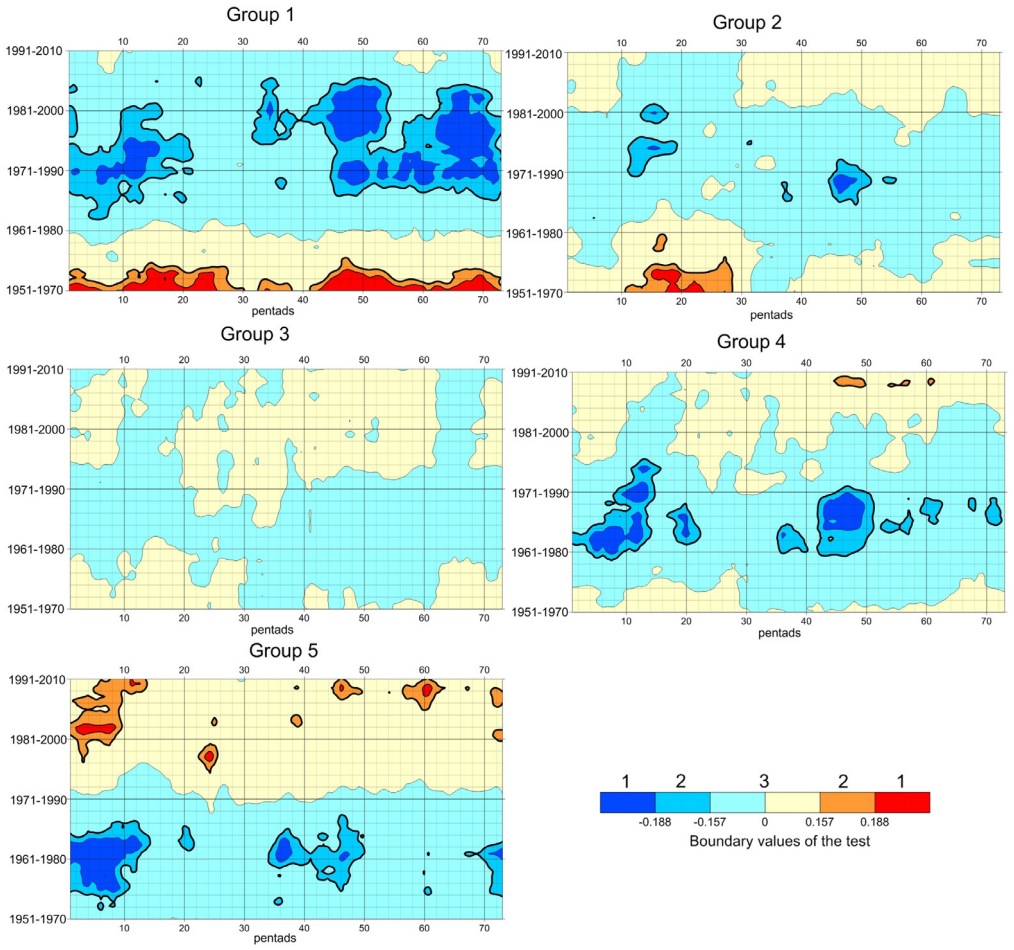

Fig. 6. Values of the maximum differences of the empirical distribution functions of the pentad sets of river flow in the successive twenty-year intervals and the significance test of their similarities in the distinguished groups of rivers (1 - dissimilar distributions, 2 - probably similar distributions, 3 - similar distributions).

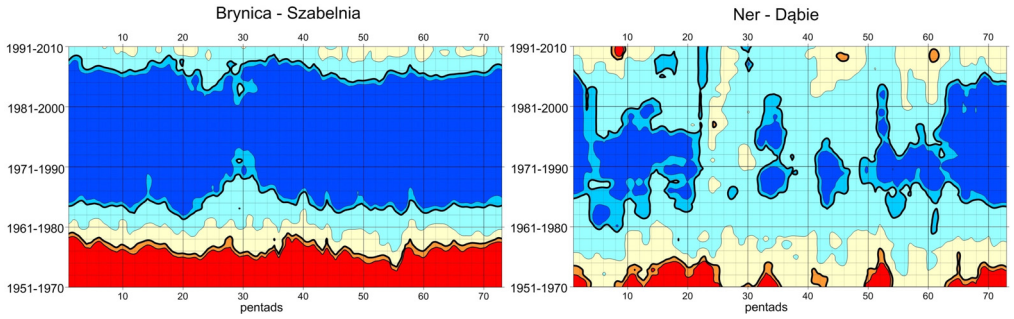

Fig. 7. Values of the maximum differences of the empirical distribution functions of the pentad sets of flow for selected rivers of group 1; legend as in Fig. 10.

In the first grouping variant rivers of the 1st group belonged to the 3rd group, while in the second grouping variant – to the 2nd or 4th group, that is with the lowest shares of similar distributions both in the 20-year periods of the analysed multi-year (1st variant) and in the 5-day periods (pentads) of the annual cycle (2nd variant).

In the 2nd group there are rivers located in the northeastern part of Poland, as for example rivers of the Narew basin (with the exception of the Bug River), some coastal rivers (the Rega, Parsęta and Słupia), and the Gwda River, which flows through the Pomeranian Lakeland. In general, the flow regime of these rivers is more stable than that of the 1st group. Nevertheless, in 1951–1970 their flows were usually lower than the average calculated for the whole investigated multi-year period, especially in winter (the Narew River between January and March). On the other hand, higher values of flow are observed in the summer-autumn periods of 1970–1989, and also in the winter seasons of 1975–2000 (Figure 6, Figure 8).

Rivers of the 3rd group represent the most stable flow regime in the investigated multi-year period. That group comprises rivers of the upper and middle parts of the Vistula River basin along with the Bug River and also tributaries of the Odra river in the Sudety Mountains (Figure 6, Figure 9), with the exceptions of the Dunajec River at Czorsztyn gauge and the Nysa Kłodzka River (5th group), as well as the Wieprz River at Zwierzyniec gauge (2nd group). In the previous variants they were classified as rivers having the highest share of similar discharge distributions (the 1st and 2nd group, respectively).

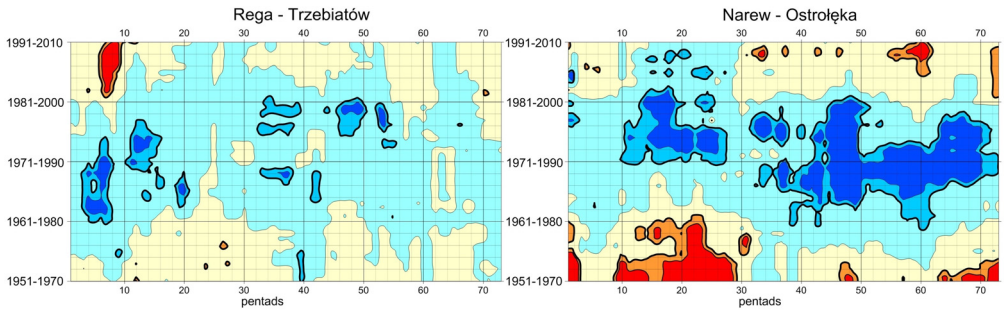

Fig. 8. Values of the maximum differences of the empirical distribution functions of the pentad sets of flow for selected rivers of group 2; legend as in Fig. 10.

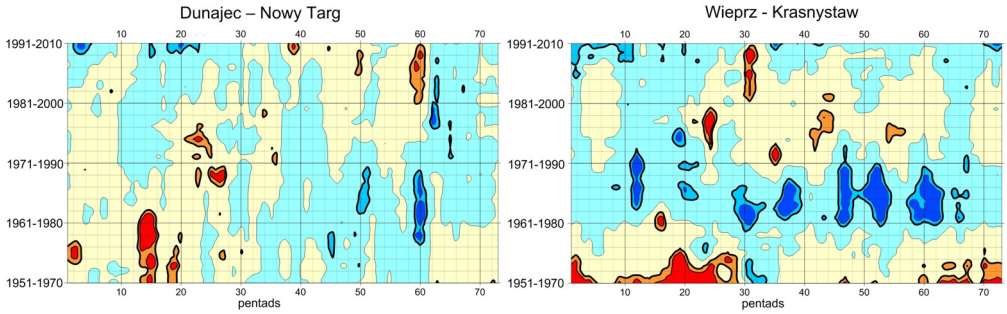

Fig. 9. Values of the maximum differences of the empirical distribution functions of the pentad sets of flow for selected rivers of group 3; legend as in Fig. 10.

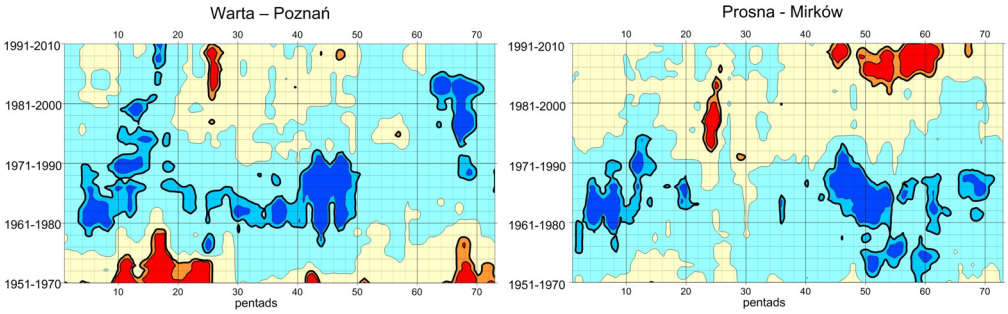

Fig. 10. Values of the maximum differences of the empirical distribution functions of the pentad sets of flow for selected rivers of group 4; legend as in Fig. 10.

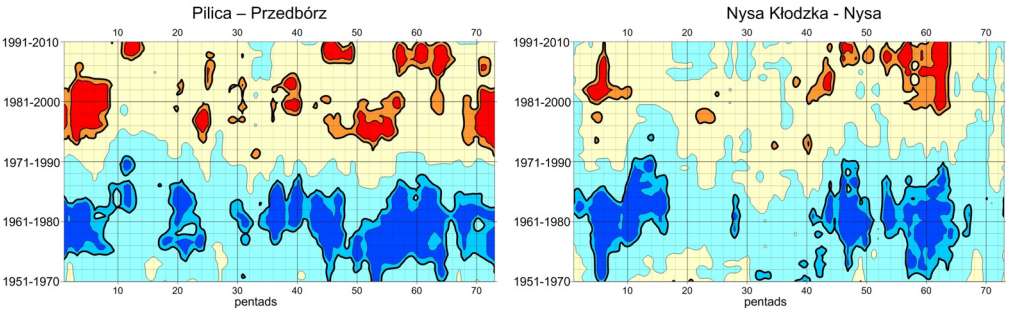

Fig. 11. Values of the maximum differences of the empirical distribution functions of the pentad sets of flow for selected rivers of group 5; legend as in Fig. 10.

The 4th group consists of most rivers of the middle and lower sections of the Warta river basin, the middle and lower Odra river, as well as the Wolbórka and Drzewiczka rivers in the Pilica River basin. In 1961–1990 all these rivers demonstrated a noticeable increase of flow in the winter season (from December to early February) and also in late spring and early summer (from May to July) (Figure 6, Figure 10).

The 5th group consists of rivers located in different regions of Poland, as the Silesian rivers Brynica and Biała Przemsza, the lower Nysa Kłodzka, the upper Warta with the Oleśnica River, the Barycz, Pilica, Łasica and Rawka rivers, the upper Noteć with the Gąsawka river, and the Wierzyca, Wda and Brda rivers in the lower Vistula (Wisła) basin. Generally, changes of flow observed in these rivers are varied. Between

1951 and 1985 the flow is higher, while between 1986 and 2010 lower than the average calculated for the whole multi-year period 1951–2010. The most significant changes usually take place at the beginning of the hydrological year (that is in November and December). In 1961–1980 these rivers showed an increase, while in 1983–2002 a decrease of flow in that months. Moreover, in 1961–1980 higher flow was observed between mid-April and early July, and in some rivers also at the end of hydrological year (in October) (Figure 6, Figure 11).

DISCUSSION AND CONCLUSION

In this study changes in the flow regime characteristics of rivers in Poland were analyzed using an improved method, originally proposed by Wrzesiński in his earlier papers. This new approach not only allows identification of the exact date of these changes, but also makes possible analysis of their tendencies. Since a relatively large data set was used in the research, rivers characterized by the greatest changes in their flow conditions (as rivers of the 1st group and – to a lesser extent – 5th group of the third variant – Figure 6, Figure 7) in the examined multi-year period 1951–2010 were detected. Those changes are related to human activity and occur in rivers flowing through industrialized and urbanized areas, as well as in rivers with strong regulatory interference into their flow conditions. It can be concluded that the stability of flow regime of the Polish rivers is varied spatially and temporarily. Since human impact destabilizes flow conditions and their characteristics, thus the observed changes are more distinct and can be easily identified. Human activity, due to its different nature, leads to multidimensional and also spatially and temporally diversified changes of flow regime. Consequently, in the case of rivers with the disturbed flow conditions it seems to be justified to adopt as the calibration period flow characteristics from the period before the human interference rather than the average conditions from the multi-year period. For comparison, Merz et al. (2016) in their study on the temporal clustering of floods in Germany besides as long as possible time series adopted criteria of a large number of gauges for a common time period and medium and large-scale catchments to reduce the impact of human interventions on the results. In the case of the remaining groups of the investigated rivers the obtained in the third variant regional distribution is more uniform (Figure 5, Figure 6 and Figures 8–11). This may suggest greater importance of climatic conditions in modification of the flow regime characteristics, with spatial differences resulting from the regional differences of flow and the environmental characteristics (conditions) of river basins. Our findings are consistent with results of studies by Bezak et al. (2015), who concluded that the identification of trends depends on the geographical location of the analyzed streams, the local watershed characteristics and other; their analysis led to the separation of six groups of stations, based on the catchment area, seasonality coefficient and flood timescales. Similarly, the primarily role of the local characteristics in shaping the seasonality of precipitation and discharges was also proved by Parajka et al. (2009), who detected relatively larger heterogeneity of runoff than precipitation in Slovakia and Austria. Also Gaál et al. (2012), investigated river catchments in Austria as a function of climatic controls (such a storm type) and catchment controls (such as soils, soil moisture geology, land form). On this basis these authors identified 13 hot spot areas in Austria, uniform in terms of the flood generating mechanisms, but different from other regions.

Interestingly, studies on the flood regime changes of European rivers by Hall et al. (2014) proved that in Poland in the multi-year period 1921–1990 the mean and the variance of the annual maximum floods decreased and spring floods decreased for the majority of major Polish rivers. After a long period without major floods, several flood events were reported in Poland from 1997 to 2010, which results in an increase of the number of regional floods for the period 1946–2010. However, our study shows that this is not translated into an increase of the annual, seasonal and maximum flow rates in 1951–2010. In the third grouping variant rivers with the highest floods in 1997 and 2010 were classified in the 3rd group comprising rivers with no significant changes both in the annual and multi-year periods, or in the 4th and 5th groups demonstrating even decreasing seasonal or annual flows in the years 1991–2010.

Our findings may provide supplementary information on the seasonal streamflow trends of the European rivers. For example, Stahl et al. (2010) analyzed datasets of near-natural streamflow records from small catchments across Europe and found positive trends over the winter months from most of them in the period 1962–2004. Our study showed an increase in the case of rivers of the north-eastern part of Poland, in the third variant classified in the 2nd group, and also the Odra and Warta rivers with their tributaries, which belong to the 4th group. That conclusion is supported by a distinct decline in winter flow and a delayed rise in spring meltwater flow recorded in many rivers in the 1950s and 1960s. On the contrary, in the 1970s and 1980s there were no winter base flows recorded in those rivers, normally resulting from a significant increase of winter flows, which sometimes prolong relatively lower increases of spring flows.

The observed regularities may indicate the significance of changes in the intensity of the macro-scale types of air circulation, as the North Atlantic Oscillation (NAO), which affects the hydrological cycle not only in Western Europe, but also in Poland, as it has been underlined in numerous publications (Pociask-Karteczka et al., 2002–2003; Wrzesiński, 2011, 2013a; Wrzesiński and Paluszkiewicz, 2011). Study by Dettinger and Diaz (2000) also showed that stream flow in most of the rest of Europe was higher than normal, when NAO is negative.

Moreover, the observed and projected changes of the global temperature should be considered. Labat et al. (2004) predicts that its increase by 1°C will increase the global runoff by 4%; however, the runoff trends will differ from continent to continent and no significant increasing or decreasing discharge trends is predicted for Europe. Regarding results of our study we think that in order to define the characteristics of transformations of flow regime triggered by climate change it is necessary to conduct further detailed analyses, based nor only on synchronous data, but also on those statistically uniform, which refer only to streams with the quasi-natural flow conditions.

REFERENCES

Arnell, N.W., 1999. The effect of climate change on hydrological regimes in Europe: a continental perspective. Global Environmental Change, 9, 5–23. DOI: 10.1016/S0959-3780(98)00015-6.

Bezak, N., Horvat, A., Šraj, M., 2015. Analysis of flood events in Slovenian streams. Journal of Hydrology and Hydromechanics, 63, 134–144. DOI: 10.1515/johh-2015-0014.

Bezak, N., Brilly, M., Sraj, M., 2016. Flood frequency analyses, statistical trends and seasonality analyses of discharge data: a case study of the Litija station on the Sava River. Journal of Flood Risk Management, 9, 2, 154–168. DOI: 10.1111/jfr3.12118.

Bower, D., Hannah, D.M., McGregor, G.R., 2004. Techniques for assessing the climatic sensitivity of river flow regimes. Hydrological Processes, 18, 2515–2543. DOI: 10.1002/hyp.1479.

Dettinger, M.D., Diaz, H.F., 2000. Global characteristics of stream flow seasonality and variability. J. Hydromet., 1, 289–310. DOI: 10.1175/15257541(2000)001<0289:GCOSFS>2.0.CO;2.

Dynowska, I., 1971. Types of River Regimes in Poland. Zeszyty Naukowe UJ, CCLXVIII, Prace Geogr., 28, 150 p. (In Polish.)

Dynowska, I. (Ed.), 1988. Antropogenic determinants of changes in river flow and river regimes in different regions of Poland. Dokumentacja Geograficzna, 4, 95 p. (In Polish.)

Dynowska, I. (Ed.), 1993. Transformations of water relations in Poland as a result of natural and anthropogenic processes. Kraków, 463 p. (In Polish.)

Dynowska, I., Pociask-Karteczka, J, 1999. Water circulation. In: Starkel L (Ed.). Geografia Polski. Środowisko przyrodnicze. PWN, Warszawa, pp. 343–373. (In Polish.)

Gaál, L., Szolgay, J., Kohnova, S., Parajka, J., Merz, R., Viglione, A., Bloeschl, G., 2012. Flood timescales: Understanding the interplay of climate and catchment processes through comparative hydrology. Water Resources Research, 48. DOI: 10.1029/2011WR011509.

Gottschalk, L., 1985. Hydrological regionalisation of Sweden. Hydrol. Sci. J., 30, 65–83. DOI: 10.1080/02626668509490972.

Gutry-Korycka, M., Rotnicka, J., 1998. The hydrological regime of rivers in the light of scenarios of global climatic change. Geographia Polonica, Papers on Global Change, 71, 61–78.

Gutry-Korycka, M. (Ed.), 2001. Geographical Conditions of River Regimes. WGSR UW, Warszawa, 192 p. (In Polish.)

Haines, A.T., Finlayson, B.L., McMahon, T.A., 1988. A global classification of river regimes. Applied Geography, 8, 255–272. DOI: 10.1016/0143-6228(88)90035-5.

Hall, J., Arheimer, B., Borga, M., Brázdil, R., Claps, P., Kiss, A., Kjeldsen, T.R., Kriaučiūnienė, J., Kundzewicz, Z.W., Lang, M., Llasat, M.C., Macdonald, N., McIntyre, N., Mediero, L., Merz, B., Merz, R., Molnar, P., Montanari, A., Neuhold, C., Parajka, J., Perdigão, R.A.P., Plavcová, L., Rogger, M., Salinas, J.L., Sauquet, E., Schär, C., Szolgay, J., Viglione, A., Blöschl, G., 2014. Understanding flood regime changes in Europe: a state-of-the-art assessment. Hydrology and Earth System Sciences, 18, 7, 2735–2772. DOI: 10.5194/hess-18-2735-2014.

Krasovskaia, I., 1995. Quantification of the stability of river flow regimes. Hydrological Sciences Journal, 40, 5, 587–598. DOI: 10.1080/02626669509491446.

Krasovskaia, I., 1996. Sensitivity of the stability of river flow regimes to small fluctuations in temperature. Hydrological Sciences Journal, 41, 2, 251–264.

Krasovskaia, I., Gottschalk, L., 1992. Stability of river flow regimes. Nordic Hydrology, 23, 137–154.

Krasovskaia, I., Gottschalk, L., 2002. River flow regimes in a changing climate. Hydrological Sciences Journal, 47, 4, 597–609.

Krasovskaia, I., Sælthun, N.R., 1997. Sensitivity of the stability of Scandinavian river flow regimes to a predicted temperature rise. Hydrological Sciences Journal, 42, 5, 693–711.

Krasovskaia, I., Gottschalk, L., Kundzewicz, Z.W., 1999. Dimensionality of Scandinavian river flow regimes. Hydrological Sciences Journal, 44, 5, 705–723.

Labat, D., Godderis, Y., Probst, J.L., Guyot, J.L., 2004. Evidence for global runoff increase related to climate warming. Advances in Water Resources, 27, 6, 631–642. DOI: 10.1016/S0309-1708(04)00047-8.

Lvovich, M.I., 1938. Experience from classification of the USSR's rivers. Trudy GGI, 6, Leningrad. (In Russian.)

Merz, R., Piock-Ellena, U., Blöschl, G., Gutknecht, D., 1999. Seasonality of flood processes in Austria. In: Gottschalk, L., Olivry, J.-C., Reed, D., Rosbjerg, D. (Ed.): Hydrological Extremes: Understanding, Predicting, Mitigating. IAHS Press, Wallingford, UK, pp. 273–278.

Merz, B., Nguyen, V.D., Vorogushyn, S., 2016. Temporal clustering of floods in Germany: Do flood-rich and flood-poor periods exist? Journal of Hydrology, 541, Part B, 824–838. DOI: 10.1016/j.jhydrol.2016.07.041.

Middelkoop, H., Daamen, K., Gellens, D., Grabs, W., Kwadijk, J.C.J., Lang, H., Parmet, B.W.A.H, Schädler, B., Schulla, J., Wilke, K., 2001. Impact of climate change on hydrological regimes and water resources management in the Rhine basin. Climatic Change, 49, 1–2, 105–128. DOI: 10.1023/A:1010784727448.

Parajka, J., Kohnova, S., Merz, R., Szolgay, J., Hlavcova, K., Blöschl, G., 2009. Comparative analysis of the seasonality of hydrological characteristics in Slovakia and Austria. Hydrol. Sci. J. , 54, 3, 456–473. DOI: 10.1623/hysj.54.3.456.

Parajka, J., Kohnova, S., Balint, G., Barbuc, M., Borga, M., Claps, P., Cheval, S., Dumitrescu, A., Gaume, E., Hlavcova, K., Merz, R., Pfaundler, M., Stancalie, G., Szolgay, J., Blöschl, G., 2010. Seasonal characteristics of flood regimes across the Alpine-Carpathian range. J. Hydrol., 394, 1–2, 78–89. DOI: 10.1016/j.jhydrol.2010.05.015.

Pardé, M., 1957. Rivers. Warszawa, PWN, 234 p. (In Polish.)

Pociask-Karteczka, J., Limanówka, D., Nieckarz, Z., 2002–2003. The North Atlantic Oscillation impact on hydrological regime in Polish Carpathians (1951-2000). Folia Geographica, series Geographica-Physica, 33–34, 89–104. (In Polish.)

Rotnicka, J., 1988. Taxonomic foundations of the classification of river regime (example of the Odra drainage basin and the Przymorze rivers). Seria Geografia 40, Wyd. UAM, Poznań, 130 p. (In Polish.)

Shorthouse, C., Arnell, N., 1999. The effects of climatic variability on spatial characteristics of European river flows. Physics and Chemistry of the Earth (B), 24, 1–2, 7–13. DOI: 10.1016/S1464-1909(98)00003-3.

Sobczyk, M., 2007. Statystyka. Wyd. Nauk. PWN, Warszawa, 417 p. (In Polish.)

Stahl, K., Hisdal, H., Hannaford, J., Tallaksen, L.M., van Lanen, H.A.J., Sauquet, E., Demuth, S., Fendekova, M., Jodar, J., 2010. Streamflow trends in Europe: evidence from a dataset of near-natural catchments. Hydrology and Earth System Sciences, 14, 12, 2367–2382. DOI: 10.5194/hess-14-2367-2010.

Ward, J.H., 1963. Hierarchical Grouping to optimize an objective function. Journal of American Statistical Association, 58, 301, 236–244.

Westmacott, J.R., Burn, D.H., 1997. Climate change effects on the hydrologic regime within the Churchill-Nelson River Basin. Journal of Hydrology, 202, 263–279. DOI: 10.1016/S0022-1694(97)00073-5.

Wilson, D., Hannah, D.M., McGregor, G.R., 2012. A large scale hydroclimatological perspective on western European river flow regimes. Hydrology Research, 44, 5, 809–833. DOI: 10.2166/nh.2012.201.

Woś, A., 2010. Climate of Poland in the Second Half of the 20th Century. Wyd. Naukowe UAM, Poznań, 489 p. (In Polish.)

Wrzesiński, D., 2005. Changes of the hydrological regime of rivers of Northern and Central Europe in various circulation periods of the North Atlantic Oscillation. Quaestiones Geographicae, 24, 97–109.

Wrzesiński, D., 2008. Typology of spatial patterns seasonality in European rivers flow regime. Quaestiones Geographicae, 27A/1, 87–98.

Wrzesiński, D., 2010a. Spatial differentiation of the stability of the flow regime of European rivers. Seria Studia i Prace z Geografii i Geologii 3. Bogucki Wydawnictwo Naukowe, Poznań, 220 p. (In Polish.)

Wrzesiński, D., 2010b. Detection of changes in the hydrological regime of the Warta in the Poznań profile in 1822–2005. In: Wrzesiński, D. (Ed.): Odpływ rzeczny i jego regionalne uwarunkowania. Bogucki Wydawnictwo Naukowe, Poznań, pp. 135–152. (In Polish.)

Wrzesiński, D., 2011. Regional differences in the influence of the North Atlantic Oscillation on seasonal river runoff in Poland. Quaestiones Geographicae, 30, 3, 127–136. DOI: 10.2478/v10117-011-0032-y.

Wrzesiński, D., 2013a. Entropy of river flows in Poland. Studia i Prace z Geografii i Geologii 33. Bogucki Wydawnictwo Naukowe, Poznań, 204 p. (In Polish.)

Wrzesiński, D., 2013b. Flow regime transformations of rivers in Poland. In: Borówka, R.K., Cedro, A., Kavetsky, I. (Eds.): Contemporary Problems of Geographical Research. PPH ZAPOL Dmochowski, Sobczyk Sp.j., Szczecin, pp. 59–69. (In Polish.)

Wrzesiński, D., Paluszkiewicz, R., 2011. Spatial differences in the impact of the North Atlantic Oscillation on the flow of rivers in Europe. Hydrological Research, 42, 1, 30–39. DOI: 10.2166/nh.2010.077.

Received 15 February 2017
Accepted 7 July 2017

J. Hydrol. Hydromech., 66, 2018, 1, 65–78
DOI: 10.1515/johh-2017-0039

Budgeting suspended sediment fluxes in tropical monsoonal watersheds with limited data: the Lake Tana basin

Fasikaw A. Zimale[1], Mamaru A. Moges[1], Muluken L. Alemu[1], Essayas K. Ayana[2, 3], Solomon S. Demissie[4], Seifu A. Tilahun[2], Tammo S. Steenhuis[2, 5*]

[1] Faculty of Civil and Water Resources Engineering, PhD program in Integrated Water Management, Bahir Dar Institute of Technology, Bahir Dar University, Bahir Dar, Ethiopia.
[2] Faculty of Civil and Water Resources Engineering, Bahir Dar Institute of Technology, Bahir Dar University, Bahir Dar, Ethiopia.
[3] Department of Ecology, Evolution and Environmental Biology, Columbia University, New York, NY, USA.
[4] Ethiopian Institute of Water Resources, Addis Ababa, Ethiopia.
[5] Department of Biological and Environmental Engineering, 206 Riley Robb Hall, Cornell University, Ithaca NY 14853 USA.
[*] Corresponding author. E-mail: tss1@cornell.edu

Abstract: Soil erosion decreases soil fertility of the uplands and causes siltation of lakes and reservoirs; the lakes and reservoirs in tropical monsoonal African highlands are especially affected by sedimentation. Efforts in reducing loads by designing management practices are hampered by lack of quantitative data on the relationship of erosion in the watersheds and sediment accumulation on flood plains, lakes and reservoirs. The objective of this study is to develop a prototype quantitative method for estimating sediment budget for tropical monsoon lakes with limited observational data. Four watersheds in the Lake Tana basin were selected for this study. The Parameter Efficient Distributed (PED) model that has shown to perform well in the Ethiopian highlands is used to overcome the data limitations and recreate the missing sediment fluxes. PED model parameters are calibrated using daily discharge data and the occasionally collected sediment concentration when establishing the sediment rating curves for the major rivers. The calibrated model parameters are then used to predict the sediment budget for the 1994–2009 period. Sediment retained in the lake is determined from two bathymetric surveys taken 20 years apart whereas the sediment leaving the lake is calculated based on measured discharge and observed sediment concentrations. Results show that annually on average 34 t/ha/year of sediment is removed from the gauged part of the Lake Tana watersheds. Depending on the up-scaling method from the gauged to the ungauged part, 21 to 32 t/ha/year (equivalent to 24–38 Mt/year) is transported from the upland watersheds of which 46% to 65% is retained in the flood plains and 93% to 96% is trapped on the flood plains and in the lake. Thus, only 4–7% of all sediment produced in the watersheds leaves the Lake Tana Basin.

Keywords: Erosion; Saturation excess; Hydrology; Discharge; Flood plain; Ethiopia; East Africa; Horn of Africa.

INTRODUCTION

Soil erosion is a serious global environmental problem (Lieskovský and Kenderessy, 2014). The consequences of land degradation and the associated nutrient depletion of soil resources have profound economic implications for low-income countries (Erkossa et al., 2015; Yitbarek et al., 2012). In addition, the increased sediment load is reducing the storage of the reservoirs faster. Moreover, increased turbidity due to sediment reduces light penetration and threatens the aquatic ecosystem; in the case of Lake Tana, the livelihood of over 500,000 people are directly or indirectly dependent on the lake and wetlands (Vijverberg et al., 2009).

Soil erosion by water is a particularly critical problem in the high-rainfall Ethiopian highlands. Although in the semi-arid northern Ethiopian highlands, sediment dynamics and gully formation have been well documented (Aerts et al., 2006; Descheemaeker et al., 2006; Frankl et al., 2011; Frankl et al., 2013; Gebrermichael et al., 2005; Gebreegziabher et al., 2009; Girmay et al., 2009; Haregeweyn et al., 2013), in the humid highlands, sediment dynamics have been less well studied. The main information available consists of data gathered in the Soil Conservation Research Program (SCRP) watersheds. For these relatively small watersheds, Guzman et al. (2013) reported soil loss rates of 5.2 t/ha/yr in the 4.8 km^2 Andit Tid watershed, 24.7 t/ha/yr in the 1.1 km^2 Anjeni watershed, and 7.4 t/ha/yr in the 1.1 km^2 Maybar watershed. Greater soil loss ranges are reported on test plots with 32 to 36 t/ha/yr for the Maybar watershed, 87 to 212 t/ha/yr for the Andit Tid watershed, and 131 to 170 t/ha/yr for Anjeni watershed (Haile et al., 2006a). Sediment loss as high as 540 t/ha/yr has been reported in a small watershed mainly due to gully erosion (Tebebu et al., 2010). Sediment data from the sampling station on the Blue Nile at the border with Sudan indicated that current losses in the 180,000 km^2 basin are in the order of 7 t/ha/yr (Yasir et al., 2014). Thus, most of the sediment that erodes from the land is deposited on its way to Sudan.

Watershed management requires accurate discharge and sediment predictions. SWAT is often employed to simulate the discharge in the Ethiopian highlands (Betrie et al., 2011; Easton et al., 2010; Setegn et al., 2008, 2009, 2010a, 2010b, 2011; Yasir et al., 2014). Easton et al. (2010) and White et al. (2011) modified SWAT to include saturation excess runoff, which is the major runoff mechanism in the highlands. However, one of the major problems in applying SWAT in any form is the scarcity of data input for validation. For that reason, water balance approaches that are based on available data have been utilized with some success (Conway, 2000; Kebede et al., 2006; Mishra and Singh, 2004; Rientjes et al., 2011; Steenhuis et al., 2009; Tilahun et al., 2015).

Early erosion predictions (Haile et al., 2006b; Haregeweyn and Yohannes, 2003; Tamene et al., 2006) in Ethiopia were either based on the sediment rating curve or the Universal Soil Loss Equation (USLE). More recently, sediment flows have

been simulated in the Blue Nile basin employing various models: SWAT, in which sediment predictions are based on Modified Universal Soil Loss Equation (MUSLE) (Betrie et al., 2011; Easton et al., 2010; Setegn et al., 2010b; Yasir et al., 2014), the modified SWAT-WB Water Balance model (Easton et al., 2010), Parameter efficient model (PED), that is based on the Hairsine and Rose model (Hairsine and Rose, 1992; Steenhuis et al., 2009), WATEM/SEDEM (Haregeweyn et al., 2013), and the Water Erosion Prediction Project (WEPP) model (Zeleke, 2000).

The studies of Easton et al. (2010) and Setegn et al. (2010b) simulated sediment loads at the gauging stations near Lake Tana. Setegn et al. (2010b) showed that sediment loads of 30 to 60 t/ha/yr are exported from the Lake Tana watersheds whereas Easton et al. (2010) predicted that a maximum of 84 t/ha/yr can be exported from the Gumara watershed. Recently, Erkossa et al. (2015) estimated unrealistically low sediment yield of less than 5 t/ha/yr.

Kaba et al. (2014) determined the sediment contribution from the Gumara watershed for a 10-year period using MODIS satellite Imagery. These lake concentrations were an order of magnitude less than the concentrations measured in the rivers at the stream gauges. Some studies estimated sediment inflow to the lake by assuming average sediment load (SMEC 2008) and using empirical equations (Lieskovský and Kenderessy, 2014). The only estimate on sediment accumulated in the lake using measurement is by Ayana et al. (2015) who analyzed two Lake Tana bathymetric surveys (1987 and 2006) and found that 200 Mm^3 of sediment had settled at the bottom of the lake during this 20-year period.

The above studies and other studies in developing countries have been severely hampered by the lack of reliable long-term records of sediment concentrations (Walling, 2008). For example, simulated sediment loads for the Gumara by Easton et al. (2010) were calibrated with two data points, while Setegn et al. (2010b) used the sediment rating curve by the Ministry of Water Resources and Energy. These rating curves severely under predicted the loads (Moges et al., 2016). According to Walling (2008), to improve sediment load predictions, greater effort should be focused on assembling available datasets. As Walling notes, this either involves seeking out new sources of data or collating and processing the basic data to provide estimates of sediment flux. In addition, standard data analyzing procedures employed in the data rich developed countries cannot be directly used and adopted in developing countries such as Ethiopia where data are limited and quality is affected by politically unstable conditions.

Due to the limitations of existing procedures in estimating sediment budgets in developing countries, this study is concerned with developing a method for recreating realistic suspended sediment fluxes. The objective of this study is, therefore, to develop procedures to reconstruct the long-term suspended sediment concentrations for quantifying sediment budgets when observational data are limited. The study is carried out in the Lake Tana basin where occasional suspended sediment data are available that were collected for generating sediment rating curves for the four major rivers.

MATERIAL AND METHODS

Study area: the Lake Tana basin

The 3000 km^2 Lake Tana is located in the headwaters of the Blue Nile at an elevation of 1,785 m. It is the largest lake in Ethiopia with a drainage area of approximately 15,000 km^2. It is the home to a unique fish population of which 20 fish species are endemic (Vijverberg et al., 2009).

In the 1920s, the lake was described as beautiful, pristine with a sandy bottom near the inlets of the major rivers (Cheesman, 1936). While river sediment loads have been decreasing generally worldwide (Wang et al., 2015), sediment concentrations in the Blue Nile and Lake Tana are still increasing (Abate et al., 2015). Currently, the lake water is polluted with sediment and nutrients. The sandy bottoms near the inlets have been replaced by muddy bottoms and deltas which, in the case of the Gilgel Abay River, is 10 km long.

The lake is fed by four major partly gauged rivers: Gilgel Abay in the south, Megech in the north, and Gumara and Rib in the east (Fig. 1). The Blue Nile exits the lake at the south end where the Chara Chara Weir was constructed in 1995 to regulate the water flow for hydropower generation. The major rivers have special morphological characteristics. For example, the Rib riverbed rose more than 1.5 m from 1990 to 2002 (SMEC, 2008) at the gauging station. Thus, the flow carrying capacity of the river is reduced. The river overflows its banks regularly during monsoon rain phase and discharge measurements are not conducted when the riverbank floods. Recent LANDSAT 8 images showed a change in flow path at the eastern flank of the lake. In the dry monsoon phase, the riverbed is dug out for sand mining. The holes created fill up with sediment during the rain phase.

Analysis of a 90-m resolution digital elevation model (DEM) shows the slope in the Lake Tana Basin ranges from 0 to 55 degrees (Table 1). Altitude of the basin varies from 1785 m to 4094 m with a mean elevation of 2418 m (Table 1). Most of the basin consists of cropland on the moderate sloping hillsides and grass in the valley bottoms (Table 1). Soils vary

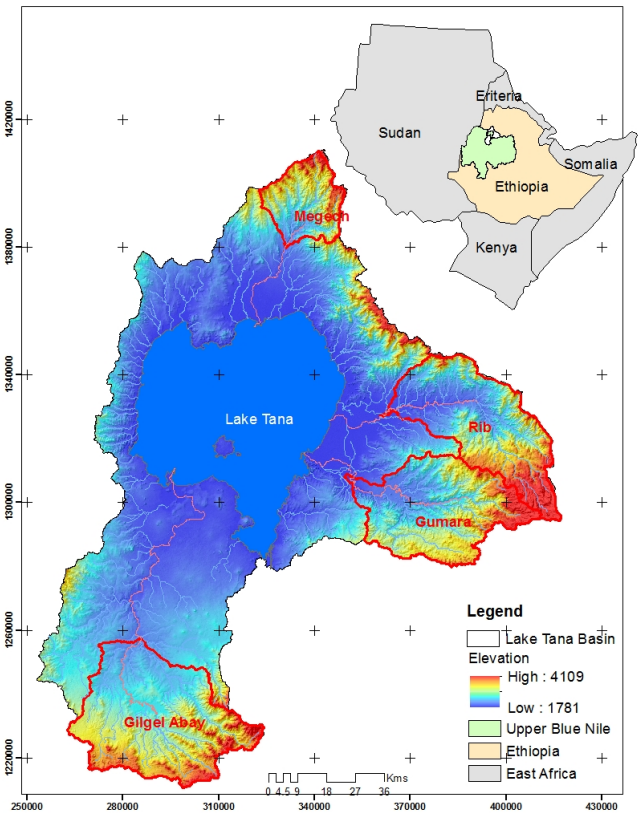

Fig. 1. The Lake Tana basin with the four major watersheds: Gilgel Abay, Gumara, Rib and Megech.

Table 1. Physiographic characteristics of the four gauged basins in percent of area: Gilgel (GA), Gumara (Gum), Rib and Megech (Meg) and ungauged parts of Lake Tana watersheds.

Slope (%)	Gauged				Whole watershed Ungauged	Ungauged parts of each watershed			
	GA	Gum	Rib	Meg		GA	Gum	Rib	Meg
0–2	22	7	7	1	29	33.4	50.1	35.4	40.7
2–8	50	25	30	17	42	51.5	28.8	21.0	46.6
8–16	19	31	25	26	15	10.6	13.5	16.8	9.8
16–30	9	28	22	32	8	3.6	6.2	15.4	2.3
>30	1	9	16	25	5	0.9	1.4	11.5	0.6
Land use (%)									
Cultivated	74	64	64	95	60	69.2	63.5	63.4	99.1
Partly Cultivated	26	32	26	3	30	20.4	32.7	6.0	0.9
Forest	0	0	0	0	0.2	0.0	0.0	0.0	0.0
Grassland	0	4	9	0.5	3.5	0.1	0.0	21.2	0.0
Water	0	0	0	0	0.2	0.0	0.0	0.0	0.0
Swamp	0	0	0	0	0.3	0.0	2.6	0.0	0.0
Plantation	0	0	0.1	0	0.1	0.0	1.1	0.3	0.0
Shrub land	0	0	0	0	6	10.3	0.0	9.0	0.0
Urban	<1	<1	<1	1.2	<1	0.1	0.0	0.1	0.0
Woodland	0	0	0	0	<1	0.0	0.0	0.0	0.0
Afro Alpine	0	0.4	0	0	0	0.0	0.0	0.0	0.0
Soil (%)									
Haplic Alisols	41	0	0	0	1	3.1	0.0	0.0	0.0
Haplic Luvisols	56	63	0	0	19	40.9	15.7	0.0	0.0
Haplic Nitosols	<1	0	0	9	2	3.7	0.0	1.3	0.0
Eutric Regosols	<1	0	0	0	<1	0.9	0.0	0.0	0.0
Euric Vertisols	2	3	0	4	23	14.1	23.1	9.5	74.2
Euric Fluvisols	0	<1	24	0	16	1.8	41.9	42.0	2.7
Eutric Leptosols	0	9	36	82	18	0.1	3.5	46.9	4.1
Chromic Luvisols	0	24	40	5	21	22.6	15.6	0.3	19.1
Urban	0	<1	<1	<1	<1	0.0	0.0	0.0	0.0
Lithic Leptosols	0	0	0	0	0	12.9	0.0	0.0	0.0

from Haplic Luvisols and Alisols in the Gilgel Abay, Luvisols in the Gumara, and Eutric Leptosols and Chromic Luvisols in the Rib and Megech (Table 1).

The climate in the Lake Tana basin is affected by the movement of the inter-tropical convergence zone which results in a single rainy season between June and September and a dry period the rest of the year. The average dry season (November–April) rainfall is 117 mm and potential evaporation is 710 mm. The wet season (May–October) rainfall is 1400 mm and potential evaporation is 645 mm for data used in the calibration and validation periods. More than 90% of the annual rainfall occurs in the wet monsoon phase. The mean annual temperature in the basin is 23°C in the relatively lower lying areas such as Bahir Dar and ranges between 15–20°C in the middle and high altitudes.

Model input and validation data

Meteorological data

Rainfall and temperature data were obtained from the Ethiopian National Meteorological Agency (ENMA) and were checked for erroneous input data. Missing and erroneous data were estimated using mean values of same dates in all years with data. Thiessen polygon method was applied on data obtained from the surrounding meteorological stations to determine the areal rainfall data for each watershed. The potential evapotranspiration was calculated from minimum and maximum air temperatures and other climate variables using the FAO Penman method with data from the Bahir Dar, Gonder and Dangila weather stations (Allen et al., 1998).

Discharge

Daily stream discharge of the Gilgel Abay, Gumara, Rib, and Megech rivers were obtained from the Ministry of Water, Irrigation and Electricity of Ethiopia (MoWIE). Discharge was measured by recording the stage, cross-section of the channel and flow velocity at the gauging stations. Flow records from 1994 to 2009 were used for calibration and validation. Missing flow data were replaced with the mean of the available discharge data for the specific day. One of the limitations of the MoWIE discharge data is that the stage discharge curves are infrequently updated (Abate et al., 2015) and as we will discuss later, this introduces errors which will become obvious when we compare model outputs with observed values of the Rib River discharge.

Suspended sediment concentrations

Suspended sediment concentrations were determined by the Ministry of Water, Irrigation and Electricity (MWIE) at the gauging stations at times when stage discharge relationships were developed by collecting water samples with plastic bottles of known volume. Elevated sediment concentrations were observed during the rainy phase in June, July, and August. Daily sediment concentrations were determined dividing the daily sediment load by the discharge measured during the same day. MWIE sediment load data were available between 1964 and 2009. The distribution of the suspended sediment measurements is uneven; some months are without any data, mainly during the dry monsoon phase when sediment concentrations

are low. The Gumara and the Rib Rivers were monitored most intensively with just over 60 data pairs of sediment load and discharge. Sediment concentration of all rivers, apart from the Gilgel Abay, peaks before the discharge. This general trend of sediment concentrations is similar to the small experimental watersheds – Andit Tid, Maybar and Anjeni (Guzman et al., 2013). According to Guzman et al. (2013) and Zegeye et al. (2010), the greatest concentrations occur at the time when the rills are formed in the newly plowed agricultural lands. From August to October when Lake Tana is filled up, most sediment is lost at the outlet. The data on sediment concentration were insufficient to have separate calibration and validation periods.

Model selection

Since the sediment concentration measurements are limited, simulation of sediment contribution from the watersheds requires understanding the local hydrology and the underlying hydrological processes (Steenhuis et al., 2009). The models discussed before (such as SWAT, WEPP etc.) were developed for temperate climates. In the temperate cold winter, the solar radiation and potential evaporation are minimum. Rainfall is distributed evenly throughout the year; it rains more than the potential evaporation during the dormant winter period (Lyon et al., 2005). Most of the runoff occurs during spring. In monsoon climates, the solar radiation and potential evaporation are approximately constant year-round. Rainfall is concentrated in three-to-four month periods and exceeds the potential evaporation (Liu et al., 2008). Soils stay dry until the beginning of the growing season and gradually become wetter; surface runoff and interflow increase as the rain progresses. During the rainy phase in the (sub) humid areas, there is more rainfall than can be evaporated or stored in the soil.

The PED model is a conceptual rainfall runoff and sediment loss model with minimum calibration parameters based on the saturation excess runoff process. It has been applied to catchments ranging from a few square kilometers (e.g. Anjeni (1.1 km^2, Tilahun et al, 2013a), Andit Tid (4.8 km^2, Engda, 2011), Enkulal (4 km^2, Tilahun et al., 2013a) and Debre Mawi (0.95km^2, Tilahun et al., 2013b; Tilahun et al., 2015)) to hundreds of thousands of square kilometers (e.g. Blue Nile, 180,000 km^2) and showed good performance (Steenhuis et al., 2009; Tilahun et al., 2013a; Tilahun et al., 2015). Comparing the predictions with other models used in the humid Blue Nile basin, PED performs as well or better. Hence, the PED model is applied in this study to avoid over parameterization and ensure process interpretability.

Description of the PED model

The PED model represents the local hydrological and erosion processes. It classifies the watershed into two runoff producing areas (periodically saturated areas and degraded hill slopes) and one recharge area (permeable hill slopes) that release the excess precipitation, the base flow and interflow. The two runoff producing areas are assumed to be sources of sediment while the base flow may pick up sediment at low concentrations from the banks. The hydrology model inputs are limited to precipitation, potential evapotranspiration, and nine landscape parameters. The sediment model uses the discharges predicted by the hydrology model and maximum six parameters for the erodibility of the soil at the beginning and end of the rainy phase for each of the three areas.

PED's hydrology module

The hydrology module is a water balance model that divides the watershed into periodically saturated areas, degraded hill slopes and permeable hill slopes. The discharge Q at the outlet is written as

$$Q = A_1 Q_1 + A_2 Q_2 + A_3 \left(Q_B + Q_I \right) \tag{1}$$

where Q_1 and Q_2 are saturation excess runoff from saturated and degraded areas (mm d^{-1}), Q_B and Q_I are base flow and interflow (mm d^{-1}), A_1, A_2 and A_3 are area fractions of the saturated, degraded areas and the recharge hillside area, respectively. Area fraction A_1 are the periodically saturated areas that consist of the relatively flatter parts of the landscape, usually in the valley bottoms. After the areas become saturated during the rain phase, they generate surface runoff. Area fraction A_2 represents the degraded areas that have a thin layer of soil over a sublayer with restrictive water movement that needs minimum rainfall to fill up to saturation and generate runoff. These areas are located at different places in the landscape. Area A_3 is the recharge areas located on the hillslope that are of sufficient depth and transmissivity to transport excess rainwater via interflow or base flow to the valley bottoms

Surface runoff is simulated as any rainfall in excess of soil saturation

$$Q_{I,2} = \frac{S_{t-\Delta t} - S_{max} + \left(P - PET \right) \Delta t}{\Delta t} \tag{2}$$

where P is precipitation (mm d^{-1}), PET is potential evapotranspiration (mm d^{-1}), $S_{t-\Delta t}$ is previous time step storage (mm), Δt is the time step (d), and S_{max} is the maximum water storage capacity in the rootzone.

The storage, S_t, in each of the three regions is calculated with the Thornthwaite-Mather procedure (Steenhuis and Van der Molen, 1986; Thornthwaite and Mather, 1955)

$$S_t = S_{t-\Delta t} + \left(P - PET \right) \Delta t \quad \text{when } P \geq PET \tag{3}$$

$$S_t = S_{t-\Delta t} \left[\exp\left(\frac{\left(P - PET \right) \Delta t}{S_{max}} \right) \right] \quad \text{when } P < PET \tag{4}$$

Base flow, Q_B, is calculated as a first order reservoir and interflow, Q_I, as a zero-order reservoir (Steenhuis et al., 2009). The groundwater storage and the recharge to the interflow compartment calculations depend on whether the groundwater storage has reached its maximum value of BS_{max}. Recharge to the interflow compartment only occurs when the base flow reservoir is full. The storage in the base flow aquifer is calculated when the groundwater storage is less than the maximum (i.e., $BS_t < BS_{max}$):

$$S_t = BS_{t-\Delta t} + \left(P_{erc} - Q_B \right) \Delta t \ . \tag{5a}$$

$$P_{erc,I} = 0 \tag{5b}$$

where P_{erc} is the total groundwater recharge from the root zone (mm d^{-1}) and $P_{erc,I}$ is the recharge to the interflow compartment (mm d^{-1}). When the groundwater exceeds the maximum storage (i.e., $BS_{t-\Delta t} + \left(P_{erc} - Q_B \right) \Delta t > BS_{max}$):

$$BS_t = BS_{max} \tag{5c}$$

$$P_{erc,I} = BS_{t-\Delta t} + \left(P_{erc} - Q_B\right)\Delta t - BS_{max} \tag{5d}$$

The base flow, Q_B, and interflow, Q_I, are then obtained as:

$$Q_B = BS_t \frac{\left[1 - \exp\left(-\alpha \Delta t\right)\right]}{\Delta t} \quad \text{when } BS_t > BS_{\max} \tag{6}$$

$$Q_I = \sum_{\tau=1}^{\tau^*} (2{*}\mathrm{P}_{\mathrm{erc,I}}\left(\tau^* - \tau\right)\left(\frac{1}{\tau^*} - \frac{\tau}{\tau^{*2}}\right), \ \tau \le \tau^* \tag{7}$$

where $\alpha = 0.69/t_{½}$ and where $t_{½}$ is time taken in days to reduce volume of the base flow reservoir by half under no recharge conditions; τ is the day after the rainstorm and $P_{erc,I}$ is the amount of the percolate that reached the interflow storage and is calculated as the recharge in excess of what can be stored in the base flow reservoir, and τ^* is the duration of interflow after any rainstorm.

PED's Sediment module

In the sediment model, the two runoff source areas are considered the main sources of sediment. Unlike in the Tilahun et al. (2013a) model application, in our model formulation the subsurface flow contains some sediment in the rainy phase (Fox and Wilson, 2010; Fox et al., 2007; Tebebu et al., 2010).

The concentration of sediment, C (g/l), in the river is obtained by dividing the sediment yield by the total watershed predicted discharge from the hydrological model.

$$C = \frac{A_1 Q_1^{1.4}\left[a_{s,1} + H\left(a_{t,1} - a_{s,1}\right)\right] + A_2 Q_2^{1.4}\left[a_{s,2} + H(a_{t,2} - a_{s,2})\right] + a_{t,3} Q_3^{1.4}}{A_1 Q_1 + A_2 Q_2 + A_3 Q_3} \tag{8}$$

where the subscript numbers refer to the three areas introduced with Eq. 1, Q is the runoff (mm/day) calculated with the hydrology model, i.e., Q_1, Q_2 are calculated with Eq. 2, and Q_3 is the sum of Q_B in Eq. 6 and Q_I in Eq. 7. H is the fraction of the contributing runoff area with active rill formation (Fig. 2) that occurs after plowing and is determined by field observations and is a constant relating the flux to the sediment concentration for each of the three areas with the subscript t for transport limited and subscript s for source limited. Note that unlike in Tilahun et al. (2013a), the base flow is not free of sediment in the large river system, especially in the beginning of the rainy phase when the sediment is dry and easily picked up.

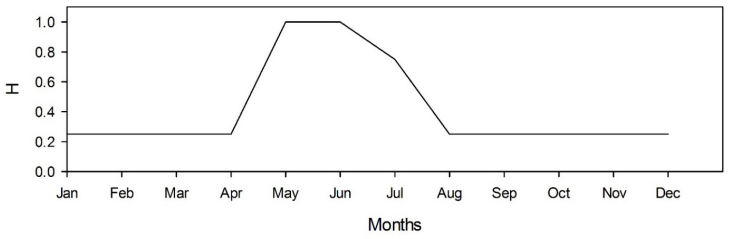

Fig. 2. Fraction of transport capacity, H, available for moving sediment. During plowing in May and the beginning of June sediment concentrations are at the transport capacity limit (H = 1) after which H is decreasing when less sediment is available for pickup.

Measured sediment concentration is required to calibrate parameters, a_t, the sediment transport limiting factor, and a_s, sediment source limiting factor, which are functions of the slope, Manning's roughness coefficient, slope length, effective deposition and vegetation cover (Yu et al., 1997). The observed data were obtained from MoWIE which measured both the concentration and the discharge as part of obtaining a rating curve. When, in the calibration period the predicted discharge did not match the observed discharge, we used the previous day's rainfall for the day of observation because of a time lag of runoff reaching the gauge.

Sediment budget

The flood plains found near the lake (Fig.1) act as flood storage (Dessie et al., 2014). During storage, sediment settles on the land and the flood plains are the sinks for sediment. SMEC (2008) found that an area of 350–450 km^2 is inundated around Lake Tana during floods. This inundated flood plain area is approximately 6% of the ungauged part (or 4% of the whole watershed).

For the purpose of the sediment budget, the flood plain includes the deltas that have been formed at the mouth of the river in the lake. Assuming, as discussed above, that the flood plain and the lake are sediment sinks and the remaining parts of the watershed are sediment sources, the sediment budget for the flood plain can then be written as:

$$S_{flplane} = M_{gauged} + M_{ungauged} - S_{lake} - M_{blNile} \tag{9}$$

where $S_{flplane}$ is the amount of sediment stored in the flood plain, M_{gauged} is the annual sediment loss from the gauged part of the basin, $M_{ungauged}$ is the sediment loss from the ungauged part of the basin, S_{lake} is the annual amount of sediment stored in the lake, and M_{blNile} is the sediment lost annually at the outlet of the lake in the Blue Nile (all in Mt/year). Consequently, the difference between the incoming sediment from the watershed and that leaving the lake is deposited in the lake and in the flood plains.

Model calibration, validation, and setup

All the model parameters were calibrated on a daily basis from 1994–1999 and validated for 2000–2009. The parameters are first determined by maximizing the efficiency criterion of the Nash–Sutcliffe efficiency coefficient (NSE), then the coefficient of determination (R^2), and finally minimizing the Root Mean Square Error (RMSE) and percent bias (Pbias). For calibration of parameters of the hydrology model, we started by giving initial values of three physical area model parameters A_1, A_2 and A_3 and the maximum storage process parameters, S_{max}, of the three areas and sub-surface parameters (BS_{max}, $\tau*$ and $t_{1/2}$). The initial values were based on the previous model runs of Steenhuis et al. (2009) and Tilahun et al. (2013a). These initial values were changed systematically until the best goodness-of-fit was achieved between simulated and observed flows. Previous sensitivity analysis has shown that the relative areas, aquifer half-life, and the duration of the interflow after a rainstorm are the most sensitive parameters

(Tilahun et al., 2013). The maximum storage, S_{max}, especially can be changed over a wide range before it affects the outflow predictions.

Daily sediment concentrations were computed by calculating daily sediment load first and then dividing the daily load by the total daily discharge. In the sediment model, there are two calibration parameters a_t and a_s for each of the two surface runoff source areas, A_1 and A_2, and for the interflow and base flow, A_3, that represents the sediment that is being picked up in the river channel during low flows. The model is calibrated in the period of 1994–2009. These constants are tweaked to yield a best fit between measured and simulated daily sediment concentrations.

RESULTS AND DISCUSSION

Hydrology

Evaluation of the hydrology module

The model parameters listed in Table 2 show a reasonable agreement (Table 3) for all four basins except for the portion of the hillside, A_3, in which the water infiltrates and supplies interflow and base flow. The area is smaller for Megech and Rib than for Gilgel Abay and Gumara.

Gilgel Abay: Using a runoff contributing area of 15% (5% saturated and 10% degraded), an aquifer half-life of 45 days and a 40-day interflow period (Table 2), the predicted and observed daily discharge for the Gilgel Abay shows good agreement for the calibration period from 1994–1999 (hydrograph in Fig. 3A and scatter plot 3C, NSE = 0.77, Table 3). The fluctuations during the high-flow periods in some of the years were not captured due in part to non-representative rainfall amounts and the sparse rain gauge network (Dessie et al., 2014), and the anomaly in the collected data in the fall of 1996. During the validation period (2000–2009), the rising and falling limbs, and most of the peaks, were reasonably estimated (Fig. 3B; NSE = 0.71, Table 3). The Pbias values of 2.62 (Table 3) for calibration also indicated that the model performed well (Pbias value for flow ±25 is acceptable, Moriasi et al., 2007) but slightly underestimated the flow initially during the calibration period and then minimally overestimated later at the end of the calibration period. The base flow after 2006, that increased unexpectedly compared to the previous years, was underestimated suggesting a change in channel configuration that was not reflected in the rating curve, as discussed later.

Table 2. PED parameter values for the hydrology simulations for four major rivers in the Lake Tana Basin.

Parameters	Units	G_Abay	Gumara	Rib	Megech
Area A_1	%	0.05	0.05	0.05	0.05
S_{max} in A_1	mm	65	90	100	100
Area A_2	%	0.1	0.12	0.1	0.1
S_{max} in A_2	mm	35	40	30	30
Area A_3	%	0.85	0.83	0.45	0.5
S_{max} in A_3	mm	125	100	135	250
BS_{max}	mm	70	75	75	80
$t_{1/2}$	Days	45	50	20	30
τ*	Days	40	40	25	20

A_1, A_2 and A_3 are area fractions of the saturated, degraded and recharge hillside areas respectively. S_{max} is the maximum water storage capacity; BS_{max} is maximum base flow storage of linear reservoir; $t_{½}$ is time taken in days to reduce volume of the base flow reservoir by half under no recharge conditions; τ^* is the duration of the period after a single rainstorm (until interflow ceases).

Table 3. PED model efficiency criteria for calibration and validation of discharge for the four major rivers in the Tana Basin. Units are mm d^{-1} for the daily values and mm $month^{-1}$ for monthly values.

			Calibration		Validation	
Watersheds	Description		Daily	Monthly	Daily	Monthly
Gilgel Abay	Mean	Predicted	2.9	87.1	3.0	92.0
		Observed	2.8	89.5	2.8	84.9
		R^2	0.77	0.91	0.75	0.94
		NSE	0.77	0.91	0.71	0.87
		RMSE	1.85	32.01	1.91	35.01
		RVE	–0.01	0.03	–0.09	–0.09
		Pbias	2.62	–8.42	2.61	–8.42
Gumara	Mean	Predicted	2.45	74..73	2.22	66.82
		Observed	2.58	78.61	2.55	77.49
		R^2	0.72	0.87	0.78	0.92
		NSE	0.70	0.86	0.77	0.90
		RMSE	2.12	40.33	1.99	36.27
		RVE	0.04	0.05	0.14	0.14
		Pbias	4.93	13.77	4.93	6.49
Rib	Mean	Predicted	1.05	31.83	1.00	30.52
		Observed	1.06	32.77	1.04	31.75
		R^2	0.72	0.91	0.64	0.84
		NSE	0.71	0.90	0.55	0.81
		RMSE	1.02	15.75	1.12	19.84
		RVE	0.01	0.03	–0.03	–0.03
		Pbias	2.88	2.88	3.89	1.53
Megech	Mean	Predicted	12	34.5	13.2	30.2
		Observed	11.5	36	10.1	39.8
	Decadal	R^2	0.85	0.91	0.79	0.84
		NSE	0.71	0.76	0.31	0.66
		RMSE	11.4	24	13.1	34.1
		RVE	0.04	–0.04	0.24	–0.32
		Pbias	–4.4	–4.4	–31.3	–31.8

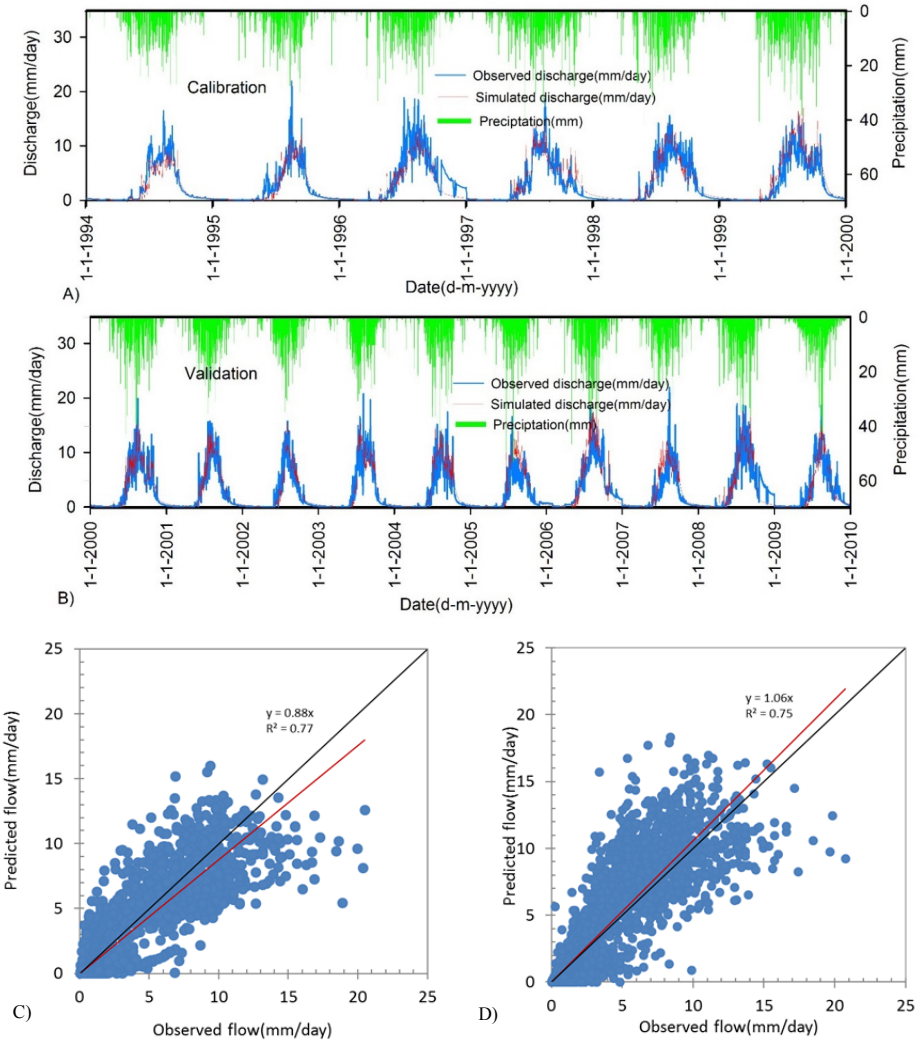

Fig. 3. Simulated and observed stream flows in mm/d for Gilgel Abay River A) Calibration (1994–1999), B) Validation(2000–2009), C) Scatter plot of simulated vs observed for calibration, D) Scatter plot of simulated vs observed validation.

Gumara: With nearly the same parameter set as for the Gilgel Abay model (Table 2), the model generally predicted discharge well. The NSE values for daily flows were 0.70 for calibration and 0.77 for the validation period (Fig. 4, Table 3). A smaller number of missing precipitation data during validation likely was related to better model performance.

Rib: Although the surface runoff parameters for areas A_1 and A_2 used in the model for the Rib are similar to both the Gumara and the Gilgel Abay, the subsurface parameters are much different (Table 2). The area contributing to the stream flow, the half-life and duration of the interflow period are all significantly less than for the Gumara and Gilgel Abay (Table 2). The daily flows were predicted reasonably well for the calibration period with NSE values for daily discharges of 0.71 (Table 3). The daily NSE decreased to 0.55 in the calibration period (Table 3). Especially in the validation period, the peak values were over predicted because the observed discharges were limited to bank full discharges equivalent to 6 mm/day as is discussed below. During the period of September to January in both 1996 and 1997, base flow was elevated similar to what was observed in the Gilgel Abay (Fig. 5A).

Megech: The Megech River has a reservoir upstream and flow is attenuated. Therefore, the flow is summarized in 10 days to avoid the effect of the reservoir. The R^2 is 0.85 and 0.79 and NSE is 0.71 and 0.31 for calibration and validation, respectively, on a 10-day basis (Table 3, Fig. 6). The latter is caused by an unexpected and unlikely reduction in observed discharge starting in 2006. A possible reason may be withdrawal of water for irrigation purposes upstream of the gauging station beginning in 2006.

Discussion of discharge predictions

It is remarkable that the surface flow parameters for all four watersheds are nearly the same especially if we take the relative insensitivity of the S_{max} value in determining the simulated discharge into account. These values are also similar compared with other watersheds where we used PED (Tilahun et al., 2013b). Moreover, it is curious that starting with the same year (2006), the observed discharge values were less for the predicted base flow of the Gilgel Abay and all of the discharge of the Megech (Figs. 3 and 5). The excessive amounts of rainfall during that year affecting the riverbed without recalibration of the rating curve is likely the explanation for the apparent change in reported discharges (SMEC, 2008).

The fractional areas for Gilgel Abay and Gumara add up to 1 but Rib and Megech are only 0.6 and 0.65 (Table 2). A fractural area proportion of 1 means that the calculated inter flow, base flow and storm flow are equal to the long-term discharge measured at the outlet. In other words, since the long-term average of the discharge in the PED model equals the average of net

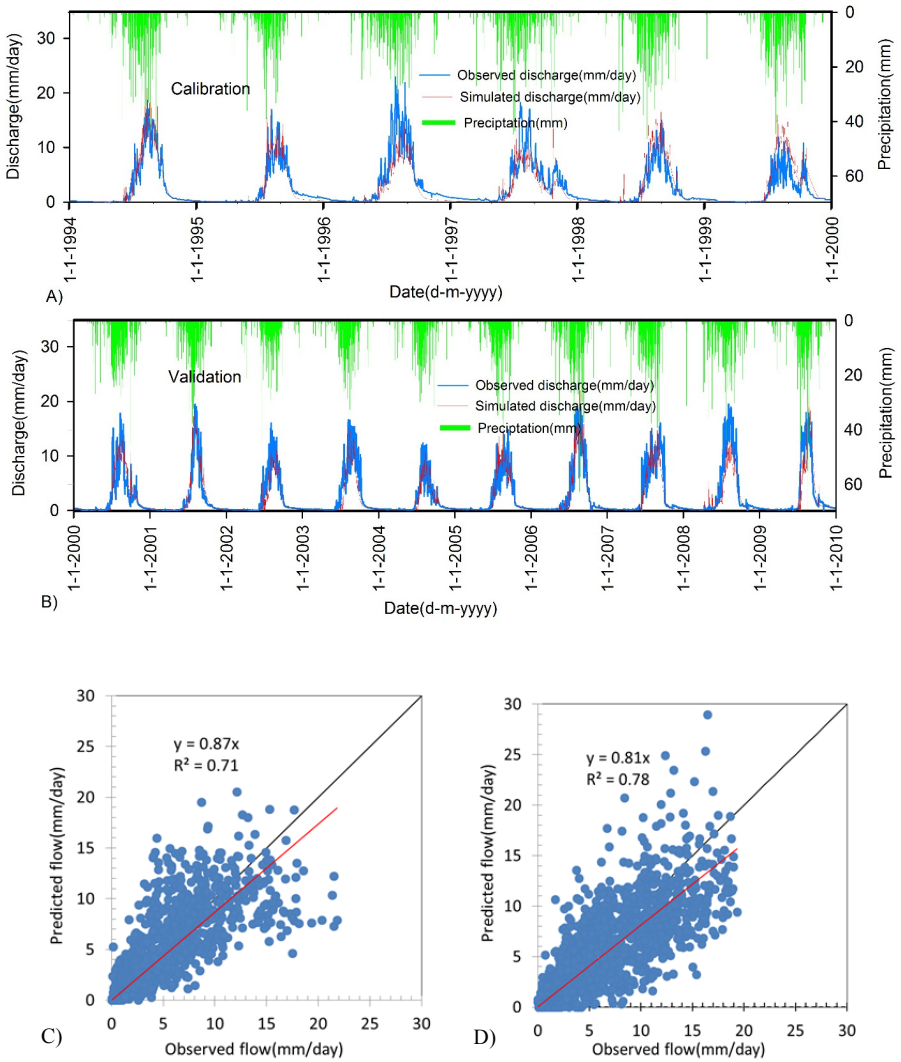

Fig. 4. Simulated and observed stream flows in mm/d for Gumara River A) Calibration (1994-1999), B) Validation(2000–2009), C) Scatter plot of simulated vs observed for calibration, D) Scatter plot of simulated vs observed validation.

precipitation (i.e., rainfall minus evaporation), all precipitation reaches the outlet eventually. However, the total contributing areas of 0.6 for Rib and 0.65 for Megech means that the net input precipitation is much more than the discharge at the outlet. Thus, the unaccounted net precipitation either flows via the subsurface under the gauge to the lake or the discharge is not measured correctly.

The under prediction of the high flows for the Rib River is a consequence of the increased riverbed levels (SMEC, 2008) and can be observed clearly in Fig. 5A and in Dessie et al. (2014). In Fig. 5A, the under prediction is indicated with ellipses 1 and 2 in which the measured flows do not exceed an equivalent of 6 mm/day with predicted flows much greater than that. The under prediction of the high flows at the Rib stream gauge is even more clear in Dessie et al. (2014) where in the period from July 10 to September 15, 2012, a newly installed upstream gauge on the Rib shows the weekly peak flows were up to 300 m^3/sec (equivalent of 22 mm/day) but in the downstream gauge, the peak flows were invariably at 150 m^3/sec (equivalent to 10 mm/day). Since rivers are extremely flashy, the peak runoff occurs only part of the day and the 6 mm/day observed over the whole day (this paper) is comparable with the 10 mm/day over part of the day (Dessie et al., 2014). The final cause for the "missing" rainfall (i.e., contributing areas not adding up to 1) is that the Rib watershed is underlain by permeable tuffs (Dessie et al., 2014) facilitating subsurface flows and this decreases the amount of the discharge at the gauge. Large springs have been observed downstream of the gauge. Some of the "missing" rainwater is resurfacing in these springs.

Under prediction of the flow by the Megech River (Fig. 6) is either due to the Angereb Dam or, since the area is volcanic, subsurface flow through faults and pipes (and not measured by the gauge) could occur as well. The over prediction of the base flow after 2006 is likely caused by a change in the riverbed as discussed above.

Sediment

Evaluation of the sediment module

The sediment concentrations were measured by the Ministry of Water, Irrigation and Electricity (MoWIE) as part of determining the sediment rating curves for each of the four rivers in the Lake Tana basin. As expected, the measured high sediment concentrations (Fig. 7) occurred during large flow events In addition, for similar runoff events, the concentrations were greater during the onset of the rainfall phase than later in the rain-phase.

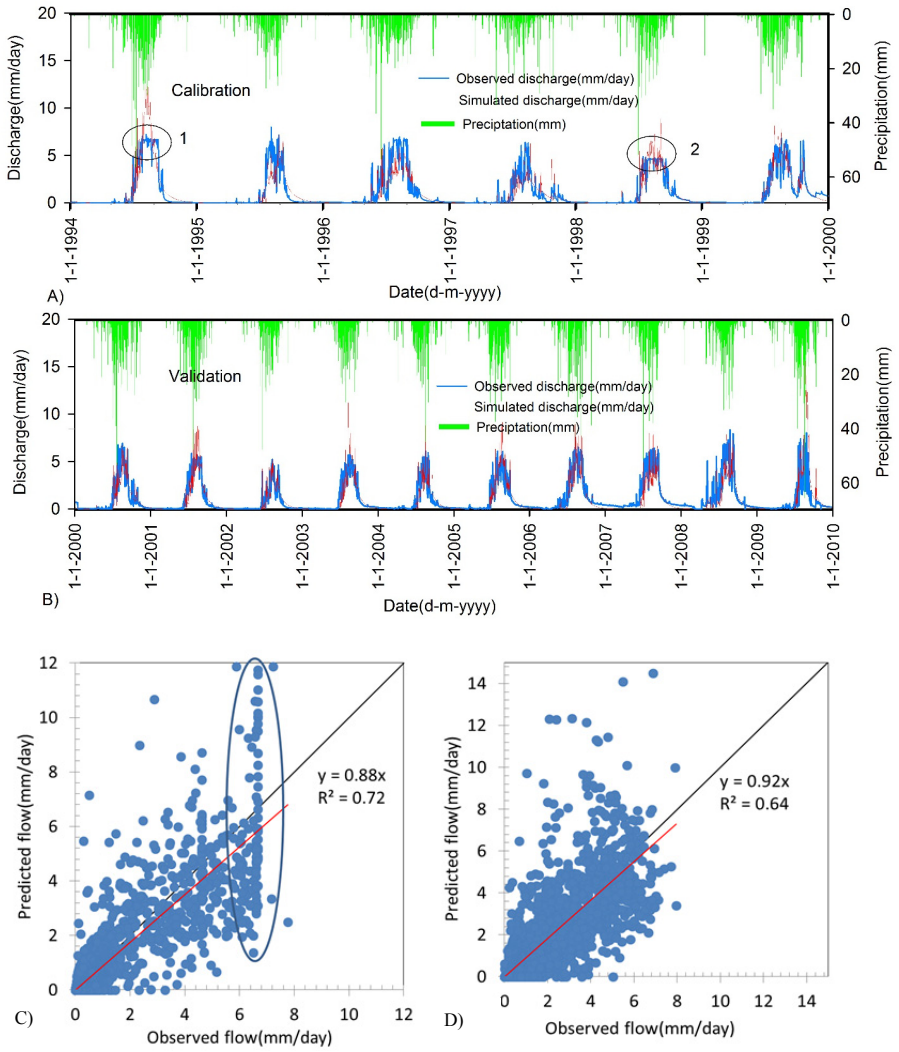

Fig. 5. Simulated and observed stream flows in mm/d for Rib River. A) Calibration (1994–1999), B) Validation (2000–2009), C) Scatter plot of simulated vs observed for calibration, D) Scatter plot of simulated vs observed validation.

The concentration measurements were employed to calibrate the "*a*" parameters (Eq. 8) in the sediment module. The surface runoff for the 16 years, originating from the saturated and degraded area and the subsurface flow (interflow and base flow) that are required for the sediment module, were predicted with the PED hydrology module. The trend of decreasing sediment concentration is captured by the H function (Eq. 8) with cumulative rainfall (Fig. 2).

The predicted and observed sediment concentrations as a function of time for the major rivers are shown in Fig. 8 with the input parameter listed in Table 4. Daily observed versus corresponding predicted sediment concentrations for the four watersheds agree well as shown in Table 5 with Nash Sutcliff values ranging from 0.5 to 0.84.

The average sediment loads from these watersheds (1994-2009) were 35 (±1.96) (±SE) t/ha/yr for the Gilgel Abay, 49 (±2.51) (±SE) t/ha/yr for the Gumara, 25 (±1.85) (±SE) t/ha/yr for the Rib, and 12 (±0.73) (±SE) t/ha/yr for the Megech (Table 6). The sediment loss per unit area in the Gumara is 49 t/ha and is greater than any other river. However, the Gilgel Abay, with 14.3 Mt/yr, transports most sediment in the lake because runoff losses are much greater than any other watershed. For reducing the sediment load to the lake, upland management practices should be concentrated in the Gilgel Abay basin but also the Gumara basin which has the greatest soil loss per ha.

Table 4. PED model input parameters for sediment concentration simulations for the transport limit, a_t and the source limit, a_s in $((g\ l^{-1})(mm\ d^{-1})^{0.4})$ for the four main rivers in the Lake Tana basin.

Source	G_Abay		Gumara		Rib		Megech	
	a_t	a_s	a_t	a_s	a_t	a_s	a_t	a_s
Saturated	3.0	2.5	7.0	4.0	8.0	5.0	2.5	1.5
Degraded	5.0	5.0	15	5.0	10	5.0	4.5	2.2
River bank	0.7	0	0.8	0	0.6	0	0.15	0

Table 5. PED model efficiency criteria for simulated vs observed sediment concentrations for the four major rivers in the Lake Tana basin.

1994–2009		Daily sediment concentration (g/l)			
		Gilgel Abay	Gumara	Rib	Megech
Mean	predicted	1.8	3.3	4.8	0.77
	observed	1.6	3.2	4.6	0.79
	R^2	0.60	0.56	0.7	0.84
	NSE	0.50	0.67	0.73	0.84
	RMSE(g/l)	0.72	1.25	1.71	0.32
	Error	–0.18	–0.08	–0.16	0.02

Table 6. Sediment budget for gauged and ungauged portions of the four Lake Tana watersheds: Gilgel Abay, Gumara, Rib, Megech.

Water-sheds	Gauged			Ungauged			Total four rivers Mt/yr
	Area (km^2)	Total Mt/year[1]	Unit area t/ha/yr	Area (km^2)	Total Mt/yr	Unit area t/ha/yr	
Megech	500	0.6	12.2	163	0.3	21	0.9
Gumara	1281	6.3	49.4	688	1.9	28	8.2
Rib	1289	3.2	24.6	379	0.7	17.7	3.9
G_Abay	1665	5.9	35.4	2362	8.4	35.4	14.3
Total	4735	16		3592	11.3		27.3
Average			33.8			31.5	32.8

[1] 10^{12} grams or 1 million tons

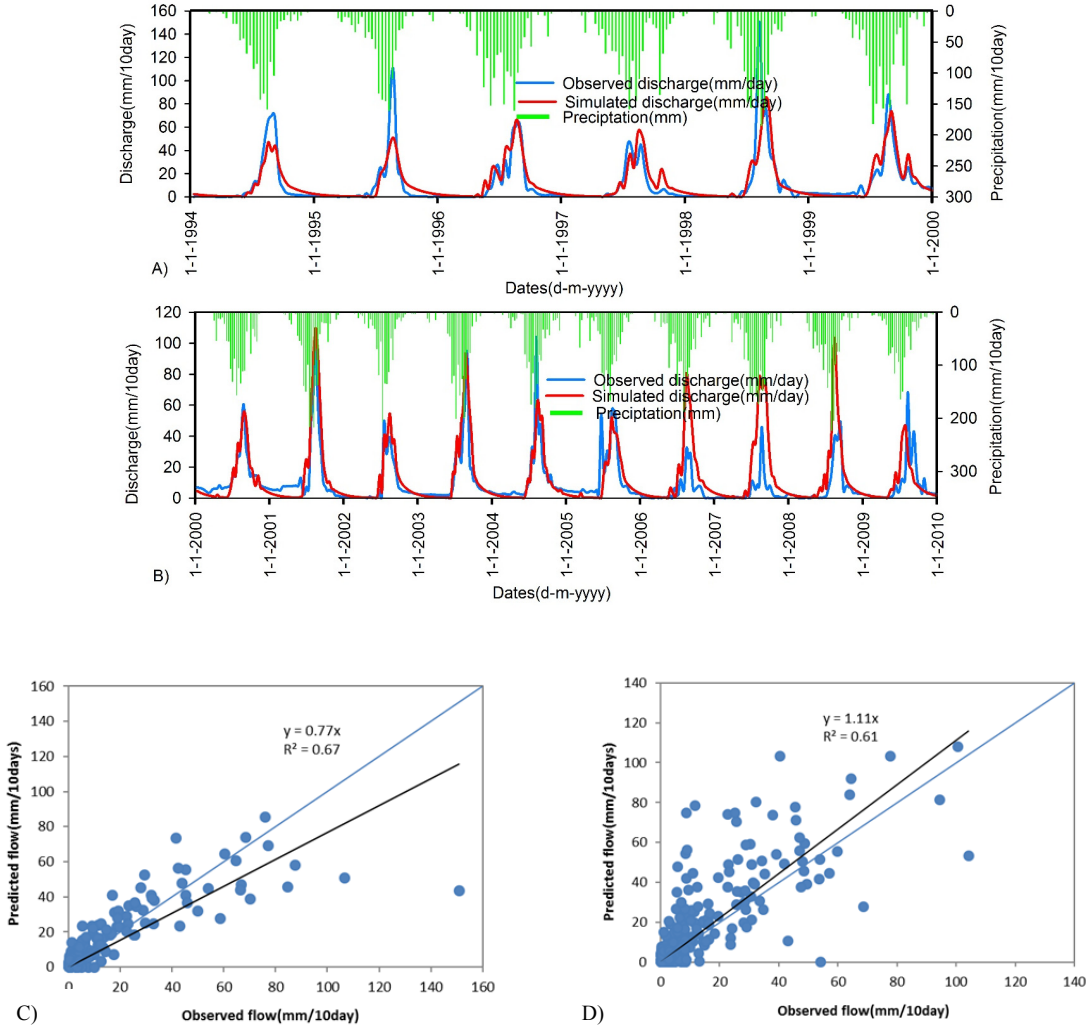

Fig. 6. Simulated and observed stream flows in mm/10 days for Megech River. A) Calibration (1994–1999), B) Validation (2000–2009), C) Scatter plot of simulated vs observed for calibration, D) Scatter plot of simulated vs observed validation.

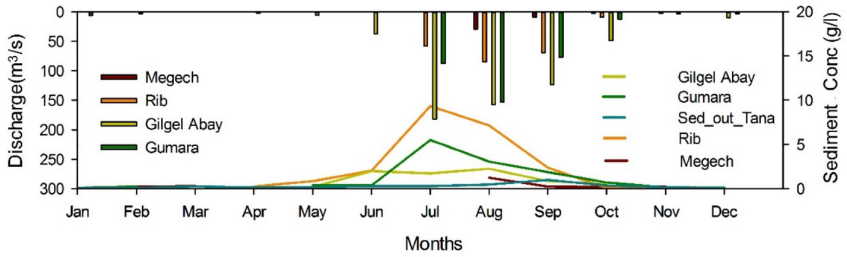

Fig. 7. Average monthly sediment concentration (lines) and discharge (bars) of the four major rivers in the Tana Basin for the years 1964–2009.

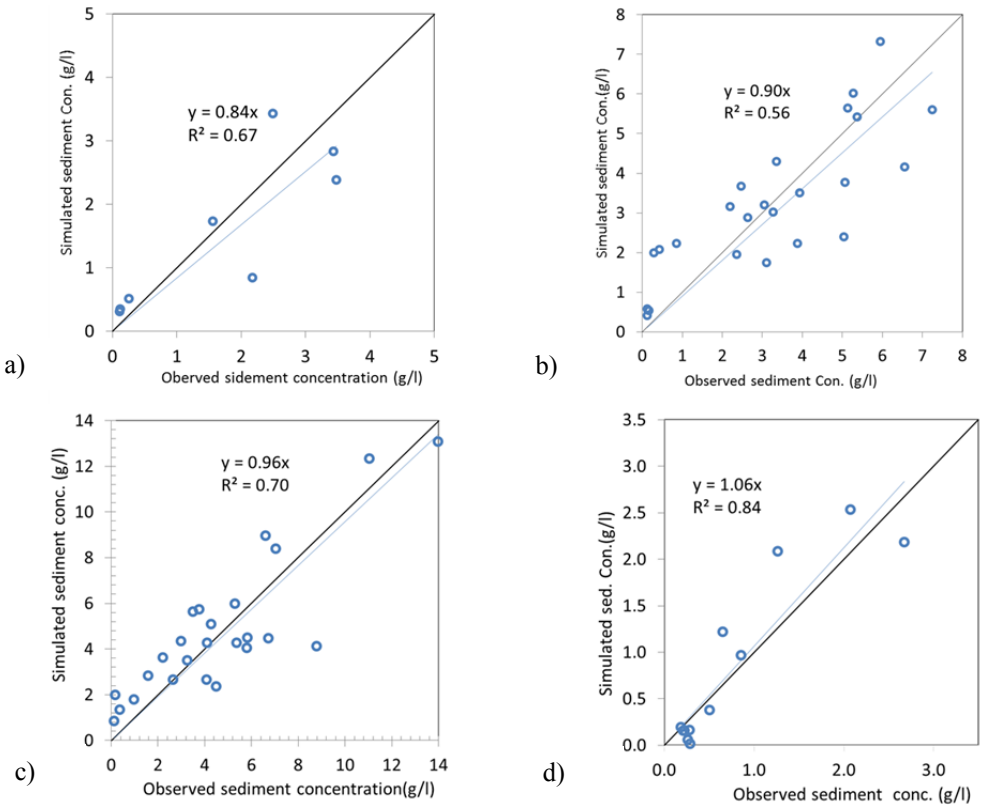

Fig. 8. Simulated vs Observed sediment concentration for a) Gilgel Abay, b) Gumara, c) Rib and d) Megech.

The concentration in the water when the rill is formed is related to the maximum amount of sediments that can be carried by the water in the rill (Tebebu et al., 2010; Zegeye et al., 2010) and is represented in the a_t coefficient in the model. Its magnitude is related to the stream power which is a function of the slope of the land (Gao, 2008). Since the slopes in the Gilgel Abay watershed are relatively flatter than the Rib and Gumara (Table 1), the transport capacity for the Gilgel Abay in Table 4 is less than for the Rib and the Gumara. The Megech has a reservoir upstream of the sampling location that takes out most of the sediment and can explain the low transport coefficient despite the steep terrain (Table 4).

Once the rill network is formed, it is reasonable that sediment concentration decreases and at the end of the rainfall monsoon phase, the concentration is source limited and depends on the cohesion of the soil and on the soil type. This is represented by the source limit term as in the model. The soils in the Gumara and Rib have a greater percentage of chromic Luvisols (loamy sand, Table 1) and thus easier to erode than the more clay-like soils in the Gilgel Abay and Megech. Therefore, the a_t and a_s values in Table 4 are less for the Gilgel Abay and the Megech than for the Gumara and Rib.

Sediment contributions to Lake Tana

Table 6 shows the amount of sediment for the four rivers of the gauged part of the basin (1994–2009) which is equal to 16 Mt/yr (Mt is equal to 10^6 t). In Table 7, the sediment budget is detailed for Lake Tana and the flood plains. Based on an analysis by Ayana et al. (2015), who compared the bathymetric surveys of Lake Tana in 1987 and 2006, the sediment amount settled at the bottom of the lake was found to be 200 Mm^3. The annual sediment load deposited in the lake, $S_{lake,}$ (Eq. 9) can be calculated from this estimate, assuming a bulk density of 1,200 kg/m^3, deducting an average organic matter accumulation in the lake, and assuming the organic matter content of the sediment at the bottom of the lake as 3.4% (Vanmaercke et al., 2010). Based on this, we calculated that the sediment accumulation was 11.6 Mt/yr (Table 7).

The 1.6 Mt/yr of sediment leaving the lake in the Blue Nile (Table 7) was found by multiplying the monthly average of the available measured concentrations at the outlet (Fig. 7) by the monthly average discharge. The sediment delivered to the lake is the sum of what is settled at the lake bottom plus that which has left the lake and equals 13.2 Mt/yr (Table 7).

As can be seen from Table 1, the topographic characteristics of the Gilgel Abay is nearly the same as the ungauged part of the basin. Thus, a reasonable estimate for the upper bound of the soil loss for the ungauged part of the four major rivers in the Lake Tana basin can be obtained by using the sediment parameters of Gilgel Abay assuming that the hydrological parameters and the rainfall remains the same as for the gauged part of the particular watershed. The results of these calculations are given in Table 6. We find that the total loss from the ungauged parts of the four rivers is 11.3 Mt/yr, or an average soil loss of 31.5 t/ha/yr (Table 6).

There are additional areas in the Lake Tana basin that are not part of the four large watersheds. We will assume that these areas have the same soil loss as the average soil loss per ha of the ungauged watersheds, which are 31.5 t/ha/yr. Thus, by multiplying the total area of ungauged basin (minus the flood plains) with the average soil loss of 31.5 t/ha, the upper bound for sediment contribution of all the ungauged parts of the basin outside the flood plain is 21.5 Mt/yr (Table 7). The lower bound is estimated by taking the 12.2 t/ha/yr soil loss in the Megech, which is the lowest of the four major gauged rivers, and use this for the entire ungauged part of the basin. This comes to 8.3 Mt/yr from the total ungauged basin, without including the flood plain (Table 7).

Table 7. Sediment budget for the Lake Tana consisting of predicted minimum and maximum contribution from the watershed and the measured sediments deposited in the lake and that leaving the Lake at the outlet. The minimum contribution assumes that the ungauged part of the Lake Tana watershed contributes at least equal to the sediment contribution of Megech (the smallest) and the maximum contribution assumes that the ungauged part has similar landscape characteristics as the Gilgel Abay.

Description	Area (km^2)	Lower bound		Upper bound	
		t/ha/yr	Mt/yr	t/ha/yr	Mt/yr
Watershed contribution					
Gauged river contributions "Mgauged" as in Eq. (9) (predicted, Table 6)	4735	33.8	16.0	33.8	16.0
Ungauged river contributions minus flood-plains "Mungauged" as in Eq. (9) (estimated, Table 6)	6829	12.2	8.3	31.5	21.5
Total watershed contribution minus flood-plains	11564	21.0	24.3	32.4	37.5
Sediment reaching the flood plain and lake					
Deposited in the lake (measured) "Slake" as in Eq. (9)	3000	38.7	11.6	38.7	11.6
Outflow from the lake (measured) "blNile" as in Eq. (9)		5.3	1.6	5.3	1.6
Total sediment reaching the lake (measured)		44.0	13.2	44.0	13.2
Retained in floodplains and deltas (calculated) "Sflplane" as in Eq. (9)	436	255	11.1	558	24.3

Table 8. Annual sediment mass balance of Lake Tana and its floodplain.

Location	Lower bound			Upper bound		
	Delivered Mt/year	Retained		Delivered Mt/year	Retained	
		Mt/year	Portion		Mt/year	Portion
Floodplain & delta (Table 7)	24.3	11.1	0.46	37.5	24.3	0.65
Lake (Table 7, measured)	13.2	11.6	0.88	13.2	11.6	0.88
Floodplain, delta and lake	24.3	22.7	0.93	37.5	35.9	0.96

The final sediment budget calculations and the portion of the sediment retained in the flood plain, the lake, and both the flood plain and lake together, are shown in Table 8 for both the lower and upper bounds of the sediment contributed by the ungauged basins. The portion retained can be calculated simply as the sediment retained minus the incoming sediment.

The amount of sediment retained in the flood plain is greatly dependent on the amount of sediment delivered from the gauged and ungauged parts. We find for the lower bound 46% of the sediment is retained in the flood plain (Table 8). For the upper bound 65% is retained in the flood plain.

The annual sediment load that comes into the lake is equal to the sediment deposited in the lake (11.6 Mt/year) plus the amount leaving the lake (1.6 Mt/yr). Since these two quantities have been measured, the retention in the lake is independent of predicted amount of sediment originating from the watershed. We find in this way that the amount of sediment retained in the lake equaled 88%. Finally, the sediment from the upland retained in both the flood plain and lake varies between 93% (lower bound) and 96% (upper bound, Table 8).

The evidence of the near shore deposition is most obvious for the Gilgel Abay (with a relatively small flood plain); it has formed a peninsula of approximately 10 km long and 2 km wide. The Gumara and Rib rivers have a large flood plain area and the additional land formed offshore, which is around 0.8 by 3 km, is comparatively smaller (Abate et al., 2015).

In addition, our prediction of the PED model can be compared with a water supply reservoir (Angereb) in the Lake Tana basin that has accumulated 1.8 Mm^3 of sediment within 11 years (Haregeweyn et al., 2012). The sediment accumulated within the reservoir is 0.2 Mt/yr for the 68 km^2 watershed; this is equivalent to 29 t/ha/yr. This value is a similar order of magnitude to the sediment delivered by other watersheds in the Ethiopian highlands (Abate et al., 2017; Dagnew et al., 2015; Tilahun et al., 2013a, 2015; Vanmaercke et al., 2010). Finally, the soil losses reported by Erkossa et al. (2015) and Lemma et al. (2017), with 2.7 t/ha/yr, are unrealistically low. Based on the average reported sediment concentration of 4.4 g/l in Lemma et al. (2017), it can be easily shown that their sediment losses should agree with our calculations of around 30 t/ha/yr.

Prioritizing upland management practices for Lake Tana

Finally, our results have implications on prioritizing management practices for reducing the sediment load to Lake Tana. The Gilgel Abay basin receives the most rainfall resulting in the greatest discharge and, of the four basins, the second highest sediment concentration at the outlet. Thus, to reduce sediment losses to the lake, the first priority should be given to installing upland best management practices at the runoff source areas in the Gilgel Abay watershed. A second priority for installing soil and water conservation practices is the Gumara watershed which has the greatest erosional soil loss per ha.

CONCLUSION

This manuscript presents a method for realistically recreating the long-term suspended sediment concentrations in a developing country watershed where data of this type is extremely scarce. The study was carried out in the Lake Tana basin where the PED model was fitted to the long-term discharge data and the occasional measurements of sediment concentrations in the four major rivers. Average annual sediment loss from the gauged part of the watershed is 33.8 t/ha. Annual accumulation of sediment in Lake Tana was measured at 10 t/ha when averaged over the watershed area. A small amount of sediment

flows out of the lake to the Blue Nile River. Bounds of sediment loss for the ungauged basin were established. The upper bound was 31.5 t/ha and the lower bound was 12.2 t/ha. Based on this, we calculated that the sediment retained in the near shore areas and in the flood plains was between 47% and 63% of the sediment generated in the uplands. The sediment coming from the uplands retained by the flood plain and lake was between 94% and 96%. The portion that entered the lake and that was retained amounted to 88%. With the greatest discharge, second highest sediment concentration, and smallest flood plain, the Gilgel Abay contributes the most sediment to the lake. To reduce soil losses to the lake, upland management practices should be concentrated in the Gilgel Abay basin because it is the greatest sediment contributor to Lake Tana.

Acknowledgements. Funding for this research was obtained from USAID through the research project called "Participatory Enhanced Engagement in Research" or PEER Science project (grant number AID-OAA-A-11-00012). Additional funding was also obtained from Higher Education for Development (HED), United States Department of Agriculture (USDA) and funds provided by Cornell University, partly through the highly-appreciated gift of an anonymous donor. Finally, Peggy Stevens improved our Ethiopian/Dutch English.

REFERENCES

Abate, M., Nyssen, J, Steenhuis, T.S., Moges, M.M., Tilahun, S.A., Enku, T., Adgo, E., 2015. Morphological changes of Gumara River channel over 50 years, upper Blue Nile basin, Ethiopia. Journal of Hydrology, 525, 152–164.

Abate, M., Nyssen, J., Moges, M.M., Enku, T., Zimale, F.A., Tilahun, S.A., Adgo, E., Steenhuis, T.S., 2017. Long-term landscape changes in the Lake Tana basin as evidenced by delta development and flood plain aggradation, Ethiopia. Land Degradation & Development, 28, 6, 1820–1830. DOI: 10.1002/ldr.2648.

Aerts, R., Maes, W., November, E., Behailu, M., Poesen, J., Deckers, J., Hermy, M., Muys, B., 2006. Surface runoff and seed trapping efficiency of shrubs in a regenerating semiarid woodland in northern Ethiopia. Catena, 65, 61–70.

Allen, R.G., Pereira, L.S., Raes, D., Smith, M., 1998. Crop evapotranspiration - Guidelines for computing crop water requirements. FAO Irrigation and drainage paper 56. FAO, Rome, 300, 9, D05109.

Ayana, E.K., Philpot, W.D., Melesse, A.M., Steenhuis, T.S., 2015. Assessing the potential of MODIS/Terra version 5 images to improve near shore lake bathymetric surveys. International Journal of Applied Earth Observation and Geoinformation, 36, 13–21.

Betrie, G.D., Mohamed, Y.A., van Griensven, A., Srinivasan, R., 2011. Sediment management modelling in the Blue Nile Basin using SWAT model. Hydrology and Earth System Sciences, 15, 807–818. DOI: 10.5194/hess-15-807-2011.

Cheesman, R.E., 1936. Lake Tana and the Blue Nile an Abyssinian quest. Macmillan and Co., Limited.

Conway, D., 2000. The climate and hydrology of the Upper Blue Nile River. The Geographical Journal, 166, 49–62.

Dagnew, D.C., Guzman, C.D., Zegeye, A.D., Tibebu, T.Y., Getaneh, M., Abate, S., Zemale, F.A., Ayana, E.K., Tilahun, S.A., Steenhuis, T.S., 2015. Impact of conservation practices on runoff and soil loss in the sub-humid Ethiopian Highlands: The Debre Mawi watershed. J. Hydrol. Hydromech, 63, 210–219. DOI: 10.1515/johh-2015-0021.

Descheemaeker, K., Nyssen, J., Poesen, J., Raes, D., Haile, M., Muys, B., Deckers, S., 2006. Runoff on slopes with restoring vegetation: a case study from the Tigray highlands, Ethiopia. Journal of Hydrology, 331, 219–241.

Dessie, M., Verhoest, N.E.C., Admasu, T., Pauwels, V.R.N., Poesen, J., Adgo, E., Deckers, J.,. Nyssen, J., 2014. Effects of the flood plain on river discharge into Lake Tana (Ethiopia). J. Hydrology, 519, 699–710.

Easton, Z.M., Fuka, D.R., White, E.D., Collick, A.S., Biruk Asharge, B., McCartney, M., Awulachew, S.B., Ahmed, A.A., Steenhuis, T.S., 2010. A multi basin SWAT model analysis of runoff and sedimentation in the Blue Nile, Ethiopia. Hydrology and Earth System Sciences Discussions, 7, 3837–3878.

Engda, T.A., Bayabil, H.K., Legesse, E.S., Ayana, E.K., Tilahun, S.A., Collick, A.S., Easton, Z.M., Rimmer, A., Awulachew, S.B., Steenhuis, T.S., 2011. Watershed hydrology of the (semi) humid Ethiopian Highlands. In: Melesse, A.M. (Ed.): Nile River Basin: Hydrology, Climate and Land Use. Springer Science Publisher, pp. 145–162.

Erkossa, T., Wudneh, A., Desalegn, B., Taye, G., 2015. Linking soil erosion to on-site financial cost: lessons from watersheds in the Blue Nile basin. Solid Earth, 6, 765–774.

Fox, G.A., Wilson, G., 2010. The role of subsurface flow in hillslope and stream bank erosion: a review. Soil Science Society of America Journal, 74, 717–733.

Fox, G.A., Wilson, G.V., Simon, A., Langendoen, E.J., Akay, O., Fuchs, J.W., 2007. Measuring streambank erosion due to ground water seepage: correlation to bank pore water pressure, precipitation and stream stage. Earth Surface Processes and Landforms, 32, 1558–1573.

Frankl, A., Nyssen, J., De Dapper, M., Haile, M., Billi, P., Munro, R.N., Deckers, J., Poesen, J., 2011. Linking long-term gully and river channel dynamics to environmental change using repeat photography (Northern Ethiopia). Geomorphology, 129, 238–251.

Frankl, A., Jacob, M., Haile, M., Poesen, J., Deckers, J., Nyssen, J., 2013. The effect of rainfall on spatio-temporal variability in cropping systems and duration of crop cover in the Northern Ethiopian Highlands. Soil Use and Management, 29, 374–383.

Gao, P., 2008. Understanding watershed suspended sediment transport. Progress in Physical Geography, 32, 243–263.

Gebreegziabher, T., Nyssen, J., Govaerts, B., Getnet, F., Behailu, M., Haile, M., Deckers, J., 2009. Contour furrows for in situ soil and water conservation, Tigray, Northern Ethiopia. Soil and Tillage Research, 103, 257–264.

Gebrermichael, D., Nyssen, J., Poesen, J., Deckers, J., Haile, M., Govers, G., Moeyersons, J., 2005. Effectiveness of stone bunds in controlling soil erosion on cropland in the Tigray highlands, Northern Ethiopia. Soil Use and Management, 21, 287–297.

Girmay G, Singh B, Nyssen J, Borrosen T. 2009. Runoff and sediment-associated nutrient losses under different land uses in Tigray, Northern Ethiopia. Journal of Hydrology, 376, 70–80.

Guzman, C.D., Tilahun, S.A., Zegeye, A.D., Steenhuis, T.S., 2013. Suspended sediment concentration–discharge relationships in the (sub-) humid Ethiopian highlands. Hydrology and Earth System Sciences, 17, 1067–1077.

Haile, M., Herweg, K., Stillhardt, B., 2006a. Sustainable land management – a new approach to soil and water conservation in Ethiopia. Land Resources Management and Environmental Protection Department, Mekelle University, Ethiopia, and Center for Development and Environment (CDE), University of Bern and Swiss National Center of Competence in Research (NCCR) North-South, Bern, Switzerland.

Haile, M., Herweg, K., Stillhardt, B., 2006b. Sustainable land management–A new approach to soil and water conservation in Ethiopia. Mekelle University, Mekelle, Ethiopia, University of Berne, Berne, Switzerland.

Hairsine, P.B., Rose, C.W., 1992. Modeling water erosion due to overland flow using physical principles: 1. Sheet flow. Water Resources Research, 28, 237–243.

Haregeweyn, N., Yohannes, F., 2003. Testing and evaluation of the agricultural non-point source pollution model (AGNPS) on Augucho catchment, western Hararghe, Ethiopia. Agriculture, Ecosystems & Environment, 99, 201–212.

Haregeweyn, N., Melesse, B., Tsunekawa, A., Tsubo, M., Meshesha, D., Balana, B.B., 2012. Reservoir sedimentation and its mitigating strategies: a case study of Angereb reservoir (NW Ethiopia). J Soils Sediments, 12, 291–305.

Haregeweyn, N., Poesen, J., Verstraeten, G., Govers, G., Vente, J., Nyssen, J., Deckers, J., Moeyersons, J., 2013. Assessing the performance of a spatially distributed soil erosion and sediment deliv-

ery model (WATEM/SEDEM) in Northern Ethiopia. Land Degradation & Development, 24, 188–204.

Kaba, E., Philpot, W., Steenhuis, T.S., 2014. Evaluating suitability of MODIS-Terra images for reproducing historic sediment concentrations in water bodies: Lake Tana, Ethiopia. International Journal of Applied Earth Observation and Geoinformation, 26, 286–297.

Kebede, S., Travi, Y., Alemayehu, T., Marc, V., 2006. Water balance of Lake Tana and its sensitivity to fluctuations in rainfall, Blue Nile basin, Ethiopia. Journal of Hydrology, 316, 233–247.

Lemma, H., Admasu, T., Dessie, M., Fentie, D., Deckers, J., Frankl, A., Poesen, J., Adgo, E., Nyssen, J., 2017. Revisiting lake sediment budgets: how the calculation of lake lifetime is strongly data and method dependent. Earth Surface Processes and Landforms.

Lieskovský, J., Kenderessy, P., 2014. Modelling the effect of vegetation cover and different tillage practices on soil erosion in vineyards: a case study in Vráble (Slovakia) using WATEM/SEDEM. Land Degradation & Development, 25, 288–296.

Liu, B.M., Collick, A.S., Zeleke, G., Adgo, E., Easton, Z.M., Steenhuis, T.S., 2008. Rainfall-discharge relationships for a monsoonal climate in the Ethiopian highlands. Hydrological Processes, 22, 1059–1067.

Lyon, S.W., Seibert, J., Lembo, A., Walter, M.F., Steenhuis, T.S., 2005. Geostatistical investigation into the temporal evolution of spatial structure in a shallow water table. Hydrology and Earth System Sciences Discussions, 2, 1683–1716. DOI: 10.5194/hessd-2-1683-2005.

Mishra, S.K., Singh, V.P., 2004. Long-term hydrological simulation based on the Soil Conservation Service curve number. Hydrological Processes, 18, 1291–1313.

Moges, M.A., Zemale, F.A., Alemu, M.L., Ayele, G.K., Dagnew, D.C., Tilahun, S.A. Steenhuis, T.S., 2016. Sediment concentration rating curves for a monsoonal climate: upper Blue Nile. Soil, 2, 3, 337–349.

Moriasi, D., Arnold, J., Van Liew, M., Bingner, R., Harmel, R., Veith, T., 2007. Model evaluation guidelines for systematic quantification of accuracy in watershed simulations. Trans. ASABE, 50, 885–900.

Rientjes, T., Haile, A., Kebede, E., Mannaerts, C., Habib, E., Steenhuis, T.S, 2011. Changes in land cover, rainfall and stream flow in Upper Gilgel Abbay catchment, Blue Nile basin-Ethiopia. Hydrology and Earth System Sciences, 15, 1979–1989.

Setegn, S.G., Srinivasan, R., Dargahi, B., 2008. Hydrological and sediment yield modelling in Lake Tana basin, Blue Nile Ethiopia. The Open Hydrology Journal, 2, 49–62.

Setegn, S.G., Srinivasan, R., Dargahi, B., Melesse, A.M., 2009. Spatial delineation of soil erosion vulnerability in the Lake Tana Basin, Ethiopia. Hydrological Processes, 23, 3738–3750.

Setegn, S.G., Darfahi, B., Srinivasan, R., Melesse, A.M., 2010a. Modeling of sediment yield from Anjeni-gauged watershed, Ethiopia using SWAT model. J. Am. Water Resour. Assoc., 46, 514–526.

Setegn, S.G., Srinivasan, R., Melesse, A.M., Dargahi, B., 2010b. SWAT model application and prediction uncertainty analysis in the Lake Tana Basin, Ethiopia. Hydrological Processes, 24, 357–367.

Setegn, S.G., Rayner, D., Melesse, A.M., Dargahi, B., Srinivasan, R., 2011. Impact of climate change on the hydroclimatology of Lake Tana Basin, Ethiopia. Water Resources Research, 47, W04511.

SMEC, 2008. Hydrological study of the Tana-Beles sub- basins, Hydrological monitoring network (Review and recommendations). Ministry of Water Resources.

Steenhuis, T.S., Collick, A.S., Easton, Z.M., Leggesse, E.S., Bayabil, H.K., White, E.D., Awulachew, S.B., Adgo, E., Ahmed, A.A., 2009. Predicting discharge and sediment for the Abay (Blue Nile) with a simple model. Hydrological Processes, 23, 3728–3737.

Steenhuis, T.S., Van der Molen, W., 1986. The Thornthwaite-Mather procedure as a simple engineering method to predict recharge. Journal of Hydrology, 84, 221–229.

Tamene, L., Park, S., Dikau, R., Vlek, P., 2006. Analysis of factors determining sediment yield variability in the highlands of northern Ethiopia. Geomorphology, 76, 76–91.

Tebebu, T., Abiy, A., Zegeye, A., Dahlke, H., Easton, Z., Tilahun, S., Collick, A., Kidnau, S., Moges, S., Dadgari, F., 2010. Surface and subsurface flow effect on permanent gully formation and upland erosion near Lake Tana in the northern highlands of Ethiopia. Hydrology and Earth System Sciences, 14, 2207–2217.

Thornthwaite, C., Mather, J., 1955. The water balance. Centerton: Drexel Institute of Technology, 1955. 104 p. Publications in Climatology, 8, 104.

Tilahun, S.A., Guzman, C.D., Zegeye, A.D., Dagnew, D.C., Collick, A.S., Yitaferu, B., Steenhuis, T.S., 2015. Distributed discharge and sediment concentration predictions in the sub-humid Ethiopian highlands: the Debre Mawi watershed. Hydrological Processes, 29, 1817–1828.

Tilahun, S.A., Guzman, C.D., Zegeye, A.D., Engda, T.A, Collick, A.S., Rimmer, A., Steenhuis, T.S., 2013a. An efficient semi-distributed hillslope erosion model for the subhumid Ethiopian Highlands. Hydrology and Earth System Sciences, 17, 1051–1063. DOI: 10.5194/hess-17-1051-2013.

Tilahun, S.A., Mukundan, R., Demisse, B.A., Engda, T.A., Guzman, C.D., Tarakegn, B.C., Easton, Z.M., Collick, A.S., Zegeye, A.D., Schneiderman, E.M., Parlange, J.Y., Steenhuis, T.S., 2013b. A saturation excess erosion model. Transactions of the ASABE 56, 681–695. DOI: 10.13031/2013.42675.

Vanmaercke, M., Zenebe, A., Poesen, J., Nyssen, J., Verstraeten, G., Deckers, J., 2010. Sediment dynamics and the role of flash floods in sediment export from medium-sized catchments: a case study from the semi-arid tropical highlands in northern Ethiopia. Journal of Soils and Sediments, 10, 611–627.

Vijverberg, J., Sibbing, F.A., Dejen, E., 2009. Lake Tana: Source of the Blue Nile. In: The Nile, Springer, pp. 163–192.

Walling, D.E., 2008. The changing sediment load of the Mekong River. Ambio, 37, 3, 150–157.

Wang, S., Fu, B., Piao, S., Lü, Y., Ciais, P., Feng, X., Wang, Y., 2015. Reduced sediment transport in the Yellow River due to anthropogenic changes. Nature Geoscience.

White, E.D., Easton, Z.M., Fuka, D.R., Collick, A.S., Adgo, E., McCartney, M., Awulachew, S.B., Selassie, Y.G., Steenhuis, T.S., 2011. Development and application of a physically based landscape water balance in the SWAT model. Hydrological Processes, 25, 915–925.

Yasir, S., Crosato, A., Mohamed, Y.A., Abdalla, S.H., Wright, N.G., 2014. Sediment balances in the Blue Nile River Basin. International Journal of Sediment Research, 29, 316–328.

Yitbarek, T., Belliethathan, S., Stringer, L., 2012. The onsite cost of gully erosion and cost-benefit of gully rehabilitation: A case study in Ethiopia. Land Degradation & Development, 23, 157–166.

Yu, B., Rose, C.W., Ciesiolka, C., Coughlan, K., Fentie, B., 1997. Toward a framework for runoff and soil loss prediction using GUEST technology. Aust. J. Soil Res., 35, 1191–1212.

Zegeye, A.D., Steenhuis, T.S., Blake, R.W., Kidnau, S., Collick, A.S., Dadgari, F., 2010. Assessment of soil erosion processes and farmer perception of land conservation in Debre Mewi watershed near Lake Tana, Ethiopia. Ecohydrology & Hydrobiology, 10, 297–306. DOI: 10.2478/v10104-011-0013-8.

Zeleke, G., 2000. Landscape dynamics and soil erosion process modeling in the north western Ethiopian highlands. African Studies Series A 16. Geographica Bernensia, Berne, Switzerland, 226 p.

Received 28 September 2016
Accepted 4 July 2017

J. Hydrol. Hydromech., 66, 2018, 1, 79–86
DOI: 10.1515/johh-2017-0043

The effects of stemflow on redistributing precipitation and infiltration around shrubs

Shengqi Jian[1], Xueli Zhang[2], Dong Li[1], Deng Wang[1], Zening Wu[1], Caihong Hu[1*]

[1] College of Water Conservancy & Environment, Zhengzhou University, Science road 100, Zhengzhou, China.
[2] Zhongyuan District Environmental Protection Bureau, Zhengzhou City, Gangpo road 4, Zhengzhou, China.
[*] Corresponding author. Tel.: +86 18603814081. E-mail: jiansq@zzu.edu.cn

Abstract: The experiments of stemflow of two semiarid shrubs (*Caragana korshinskii* and *Hippophae rhamnoides*) and its effect on soil water enhancement were conducted from 1st May to 30th September of 2009–2013 in the Chinese Loess Plateau. Stemflow values in *C. korshinskii* and *H. rhamnoides* averaged 6.7% and 2.4% of total rainfall. The rainfall threshold for stemflow generation was 0.5 and 2.5 mm for *C. korshinskii* and *H. rhamnoides*. When rainfall was less than 17.0 mm, the funnelling ratios were highly variable, however, stable funnelling ratios were found for rainfall greater than 17.0 mm for *C. korshinskii*. The funnelling ratios of *H. rhamnoides* first increased until a threshold value of 10.0 mm and then the funnelling ratios begin stabilize. The wetting front depths in the area around stem was 1.4–6.7 and 1.3–2.9 times deeper than area outside the canopy for *C. korshinskii* and *H. rhamnoides*. Soil moisture at soil depth 0–200 cm was 25.6% and 23.4% higher in soil around stem than that outside canopy for *C. korshinskii* and *H. rhamnoides*. The wetting front advanced to depths of 120 and 100 cm in the area around stem and to depths of 50 cm in the area outside the canopy for *C. korshinskii* and *H. rhamnoides* suggested that more rain water can be conserved into the deep soil layers through shrub stemflow. Soil moisture was enhanced in the area outside the shrub canopy, only when rainfall depth is > 4.7 and 5.1 mm, which is an effective rainfall for the area for *C. korshinskii* and *H. rhamnoides*. While for the area around stem of *C. korshinskii* and *H. rhamnoides*, the corresponding threshold values are 3.2 and 4.3 mm. These results confirmed that stemflow has a positive effect on soil moisture balance of the root zone and the enhancement in soil moisture of deeper soil layers.

Keywords: Stemflow; Wetting front; *C. korshinskii*; *H. rhamnoides*; Loess Plateau; China.

INTRODUCTION

Vegetation growth and ecosystem processes are typically limited by water availability in semi-arid ecosystems (Kéfi et al., 2007; Noy-Meir, 1973). Revegetation experiments have been established for more than 50 years in Loess Plateau, northwestern China, using mainly xerophytic shrubs such as *Caragana korshinskii*, and *Hippophae rhamnoides*, which are considered as a successful model for soil and water conservation and ecological restoration. Since rainfall is often the sole source of water replenishment in semiarid area, the availability of water for vegetation growth and survival is critical to the development of this rainfed revegetated ecosystem (Li et al., 2008; Wang et al., 2005) and merits great attention in the research of ecological restoration.

Understory rainfall within forested environments comprises throughfall, which reaches forest floors by passing directly through or dripping from tree canopies, and stemflow, which reaches forest floors after the incident rainfall is intercepted by leaves and branches and subsequently diverted to the boles of trees. Throughfall is usually the major understory rainfall flux with growing-season values often representing >70% of the incident rainfall. Levia and Germer (2015) found that stemflow values accounted for 3.5%, 11.3% and 19.0% of rainfall for tropical, temperate and semiarid regions, respectively.

Although stemflow may be volumetrically minor compared to throughfall at the stand scale, stemflow has been shown to be an important point-scale water flux. Stemflow is the process that directs precipitation down plant branches and stems. The redirection of water by this process is of ecohydrological and biogeochemical importance in forested and agricultural ecosystems because it is a spatially localized point input of water and nutrients at the plant stem (Levia and Frost, 2003; Moran et al., 2009; Voigt, 1960). Stemflow has a significant influence on runoff generation, soil erosion, groundwater recharge, spatial patterning of soil moisture, soil solution chemistry and the distribution of understory vegetation and epiphytes (Levia and Frost, 2003). However, stemflow is almost always considered as a minor component of forest canopy water budgets as compared to interception and throughfall, and therefore it receives minor attention and is under-represented in the literature (Llorens and Domingo, 2007). Most previous studies about stemflow have been conducted in tropical and temperate forests primarily (Levia and Germer, 2015; Tang, 1992; Wang et al., 2013); by contrast, relatively few studies on the characteristics of stemflow were documented for shrub vegetation in semiarid and arid regions (Carlyle-Moses, 2004), and almost no long-term experiments were conducted (more than 5 years).

Stemflow can be an important source to replenish soil moisture in arid and semiarid lands where water resources are limited (Tromble, 1987; Wang et al., 2011a). Wang et al. (2011a) found that stemflow water of *C. korshinskii* can reach a soil depth of 90 cm in Tengger Desert, it is favourable for the infiltrated water redistribution in the deeper soil profile of the root zone. Also, Zhang et al. (2013) agreed to the findings, he thought infiltration of stemflow alongside stems into deep soil profiles, creating islands of soil moisture, can be an important potential source of soil moisture allowing shrubs to remain physiologically active during drought spells. Návar and Bryan (1990) found that stemflow transported into the soil area close to the shrub stems showed a water input that was five times higher than by other areas beneath the shrub canopies in northeastern Mexico. Mauchamp and Janeau (1993) calculated that *Flourensia cernua* can channel approximately 50.0% of the

incident gross precipitation to the base of plant stems. Nulsen et al. (1986) reported that the infiltration depth of stemflow in mallee is as great as 28 m, and that this input water is possibly consumed in the dry period (Martinez-Meza and Whitford, 1996). In addition, other semiarid shrubs are also adapted to divert rainfall to their stems base as stemflow where it subsequently infiltrates the soil and remains available for plant uptake at deeper soil layers (Jiao et al., 2011; Li et al., 2008; Martinez-Meza and Whitford, 1996).

C. korshinskii and *H. rhamnoides* are the dominant woody species in the Loess Plateau. They are widely used for ecological restoration (Wei et al., 2007; Zhang et al., 2009). The effects of both rainfall and soil surface characteristics on soil water replenishment in re-vegetated ecosystems have been studied (Wang et al., 2011b; Wang et al., 2013; Zhang et al., 2013). However, the previous studies were mainly based on one year experiment data, the results obtained had occasionality. Thus, the current study prolonged the time of experiment (5 years) to improve the credibility of the results. Also, the effect of stemflow on infiltration patterns associated with the soil moisture replenishment is almost totally unexplored.

The aims of the study were to (1) determine the influence of rainfall on stemflow production and funnelling ratios of *C. korshinskii* and *H. rhamnoides* in a long-term observation; (2) understand the effect of stemflow on soil moisture in the Loess Plateau, China; (3) evaluate the infiltration process of stemflow water in the semiarid shrubs of vegetation restoration in the Loess Plateau, China.

MATERIALS AND METHODS

Study site

The experiments were conducted in *C. korshinskii* and *H. rhamnoides* plantations from 1st May to 30th September of 2009–2013 in the Anjiapo catchment, Dingxi County (35°35′N, 104°39′E) of Gansu province in western Chinese Loess Plateau. The annual mean precipitation is 420.0 mm with great seasonal variations. Over 60.0% of the precipitation falls between July and September and over 50.0% occurs in the form of storms. The average monthly air temperature ranges from –7.4 to 27.5˚C, with mean annual temperature of 6.3˚C. Average annual pan evaporation is 1510.0 mm. The range of altitude above sea level is from 1850 m to 2000 m. The soil belongs to Chernozem according to IUSS Working Group WRB (2006). It is developed on loess parent material has a relatively thick profile (Wang et al., 2010). The land uses in the study area include croplands, grasslands, artificial shrublands, and woodlands.

Vegetation restoration has been widely implemented in the area where *C. korshinskii* and *H. rhamnoides* were planted at 3×3 m spacing. *C. korshinkii* is nitrogen fixating leguminous shrub with even pinnate compound leaves and numerous slender branches, plant surface is smooth. Each specimen occupies the shape of a semi–sphere. Each pinna has 5–8 pairs of leaflets, which are ovate in shape with 7–8 mm in length and 2–5 mm in width. *H. rhamnoides* is non–leguminous shrub, the bulk of the plant is shaped like a cone with a main stem and narrow but thick leaves (length, 30–60 mm; width, 5–l0mm), and has rough bark. *C. korshinskii* had more developed root systems than *H. rhamnoides*, and more than 50.0% of fine root length was concentrated at depths between 0 and 40 cm for *C. korshinskii* and *H. rhamnoides* (Jian et al., 2014a). The sparse grasses were observed beneath the shrub canopies in *C. korshinskii* and *H. rhamnoides* plantation. Fig. 1 displays the general view the two shrub species and their leaf characteristics.

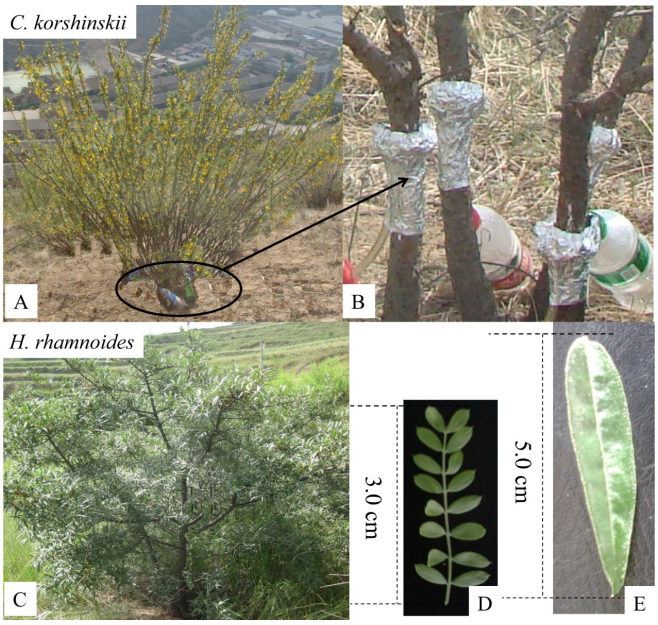

Fig. 1. Photographs showing *C. korshinskii* (A) and *H. rhamnoides* (C), the stemflow collection systems (B) and their leaf characteristics (D, *C. korshinskii*; E, *H. rhamnoides*).

Experimental design

Stemflow was measured for 10 fully mature *C. korshinskii* individuals and 10 fully mature *H. rhamnoides* individuals of 32 years old that were planted in 1989 as 2-year-old seedlings, which were located in flat terrain (we presumed that all of the stemflow infiltrated the soil beneath the shrubs), and they were exposed to sun and wind. The number, length, height and diameter of the branches were measured. The branch angle was calculated by the branch height from the ground surface to the tip of the branch vertically and the distance of the branch away from the stem horizontally. The shrub canopy projected area was calculated by taking the longest and shortest diameters through the centre of the fullest part of the canopy. Canopy bulk volume was calculated with the formula of an inverted cone (Table 1). The selected branch surface was burnished by fine sandpaper about 10 cm above the ground. Then, stemflow was collected using collars constructed from flexible aluminum foil plates that were fitted around the entire circumference of the branches. Each collar was sealed to the branch using all weather silicon caulking. The aluminium plate stemflow collectors extend less than 0.5 cm from the stem to prevent catching throughfall water as stemflow. Stemflow was caught from the collar to a collection container through a plastic hose (Fig. 1). By dividing stemflow volume of each shrub by its canopy projected area, we got the stemflow depth. Rainfall amount and intensity were measured with a standard rain gauge and a siphon–type recording rain gauge (model TE525, metric; Texas Electronics, Dallas, TX). An individual rainfall event was defined as a rainfall separated by a dry period of at least 6 h according to Dunkerley (2008).

Herwitz (1986) suggested that the quantitative importance of stemflow at the point scale can be expressed as a funnelling ratio, F:

$$F = V/(B \times P) \quad (1)$$

where, V is the stemflow volume (l), B is basal area of the tree (m^2), and P is the incident rainfall at the top of the canopy (mm).

Table 1. Descriptive statistics (mean ± standard deviation) of branches and canopy projection of the 10 sampled *C. korshinskii* individuals and 10 *H. rhamnoides* individuals used in the experiments.

	Shrub branch						
Species	Number	Diameter (cm)	Length (cm)	Height (cm)	Angle (°)[a]	Projected area (m^2)	Canopy bulk (m^3)
C. korshinskii	19±6	1.56±0.22	194±22	170±11	55±9	5.01±1.10	2.84±0.59
H. rhamnoides	11±3	1.69±0.34	206±27	191±17	59±11	4.24±1.47	2.69±0.67

[a] Angle in degree of the upward branch to the ground surface.

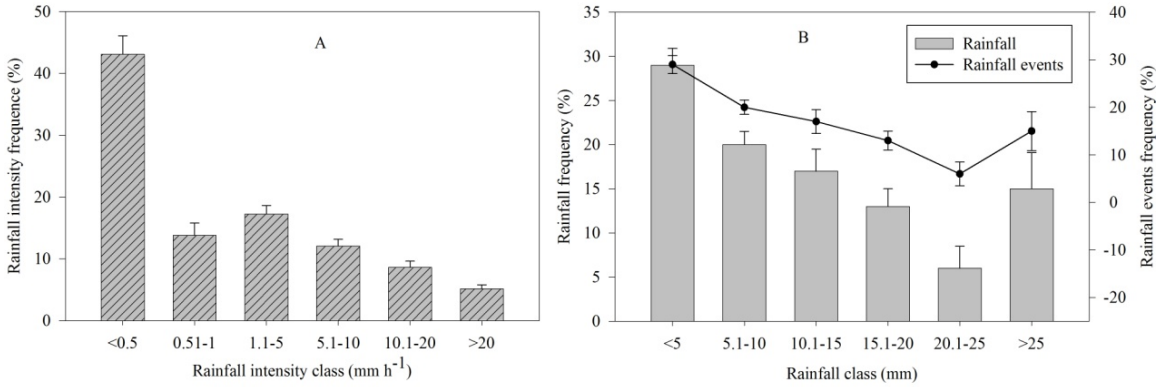

Fig. 2. The frequency distributions on the rainfall intensity, rainfall and rainfall events from 1st May to 30th September of 2009–2013.

The product $B \times P$ provides the volume of water that would have been caught by a rain gauge having an opening equal to that of the tree B. Thus, F represents the ratio of the amount of precipitation delivered to the base of the tree to the rainfall that would have reached the ground if the tree were not present. Funnelling ratios >1 indicate that canopy components other than the tree bole are contributing to stemflow (Carlyle-Moses and Price, 2006; Herwitz, 1986).

Another two shrub individuals for each species were selected to assess the influence on stemflow in soil moisture and the advancement patterning of stemflow in the soil, which were located in flat terrain to make sure no stemflow water and throughfall water to run off along the soil surface, and all of the stemflow infiltrated the soil beneath the shrubs. Volumetric soil moisture was measured by means of probes (Em 50, Decagon Devices, Pullman, WA, USA), installed at twenty depths in the area around the shrub stem and at about 30 cm from the plant periphery in the bare area (5, 10, 15, 20, 25, 30, 35, 40, 45, 50, 60, 70, 80, 90, 100, 120, 140, 160, 180, and 200 cm). The probe has three rods with 5.5 cm length interval at 1.5 cm. For probe installation, two same trenches were dug into the soil (around the shrub stem and at about 30 cm from the plant periphery in the bare area) with a sufficient width, the probes can be inserted. The probes were inserted into the soil through the undisturbed side of the trench and placed horizontally in the direction of the shrub site. The trenches were carefully refilled after the probes installation was completed, avoiding disturbance as far as possible, and the surface was contoured similar to the surrounding area. We installed the probes in April of 2008, the stabilization time is more than one year. We collected the data of wetting front depths within 24 hours after each rainfall event. Also, soil water content was measured every 30 days by means of oven–drying to validate the soil moisture data provided by the probes during the study period. Soil bulk density was measured at each soil layer where the soil moisture probes were installed by cutting ring method, the averaged soil bulk density is 1.24 g cm^{-3} and 1.31 g cm^{-3} for beneath the shrub canopies and in the interspaces, respectively (Jian et al., 2014a). In the current study, we ignored the water intercepted by organic litter of leaves and other materials beneath the shrub canopies, this is because of there were few organic litter of leaves and sparse grasses were observed beneath the shrub canopies. Also, in our previous study (Jian et al., 2014b), we found that there were small differences in soil evaporation between the area around the shrub stem and outside the shrub canopy, and this is due to the sparse vegetation (at 3 m ×3 m spacing), thus we ignored the influence of shading beneath shrubs to soil moisture.

Data analysis

Descriptive statistics were compiled for rainfall characteristics (depth and intensity), stemflow mounts, funnelling ratios and soil moisture. Data on soil moistures of these five types were analyzed using SPSS for Windows 18.0. A one-way ANOVA was performed to test the effects of the different locations (area around the stem and area outside the canopy for *C. korshinskii* and *H. rhamnoides*) on soil moisture. Stepwise multiple linear regressions (the type is backward elimination) (SPSS v18.0 for Windows) were used to analyze the relationship between stemflow and the canopy structures (height, projected area, canopy bulk, branch length, diameter and angle).

The multicollinearity was addressed. The soil moisture was measured with a probe matching the different depths of the soil profiles. Based on the principle of soil water balance, the cumulative infiltration can therefore be described as:

$$I = (S_e - S_b) \times Z_f \quad (2)$$

where S_e is the soil moisture (%) at the end stage, S_b is the soil moisture (%) in the beginning, Z_f is the infiltration depth (cm), and I is the cumulative infiltration (mm).

RESULTS AND DISCUSSION

Rainfall characteristics

There were 236 rainfall events during the experimental period (from 1st May to 30th September of 2009–2013). There were 75 rainfall events occurred during the day and 161 rainfall events occurred at night. The plants were not completely dry before 37 rainfall events. The results indicated that small rainfall intensity (< 0.5 mm h^{-1}) accounted for 43.9% of rainfall events (Fig. 2A). The annual rainfall averaged 363.2 mm, and

the distribution of rainfall was presented in Fig. 2B. Stemflow was measurable for 151 rainfall events during the experimental period.

Stemflow characteristics

The stemflow was strongly related to rainfall. The stemflow increased with increasing rainfall depth and there was a significantly positive linear relationship between them (Fig. 3). The rainfall threshold for stemflow generation was 0.5 and 2.5 mm for *C. korshinskii* and *H. rhamnoides* according to the linear regression equations (Diskin, 1970). The correlations between stemflow and mean rainfall intensity and maximum rainfall intensity in 10 minutes were weak (Data not shown). Stemflow values averaged 6.7% and 2.4% of total rainfall with a range of 1.6–17.8% and 0.06–4.6% for *C. korshinskii* and *H. rhamnoides* (Fig. 4).

Stepwise multiple linear regression equation of stemflow with the canopy structures (height, projected area, canopy bulk, branch length, diameter and angle) set out in Eq. (3) and (4) for *C. korshinskii* and *H. rhamnoides* (Aboal et al., 1999). The equation contained two independent variables indicated that stemflow increase with the increases in the projected area and branch angle.

$$SF_{C.korshinskii} = 0.24X_1+0.53X_2+32.25, \quad R^2 = 0.88, F = 26.47, P<0.001 \quad (3)$$

$$SF_{H.\ rhamnoides} = 0.16X_1+0.46X_2+27.13 \quad R^2 = 0.79, F = 20.00, P<0.001 \quad (4)$$

where, $SF_{C.korshinskii}$ and $SF_{H.\ rhamnoides}$, stemflow volume (ml); X_1, Projected area (m^2); X_2, branch angle (°).

Multiple linear regression equations of stemflow with the rainfall depth, mean rainfall intensity and maximum rain intensity in 10 minutes (I_{10}) were presented in Table 2 suggested that stemflow increased as 12.6–18.0% and 0.7–5.9% with increasing the rainfall and I_{10}, respectively, but as 1.1–2.6% with the decrease in the mean rainfall intensity, indicating that stemflow was more governed by the rainfall depth than the mean rainfall intensity and I_{10} for *C. korshinskii* and *H. rhamnoides*.

Funnelling ratios

When rainfall was less than 17.0 mm, the funnelling ratios were highly variable, however, the stable funnelling ratios were found when rainfall was greater than 17.0 mm for *C. korshinskii* (Fig. 5). The funnelling ratios of *H. rhamnoides* first increased until a threshold value of 10.0 mm and then the funnelling ratios began to be stable. The mean funnelling ratio was 167.4 and 59.1, and ranging from 38.9 to 444.4, 1.5 to 114.7 for *C. korshinskii* and *H. rhamnoides*.

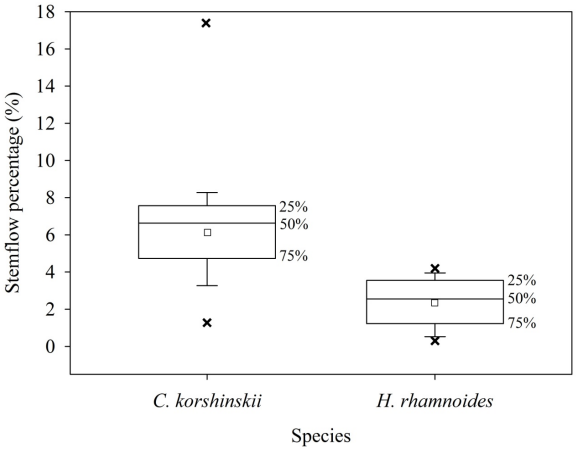

Fig. 4. Box–and–whisker diagrams showing median, 25, 50 and 75 percentiles and standard deviation for individual stemflow percentage from May to September of 2009–2013 for *C. korshinskii* and *H. rhamnoides*. (□) represents mean value, (×) maximum and minimum value.

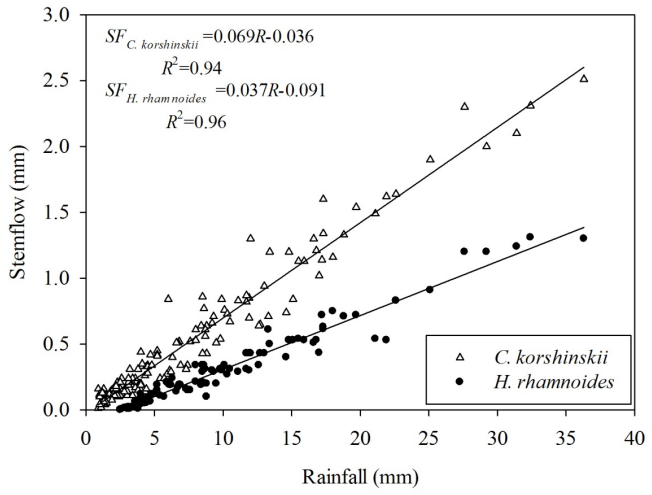

Fig. 3. Relationship between rainfall and individual stemflow from May to September of 2009–2013 for *C. korshinskii* and *H. rhamnoides*.

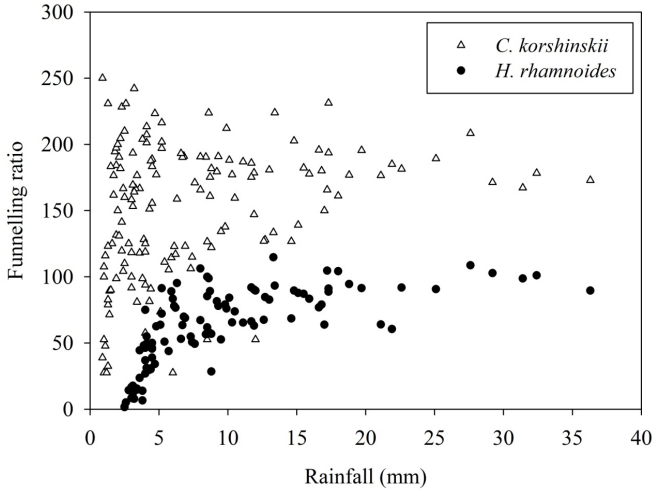

Fig. 5. Relationship between funneling ratio and daily rainfall from May to September of 2009–2013 for *C. korshinskii* and *H. rhamnoides*.

Table 2. Regression equations and coefficient values between stemflow and rainfall depth, mean rainfall intensity and maximum rain intensity in 10 minutes.

Shrubs	Equation	*r*	*F* value	Sig. level
C. korshinskii	$SF = -0.16+ 0.18P - 0.026I + 0.059I_{10}$	0.831	40.56	<0.0001
H. rhamnoides	$SF = -0.14+0.13P - 0.011I + 0.007I_{10}$	0.724	31.29	<0.0001

**SF*, stemflow (mm); *P*, rainfall depth (mm); *I*, rainfall intensity (mm h^{-1}); I_{10}, maximum rain intensity in 10 minutes; *r*, correlation coefficient.

Soil water status

Stemflow water can be transported into deeper soil layers around shrub stem than that outside the shrub canopy, producing more infiltration of water in the root zone. The wetting front depths increased with increasing rainfall depths and followed significant logarithmic equations for *C. korshinskii* and *H. rhamnoides* (Fig. 6). The wetting front depths in the area around stem were 1.4–6.7 and 1.3–2.9 times deeper than that outside the canopy for *C. korshinskii* and *H. rhamnoides* (rainfall depths were ranging from 1.1 to 36.3 mm). Soil moisture at soil depth 0–200 cm was 25.6% and 23.4% higher in area around stem than that away from the shrubs for *C. korshinskii* and *H. rhamnoides* from May to September of 2012. During the experimental period (from May to September of 2009–2013), the soil moisture in the other four years (2009, 2010, 2011 and 2013) had the similar trend with the year of 2012 (Data not shown) (Fig. 7).

Advance of the wetting front

The heaviest rainfall event, it occurred on 12th August, which was used to analyze the advance of the wetting front (Fig. 8A). In the area around the stem of *C. korshinskii*, after rainfall lasted for 140 min, the wetting front reached 5 cm. The soil moisture increased rapidly. The wetting front took about 60 min from 5 cm to 10 cm, 10 cm to 15 cm and 15 cm to 20 cm, and reached the constant values of 27.4%, 23.2% and 20.5%, respectively. After approximately 130 min of slow increase, the soil moisture became stable at 14.0% in a depth of 25 cm. The wetting front reached a depth of 30 cm after 12 h. The soil moisture reached approximately 12.1% at a depth of 50 cm after a period of slow increase. The wetting front of this position was as depth as 120 cm approximately 7 days later (Fig. 8B).

In the area outside the canopy of *C. korshinskii*, the wetting front reached a depth of 5 cm approximately 90 min earlier than that around the stem of *C. korshinskii*, but took longer time to achieve the second stable level (10 cm), at 25.6% after the initial 10.8%. At this position, the wetting front took approximately 13 h to reach the depths of 15 cm. The water infiltrated to a depth of 50 cm ultimately (Fig. 8C).

The wetting front reached a depth of 5 cm approximately 60 min later in the area around the stem of *H. rhamnoides* than that around the stem of *C. korshinskii*. After approximately 220 min of rapid increase, the soil moisture remained at a constant value of 23.0% in a depth of 10 cm. At this position, the wetting front took approximately 7 and 9 h to reach the depths of 15 cm and 20 cm. The water finally infiltrated to a depth of 100 cm (Fig. 8D).

The area outside the canopy of *H. rhamnoides* had the lowest initial soil moisture. The wetting front took 70 min from the beginning of precipitation to reach a depth of 5 cm. After 360 min with a nearly linear slow increase, the soil moisture tented to be constant at a value of 22.4%. The wetting front moved

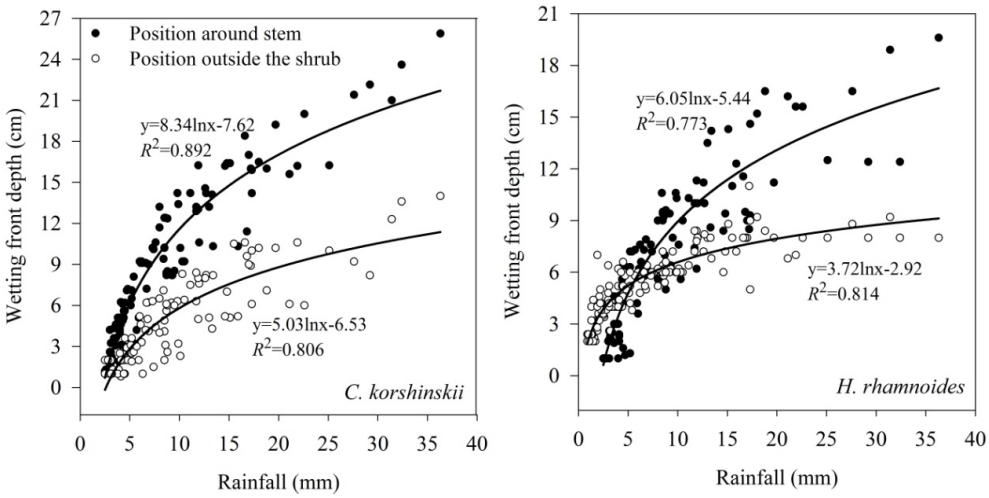

Fig. 6. Relationship between rainfall depths and wetting front depths in the soil around the stem and outside the canopy from May to September of 2009–2013 for *C. korshinskii* and *H. rhamnoides*.

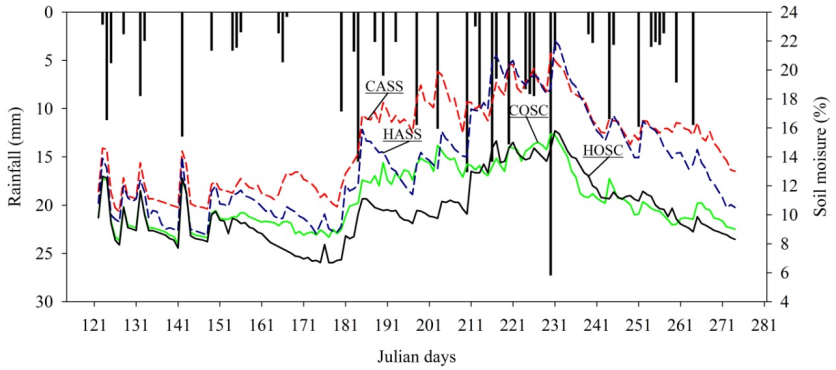

Fig. 7. Soil moisture distribution in the soil profile around the shrub stem and outside the shrub canopy from May to September of 2012 for *C. korshinskii* and *H. rhamnoides*. Red line, *C. korshinskii* around the shrub stem (CASS); green line, *C. korshinskii* outside the shrub canopy (COSC); blue line, *H. rhamnoides* around the shrub stem (HASS); black line, *H. rhamnoides* outside the shrub canopy (HOSC); the bar, rainfall.

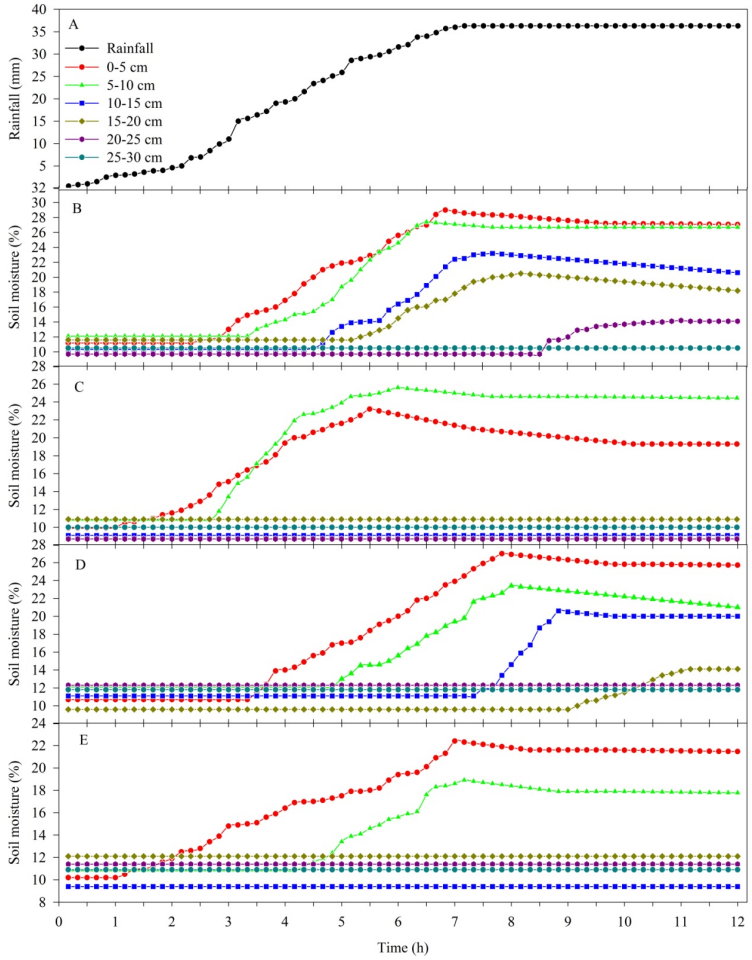

Fig. 8. The wetting front infiltration processes in the area around the shrub stem and that outside the shrub canopy for *C. korshinskii* and *H. rhamnoides*. A, rainfall processes; B and C, the area around the shrub stem and that outside the shrub canopy for *C. korshinskii*; D and E, the area around the shrub stem and that outside the shrub canopy for *H. rhamnoides*.

from 5 cm to 10 cm, which took 190 min. At this position, the soil moisture at a depth of 15 cm until 14 h later. The water infiltrated to a depth of 50 cm approximately 4 days later. The soil moisture below 50 cm depth did not change (Fig. 8E).

The relationship between rainfall and cumulative infiltration

The cumulative infiltration I (mm) increased with increasing rainfall depth P (mm), followed significantly positive linear relationships in the area around shrub stem and outside the canopy for *C. korshinskii* and *H. rhamnoides* (Fig. 9). They can be presented mathematically as:

$$\begin{aligned} I_{\text{around stem of } C.\ korshinskii} &= 0.58P - 1.31, & R^2 &= 0.92 \\ I_{\text{outside canopy of } C.\ korshinskii} &= 0.36P - 1.16, & R^2 &= 0.78 \\ I_{\text{around stem of } H.\ rhamnoides} &= 0.48P - 1.43, & R^2 &= 0.87 \\ I_{\text{outside canopy of } H.\ rhamnoides} &= 0.47P - 1.80, & R^2 &= 0.88 \end{aligned} \quad (5)$$

Stemflow properties

The cumulative stemflow amounts were 76.9 and 31.5 mm during the experimental period (from May to September of 2009–2013) for *C. korshinskii* and *H. rhamnoides*. However, expressed as percentages of gross rainfall, the mean stemflow percentage of *C. korshinskii* was 6.9%, which was 2.5 times greater than *H. rhamnoides*. All these results indicated that *C. korshinskii* had stronger ability of stemflow generation than *H. rhamnoides*.

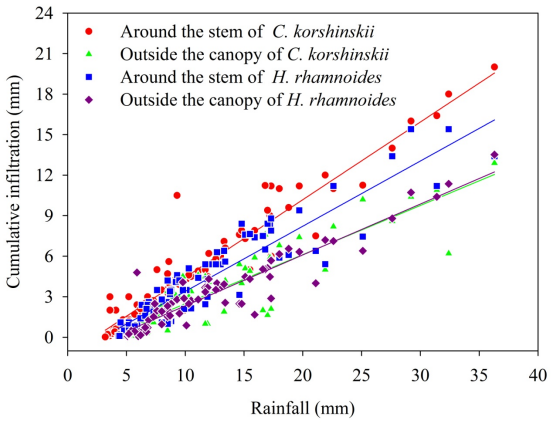

Fig. 9. The relationship between precipitation and cumulative infiltration.

Rainfall of at least 0.5 and 2.5 mm was necessary to initiate stemflow according to the linear regression based on the five years experiment (Fig. 3). Almost all the previous studies obtained the rainfall threshold according to one year experiment (Carlyle-Moses, 2004; Li et al., 2008). This threshold is consistent with the values reported by previous studies about shrubs in arid and semiarid regions (Enright, 1987; Martinez-Meza and Whitford, 1996; Li et al., 2008; Wang et al., 2013). The studies of Wang et al. (2011b) and Zhang et al. (2013) were based on one year experiment data in the Tengger Desert which reported that an antecedent precipitation of 2.2 and 1.3 mm was necessary for stemflow initiation for *C. korshinskii*. Our result (0.5 mm) was less than the above studies, this may be due to the different amount of data, different rainfall characteristics and environmental conditions. *C. korshinskii* had lower rainfall threshold and stronger ability to generate stemflow than *H. rhamnoides*, which may be due to the smooth bark associated with *C. korshinskii*. *C. korshinskii* has small strip- or linear-shaped leaves, and the twigs, branches and leaves are covered by wax layers, which result in a smooth "funnel" to generate stemflow. Our previous study found that *H. rhamnoides* has the greater water storage capacity than *C. korshinskii*, which is associated with smooth bark had been shown to be considerably less than that of rough bark (Jian et al., 2013). By contrast, *H. rhamnoides* has numerous branches with thick dense leaves, and there are many diagonal cracks in the surface of branches. The relative rough bark and thick leaves in *H. rhamnoides* than *C. korshinskii* may store more rain water, therefore leading to greater water storage capacity and lower efficiency of stemflow production.

Stemflow increased with increasing rainfall depth, followed a positive linear function, which has been reported by other studies (Carlyle-Moses, 2004; Carlyle-Moses and Price, 2006; Martinez-Meza and Whitford, 1996; Wang et al., 2013). The weak correlations were found between stemflow and mean rainfall intensity, maximum rain intensity in 10 minutes, this may be because of most of the initial rainfall was stored by the canopy during rainfall events with low intensity. With the increase of rainfall input, the shrub canopy becomes saturated gradually

and thus the area contributing to stemflow increased until a rainfall threshold was reached that saturated the whole canopy (Llorens and Gallart, 2000).

Multiple Stepwise linear regression equation of stemflow with the canopy structures indicated that projected area and branch angle governed the stemflow production for *C. korshinskii* and *H. rhamnoides* (Eqs. (3)–(4)). The inclination of the main branches was various in all the shrubs, with a relatively wide range of insertion angles (46–64°, *C. korshinskii*; 48–70°, *H. rhamnoides*; Table 1). It is known that stemflow is enhanced when the plant structure is cone or funnel shaped, since vertically orientated branches with insertion angles greater than 45° measured above the horizontal promote water flow towards the trunk (Levia and Germer, 2015; Pypker et al., 2005). A funnel shape is indeed a prerequisite for high stemflow production but is not sufficient on its own because the position of the leaves and their orientation and size also affect stemflow (Nanko et al., 2006; Park and Cameron, 2008).

The funnelling ratio differed greatly for different rainfall events, depending on the rainfall depth and rainfall intensity. There were rainfall depths thresholds of 17 and 10.0 mm for *C. korshinskii* and *H. rhamnoides*. When rainfall was less than the threshold, the funnelling ratio increased with increasing rainfall depth and had a stable trend when the rainfall threshold was reached. Funnelling ratios have been found to be greater than 10, and in some rainfall events, far greater than 10. Our studies found that there can be ten or even a hundred times the rainfall amount that may be transported into the root area by stemflow as compared to the area outside the shrub canopy. The excess water effectively supplied the moisture of the upper soil layer, and then formed a greater water potential gradient among the different soil layers. Therefore, the water can infiltrate to the deeper soil becomes higher around shrub stems. Also, stemflow water of shrubs in semiarid regions may be distributed to a deep soil layer by preferential flow along root channels (Martinez-Meza and Whitford, 1996; Wang et al., 2011b).

Soil water

The soil moisture profiles display different vertical structures among the area around stem and outside the canopy for *C. korshinskii* and *H. rhamnoides*. The infiltration process is controlled by several biophysical factors, including ground cover, soil type, hydraulic properties, rainfall characteristics (such as rainfall amount, intensity and duration), meteorological conditions, seasonality and shrub canopy structure and soil surface features (Laio et al., 2001; Zhang et al., 2013). The wetting fronts of the area outside the canopy reached a depth of 5 cm more quickly than that around stem because most of the initial rainfall was intercepted by the canopy without producing stemflow for *C. korshinskii* and *H. rhamnoides*. With increasing soil depth, the advance of the wetting front moved quicker in the area around stem than that outside the canopy, this may be due to the existence of the preferential flow and roots (Fig. 8). The wetting front advanced to depths of 120 and 100 cm at the area around stem and to depths of 50 cm at the area outside the canopy for *C. korshinskii* and *H. rhamnoides* suggested that more rain water can be conserved into the deeper soil layers through shrub stemflow. Wang et al. (2011a) also found that stemflow can double the effective rainfall in terms of the soil moisture replenishment in the root zone below 5 cm depth. Our previous study found that *C. korshinskii* had more developed root systems than *H. rhamnoides*, which resulted in more soil macropore and preferential flow (Jian et al., 2014a). Stemflow water can effectively supply the soil profile and increase the cumulative infiltration (Fig. 9). Soil moisture was enhanced in the area outside the shrub canopy, only when rainfall depth is > 4.7 and 5.1 mm, which is an effective rainfall for the area for *C. korshinskii* and *H. rhamnoides*. While for the area around stem of *C. korshinskii* and *H. rhamnoides*, the corresponding threshold values are 3.2 and 4.3 mm (Fig. 9). Consequently, stemflow strengthened the effective rainfall in terms of the soil moisture enhancement in the root zone. Also, Wang et al. (2011b) found that the soil profile can be effectively replenished by stemflow water and increase the cumulative infiltration for medium and large rainfall. The corresponding threshold value is about 4 mm which replenish the soil moisture at the profile deeper than 5 cm for the stem basal area of *C. korshinskii*, comparing it to the rainfall of 3.5 mm that limited the soil moisture increment within the upper layer of 5 cm. Zheng et al. (2015) and Wei and Wu (2013) reported that the litter intercepting rate averaged 14.2% in *C. korshinskii* and 20.8% in *H. rhamnoides* stands, respectively in west of Liaoning Province, China. However, there were few organic litter of leaves and sparse grasses were observed beneath the shrub canopies in the current study, so we ignored the water intercepted by them. Also, in our previous study (Jian et al., 2014b), we found that there were little differences in soil evaporation between the area around the shrub stem and outside the shrub canopy, thus, we eliminated the disturbance of shading beneath shrubs to soil moisture.

CONCLUSIONS

A better understanding of the stemflow variability and its contribution to soil moisture is essential in the re-vegetation efforts of inhabited semiarid regions. Funnelling ratios all are larger than 1 for *C. korshinskii* and *H. rhamnoides*, indicating that branches and stem were fully contributing to stemflow generation. Relatively larger values of funnelling ratios for *C. korshinskii* suggests that *C. korshinskii* was most effective for stemflow production, which results in more water that can be conserved into the deep layers of the soil. Deeper wetting fronts and higher water contents in the root area around the two shrubs than that in the area outside the shrub canopy in the study suggests that shrub stemflow can be an available moisture source for plant growth under arid conditions and that water redistribution by shrubs can be considered an essential property of the plants that contributes to the stability of shrub communities in harsh environments.

Because of the structural properties of the shrubs and the surface characteristics of their leaves provide the potential for deposition and accumulation of dust and dry fall on the leaf surfaces, so stemflow could transport those materials to the soil under the shrub, which could contribute to the development of 'fertile islands' under shrub canopies. Higher values of funnelling ratios for *C. korshinskii* and *H. rhamnoides* imply that stemflow in the two shrubs can also be an available nutrient source for plant growth under semiarid conditions.

Acknowledgements. This project was supported by National Key Research Priorities Program of China (2016YFC0402402); National Natural Science Foundation of China (31700370); National Natural Science Foundation of China (51409116); Startup Research Fund of Zhengzhou University (1512323001); Institution of higher learning key scientific research project, Henan Province (16A570010); China postdoctoral science foundation (2016M602255); Henan province postdoctoral science foundation; National Natural Science Foundation of China (91025015).

REFERENCES

Aboal, J. R., Morales, D., Hernandez, M., 1999. The measurement and modelling of the variation of stemflow in a laurel forest in Tenerife, Canary Islands. Journal of Hydrology, 221, 3–4, 161–175.

Carlyle-Moses, D.E., 2004. Throughfall, stemflow and canopy interception loss fluxes in a semi–arid Sierra Madre Oriental matorral community. Journal of Arid Environments, 58, 181–202.

Carlyle-Moses, D.E., Price, A.G., 2006. Growing–season stemflow production within a deciduous forest of southern Ontario. Hydrological Processes, 20, 3651–3663.

Diskin, M.H., 1970. Definition and uses of the linear regression model. Water Resources Research, 6, 1668–1673.

Dunkerley, D., 2008. Identifying individual rain events from pluviograph records: a review with analysis of data from an Australian dry land site. Hydrology Processes, 22, 5024–5036.

Enright, N.J., 1987. Stemflow as a nutrient source for nikau palm (*Rhopalostylis sapida*) in a New Zealand forest. Australian Journal of Ecology, 12, 17–24.

Herwitz, S.R., 1986. Infiltration–excess caused by stemflow in a cyclone–prone tropical rainforest. Earth Surface Processes and Landforms 11, 401–412.

IUSS Working Group WRB., 2006. World reference base for soil resources 2006. 2nd edition. World Soil Resources Reports No. 203. FAO, Rome.

Jian, S.Q., Zhao, C.Y., Fang, S.M., Yu, K., 2013. Water storage capacity of the canopy dominated by *Caragana korshinsk*ii and *Hippophae rhamnoides* in hilly and gully region on the Loess Plateau of Northwest China. Chinese Journal of Plant Ecology, 37, 1, 45–51. (In Chinese with English abstract.)

Jian, S.Q., Zhao, C.Y., Fang, S.M., Yu, K., 2014a. Distribution of fine root biomass of main planting tree species in Loess Plateau, China. Chinese Journal of Applied Ecology, 25, 7, 1905–1911. (In Chinese with English abstract.)

Jian, S.Q., Zhao, C.Y., Fang, S.M., Yu, K., 2014b. Soil water content and water balance simulation of *Caragana korshinskii* Kom. in the semiarid Chinese Loess Plateau. Journal of Hydrology and Hydromechanics, 62, 2, 89–96.

Jiao, F., Wen, Z.M., An, S.S., 2011. Changes in soil properties across a chronosequence of vegetation restoration on the Loess Plateau of China. Catena, 86, 110–116.

Kéfi, S., Rietkerk, M., Alados, C., Pueyo, Y., Papanastasis, V., Elaich, A., De Ruiter, P. 2007. Spatial vegetation patterns and imminent desertification in Mediterranean arid ecosystems. Nature, 449, 213–217.

Laio, F., Porporatro, A., Ridolfi, L., Rodriguez–Iturbe, I., 2001. Plants in water–controlled ecosystems: active role in hydrologic processes and response to water stress. Advances in Water Resources, 24, 707–723.

Levia, D.F., Frost, E.E. 2003. A review and evaluation of stemflow literature in the hydrologic and biogeochemical cycles of forested and agricultural ecosystems. Journal of Hydrology, 274, 1–4, 1–29.

Levia, D.F., Germer, S., 2015. A review of stemflow generation dynamics and stemflow–environment interactions in forests and shrublands. Reviews of Geophysics, 53, DOI: 10.1002/2015RG000479.

Li, X.Y., Liu, L.Y., Gao, S.Y., Ma, Y.J., Yang, Z.P., 2008. Stemflow in three shrubs and its effect on soil water enhancement in semiarid loess region of China. Agricultural and Forest Meteorology, 148, 10, 1501–1507.

Llorens, P., Domingo, F., 2007. Rainfall partitioning by vegetation under Mediterranean conditions. A review of studies in Europe. Journal of Hydrology, 335, 37–54.

Llorens, P., Gallart, F., 2000. A simplified method for forest water storage capacity measurement. Journal of Hydrology, 240, 131–144.

Martinez-Meza, E., Whitford, W.G., 1996. Stemflow, throughfall and channelization of stemflow by roots in three Chihuahuan desert shrubs. Journal of Arid Environments, 32, 3, 271–287.

Mauchamp, A., Janeau, J.L., 1993. Water funnelling by the crown of *Flourensia cernua*, a Chihuahuan Desert shrub. Journal of Arid Environments, 25, 299–306.

Moran, M.S., Scott, R.L., Keefer, T.O., Emmerich, W.E., Hernandez, M., Nearing, G.S., Paige, G.B., Cosh, M.H., O'Neill, P.E., 2009. Partitioning evapotranspiration in semiarid grassland and shrubland ecosystems using time series of soil surface temperature. Agricultural and Forest Meteorology, 149, 59–72.

Nanko, K., Hotta, N., Suzuki, M., 2006. Evaluating the influence of canopy species and meteorological factors on throughfall drop size distribution. Journal of Hydrology, 329, 422–431.

Návar, J., Bryan, R.B., 1990. Interception loss and rainfall redistribution by three semi–arid growing shrubs in northeastern Mexico. Journal of Hydrology, 115, 51–63.

Noy-Meir, I. 1973. Desert ecosystems: environment and producers. Annual Review of Ecology and Systematics, 4, 25–51.

Nulsen, R.A., Bligh, K.J., Baxter, I.N.E.J.S., Imrie, D.H., 1986. The fate of rainfall in a mallee and heath vegetated catchment in southern Western Australia. Australian Journal of Ecology, 11, 361–371.

Park, A., Cameron, J.L., 2008. The influence of canopy traits on throughfall and stemflow in five tropical trees growing in a Panamanian plantation. Forest Ecology and Management, 255, 1915–1925.

Pypker, T.G., Bond, B.J., Link, T.E., Marks, D., Unsworth, M.H., 2005. The importance of canopy structure in controlling the interception loss: examples from a young and old-growth Douglas-fir forests. Agricultural and Forest Meteorology, 130, 113–129.

Tang, C.Y., 1992. A research on the effects of artificial masson pinus forest on rainfall partitioning in subtropical area. Acta Geographica Sinica, 47, 6, 545–551. (In Chinese with English abstract.)

Tromble, J.M., 1987. Water interception by two arid land shrubs. Journal of Arid Environments, 15, 65–70.

Voigt, G.K. 1960. Distribution of rainfall under forest stands. Forest Science, 6, 1, 2–10.

Wang, X.P., Li, X.R., Zhang, J.G., Zhang, Z.S., Berndtsson, R. 2005. Measurement of rainfall interception by xerophytic shrubs in revegetated sand dunes. Hydrological Sciences Journal 50: 897–910.

Wang, X.P., Wang, Z.N., Berndtsson, R., Zhang, Y.F., Pan, Y.X., 2011a. Desert shrub stemflow and its significance in soil moisture replenishment. Hydrology and Earth System Sciences, 15, 561–567.

Wang, X.P., Zhang Y.F., Wang, Z.N., Pan, Y.X., Hu, R., Li, X.J., Zhang, H., 2013. Influence of shrub canopy morphology and rainfall characteristics on stemflow within a revegetated sand dune in the Tengger Desert, NW China. Hydrological Processes, 27, 10, 1501–1509.

Wang, Y.Q., Shao, M.A., Shao, H.B., 2010. A preliminary investigation of the dynamic characteristics of dried soil layers on the Loess Plateau of China. Journal of Hydrology, 381, 1–2, 9–17.

Wang, Y.Q., Shao, M.A., Zhu, Y.J., Liu, Z.P., 2011b. Impacts of land use and plant characteristics on dried soil layers in different climatic regions on the Loess Plateau of China. Agricultural and Forest Meteorology, 151, 437–448.

Wei, T.X., Zhu, J.Z., Zhang, J.J., Bi, H.X., Zhu, Q.K., 2007. Protective forest system at small watershed in the gullied-hilly loess area based on water balance on the Loess Plateau. Research Soil Water Conservation 14, 179–183. (In Chinese with English abstract.)

Wei, Y.L., Wu, Y.Z., 2013. Study on interception characteristics of different plants. Journal of Soil and Water Conservation, 29, 3, 46–53. (In Chinese with English abstract.)

Zhang, G.H., Tang, M.K., Zhang, X.C., 2009. Temporal variation in soil detachment under different land uses in the Loess Plateau of China. Earth Surface Processes and Landforms, 34, 1302–1309.

Zhang, Y.F., Wang, X.P., Hu, R., Pan, Y.X., Zhang, H., 2013. Stemflow in two xerophytic shrubs and its significance to soil water and nutrient enrichment. Ecological Research, 28, 567–579.

Zheng, Y.Y, Xu, X. H., Zhang, Y., Ou, Y., Yan, B.X.，Wang, P.J., Cui, H., F., Cui B., 2015. Characteristics of precipitation interception in soil and water conservation forests of the Northeast black soil areas of China. Acta Prataculturae Sinica, 24, 6, 16–24. (In Chinese with English abstract.)

Received 12 June 2017
Accepted 11 September 2017

J. Hydrol. Hydromech., 66, 2018, 1, 87–96
DOI: 10.1515/johh-2017-0031

Microstructural strength of tidal soils – a rheometric approach to develop pedotransfer functions

Nina Stoppe*, Rainer Horn

Institute of Plant Nutrition and Soil Science, Christian-Albrechts-University Kiel, Hermann-Rodewaldstr. 2, D-24118 Kiel, Germany.
* Corresponding author. Tel.: 0049 431 880-4079. Fax: 0049 431 880-2940. E-mail: n.stoppe@soils.uni-kiel.de

Abstract: Differences in soil stability, especially in visually comparable soils can occur due to microstructural processes and interactions. By investigating these microstructural processes with rheological investigations, it is possible to achieve a better understanding of soil behaviour from the mesoscale (soil aggregates) to macroscale (bulk soil). In this paper, a rheological investigation of the factors influencing microstructural stability of riparian soils was conducted. Homogenized samples of Marshland soils from the riparian zone of the Elbe River (North Germany) were analyzed with amplitude sweeps (AS) under controlled shear deformation in a modular compact rheometer MCR 300 (Anton Paar, Germany) at different matric potentials. A range physicochemical parameters were determined (texture, pH, organic matter, $CaCO_3$ etc.) and these factors were used to parameterize pedotransfer functions.

The results indicate a clear dependence of microstructural elasticity on texture and water content. Although the influence of individual physicochemical factors varies depending on texture, the relevant features were identified taking combined effects into account. Thus, stabilizing factors are: organic matter, calcium ions, $CaCO_3$ and pedogenic iron oxides; whereas sodium ions and water content represent structurally unfavorable factors. Based on the determined statistical relationships between rheological and physicochemical parameters, pedotransfer functions (PTF) have been developed.

Keywords: Rheology; Deformation; Soil micromechanics; Structural stability; Structure degradation; Pedotransfer functions.

INTRODUCTION

The tidal part of the Elbe River (North Germany) has been modified several times over the past decades by dredging and riverbank reinforcement to meet cargo vessel requirements. This has changed the hydromorphology of the Tidal Elbe estuary by an enhanced volume of sediment being transported upstream and a more pronounced gradient in salinity (Bergemann, 1995; Freitag et al., 2007; Garniel and Mierwald, 1996). Through specific hydraulic-engineering structures, dynamic processes in stream margins and riparian zones are suppressed. To return the Tidal Elbe estuary to a more natural state, anthropogenic structures such as artificial rip-rap revetments could be removed and dynamic processes driven by the tide enhanced. However, the impact of these interventions to tidal soil stability is unknown and requires investigation.

The quantification of structural stability is a central field of research, as soil structure possesses many functions e.g. resistance against deformation and erosion, and there have been ambitious projects and discussions on it for several decades as reviewed by e.g. Bronick and Lal (2005) or Warkentin (2008). In classical soil mechanics, the stability of soil structure is often characterized by examining compression and/or shear behavior. These analyses on the mesoscale provide information about the reaction of the regarded total soil volume towards stresses at defined boundary conditions. Parameters such as precompression stress (Pc), angle of internal friction (ϕ) and cohesion (c) at the aggregate or bulk soil scale provide valuable information about mechanical response, but cannot identify the causes of mechanical stability (Hartge and Horn, 2016). The reasons for different strength properties, particularly in visually comparable soils that to the eye have similar colour, texture and structure, can manifest at the microscale from interparticle to microaggregate interactions. Knowledge of the processes at the microscale has been made possible in recent years by rheological studies of natural soils (e.g. Ghezzehei and Or, 2001; Holthusen, 2010; Markgraf and Horn, 2009; Pértile et al., 2016; Torrance, 1999). Key drivers of rheological behavior identified in these studies are soil organic matter and varying electrolyte concentrations (e.g. Carotenuto et al., 2015; Holthusen et al., 2012c; Markgraf et al., 2012b). In tidal soils, Markgraf et al. (2012a) found differences in the rheology and therefore the microstructural stability between natural, Na-affected and cultivated gypsum amended in a Salic Tidalic Fluvisol from Sevilla, Spain. They found dispersing effects due to repulsive forces related to Na^+ under natural, sodic-saline conditions, and aggregating effects from gypsum amelioration based on attractive forces for Ca^{2+}. In a more humid climate, the repulsive forces of Na^+ and the strengthening effect of Ca^{2+} were observed in the micro-mechanical strength of soils from two sites of the riparian zone of the Elbe River estuary, taking salinity gradient and soil maturation into account (Baumgarten et al., 2012).

Recent studies confirm that many further physicochemical parameters affect the rheological response of soils including: soil texture and water content (Jeong et al., 2010; Markgraf et al., 2006), cation exchange capacity and electric conductivity (EC) (Baumgarten et al., 2012; Markgraf and Horn, 2006), carbonate content and pH (Markgraf et al., 2012a) as well as iron (hydr)oxides (Markgraf and Horn, 2007). However, the combined effect of physicochemical parameters influencing the microstructural stability has received limited attention. For tidal soils, such information is extremely important to assess the potential risks and benefits of interventions to alter the hydrodynamic properties of rivers or to remove past anthropogenic structures that affect tidal response. To address this gap in knowledge, this study compares physicochemical factors to rheological response of tidal soils. Samples are taken from a natural gradient in salinity and sodicity along the estuary and from chronosequences of Salic Fluvisols to Calcaric Fluvisols. By exploring a wide range of physicochemical parameters we identify the statistically significant factors and attempt to parameterize them into pedotransfer functions.

The aim is to facilitate a mathematical estimate of the rheological parameter *integral z*, which has been introduced by Markgraf and Horn (2009) and quantifies the microstructural stiffness.

MATERIAL AND METHODS

Soil samples

Twenty-two sites along the North German Elbe estuary were chosen to provide a gradient in salinity and sodicity (Fig. 1).

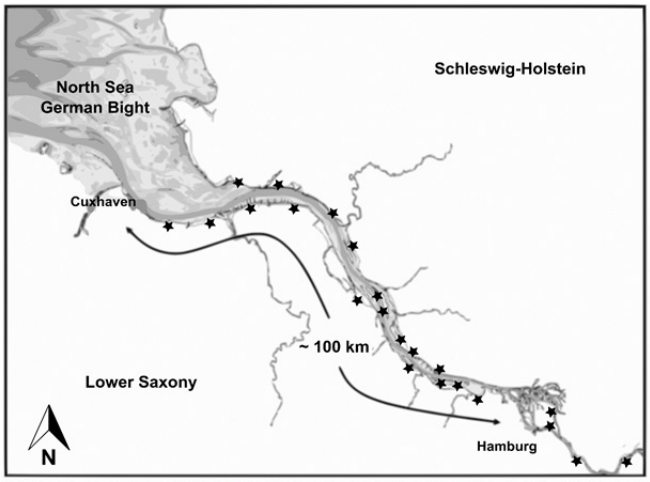

Fig. 1. The Elbe estuary sampling locations: stars depict the sites (modified after Freitag et al. (2007)).

At each site, three soil pits were dug in the embankment foreland at three elevations in relation to the mean water levels: profile 1 above mean high tide (MHWL), where commonly grassland had developed; profile 2 in the range of MHWL with partly extensive reed vegetation and profile 3 below MHWL with sparse vegetation (Fig. 2). Disturbed samples were taken from each profile at defined depths: in profile 1 at 10, 30, 50 and 70 cm; in profile 2 at 10, 30 and 50 cm; in profile 3 at 10 and 30 cm beneath ground level. After transferring the soil to the laboratory in properly sealed plastic bags, the samples were air dried, homogenized with a pestle and passed through a sieve with a mesh size of 2 mm.

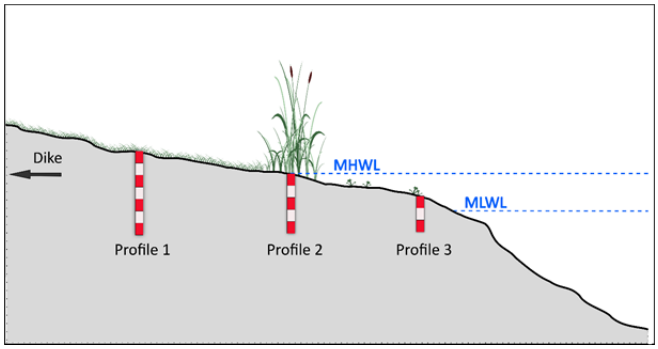

Fig. 2. Schematic illustration of the sampling design in the embankment foreland of the Elbe estuary. (MHWL = mean high water level, MLWL = mean low water level).

Standard physicochemical analyses

The laboratory analyses described in the following were performed according to Blume et al. (2011) and Schlichting et al. (1995). Sieved soil material was was mixed at 1:2.5 (w/w) with 0.01 M $CaCl_2$ to determine pH and deionized water to determine electric conductivity (*EC*). Particle size distribution was analyzed by sieving and sedimentation after destroying soil organic matter with H_2O_2 (30%), and dissolving calcite ($CaCO_3$) by HCl. Total soil carbon was measured by means of finely ground soil material, which was ashed in a Ströhlein apparatus based on the principle of coulometry. The content of $CaCO_3$ was determined according to Scheibler´s method by gas volumetric determination of the released CO_2. The difference between inorganic and total carbon is equivalent to the organic C. Exchangeable cations were extracted by 0.1 M $BaCl_2$. Concentrations of Ca^{2+}, Mg^{2+}, K^+ and Na^+ were measured against standard solutions using a flame AAS system. The total amount of pedogenic iron oxides (Fe_d), which develop during pedogenese, were analyzed by extraction with 0.3 M Na-citrate solution, 1 M $NaHCO_3$ solution and Na-dithionite according to the method described by Mehra and Jackson (1960). The iron concentration was determined by atomic absorption spectrometry.

Rheometry

Amplitude sweeps (AS) with controlled shear deformation were conducted with a modular compact rheometer MCR 300 (Anton Paar, Ostfildern, Germany) with a profiled 25 mm diameter parallel-plate measuring system at a plate distance of 4 mm in oscillating mode. The configurations of the tests were carried out in accordance with Markgraf (2006) (Table 1), since these configurations already have shown good performance and reproducibility in previous studies (e.g. Ajayi Ayodele and Horn, 2016; Baumgarten et al., 2013; Holthusen et al., 2010, 2012b). However, some settings vary from conventional rheological test settings. To consider the greatest possible particle/cluster size of the sieved soil material, the measuring gap is fixed to 4 mm as a compromise, because it is the smallest possible plate distance to produce reliable rheological data without removing a significant portion of primary particles and breakdown of microaggregate structures that are of interest. The frequency is kept constant at 0.5 Hz – common values are around 1.6 Hz – to ensure that the determined rheological parameters (G′, G″) describe the actual structural character of the soil and not a more inflexible structure because of faster oscillation, which may occur at frequencies 5–10 times higher (Mezger, 2014).

Table 1. Configuration of amplitude sweeps with controlled shear deformation (after Markgraf (2006)).

Parameter	
Measuring system	crosshatched parallel-plate system, diameter = 25 mm
Plate distance (h)	h = 4 mm
Shear deformation (γ)	continuous deformation ramp with γ = 0.0001 to 100%
Frequency (f)	f = 0.5 Hz ($\omega = \pi 1$/s)
Temperature (T)	T = 20 °C (regulated by Peltier unit)
Measuring points	30 pts.
Test duration	appr. 15 min.

Air dried, homogenized and sieved (< 2 mm) samples from all sites and depths were repacked into stainless steel cylinders (45 cm^3) to a standard bulk density of 1.4 Mg m^{-3}. Afterwards, the repacked samples were capillary saturated with deionized water to achieve quasi-saturated conditions (0 kPa). Subsequently, a portion of the prepared cylinders was drained and equilibrated to a matric potential of –6 kPa on ceramic plates.

Repacked soil samples from profile 1 were additionally equilibrated to a matric potential of –15 kPa.

For the rheological measurement, a small amount of soil was taken with a spatula from each cylinder and put on the fixed measuring plate of the rheometer. After lowering the upper plate to the defined measuring gap (4 mm) automatically, the normal force was checked to maintain an undisturbed quasi-elastic soil structure (i.e. $F_N \leq 12$ N). Operation of the rheometer, monitoring of the ASs and generation of the rheological parameters (G', G'', tan δ, *integral z*) were carried out by the software Rheoplus/32 V3.21. Five replicates were performed per depth and dewatering state. The water content of the samples (w/w) was determined before and after each test.

Loss factor tan δ and integral z

Since soil can be defined as a viscoelastic substance (Markgraf, 2006), amplitude sweeps are a suitable method to investigate the structural character of soils. During amplitude sweeps soil samples experience a gradual degradation of microstructural stiffness (Fig. 3). This destruction of internal structure can be characterized by the well-established rheological parameters storage modulus (G'), loss modulus (G''), their intersection at the flow point and the linear viscoelastic range (*LVE*) where G' and G'' do not change with increasing applied shear deformation. Moreover, the microstructure of soils can be specified by the loss factor tan δ, which is the ratio of G'' to G' and describes the viscous part to the elastic part of the deformation energy. A tan $\delta < 1$ indicates that the G' is greater than G'', so elastic processes prevail and the soil exhibits a quasi-elastic behavior, i.e. applied deformation leads to full or at least partial microstructural regeneration. When tan $\delta = 1$ the flow point ("cross-over") is reached ($G' = G''$). If $G' < G''$ a viscous character predominates, tan $\delta > 1$ (i.e. $G'' > G'$) and irreversible microstructural failure occurs (Mezger, 2014).

For further comparison of the quasi-elastic range (tan $\delta < 1$) in absolute terms, the dimensionless area parameter *integral z* can be used. The greater the value of *integral z*, the more elastic or rigid the soil is (Markgraf and Horn, 2009). Thus, *integral z* quantifies the structural strength in consideration of elasticity loss due to increasing shear deformation γ over time. The integral of tan $\delta(\gamma)$ with tan $\delta = 1$ as the defined limit was calculated from equation (1).

$$\int_{0.001}^{"cross-over"} \left(1 - \tan\delta\right) d\gamma \qquad (1)$$

Statistics

All statistical analysis was done using R (Version 3.1.1) (R Developement Core Team, 2013) based on mixed models

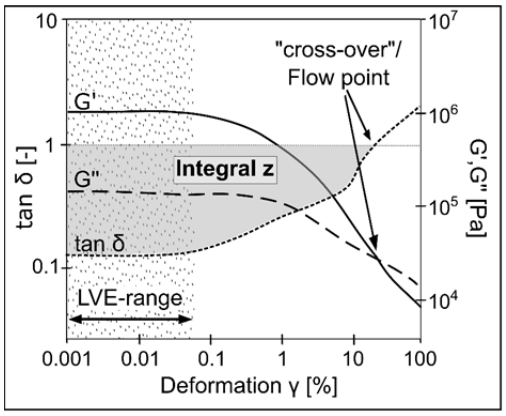

Fig. 3. Schematic result of an AST depicted as deformation function. Loss factor tan δ equals the ratio of loss modulus to storage modulus (= G''/G') and functions as analogue expression of elastic (tan $\delta \approx$ const.), viscoelastic (tan $\delta \leq 1$) or viscous behavior (tan $\delta > 1$). For further comparison, the *integral z* of tan $\delta(\gamma)$ with tan $\delta = 1$ as defined limit on the ordinate can be calculated. (solid line = G', dashed line = G'', dotted line = tan δ, grey area = *integral z*, dotted area = *LVE*-range).

(Laird and Ware, 1982; Verbeke and Molenberghs, 2008) by means of analyses of covariance and variance (ANCOVA resp. ANOVA).

First, all chemical parameters (pH, EC, $CaCO_3$ etc.) were tested on multicollinearity, as parameters that strongly correlate with one another would distort further statistical analyses. Based on this test the explanatory variables shown in Table 2 (col. 4) have been designated as non-correlated initial input parameters to run ANCOVA. Subsequently performed ANOVA permits the identification of the significant predictor variables.

RESULTS

Rheological properties: Integral z

The microstructural elasticities of the studied soils determined by amplitude sweeps under deformation-controlled conditions and characterized by the dimensionless area parameter *integral z* and flow point are summarized in Table 3.

At saturation, the soil samples from profile 3, which represents the initial stage of soil maturation, had the smallest *integral z* values (10–15). At a slightly higher elevation, usually under extensive reed vegetation (profile 2), the *integral z* values were of the same magnitude as in profile 3. For both profiles, loamy soil samples exhibited the greatest microstructural elasticity. This was also evident due to the shift of the flow point to a slightly greater deformation. The grassland profiles (profile 1) show a wide range of *integral z* values from 10 to 57 at quasi saturated conditions. Again, the largest values were obtained

Table 2. Initial input parameters for statistical analyses (ANCOVA resp. ANOVA) and determined key factors significantly affecting the microstructure of the soils under study.

Parameter	Acronym	Unit	Initial input parameters	Significant key factors (α = 0.05)
Electric conductivity	*EC*	mS cm^{-1}	**x**	
Organic matter	*OM*	g 100 g^{-1}	**x**	**x**
Calcite content	$CaCO_3$	g 100 g^{-1}	**x**	**x**
Pedogenic iron oxides	Fe_d	g kg^{-1}	**x**	**x**
Calcium concentration	Ca^{2+}	$cmol_c$ kg^{-1}	**x**	**x**
Sodium concentration	Na^{+}	$cmol_c$ kg^{-1}	**x**	**x**
Water content	Θ_g	w/w	**x**	**x**
Depth beneath ground level	*depth*	cm	**x**	**x**

Table 3. Summarized results of microstructural elasticity represented by the dimensionless area parameter *integral z* and the flow point γ_f given in terms of deformation (%) (mean values with SD), considering different profiles, soil texture [a], salinity and three matric potentials: quasi-saturated (0 kPa), –6 kPa and –15 kPa. NR = flow point not reached.

	Texture	Salinity	0 kPa		–6 kPa		–15 kPa	
			integral z	γ_f	*integral z*	γ_f	*integral z*	γ_f
Profile 1	Sand	fluvial	19.3 ± 1.9	48 ± 6	54.9 ± 13.0	NR	41.2 ± 10.6	75 ± 10
		brackish	14.4 ± 3.1	34 ± 8	13.5 ± 3.7	35 ± 12	59.7 ± 3.1	NR
		marine	11.8 ± 2.6	29 ± 5	11.1 ± 1.4	28 ± 5	‣ 25.3 ± 5.8 ‣ 57.3 ± 5.7	62 ± 12 NR
	Loam	fluvial	27.2 ± 3.0	42 ± 8	58.3 ± 0.8	NR	51.1 ± 3.5	NR
		brackish	18.2 ± 4.6	48 ± 17	‣ 15.7 ± 8.2 ‣ 47.8 ± 6.2	42 ± 18 NR	57.3 ± 7.8	NR
		marine	12.9 ± 1.4	32 ± 7	13.1 ± 4.2	37 ± 14	63.1 ± 1.7	NR
	Silt	fluvial	–	–	–	–	–	–
		brackish	14.9 ± 3.6	35 ± 9	‣ 10.7 ± 2.2 ‣ 61.0 ± 3.8	26 ± 5 NR	60.9 ± 2.4	NR
		marine	12.7 ± 1.4	34 ± 8	13.7 ± 2.6	39 ± 11	19.7 ± 20.3	37 ± 27
	Clay	fluvial	10.2 ± 0.3	30 ± 5	‣ 15.0 ± 5.9 ‣ 57.9 ± 2.4	44 ± 14 NR	59.5 ± 1.0	NR
		brackish	‣ 10.7 ± 3.1 ‣ 56.8 ± 6.6	36 ± 12 NR	‣ 7.4 ± 5.0 ‣ 57.3 ± 1.8	20 ± 16 NR	55.2 ± 8.1	NR
		marine	25.7 ± 9.6	57 ± 12	34.6 ± 3.1	NR	52.3 ± 5.6	NR
Profile 2	Sand	fluvial	–	–	–	–	–	–
		brackish	15.1 ± 3.3	37 ± 8	20.2 ± 10.8	51 ± 19	–	–
		marine	13.2 ± 4.1	33 ± 9	13.2 ± 2.3	33 ± 6	–	–
	Loam	fluvial	-	–	–	–	–	–
		brackish	15.6 ± 3.4	40 ± 13	11.7 ± 1.2	38 ± 8	–	–
		marine	17.1 ± 2.7	43 ± 6	13.8 ± 0.6	38 ± 12	–	–
	Silt	fluvial	–	–	–	–	–	–
		brackish	14.4 ± 2.7	34 ± 7	‣ 12.8 ± 3.4 ‣ 58.3 ± 3.0	34 ± 12 NR	–	–
		marine	12.1 ± 1.7	28 ± 5	12.7 ± 4.5	32 ± 10	–	–
Profile 3	Sand	fluvial	–	–	–	–	–	–
		brackish	9.9 ± 2.9	25 ± 6	12.7 ± 5.7	33 ± 15	–	–
		marine	10.2 ± 2.4	25 ± 5	11.3 ± 1.8	29 ± 8	–	–
	Loam	fluvial	–	–	–	–	–	–
		brackish	–	–	–	–	–	–
		marine	15.4 ± 2.8	35 ± 7	10.9 ± 2.2	27 ± 6	–	–
	Silt	fluvial	11.4 ± 1.3	28 ± 4	10.2 ± 1.5	27 ± 5	–	–
		brackish	9.0 ± 1.0	24 ± 3	10.9 ± 1.3	27 ± 2	–	–
		marine	12.6 ± 0.6	28 ± 3	11.2 ± 3.3	28 ± 8	–	–

[a] Texture groups were defined according to the German soil texture classification (further details regarding the texture groups are available in Stoppe and Horn (2017)), thus the sand-group corresponds approx. to LS, SL and SCL after WRB, the loam-group to CL, SiCL and partly to C, SiC, SiL and L, the silt-group approx. to SiL and Si, the clay-group to C and SC.

for loamy soil samples, but also for some clay samples in brackish waters. These clay samples did not reach the flow point during AS. Nevertheless, most samples exhibited a small microstructural elasticity and samples originating from marine sedimentation regions and clayey soil samples had the least elastic microstructure. For many soil samples it should be noted that larger *integral z* values were reached when the flow point shifted to greater deformation values. Occasionally, deformation values at the flow point differ for similar *integral z* values. In such cases the additional consideration of the flow point allows a more sophisticated assessment of the rheological behavior. Drainage to field capacity (–6 kPa) induced no changes for recently deposited sediments (profile 3), but caused a marginally enhanced microstructural stiffness for the soil samples from profile 2, as indicated by slightly larger *integral z* values. However, under reed vegetation, silty soil samples sometimes do not reach the flow point and therefore achieve large *integral z* values. As under quasi-saturated conditions, the widest range of *integral z* values was attained under grassland (11–61), but at field capacity the microstructural elasticity seemed to be intertwined with texture and the area of sedimentation: very small *integral z* values (< 15) in the marine region and larger values (> 45) in the fluvial region. Moreover, it was notable that the values obtained at a matric potential of –6 kPa were characterized by variable data. In brackish waters in particular, both small and very large *integral z* values were acquired.

At a matric potential of –15 kPa the *integral z* values were usually relatively large (> 40), implying a more rigid microstructure. Exceptions were silty soil samples from the marine region, which also had a large standard deviation and did not reach the flow point within the deformation range applied.

In general, the *integral z* exhibited relatively small values and standard deviations under quasi-saturated conditions. Larger values were reached with increasing desiccation, but drainage also lead to greater deviations reflected by outliers and/or wider ranges. Although significant differences between the topsoils of profile 1 and profile 3 were determined at saturation, these differences vanished as the soils dried to field capacity. Topsoils and subsoils differed from each other under grassland and under reed for all applied matric potentials (data not shown). Rheological behavior appears to be affected less by soil maturation than the area of sedimentation and therefore physicochemical properties including texture and particle size distribution.

Texture effect and impact of drainage

Figure 4 shows strongly generalized curves for the main texture groups (sand, loam, silt, clay) and tan δ at different matric potentials. The curves illustrate the rheological response to oscillatory stresses for representative soil samples, which possess the average chemical features of the specific texture group.

The stiffness degradation under quasi-saturated conditions was comparable for sandy, silty and loamy soils. An increase of tan δ at γ = 0.01–10% was evident and mainly due to the uppiling and re-orientation of soil particles and clusters, leading to a temporary stabilization of microstructure before its complete collapse. This re-orientation is more pronounced in sandy and silty soils than in loamy soils. Moreover, sand and silt showed a steeper increase in tan δ after re-orientation, resulting in an earlier intersection with the tan δ = 1. Loam required greater deformation to reach tan δ = 1 and had a less distinct slope. In contrast, clayey soils exhibited a gradual decrease of microstructure for the entire deformation range under quasi-saturated conditions.

Desiccation to –6 kPa did not substantially alter the curve characteristics for loamy soils. In most cases this was also true for sandy and silty soils, but for these texture groups drainage to field capacity occasionally provoked a shift of the flow point to greater deformation, preventing deformation into the viscous regime and indicating a greater elastic microstructure measured by larger *integral z* values. Clay retained its curve shape, depicting the gradual degradation of microstructure at field capacity. For this texture the flow point and transition into viscous flow was also not reached.

The effect of drainage was most pronounced at a matric potential of –15 kPa. All texture groups showed curve characteristics that indicated a rigid microstructure as over a range of deformations the elastically dominated regime stayed below the tan δ = 1 line.

Interaction of texture and water content

The rheological response of soils under oscillatory conditions was influenced considerably by particle size distribution and water content (see above and Fig. 5). Depending on particle size and specific surface, which increases with decreasing grain size, the water content varied at a given matric potential. Accordingly, as median of grain size (d_{50}) increases, less water was retained. At saturation, coarser textures with d_{50} > 100 µm had gravimetric water contents between 20 and 40%, whereas at a matric potential of –15 kPa the water contents were below 20%. Fine textured soils with d_{50} between 5 and 20 µm had gravimetric water contents around 60% at saturation, whereas the water content decreased to below 40% through drainage to –15 kPa (Fig. 5a and b).

The coefficient of determination (R^2) between *integral z* and matric potential under quasi-saturated conditions showed a weak relationship if the textures of all analyzed samples, with varying chemical properties, were considered. However, under saturated conditions the *integral z* values increases with the median of grain size (Fig. 5c). At a matric potential of –15 kPa capillary stresses influence the rheological response resulting in larger *integral z* values. In addition, the *integral z* values become greater with decreasing median of grain size (Fig. 5d). Consequently, desiccation has a stabilizing effect on the soil microstructure and this effect becomes more distinct the more fine-grained the soil.

Pedotransfer functions

Due to the considerable impact of particle size distribution, the textures were grouped according to the German soil texture classification (KA5; Ad-Hoc-Arbeitsgruppe Boden (2005)). Based on defined texture groups, the statistical evaluations (ANCOVA, ANOVA) were conducted and the physicochemical

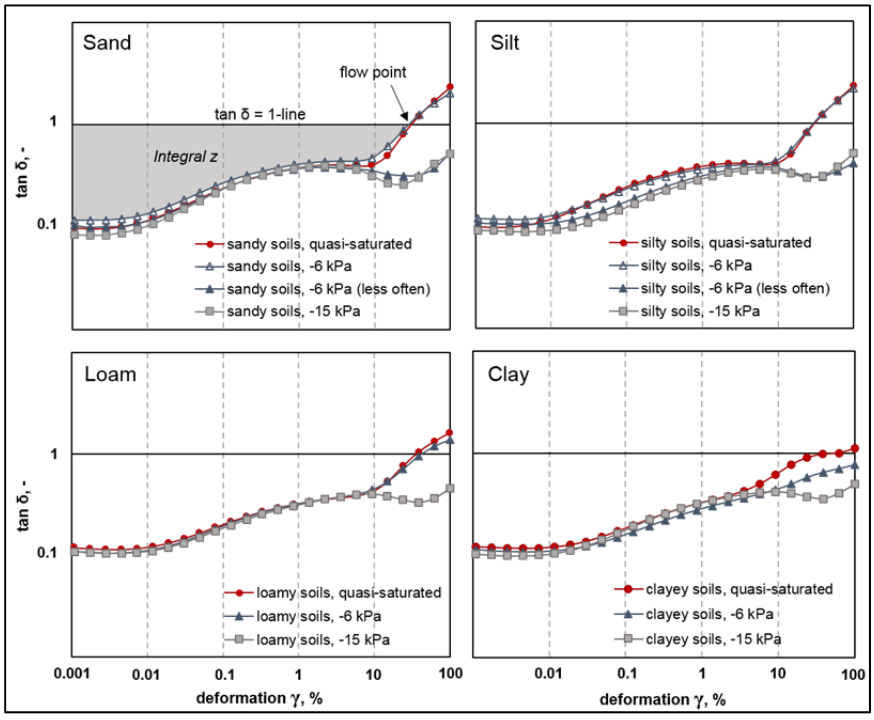

Fig. 4. Generalized graphs for loss factor (tan δ) and *integral z* – quantifying microstructural elasticity – for each studied texture group (sand, loam, silt, clay) and matric potential (0, –6, –15 kPa) portrayed based on representative soil samples and derived from amplitude sweeps under oscillatory and controlled shear deformation.

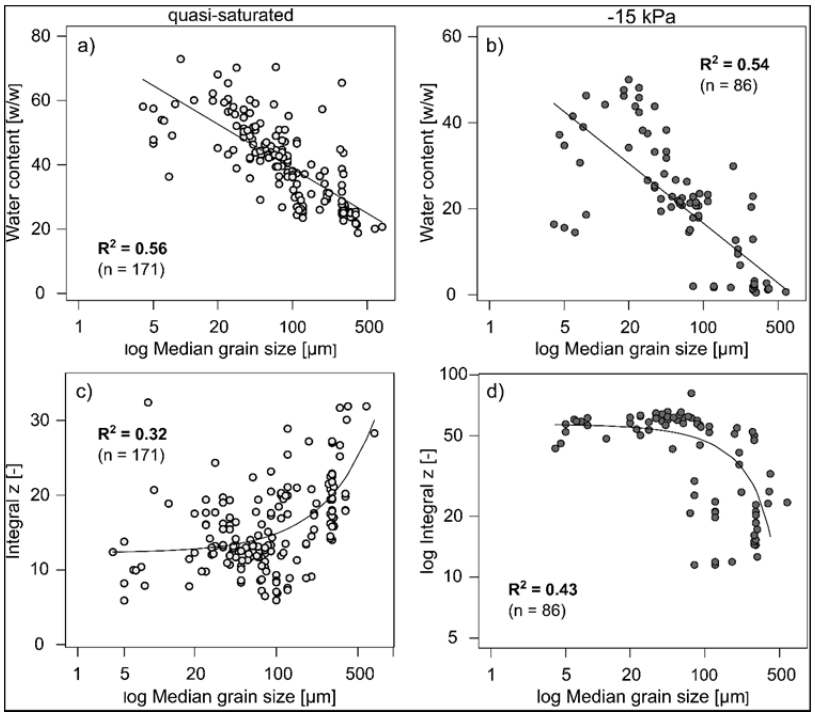

Fig. 5. Texture effect depicted as log median grain size in µm on water content (a and b) and microstructural stiffness (c and d) for different matric potentials (open circles: quasi-saturated, n = 171; filled circles: –15 kPa, n = 86). Single data points indicate the average of five replicates.

Table 4. Pedotransfer functions for mathematical estimation of microstructural stability depending on soil texture.

Texture group	Pedotransfer function	R^2
Sand (n = 48)	$integral\ z = 40.2 + 3.2\ OM + 2.1\ Ca^{2+} + 2.7\ Fe_d - 1.2\ \Theta_g - 0.1\ depth$	0.64
Loam (n = 25)	$integral\ z = 67.9 + 4.6\ OM + 0.2\ CaCO_3 - 1.4\ \Theta_g$	0.56
Silt (n = 27)	$integral\ z = 41.3 + 6.8\ OM + 0.5\ CaCO_3 + 2.3\ Fe_d - 1.2\ \Theta_g$	0.50
Clay (n = 15)	$integral\ z = 46.7 + 5.0\ OM + 2.3\ CaCO_3 - 3.6\ Na^{+} - 0.8\ \Theta_g - 0.2\ depth$	0.62

parameters shown in Table 2 (col. 5) were identified to significantly affect microstructural stability. Electric conductivity was eliminated during model simplification as water-soluble salts did not explain the variance of the *integral z* values. All other parameters had a significant influence on the elasticity of the soil microstructure.

Additionally, the specific statistical relationships between the rheological parameter *integral z* and factors influencing microstructural stiffness allowed the development of pedotransfer functions (PTF). These provide a mathematical estimation of the microscale stability parameter *integral z*. The slopes of the relationships between individual parameters and *integral z* was highly texture dependent, so texture specific PTFs were generated. For reasons of simplicity, those parameters, which have just a minor impact on the soil microstructure, remain unconsidered, if the model quality and accuracy of PTFs does not worsen through their omission. Hence, not every parameter was required for each texture group to predict the *integral z* value reliably. Table 4 summarizes the developed PTFs for each texture group.

As far as the intersection with the ordinate is concerned, it can be ascertained that the transfer function for loam exhibits the highest intercept, which coincides with the results presented in Table 3, where frequently the largest *integral z* values were observed in loamy soils. However, organic matter was included in each transfer function, which corroborates its well-known beneficial influence on soil (micro-) structure. Moreover, it is apparent that in sandy soils less organic matter was needed to enhance microstructural stiffness. Likewise the gravimetric water content was included in each function, but with a negative sign indicating its adverse effect (see above). Furthermore, calcite and Ca^{2+} had a positive effect on elasticity but only one of these parameters was needed in the PTF. Finally pedogenic iron (hydr)oxides had an advantageous impact solely on sand and silt, whereas the detrimental effect of sodium was integrated in the transfer function for clay. It emerged that when the combined effects of the physicochemical parameters were considered, the stabilizing factors were: soil organic matter, concentration of Ca^{2+}, content of $CaCO_3$ and pedogenic iron oxides (Fe_d). The concentration of Na^{+}, water content and the depth beneath ground level represented structurally unfavorable factors.

DISCUSSION

Texture effect

The loss factor tan δ, which represents the ratio of viscous to elastic behaviour, can be considered as a measure of the ability to store mechanical energy. Therefore, the capability to retain energy for reversing deformation is greater the smaller the value of tan δ. Furthermore, it decreases with increasing deformation and a characteristic degradation of internal structure takes place under oscillatory stress, which depends on particle size distribution. The textural effect on the curves of tan δ and

thereby on the absolute value of *integral z* was already emphasized by Markgraf and Horn (2009) and Baumgarten (2013) and is also evidenced by the results presented here.

Under oscillatory shearing coarse-grained textures initially had a fast reduction of elasticity with increasing deformation. But as a consequence of relative motions (rotation, interlocking, up-piling, reorganization) coarser particles were likely able to attain an energetically more favorable (i.e. more stable) arrangement whereby the complete destruction of microstructure was delayed. While rounded and angular particles exhibit rolling shear behavior (Cho et al., 2006), an increase in platy particles (i.e. clay platelets) leads to a more sliding shear behavior (Smith and Reitsma, 2002), assuming no pronounced aggregation. Sliding shear behavior and the formation of slickensides result in a reduced shear strength (Li et al., 2012) caused by depletion of internal structure. Accordingly, the greater the silt and/or clay content, the less often interlocking between particles occurs and elasticity decreases gradually with increasing shear deformation (Baumgarten, 2013). A theoretical consideration of the pore space provides an explanation of why and to what extent the shear behavior on the microscale changes with different particle size distributions. This can be conceptualized by considering a pure sand to which clay is amended at increasing concentrations. At first the contact points between particles in a pure sand remain unchanged after adding a small amount of clay as the clay particles and clusters merely partially occupy the pore space. Increasing the clay content decreases the porosity until the pore space becomes completely filled. Further clay particles are then exclusively deposited between sand particles, so the sand grains become separated and float in the clay matrix, which hence determines the shear behavior (Vallejo and Mawby, 2000).

Moreover, excess pore water pressure may arise under mechanical stress, which reduces effective stress contributed by capillary cohesion. Convex menisci support the displacement of particles relative to one another and therefore deformation of microstructure during shear strain. Depletion and/or redistribution of positive pore water pressure are dependent on hydraulic conductivity, tortuosity of pore space and hydraulic gradient. The reallocation of excess pore water pressures is therefore closely related to particle size distribution and (micro) aggregation of soils: short flow paths and/ or high conductivity favor the reduction of positive pore water pressure. Concave and thus contractive menisci are established when a new equilibrium is reached (Peth et al., 2010).

Finally, in addition to the induced shear behavior, chemical surface properties prevail in clayey soils, because of their smaller particle size. There are diverse clay mineral associations that which react differently to shearing, so the rheological properties may vary substantially. Dolinar and Trauner (2007) found for kaolinite samples saturated with distilled water (pH ~ 4) a relatively large undrained shear strength due to the opposite charged edges and faces establishing a stable card-house structure. Small amounts of NaCl induced the collapse of this arrangement, resulting in reduced undrained shear strength through diminished edge-face-attraction and face-face-repulsion and therefore alignment of clay platelets. A similar behavior was observed for Na-smectite suspensions, which also exhibit a greater shear strength at low pH than at high pH and high NaCl concentration based on compressed double layers (Brandenburg and Lagaly, 1988). Furthermore, the authors revealed that in the presence of Ca^{2+}, the attractive forces between edges and faces are enhanced as well as the formation of stable face-face-associations due to a shared double layer. However, it is obvious that the rheological characteristics and degradation of soil microstructure are not exclusively regulated by soil texture. Varying soil chemical features and especially varying water contents affect the rheology of soils as well.

Menisci forces

The soil microstructure in our study was weakened by increasing water content. Furthermore, the more fine-grained the soil material, the more sensitive it reacted towards shearing under saturated conditions. With increasing saturation, additional water layers were absorbed, which enlarge the distance between individual particles and act as a lubricant. The more water layers that are attached to the mineral surface, the greater the mobility of single particles (Santamarina and Shin, 2009). If chemically active particles are involved, existing interactions are reduced as well capillary suction, i.e. the negative pore water pressure, disappears when complete saturation is reached (Al-Shayea, 2001). Furthermore, because of mechanical strain, positive pore water pressures may occur, promoting the alignment of plate-like particles parallel to the shear direction.

By contrast, increasing desiccation stabilizes the microstructure of soil by water menisci forces, whereby fine-grained soils show a stronger reaction towards dewatering. In unsaturated soils, i.e. at negative pore water pressure, water menisci between soil particles provoke a contractive force such that the matric potential acts as a binding force between particles and stable connections are formed at rest (Osipov, 2014). Therefore, any change in matric potential also causes a change in pore water pressure. By successive drainage, soil particles are pulled together (Horn, 1990) and apparent cohesion increases (Santamarina, 2001), so the resistance of soils against external stresses is enhanced (Kézdi, 1974). Many authors observed the stabilizing effect of menisci forces on the aggregate scale (e.g. Çokça and Tilgen, 2010; Gallipoli et al., 2003; Hoyos et al., 2014). At the microscale the stabilization through menisci forces have also been shown based on various rheological parameters (Baumgarten, 2013; Czibulya et al., 2014; Holthusen et al., 2012b). Ghezzehei and Or (2001) reported an increase of the shear modulus (G) and higher yield stresses with decreasing water content. Markgraf and Horn (2006) observed an enhanced storage modulus (G′) with reduced water content. Holthusen et al. (2010) determined a higher shear resistance at the end of the linear-viscoelastic range (LVE) as well as higher values for the maximum shear resistance with drainage. On the microscale, the stabilizing effect of desiccation is also related to reduced layers of water molecules. The closer the water molecules to the particle surface, the tighter they are bound to this surface, leading to a lower mobility of the molecules and accordingly to a high viscosity and a higher shear strength of the water films (Israelachvili et al., 1988). Additionally, the decreased distance between particles favors particle-particle interactions (Santamarina and Shin, 2009).

Physicochemical parameters

The presented results confirm that the microstructure of soils is the product of a multitude of chemical, physical and biological interactions. Considering the combined effect of all relevant physicochemical properties, soil organic matter, concentration of Ca^{2+}, calcite content ($CaCO_3$) and pedogenic iron oxides (Fe_d) represent stabilizing features, whereas the concentration of Na^{+}, water content and the depth beneath ground level were found to be structurally disadvantageous factors. The positive impact of the beneficial factors was mainly attributable to their gluing and cementing effects. Soil organic matter has a marked

influence on soil structure at different scales and by several mechanisms due to its complexity (Tisdall and Oades, 1982). Extracellular polymeric substances (*EPS*), metabolites and other breakdown products generated by microbial decomposition act as binding agents, stick soil particles together and improve soil (micro) aggregation (Oades, 1984; Tisdall and Oades, 1982). Another effect of stabilization emerges due to hydrophobization of aggregates: adsorbed hydrophobic organic molecules decrease the wettability and therefore the dispersibility of aggregates (Goebel et al., 2005). The stabilizing effect of organic matter has been thoroughly proven not only on the aggregate scale (e.g. Chenu et al., 2000; De Gryze et al., 2005; Denef et al., 2002; Six et al., 2002), but also on the particle-particle-scale. Holthusen et al. (2012a) examined the impact of organic and mineral fertilization on the rheological behavior of soils from a long-term fertilization trial (Bonn, Germany) and corroborated a decreased sensitivity towards oscillatory shearing with increasing organic matter content. The rheological response of natural slurries was investigated based on rotational experiments by Carotenuto et al. (2015), who reported a decrease in viscosity and yield stress upon the selective removal of soil organic carbon. Majzik and Tombácz (2007) observed an improved microstructure of montmorillonite by adding humic acids (pH 6–6.5). However, this strengthening effect was associated with the presence of Ca^{2+}, because otherwise humic acids are bound to the positive charged edges of the clay particles and thus support the dispersion of the microstructure. The importance of the relation between Ca^{2+} and organic matter was also emphasized by Czibulya et al. (2014).

It is well known, that calcium ions induce the formation of a stable card house structure of clays (Jasmund and Lagaly, 1993) and many authors emphasize the stabilizing effect of Ca^{2+} (e.g. Paradelo et al., 2013; Wuddivira and Camps-Roach, 2007). Thereby the formation of Ca^{2+} bridges represents a long-term effect (Six et al., 2004), which is further intensified through the addition of organic substances (Baldock et al., 1994). In this respect, it seems plausible that Ca^{2+} as well as $CaCO_3$ appeared with a positive sign in the pedotransfer functions, as calcite serves as a Ca^{2+} source. In addition to its function as a bridging cation, dissolved Ca^{2+} increases the electrolyte concentration of the soil solution, leading to compressed double layers and diminished dispersibility of clay particles. Chan et al. (2007) ascribed the enhanced soil structure of acid soils after application of $CaCO_3$ to an increase of the electrolyte concentration. Furthermore, Ca^{2+} may exchange Na^{2+} and partially Mg^{2+} at negatively charged exchange sites (Armstrong and Tanton, 1992), because it is preferably bound due to its smaller hydration shell (Zhang and Norton, 2002).

Cementation of mineral particles occurs with an increasing content of iron oxides (Schwertmann and Niederbudde, 1993). Strong interdependencies between iron oxides and organic substances benefit the formation of organo-mineral complexes, which on the one hand stabilize (micro) aggregates and on the other hand soil organic matter (Pronk et al., 2011). Markgraf and Horn (2007) found the development of pseudosand in association with the cementation by iron oxides. Moreover, they described a significant reduction in microstructural stiffness after chemically extracting pedogenic iron oxides from the soils under study.

For clayey soils the pedotransfer function includes sodium with a negative sign, representing the well documented dispersive effect of Na^{+} (e.g. Sumner and Naidu, 1998), which is attributed to its monovalency and its large hydrated radius. Although it is generally known that in natural soils soil moisture is insufficient to completely hydrate exchangeable cations (Schwertmann and Niederbudde, 1993), Na^{+}-clay-connections are inherently unstable, as Na^{+} mainly forms ionic bonds (Rengasamy and Olsson, 1991). Finally, the water content negatively affects the elasticity of soils: increasing water content weakens the microstructure of soils due to smaller menisci forces as described above.

CONCLUSION

The rheological analyses of the investigated riparian Marshland soils provide new insight into the dynamic interactions between soil particles and the combined effects of stabilizing and destabilizing factors. The microstructural stiffness of the studied soils was evaluated by amplitude sweeps with controlled shear deformation. The results show a clear dependence on soil texture and water content. Rolling shear behavior in coarse-grained textures may cause a delay of microstructural collapse due to interlocking and/or rotation of soil particles and clusters. In fine-textured soils, sliding shear behaviour predominates and elasticity decreases gradually with increasing deformation. Increasing water content weakens the microstructure of soils due to smaller menisci forces, while desiccation stabilizes the microstructure through amplified menisci forces. The results corroborate the fact that the microstructure of soil is the product of a variety of processes and factors: the factors that significantly affect the soil microstructure in a positive way are soil organic matter, the concentration of Ca^{2+}, calcite content ($CaCO_3$) and pedogenic iron oxides (Fe_d); detrimental factors are the concentration of Na^{+}, water content and the depth beneath ground level. In particular, the consideration of the combined effects of physicochemical features is appropriate to characterize the elasticity of soil microstructure and therefore to develop proper and plausible pedotransfer functions.

Acknowledgements. This study was funded by the Federal Institute of Hydrology (BfG, Koblenz, Germany) and the German Waterways- and Shipping Administration (WSV, in particular Waterways- and Shipping Office, WSA, Hamburg, Germany). We thank Fred Shepherd for proofreading.

REFERENCES

Ad-Hoc-Arbeitsgruppe Boden, 2005. Bodenkundliche Kartieranleitung. E. Schweizerbart´sche Verlagsbuchhandlung, Stuttgart.

Ajayi Ayodele, E., Horn, R., 2016. Comparing the potentials of clay and biochar in improving water retention and mechanical resilience of sandy soil. Int. Agrophys., 30, 391–399.

Al-Shayea, N.A., 2001. The combined effect of clay and moisture content on the behavior of remolded unsaturated soils. Eng. Geol., 62, 319–342.

Armstrong, A.S.B., Tanton, T.W., 1992. Gypsum applications to aggregated saline sodic clay topsoils. J. Soil Sci., 43, 2, 249–260.

Baldock, J.A., Aoyama, M., Oades, J.M., Susanto, Grant, C.D., 1994. Structural amelioration of a South Australian red-brown earth using calcium and organic amendments. Aust. J. Soil Res., 32, 3, 571–594.

Baumgarten, W., 2013. Soil microstructural stability as influenced by physicochemical parameters and its environmental relevance on multiple scales. Habilitation Thesis, Christian-Albrechts-Universität Kiel.

Baumgarten, W., Dörner, J., Horn, R., 2013. Microstructural development in volcanic ash soils from South Chile. Soil Tillage Res., 129, 48–60.

Baumgarten, W., Neugebauer, T., Fuchs, E., Horn, R., 2012. Structural stability of Marshland soils of the riparian zone of the Tidal Elbe River. Soil Tillage Res., 125, 80–88.

Bergemann, M., 1995. Die Lage der oberen Brackwassergrenze im Elbeästuar. Deutsche Gewässerkundliche Mitteilungen, 39, 4–5, 134–137.

Blume, H.-P., Stahr, K., Leinweber, P., 2011. Bodenkundliches Praktikum. Eine Einführung in pedologisches Arbeiten für Ökologen, insbesondere Land- und Forstwirte, und für Geowissenschaftler. Spektrum Akademischer Verlag, Heidelberg.

Brandenburg, U., Lagaly, G., 1988. Rheological properties of sodium montmorillonite dispersions. Appl. Clay Sci., 3, 3, 263–279.

Bronick, C.J., Lal, R., 2005. Soil structure and management: a review. Geoderma, 124, 1–2, 3–22.

Carotenuto, C., Merola, M.C., Álvarez-Romero, M., Coppola, E., Minale, M., 2015. Rheology of natural slurries involved in a rapid mudflow with different soil organic carbon content. Colloid Surface A, 466, 57–65.

Chan, K.Y., Conyers, M.K., Scott, B.J., 2007. Improved structural stability of an acidic hardsetting soil attributable to lime application. Commun Soil Sci. Plan., 38, 15–16, 2163–2175.

Chenu, C., Le Bissonnais, Y., Arrouays, D., 2000. Organic matter influence on clay wettability and soil aggregate stability. Soil Sci. Soc. Am. J., 64, 4, 1479–1486.

Cho, G.C., Dodds, J., Santamarina, J.C., 2006. Particle shape effects on packing density, stiffness, and strength: Natural and crushed sands. Journal of Geotechnical and Geoenvironmental Engineering, 132, 5, 591–602.

Çokça, E., Tilgen, H.P., 2010. Shear strength-suction relationship of compacted Ankara clay. Appl. Clay Sci., 49, 4, 400–404.

Czibulya, Z., Szegi, T., Michéli, E., Tombácz, E., 2014. Rheological measurements for indicating structural changes in selected soil catenas of European experimental fields. Int. J. Agric. Sci. Technol., 2, 1, 22–31.

De Gryze, S., Six, J., Brits, C., Merckx, R., 2005. A quantification of short-term macroaggregate dynamics: influences of wheat residue input and texture. Soil Biol. Biochem., 37, 1, 55–66.

Denef, K., Six, J., Merckx, R., Paustian, K., 2002. Short-term effects of biological and physical forces on aggregate formation in soils with different clay mineralogy. Plant Soil, 246, 2, 185–200.

Dolinar, B., Trauner, L., 2007. The impact of structure on the undrained shear strength of cohesive soils. Eng. Geol., 92, 1–2, 88–96.

Freitag, C., Hochfeld, B., Ohle, N., 2007. Lebensraum Tiedeelbe. Coastline Reports, 9, 69–79.

Gallipoli, D., Gens, A., Sharma, R., Vaunat, J., 2003. An elasto-plastic model for unsaturated soil incorporating the effects of suction and degree of saturation on mechanical behaviour. Geotechnique, 53, 9, 844–844.

Garniel, A., Mierwald, U., 1996. Changes in the morphology and vegetation along the human-altered shoreline of the Lower Elbe. In: Nordstrom, K.F., Roman, C.T. (Eds.): Estuarine Shores: Evolution, Environments and Human Alterations. John Wiley & Sons Ltd., New York, USA, pp. 375–396.

Ghezzehei, T.A., Or, D., 2001. Rheological properties of wet soils and clays under steady and oscillatory stresses. Soil Sci. Soc. Am. J., 65, 3, 624–637.

Goebel, M.O., Bachmann, J., Woche, S.K., Fischer, W.R., 2005. Soil wettability, aggregate stability, and the decomposition of soil organic matter. Geoderma, 128, 1–2, 80–93.

Hartge, K.H., Horn, R., 2016. Essential Soil Physics. An Introduction to Soil Processes, Functions, Structure and Mechanics. Schweizerbart, Stuttgard, 389 p.

Holthusen, D., 2010. Fertilization induced changes in soil stability at the microscale revealed by rheometry. Dissertation Thesis. Christian-Albrechts-Universität Kiel.

Holthusen, D., Peth, S., Horn, R., 2010. Impact of potassium concentration and matric potential on soil stability derived from rheological parameters. Soil Tillage Res., 111, 1, 75–85.

Holthusen, D., Jänicke, M., Peth, S., Horn, R., 2012a. Physical properties of a Luvisol for different long-term fertilization treatments II. Microscale behavior and its relation to the mesoscale. J. Plant Nutr. Soil Sci., 175, 1, 14–23.

Holthusen, D., Peth, S., Horn, R., Kuhn, T., 2012b. Flow and deformation behavior at the microscale of soils from several long-term potassium fertilization trials in Germany. J. Plant Nutr. Soil Sci., 175, 4, 535–547.

Holthusen, D., Reeb, D., Horn, R., 2012c. Influence of potassium fertilization, water and salt stress, and their interference on rheological soil parameters in planted containers. Soil Tillage Res., 125, 72–79.

Horn, R., 1990. Aggregate characterization as compared to soil bulk properties. Soil Tillage Res., 17, 3–4, 265–289.

Hoyos, L.R., Velosa, C.L., Puppala, A.J., 2014. Residual shear strength of unsaturated soils via suction-controlled ring shear testing. Eng. Geol., 172, 1–11.

Israelachvili, J.N., Mcguiggan, P.M., Homola, A.M., 1988. Dynamic properties of molecularly thin liquid-films. Science, 240, 4849, 189–191.

Jasmund, K., Lagaly, G., 1993. Tonminerale und Tone. Struktur, Eigenschaften, Anwendung und Einsatz in Industrie und Umwelt. Steinkopff Verlag, Darmstadt.

Jeong, S.W., Locat, J., Leroueil, S., Malet, J.P., 2010. Rheological properties of fine-grained sediment: the roles of texture and mineralogy. Canadian Geotechnical Journal, 47, 10, 1085–1100.

Kézdi, Á., 1974. Handbook of Soil Mechanics, Vol. 1: Soil Physics. Elsevier, Amsterdam.

Laird, N.M., Ware, J.H., 1982. Random-effects models for longitudinal data. Biometrics, 38, 4, 963–974.

Li, Y.R., Aydin, A., Xu, Q., Chen, J., 2012. Constitutive behavior of binary mixtures of kaolin and glass beads in direct shear. KSCE J. Civ. Eng., 16, 7, 1152–1159.

Majzik, A., Tombácz, E., 2007. Interaction between humic acid and montmorillonite in the presence of calcium ions I. Interfacial and aqueous phase equilibria: Adsorption and complexation. Org Geochem, 38, 8, 1319–1329.

Markgraf, W., 2006. Microstructural changes in soils. rheological investigations in soil mechanics. Dissertation Thesis. Christian-Albrechts-Universität Kiel.

Markgraf, W., Horn, R., 2006. Rheological-stiffness analysis of K^+-treated and $CaCO_3$-rich soils. J. Plant Nutr. Soil. Sci., 169, 3, 411–419.

Markgraf, W., Horn, R., 2007. Scanning electron microscopy-energy dispersive scan analyses and rheological investigations of south-Brazilian soils. Soil Sci. Soc. Am. J., 71, 3, 851–859.

Markgraf, W., Horn, R., 2009. Rheological investigations in soil micro mechanics: Measuring stiffness degradation and structural stability on a particle scale. In: Gragg, L.P., Cassell, J.M. (Eds.): Progress in Management Engineering. Nova Science Publishers, Inc., New York, pp. 237–279.

Markgraf, W., Horn, R., Peth, S., 2006. An approach to rheometry in soil mechanics - Structural changes in bentonite, clayey and silty soils. Soil Till. Res., 91, 1–2, 1–14.

Markgraf, W., Moreno, F., Horn, R., 2012a. Quantification of microstructural changes in Salorthidic Fluvaquents using rheological and particle charge techniques. Vadose Zone J., 11, 1. DOI:10.2136/vzj2011.0061.

Markgraf, W., Watts, C.W., Whalley, W.R., Hrkac, T., Horn, R., 2012b. Influence of organic matter on rheological properties of soil. Appl. Clay Sci., 64, 25–33.

Mehra, O.P., Jackson, M.L., 1960. Iron oxide removal from soils and clays by a dithionite-citrate system buffered with sodium bicarbonate. Clay Clay Miner., 7, 317–327.

Mezger, T.G., 2014. The Rheology Handbook: For Users of Rotational and Oscillatory Rheometers. Vincentz Network, Hannover, Germany.

Oades, J.M., 1984. Soil organic-matter and structural stability - Mechanisms and implications for management. Plant Soil, 76, 1–3, 319–337.

Osipov, V.I., 2014. Physicochemical theory of effective stresses in soils. Water Resources, 41, 7, 801–818.

Paradelo, R., van Oort, F., Chenu, C., 2013. Water-dispersible clay in bare fallow soils after 80 years of continuous fertilizer addition. Geoderma, 200, 40–44.

Pértile, P., Reichert, J.M., Gubiani, P.I., Holthusen, D., Costa, A.d., 2016. Rheological parameters as affected by water tension in subtropical soils. Rev. Bras. Cienc. Solo, 40, e0150286.

Peth, S., Rostek, J., Zink, A., Mordhorst, A., Horn, R., 2010. Soil testing of dynamic deformation processes of arable soils. Soil Tillage Res., 106, 2, 317–328.

Pronk, G.J., Heister, K., Kogel-Knabner, I., 2011. Iron oxides as major available interface component in loamy arable topsoils. Soil Sci. Soc. Am. J., 75, 6, 2158–2168.

R Developement Core Team, 2013. R: A language and environment for statistical computing.

Rengasamy, P., Olsson, K.A., 1991. Sodicity and soil structure. Aust. J. Soil Res., 29, 6, 935–952.

Santamarina, J.C., 2001. Soil behavior at the microscale: Particle forces. In: Proceedings of the Symposium of Soil Behavior and Soft Ground Construction, in honor of Charles C. Ladd. MIT, pp. 1–32.

Santamarina, J.C., Shin, H., 2009. Friction in granular media. In: Hatzor, Y.H., Sulem, J., Vardoulakis, I. (Eds.): Meso-Scale Shear Physics in Earthquake and Landslide Mechanics. CRC Press, Boca Raton, London.

Schlichting, E., Blume, H.-P., Stahr, K., 1995. Bodenkundliches Praktikum. Eine Einführung in und Forstwirte und für Geowissenschaftler. Blackwell Wissenschafts-Verlag, Berlin, Wien.

Schwertmann, U., Niederbudde, E.-A., 1993. Tonminerale in Böden. In: Jasmund, K., Lagaly, G. (Eds.): Tonminerale und Tone. Struktur, Eigenschaften, Anwendungen und Einsatz in Industrie und Umwelt. Steinkopff Verlag, Darmstadt, pp. 212–265.

Six, J., Feller, C., Denef, K., Ogle, S.M., Sa, J.C.D., Albrecht, A., 2002. Soil organic matter, biota and aggregation in temperate and tropical soils - Effects of no-tillage. Agronomie, 22, 7–8, 755–775.

Six, J., Bossuyt, H., Degryze, S., Denef, K., 2004. A history of research on the link between (micro)aggregates, soil biota, and soil organic matter dynamics. Soil Till. Res., 79, 1, 7–31.

Smith, D.W., Reitsma, M.G., 2002. Towards an explanation for the residual friction angle in montmorillonite clay soils. In: Vulliet, L., Laloui, L., Schrefler, B. (Eds.): Environmental Geomechanics. EPFL/ Centre Midi, Lausanne, Schweiz, pp. 27–44.

Stoppe, N., Horn, R., 2017. How far are rheological parameters from amplitude sweep tests predictable using common physicochemical soil properties? IOP Conference Series: Journal of Physics: Conference Series, 790(1)012032.

Sumner, M.E., Naidu, R., 1998. Sodic Soils: Distribution, Properties, Management and Environmental Consequences. Oxford University Press Inc., New York.

Tisdall, J.M., Oades, J.M., 1982. Organic matter and water-stable aggregates in soils. J. Soil Sci., 33, 2, 141–163.

Torrance, J.K., 1999. Physical, chemical and mineralogical influences on the rheology of remoulded low-activity sensitive marine clay. Appl. Clay Sci., 14, 4, 199–223.

Vallejo, L.E., Mawby, R., 2000. Porosity influence on the shear strength of granular material–clay mixtures. Eng. Geol., 58, 2, 125–136.

Verbeke, G., Molenberghs, G., 2008. Linear Mixed Models for Longitudinal Data. Springer Verlag, New York.

Warkentin, B.R., 2008. Soil structure: A history from tilth to habitat. Adv. Agron., 97, 239–272.

Wuddivira, M.N., Camps-Roach, G., 2007. Effects of organic matter and calcium on soil structural stability. Eur. J. Soil Sci., 58, 3, 722–727.

Zhang, X.C., Norton, L.D., 2002. Effect of exchangeable Mg on saturated hydraulic conductivity, disaggregation and clay dispersion of disturbed soils. J. Hydrol., 260, 194–205.

Received 2 November 2016
Accepted 16 May 2017

J. Hydrol. Hydromech., 66, 2018, 1, 97–106
DOI: 10.1515/johh-2017-0034

Spatio-temporal variation of throughfall in a hyrcanian plain forest stand in Northern Iran

Saleh Yousefi[1], Seyed Hamidreza Sadeghi[2*], Somayeh Mirzaee[3], Martine van der Ploeg[4], Saskia Keesstra[4], Artemi Cerdà[5]

[1] Department of Watershed Management, Faculty of Natural Resources, Tarbiat Modares University, Tehran, Iran.
E-mail: saleh.yousefi@modares.ac.ir
[2] Department of Watershed Management Engineering, Faculty of Natural Resources, Tarbiat Modares University, Noor 46417-76489, Iran.
[3] Department of Watershed Management, Faculty of Natural Resources, Lorestan University, Khoramabad, Iran.
E-mail: s.mirzaee90@yahoo.com
[4] Soil Physics and Land Management Group, Wageningen University, Droevendaalsesteeg 4, 6708PB Wageningen, The Netherlands.
E-mails: martine.vanderploeg@wur.nl, saskia.keesstra@wur.nl
[5] Soil Erosion and Degradation Research Group, Department of Geography, University of Valencia, Valencia, Spain.
E-mail: artemio.cerda@uv.es
[*] Corresponding author. Tel.: +98 11 44553102. Fax: +98 11 44553909. E-mail: sadeghi@modares.ac.ir

Abstract: Elucidating segregation of precipitation in different components in forest stands is important for proper forest ecosystems management. However, there is a lack of information on important rainfall components viz. throughfall, interception and stemflow in forest watersheds particularly in developing countries. We therefore investigated the spatio-temporal variation of important component of throughfall for a forest stand in a Hyrcanian plain forest in Noor City, northern Iran. The study area contained five species of *Quercus castaneifolia*, *Carpinus betulus, Populus caspica* and *Parrotia persica*. The research was conducted from July 2013 to July 2014 using a systematic sampling method. Ninety-six throughfall collectors were installed in a 3.5 m × 3.5 m grid cells. The canopy covers during the growing/leaf-on (i.e., from May to November) and non-growing/leaf-off (i.e., from December to March) seasons were approximately 41% and 81%, respectively. The mean cumulative throughfall during the study period was 623±31 mm. The average throughfall (*TF*) as % of rainfall (*TFPR*) during leaf-on and leaf-off periods were calculated 56±14% and 77±10%, respectively. *TF* was significantly ($R^2 = 0.97$, $p = 0.00006$) correlated with gross precipitation. Percent of canopy cover was not correlated with *TF* except when gross precipitation was <30 mm. A comparison between leaf-off and leaf-on conditions indicated a significantly higher *TFPR* and corresponding hotspots during leaf-on period. *TFPR* also differed between seasons with a maximum amount in winter (82%). The results of the study can be effectively used by forest watershed managers for better perception of hydrological behavior of the Hyrcanian forest in the north of Iran under different silvicultural circumstances leading to getting better ecosystem services.

Keywords: Caspian Hyrcanian Forest; Deciduous forest; Forest hydrology; Interception storage; Precipitation loss.

INTRODUCTION

To understand the hydrological cycle and ecosystem services, it is necessary to quantify the role of vegetation in partitioning rainfall resulting in water balance at pedon, slope and watershed scale, and correspondingly the runoff, sediment, nutrients, contaminants and even biota redistribution (Buendia et al., 2016; Cao et al., 2008; Celentano et al., 2016; Cox et al., 2006; Davudirad et al., 2016; Gabarrón-Galeote et al., 2013; García-Fayos et al., 2010; Hosseini et al., 2016; Keesstra et al., 2009; Keesstra et al., 2012; Lal, 1997; Novara et al., 2013; Pereira et al., 2013; Sadeghi et al., 2015; Yousefi et al., 2016; Vega et al., 2005). Improving our understanding about rainfall partitioning in forests ecosystems is very important for studies that focus on forest hydrology to better management and decision making on this vital ecosystems (Ajami et al., 2011; Brecciaroli et al., 2012; Davudirad et al., 2015; Dohnal et al., 2014; Frot et al., 2007; Holko et al., 2009; Xu et al., 2014). Such eco-hydrological studies lead to a proper hydrological balance analysis and therefore have been well considered in forest hydrology studies during last few decades (Adriaenssens et al., 2012; Bosch and Hewlett, 1982; Carlyle-Moses, 2004; Devlaeminck et al., 2005; Gurav et al., 2012; Marin et al., 2000; Llorens and Domingo, 2007; Mitchell et al., 1986; Molina and Campo, 2012; Nanko et al., 2006; Park and Cameron, 2008; Rahmani et al., 2011; Shachnovich et al., 2008; Tcherepanov et al., 2005; Xu et al., 2014).

Net rainfall reaches the forest floor through the tree canopy by throughfall and stem flow (Aikawa et al., 2006; Deng et al., 2013; Hinko-Najera et al., 2015; Rahmani et al., 2011; Zhang et al., 2009). Throughfall is the part of rainfall that reaches forest floor either through dripping from the tree canopies and after fulfilling initial interception storage or direct passing the canopy gaps (Chappell and Bidin, 2001; David et al., 2011; Díaz et al., 2007; Guswa and Spence, 2012; Huber and Iroumé, 2001; Rahmani et al., 2011; Roberts and Rosier, 2005; Wuyts et al., 2008; Zhang et al., 2006; Zimmermann and Zimmermann, 2014).

Many important factors viz. rainfall characteristics, canopy architecture, branch angle, canopy cover, tree age, leaves shapes, types and dimensions, phonological stages, and even silvicutural practices affect hydrologic behavior of forest stand against input rainfall (Brandt, 1987; Bruijnzeel, 2005; Davudirad et al., 2015; Davudirad et al., 2016; Gay et al., 2015; Guswa and Spence, 2012; Huber and Iroumé, 2001; Molina and Campo, 2012; Nanko et al., 2006; Onozawa et al., 2009; Pérez-Suárez et al., 2008; Pypker et al., 2005; Staelens et al., 2007; Van Stan et al., 2012; Xu et al., 2014). Due to dynamic varia-

bility of affecting factors in space and time, the throughfall as an important component of hydrologic cycle in forest ecosystems (Sadeghi et al., 2008) varies temporally and spatially (Forti and Neal, 1992; Staelens et al., 2006). Previous research signified the effects of canopy gaps on spatio-temporal variability of throughfall (Forti and Neal, 1992; Keim et al., 2005; Loescher et al., 2002; Zirlewagen and von Wilpert, 2001). The importance of spatio-temporal variation in throughfall in forest ecosystems has also been reported in water balance modeling studies in forest watersheds (Zirlewagen and von Wilpert, 2001), forest lands nutrients exchange (Vernimmen et al., 2007; Zimmermann et al., 2008), soil erosion processes (Sadeghi et al., 2008) and fauna and flora studies (Xiao et al., 2000).

The Hyrcanian forest near the southern shores of the Caspian Sea of Iran and Azerbaijan (from –25 m to +10 m above mean sea level) is a unique ecosystem due to having a markedly different climate compared to other parts of Iran, and is very important in different ecological and hydrological aspects (Ebrahimpour et al., 2011; Rahmani et al., 2011). The location of the Caspian Sea and the Alborz Mountains mainly control the climate and the hydrology of the Hyrcanian forest. The average annual precipitation is around 1000 mm; three times more compared to the average precipitation in Iran (Rahmani et al., 2011). Most of the tree species in the Caspian Hyrcanian Forests are deciduous means their leaves falling off at maturity or tending to fall off during cold season. Therefore, two main phenological stages of leaf-on and leaf-off can be defined. Unfortunately, the Hyrcanian plain forests are drastically threatened by human encroachment and overexploitation, despite their importance in ecological stability, and the hydrological balance.

Scrutinizing available literature showed that only a few studies have been conducted to quantitatively determine the vital role of the Hyrcanian forest on hydrological conditions. While the positive roles of Hyrcanian forest in decreasing frequency and intensity of floods and even regulating hydroclimatical conditions of the region are qualitatively known. It is necessarily needed to obtain precise estimations on hydrological components of the Hyrcanian forest to properly develop and calibrate hydrological models (Sadeghi and Mizuyama, 2007; Sadeghi et al., 2007; Sadeghi and Saeidi, 2010) in the area where the input rainfall is potentially erosive and offensive compared to other parts of Iran (Sadeghi et al., 2011). The present study has been therefore planned to investigate the spatio-temporal variations of throughfall as a main factor in rainfall partitioning in a part of the Hyrcanian plain forests. The present study aimed i) to determine the throughfall in a mixed Hyrcanian stand forest; ii) to identify the relationship between canopy cover and throuhfall and iii) to investigate the spatio-temporal variations of the throughfall in different seasons and leaf-off and leaf-on periods. The results of the present study may justify decision makers and planners to appropriately preserve the precious heritage of Hyrcanian plain forests as an important unique ecosystem in the world for the next generations due to vital services of this ecosystem in regulation of hydrological regimen of the area.

MATERIAL AND METHODS

Study site

The study area has been located in the Hyrcanian plain forest at International Campus of Tarbiat Modares University at Faculty of Natural Resource in Noor City, Iran. The site was chosen due to accessibility, possibility of accurate monitoring and controlled conditions. The study site is not threatened by anthropogenic activities and therefore is representing all original Hyrcanian plain forest situated in southern Caspian Sea shores. Average annual precipitation in the study site is 1030 mm according to the data (1968–2013) from the nearest meteorological (i.e, Noor Station just 2 km away). The study area was confined to an area of 943.25 m^2 (38.5 m x 24.5 m) covered by different species viz. *Carpinus betulus* (55%), *Quercus castaneifolia* (10%), *Parrotia persica* (10%) and *Populus caspica* (7%) with respective number of trees of 35, 5, 2 and 2; also 18% is covered by grass and bare soil. The measured mean breast height diameter at the beginning of the study was measured as 26±7.5 cm for *Quercus castaneifolia,* 31±7.82 cm for *Carpinus betulus,* 104±16.5 cm for *Populus caspica* and 33±6.5 cm for *Parrotia persica*. No border effects could be recognized and therefore considered in the study, since the study area is just a small piece which has been surrounded by a similar forest stand.

Sampling design

The study was planned in a grid design of 3.5 m × 3.5 m according to the canopy cover distribution and density, for which 96 throughfall collectors were installed at all corners of the squares (Lloyd, 1988; Rahmani et al., 2011). Since the measurement of throughfall in the entire selected area was concerned, the distribution pattern of the collectors was set systematically to try to mimic natural conditions where dense and sparse canopy covers, and clear areas are all together. The study design along with corresponding details has been depicted in Figure 1. The study was carried out for all incidents (24 events) during one year from July 2013 to July 2014.

Gross precipitation was directly measured at the nearest open area 200 m from the study site to minimize the introduction of errors (Holder, 2003, 2004; Rahmani et al., 2011). Cylindrical rainwater collectors with diameters of 9 cm were mounted on iron rods 35 cm above the forest floor to measure throughfall after each rainfall event and one collector was used to measure gross precipitation. Since there was no automatic rain gage in the study area, just the depth of rainfall was recorded after each individual storm event. Since there was no automatic rain gage in the study area, just the depth of rainfall was recorded after each individual storm event. The spatial distribution of gross precipitation was assumed to be homogeneous over the small study site. The volume of the collected rainwater was determined using weighting method with the help of a portable digital scale with an accuracy of ±0.1 g (≈ 0.017 mm of water in collector). The depth of the throughfall was consequently determined for each collector by dividing the volume of water by the collection area (63.59 cm^2). All 96 throughfall collectors (Figure 1) were inspected and cleaned after each instant measurement. Some data were missed for some collectors, since they have been destructed due to passing wild animals or blowing wind. The throughfall as % of rainfall (*TFPR*), as the principal factor of the present study, was calculated using the following equation and applying gross precipitation (*Pg*) and throughfall (*TF*), both in mm.

$$TFPR = \frac{TF}{Pg} \times 100 \quad (1)$$

The values of *TFPR* more than 100 indicate that the depth of throughfall was more than gross rainfall and therefore denote throughfall hotspots. In addition, the hotspots were detected using Getis Ord Hot-spot analysis in Arc GIS 10.2 at three significant levels ($\alpha = 0.10$, 0.05 and 0.01) and using an Inverse-Distance spatial relationship concept (Getis and Ord, 1992).

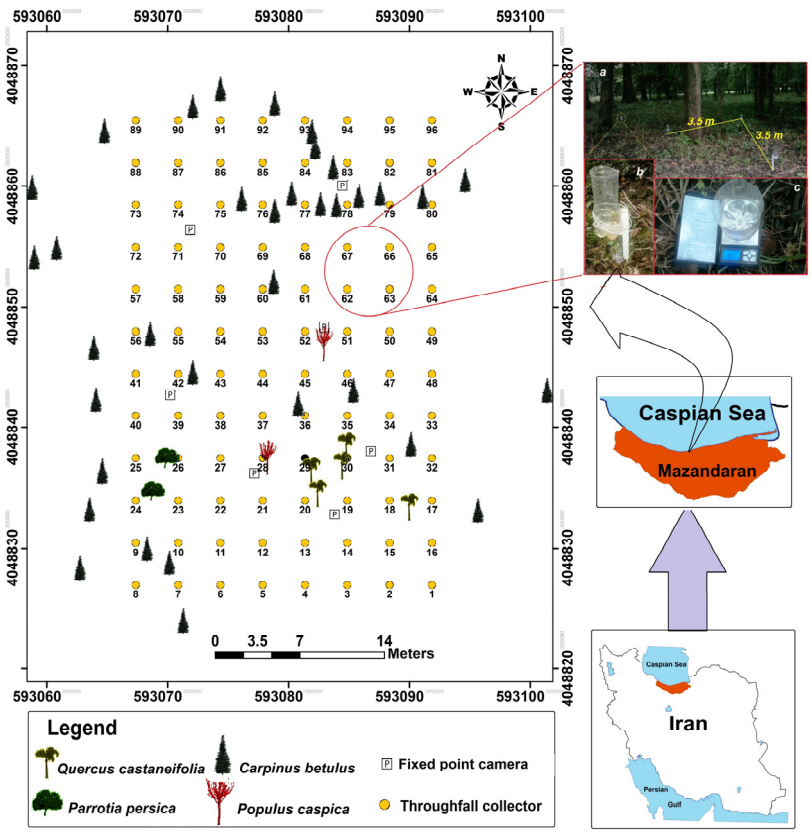

Fig. 1. General location of the study area and a ground view of the study site (a), throughfall collector (b) and weighting stage of collected throughfall (c).

Table 1. Precipitation and throughfall in a Hyrcanian forest stand during the study period.

Temporal scale	Date	No. of events	Gross precipitation (mm)	No. of correct samples	No. of hotspot points	Throughfall as % of rainfall				Canopy cover (%)
						Mean	Minimum	Maximum	Standard Deviation	
Event	30-Jul-2013	24	18.95	64	10	73.1	21.2	160.4	27	85.0
	6-Aug-2013		8.81	94	12	75.9	25.6	165.8	27	86.0
	9-Aug-2013		36.17	94	0	58.3	29.5	118.5	14	87.5
	10-Aug-2013		12.38	95	0	46.4	13.7	89.5	13	87.5
	22-Aug-2013		23.18	94	2	59.1	21.2	116.1	16	87.8
	9-Sep-2013		124.65	90	2	55.5	21.5	112.6	18	89.6
	27-Sep-2013		27.94	92	9	74.9	35.4	114.3	18	87.0
	5-Oct-2013		12.58	92	2	54.2	18.3	157.5	20	85.0
	9-Oct-2013		92.32	93	2	62.1	33.0	136.4	16	84.0
	21-Oct-2013		89.33	64	7	82.9	60.0	230.4	26	83.5
	24-Oct-2013		26.01	91	3	67.5	32.8	139.2	17	83.0
	2-Nov-2013		79.45	71	6	72.4	15.2	248.6	27	78.0
	23-Dec-2013		178.66	42	1	68.5	29.2	112.5	15	76.0
	4-Jan-2014		44.82	90	3	62.4	35.4	134.5	16	70.0
	8-Jan-2014		30.53	88	8	70.7	24.6	169.8	26	67.5
	15-Mar-2014		65.27	84	12	79.9	41.9	172.9	26	57.8
	9-Apr-2014		3.33	89	2	47.6	11.6	105.3	21	34.1
	8-May-2014		4.74	92	2	51.6	19.3	127.1	21	68.8
	4-Jun-2014		8.33	94	5	48.8	5.2	163.8	32	83.8
	22-Jun-2014		23.71	94	6	58.5	17.2	124.4	17	84.0
	4-Jul-2014		11.08	95	1	47.8	15.9	107.0	22	84.5
	8-Jul-2014		4.43	92	7	52.4	18.8	136.1	21	85.0
	14-Jul-2014		5.53	94	4	48.9	15.0	120.4	20	85.3
	21-Jul-2014		6.10	95	4	49.7	20.6	115.0	21	86.5
Seasons	Spring	3	5.4	91	3	51.3	15.2	111.9	20	62.2
	Summer	9	24.9	91	4	57.5	24.4	99.7	14	86.2
	Fall	8	68.9	77	4	58.5	24.3	130.4	17	82.3
	Winter	4	46.8	87	8	82.4	41.9	172.9	24	65.1
Growth periods	Leaf-on	19	44.7	89	6	56.6	18.1	103.9	15	83.9
	Leaf-off	5	22.4	86	4	77.2	42.4	138.2	21	62.4

The *TFPR* spatial distribution was investigated for each individual storm event using ordinary kriging method in Arc GIS 10.2 (Staelens et al., 2006) and corresponding maps were also developed in four seasons and two growth conditions. Rain events in this study were categorized in three classes of gross precipitation <10 mm, 10–30 mm and >30 mm as already suggested by Hosseini Ghaleh Bahmani et al. (2012).

The canopy cover of the forest stand was determined by 119 photos taken during 17 date (times) to consider intra variation of canopy cover (Sadeghi et al., 2007) at seven fixed points randomly distributed throughout the study area. The photography localities and other details have been shown in Figure 1. A Nikon Coolpix camera (20 megapixels) mounted on an wooden stack stand at 50 cm above the forest floor was applied to take vertical pictures to be further processed based on K-mean classification method (Vattani, 2011) and ultimately to determine percent of canopy cover (*PCC*).

All the statistical analyses were applied by IBM SPSS Statistics 22 software in 95% confidence level ($P < 0.05$). The influence of vegetation cover situations i.e. leaf-on and leaf-off periods on amount of TFPR and frequency of hotspot points were analyzed by paired t-test. Influence of seasonality on amount of TFPR was also analyzed by one-way ANOVA on the basis of Duncan's multiple comparison test (Rahmani et al., 2011; Ritter et al., 2005). The relation between *PCC* and *TFPR* was additionally determined by Pearson correlation test (Rahmani et al., 2011; Staelens et al., 2006).

RESULTS

Throughfall

A total of 938 mm of rain consisted of 24 events excluding a snow event was recorded between July 2013 and July 2014 (Table 1). A rare snowfall event of 120 cm occurred on 3 and 4 February 2014. The heavy snow covered all collectors at the study site, therefore no throughfall data were collected for this period.

The mean cumulative throughfall during the study period was 623±31 mm (≈ 66% of total rainfall). The average values of throughfall as % of rainfall (*TFPR*) were also found 56±14% and 78±10% for leaf-on and leaf-off periods, respectively. The difference was due to changes in canopy cover of the trees in the study area during leaf-on (growing) and leaf-off (non-growing) seasons as shown in Figure 2. The corresponding variations of mean canopy cover percentage of the study forest stand have also been presented in Figure 3.

According to the results, the average percent of canopy cover site for the entire study period was 66% varied from 41% to 81% for leaf-off and leaf-on periods, respectively. The minimum and maximum canopy covers were also recorded as 34% for 14 April 2014 and 89% for 8 September 2013.

Statistical analyses

The relationship between gross precipitation and *TF* both normally distributed attested by Kolmogorov-Smirnov test was considered by Pearson correlation test whose corresponding results have been summarized in Table 2. The results showed that there was a significant correlation between TF and gross precipitation at 99% confidence level.

The percent of canopy cover was determined for all storm events and correlated with *TF*. The results of Pearson correlation showed that there was no significant correlation ($P = 0.144$) between *PCC* and *TF* for gross precipitation data set >30 mm. However, this correlation was significant ($P < 0.04$)

Fig. 2. Canopy pictures taken from seven photography fixed points (P1–P7) during leaf-on (right) and leaf-off (left) periods.

Table 2. Results of Pearson correlations ($p<0.001$) among main study variables.

Factor	Statistical factor	Canopy cover (%)	Throughfall (mm)
Gross precipitation	No. of data Correlation coefficient Significant level	–	24 0.987** 0.00006
TF (gross precipitation <10 mm)	No. of data Correlation coefficient Significant level	7 0.960** 0.00004	
TF (10> gross precipitation <30 mm)	No. of data Correlation coefficient Significant level	8 0.882** 0.004	–
TF (gross precipitation >30 mm)	No. of data Correlation coefficient Significant level	9 0.529 0.144	

** Significant at 99% level of confidence

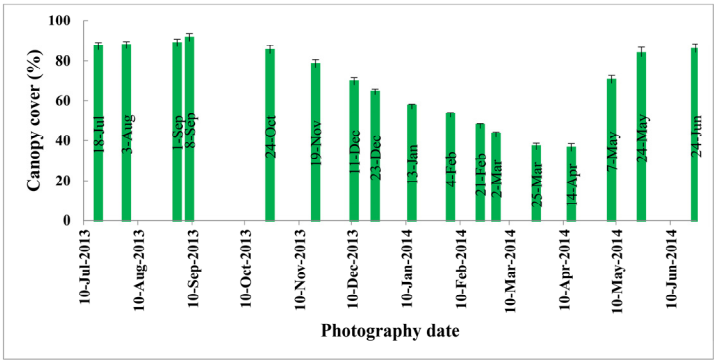

Fig. 3. Mean canopy cover variation during study period for a small Hyrcanian forest in Northern Iran.

Table 3. Results of paired t-test ($p < 0.001$) in leaf-on and leaf-off conditions in view point of throughfall as % of rainfall (*TFPR*) and hotspot frequency.

Study variables	Paired Differences					t-value	Degree of freedom	Significant level (2-tailed)
	Mean	Standard deviation	Standard error mean	95% Confidence interval of the difference				
				Lower	Upper			
TFPR	19.3	23.1	2.3	14.6	24.07	8.19	95	0.00005
Hotspot frequency	1.87	2.12	0.38	1.091	2.65	4.90	30	0.00003

Table 4. Results of ANOVA for comparison among *TF* in different seasons in study forest.

Source	Sum of squares	Degree of freedom	Mean squared	F-value	Significant level
Between Groups	47965.285	3	15988.4	41.7	0.0003
Within Groups	145594.736	380	383.1		
Total	193560.021	383			

for gross precipitation <10 mm and 10–30 mm at 99% confidence level.

The *TF* in two forest conditions (leaf-off and leaf-on) was also compared using paired t-test. The results showed that there was a significant difference ($P < 0.007$) between lower amounts of *TF* in leaf-off and higher amounts of *TF* in leaf-on season at 99% confidence level. The hotspots frequency in leaf-on and leaf-off conditions was also assessed by paired t-test and reported in Table 3. The results further showed that there was a significant difference ($P < 0.01$) between frequency of hotspots in leaf-on and leaf-off conditions, and the frequency of hotspots in leaf-on conditions was obviously more than those of leaf-off season.

One-way ANOVA on the basis of Duncan's multiple comparison test ($p < 0.05$) was also used to compare *TF* in different seasons whose results have been given in Table 4. Results showed that the amounts of *TF* in different seasons had significant difference at 99% confidence level as the maximum *TFPR* occurred in winter (82.36%) and the minimum *TFPR* was in spring (51.29%). The results of Duncan's test also showed that there was no significant difference between *TFPR* in autumn (58.49%) and summer (57.43%) seasons.

Spatio-temporal analysis of throughfall

The spatial distribution of throughfall as % of rainfall was mapped for the seasonal and growing/non-growing periods as shown in Figure 4. Results of spatio-temporal variations for *TFPR* showed there were miscellaneous patterns of *TFPR* distribution in different seasons, especially between leaf-on and leaf-of periods.

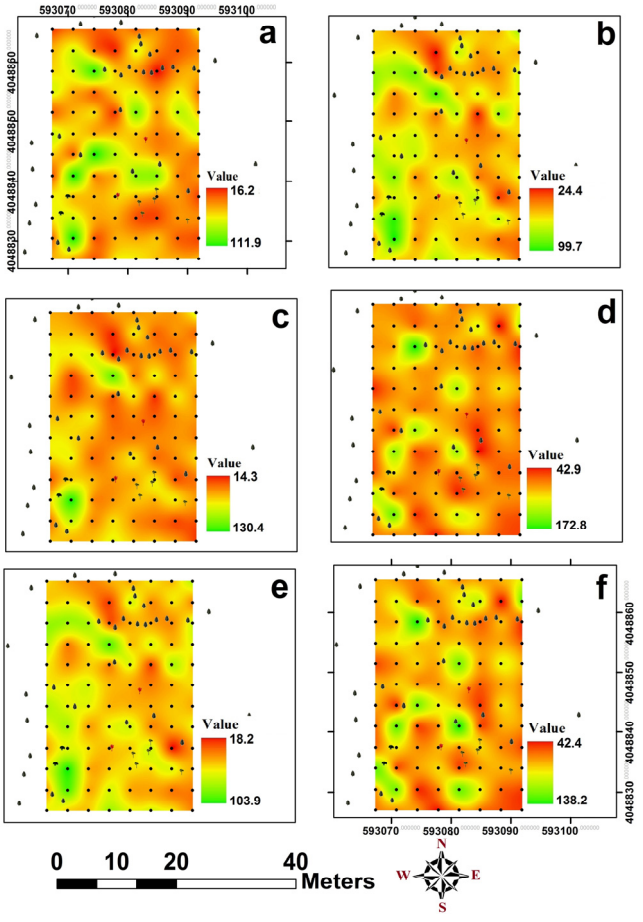

Fig. 4. Spatial variations in throughfall as % of rainfall for spring (a), summer (b), autumn (c), winter (d), leaf-on (e) and leaf-off (f) for a representative Hyrcanian forest stand, northern Iran.

In forest floor during rainfall, *TFPR* in some points was more than the gross rainfall, signifying hotspots (Figure 5). These hotspots occurred through directing rainfall to spatial points by leaves and branches of trees. In addition and based on anecdotal evaluation, the hotspot frequency in collectors located

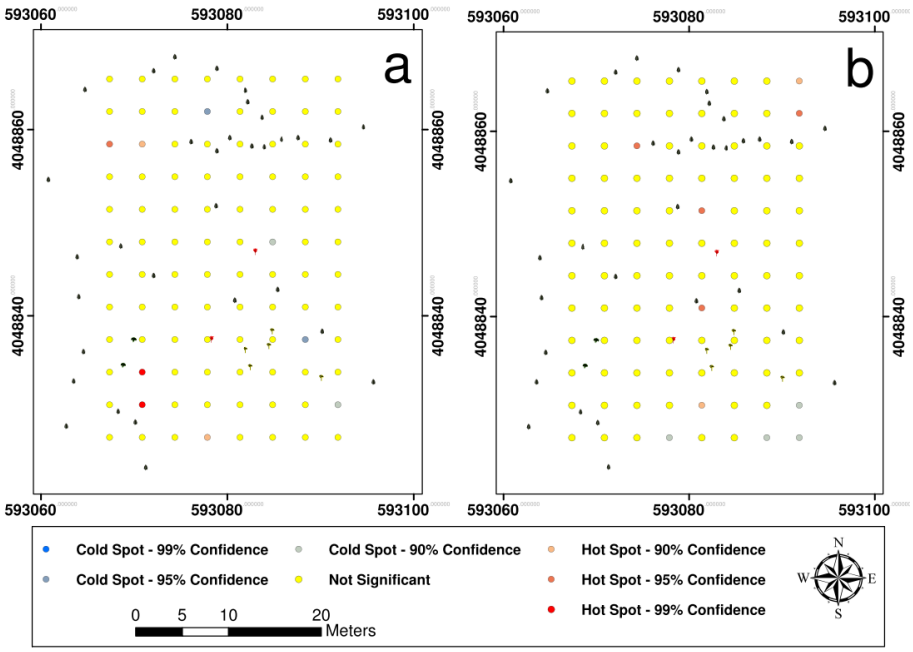

Fig. 5. Hot/cold spot analysis of *TFPR* for Leaf-on (a) and Leaf-off (b) periods.

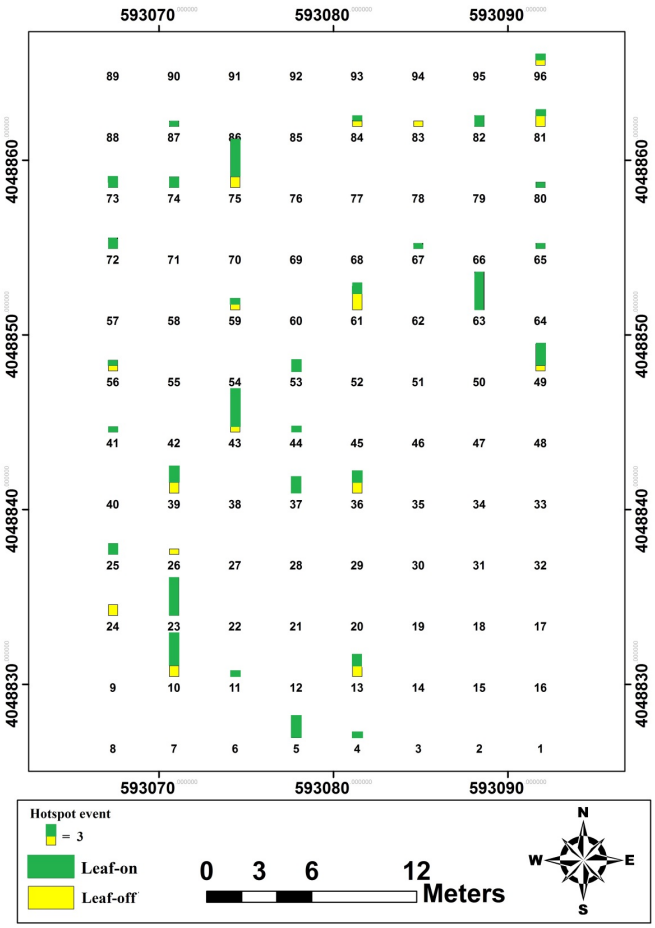

Fig. 6. Distribution of hotspot frequencies (No. of events with amounts of throughfall more than gross rainfall; the higher bar the more frequency of hotspots) during leaf-on and leaf-off periods.

in 2–6 m away from trees was more than collectors located closer than 2 m or beyond 6 m. The hotspot frequency around the *Quercus castaneifolia* and *Populus caspica* in the both study conditions (leaf-on and leaf-off seasons) was very low. Frequency of hotspots in the study time was determined during leaf-off and leaf-on periods represented in Figure 6.

DISCUSSION

The results of ANOVA confirmed that *TF* in different seasons had significant difference at 99% confidence level and PRT in spring was more than other seasons. However, Duncan's classification showed that there was no significant difference between summer and fall seasons in *TF*. The graphical comparison among maps developed for seasons and growing condition of the study stand (Figure 4) verified a general symmetric condition between *TF* distribution in summer and growing season as well as *TF* distribution in winter and non-growing season. It clearly verified that spring and autumn played a transitional situation in two other seasons and conditions. It was also implied from the results that the Hyrcanian plain forest did not have more variation in canopy cover during summer and fall seasons. The lack of leaves in forest decreased the value of interception and increased the throughfall (Nasiri et al., 2012; Xiao et al., 2000). Besides those, the results showed that in all maps around the *Parrotia persica* trees, the value of *TF* was higher than other species because of different morphologies among study species. This can be attributed to *Parrotia persica* having smooth leaves and branches and the frequency of grooves in this species is lower than other species leading to less interception and rain loss as reported by Nasiri et al. (2012).

The results of Pearson correlation showed that there was a significant correlation (r = 0.987) between *TF* and gross precipitation. The high correlations between *TF* and gross precipitation have already been reported by former researches (e.g., Carlyle-Moses, 2004; Gurav et al., 2012; Park and Cameron, 2008; Shachnovich et al., 2008) as 0.998, 0.988, 0.996 and 0.979, respectively for different forest stands throughout the globe. The correlation results also showed that the influence of canopy cover to absorb the rainfall was significant just for rain events smaller than 30 mm. This results additionally showed that the Pearson correlation coefficient for gross precipitation <10 mm was more than rain events for 10 mm < gross precipitation <30 mm. The amount of interception in rainfalls with high duration and low volume was high, while it was low in events with high intensity and more volume. This is consistent with other studies (Herold et al., 2005; Hosseini Ghaleh Bahmani et al. 2012; Nasiri et al., 2012; Rahmani et al., 2011; Xiao et al., 2000). Interestingly, the throughfall values obtained for the study area as a representative area for the Hyrcanian plain were similar to the findings for mountain ecosystems in Slovakia and the Czech Republic by Holko et al. (2009) and Dohnal et al. (2014).

Results of paired sample t-test showed that there was significant difference (P = 0.007) between leaf-on and leaf-off periods in TFPR and hotspot frequency. Canopy cover in leaf-on period prepared conditions to reduce the amount of rain by increasing leaves and branches soak. Hotspots frequency in leaf-on period was more than leaf-off condition. Hotspots in interception system show the behavior of canopy drainage pattern (Coenders-Gerrits et al., 2013; Hopp and McDonnell, 2011). Hence, the whole branches stand downward and therefore allow easy drainage of the throughfall during leaf-on conditions. Accordingly, the hotspot frequency in collectors located in 2–6 m away from trees was more than other far points. This was also noticed by (Coenders-Gerrits et al., 2013; Germer et al., 2006; Ziegler et al., 2007). In addition, results showed that the hotspot frequency around the *Quercus castaneifolia* and *Populus caspica* in the both leaf-on and leaf-off periods was very low (Figure 4). The main reason for this observation was the tall growth and contact acute angel of the tributaries to the main trunk of these species as reported by Nasiri et al. (2012).

Only 66 % of the annual rainfall was able to penetrate the canopy of the study forest on the study Hyrcanian plain, and the canopy spatially redistributed the precipitation reaching the forest floor. Rahmani et al. (2011), reported that an average of 43% of the total gross precipitation penetrated through the canopy as throughfall in another Hyrcanian mountain forest stand located in hilly areas (900 m above mean sea level). The maximum value of throughfall as % of rainfall in the study area and during study period was 248% at collector number 23 (Figure 1) for the rain (79.4 mm) on 3 November 2013. The *TF* was approximately 197 mm at this collector. The mean *TF* at the study site for this rain was 23%. Collector 23 was near a *Parrotia persica* tree. *P. persica* is a multi-branched tree with an earlier leaf-off period than other species. The minimum *TFPR* during the study was 6% at collector 85 during a rainstorm (8 mm) on 4 June 2014. Collector 85 was surrounded by *Carpinus betulus* trees. The mean *TFPR* for this storm was 49%. *C. betulus* has dense foliage, and raindrops cannot easily pass directly through the crown without interacting with the foliage, especially during the growing season.

CONCLUSION

The present study figured out an approximation for throughfall rates and its variability in a Hyrcanian plain forest, northern Iran. The relevances between spatio-temporal variations of throughfall with distribution and phonological and morphological characteristics of existing species, and rainfall properties were also elucidated in the study deciduous Hyrcanian forest. Hence, the seasonal and periodical changes of throughfall were revealed at respective tunes of 49, 43, 42 and 18% for spring, summer, autumn and winter. The study forest could also intercept some 43 and 23% of the rainfall in the leaf-on and leaf-off periods. The results of the present study can be effectively used by forest hydrologist to help decision makers, planner and foresters adopt appropriate silvicultural measures for better management of hydrological behavior of the Hyrcanian forest in the north of Iran. Though further insight studies with longer period and more extensive areas and even in different forest stands are essentially needed to allow drawing comprehensive conclusions.

REFERENCES

Adriaenssens, S., Hansen, K., Staelens, J., Wuyts, K., De Schrijver, A., Baeten, L., Boeckx, P., Samson, R., Verheyen, K., 2012. Throughfall deposition and canopy exchange processes along a vertical gradient within the canopy of beech (*Fagus sylvatica* L.) and Norway spruce (*Picea abies* (L.) Karst). Sci. Total Environ., 420, 168–182. DOI: 10.1016/j.scitotenv.2011.12.029.

Aikawa, M., Hiraki, T., Tamaki, M., 2006. Comparative field study on precipitation, throughfall, stemflow, fog water, and atmospheric aerosol and gases at urban and rural sites in Japan. Sci. Total Environ., 366, 1, 275–285. DOI: 10.1016/j.scitotenv.2005.06.027.

Ajami, H., Troch, P.a., Maddock, T., Meixner, T., Eastoe, C., 2011. Quantifying mountain block recharge by means of catchment-scale storage-discharge relationships. Water Resour. Res., 47, 4, 1–14. DOI: 10.1029/2010WR009598.

Bosch, J.M., Hewlett, J.D., 1982. A review of catchment experiments to determine the effect of vegetation changes on water yield and evaoptranspiration. J. Hydrol., 55, 3–23.

Brandt, J., 1987. The effect of different types of forest management on the transformation of rainfall energy by the

canopy in relation to soil erosion. In: Proc. Vancouver Symposium Forest Hydrology and Watershed Management. IAHS Press, Wallingford, pp. 213–222.

Brecciaroli, G., Cocco, S., Agnelli, A., Courchesne, F., Corti, G., 2012. From rainfall to throughfall in a maritime vineyard. Sci. Total Environ., 438, 174–188. DOI: 10.1016/j.scitotenv.2012.08.044.

Bruijnzeel, L.A., 2005. Tropical montane cloud forest: a unique hydrological case. In: Bonell, M., Bruijnzeel, L.A. (Eds.): Forests, Water and People in the Humid Tropics: Past, Present and Future Hydrological Research for Integrated Land and Water Management. Cambridge University Press, Cambridge, UK.

Buendia, C., Batalla, R.J., Sabater, S., Palau, A., Marcé, R., 2016. Runoff trends driven by climate and afforestation in a pyrenean basin. Land Degrad. Dev., 27, 3, 823–838. DOI: 10.1002/ldr.2384.

Cao, Y., Ouyang, Z. Y., Zheng, H., Huang, Z.G., Wang, X.K., Miao, H., 2008. Effects of forest plantations on rainfall redistribution and erosion in the red soil region of Southern China, Land Degrad. Dev., 19, 3, 321–330. DOI: 10.1002/ldr.812.

Carlyle-Moses, D.E., 2004. Throughfall, stemflow, and canopy interception loss fluxes in a semi-arid Sierra Madre Oriental matorral community. J. Arid. Environ., 58, 2, 181–202. DOI: 10.1016/S0140-1963(03)00125-3.

Celentano, D., Rousseau, G.X., Engel, V.L., Zelarayán, M., Oliveira, E.C., Araujo, A.C.M., de Moura, E.G., 2016. Degradation of riparian forest affects soil properties and ecosystem services provision in eastern Amazon of Brazil. Land Degrad. Dev., DOI: 10.1002/ldr.2547.

Chappell, N.A., Bidin, K., 2001. Modelling rainfall and canopy controls on net-precipitation beneath selectively-logged tropical forest. plant. Ecol., 153, 1, 215–229. DOI: 10.1023/A:1017532411978.

Coenders-Gerrits, A.M.J., Hopp, L., Savenije, H.H.G., Pfister, L., 2013. The effect of spatial throughfall patterns on soil moisture patterns at the hillslope scale. Hydrol. Earth Syst. Sci., 17, 5, 1749–1763. DOI: 10.5194/hess-17-1749-2013.

Cox, C.A., Sarangi, A., Madramootoo, C.A., 2006. Effect of land management on runoff and soil losses from two small watersheds in St Lucia. Land Degrad. Dev., 17, 1, 55–72. DOI: 10.1002/ldr.694.

David, J.S., Bellot, J., Birot, Y., David, T.S., 2011. Water fluxes in forests. In: Birot, Y., Gracia, C., Palahi, M. (Eds.): Water for Forests and People in the Mediterranean Region – A Challenging Balance. What Science Can Tell Us? European Forest Institute, Sarjanr, Finland, pp. 32–36.

Davudirad, A.A., Sadeghi, S.H.R., Sadoddin, A., 2015. Monitoring temporal and spatial changes in land use in the Shazand Watershed, Iran. J. Ecohydrol., 2, 4, 405–415. (In Persian.)

Davudirad, A.A., Sadeghi, S.H.R., Sadoddin, A., 2016. The impact of development plans on hydrological changes in the Shazand Watershed, Iran. Land Degrad. Dev., 27, 4, 1236–1244. DOI: 10.1002/ldr.2523.

Deng, Z., Priestley, S.C., Guan, H., Love, A.J., Simmons, C.T., 2013. Canopy enhanced chloride deposition in coastal South Australia and its application for the chloride mass balance method. J. Hydrol., 497, 62–70. DOI: 10.1016/j.jhydrol.2013.05.040.

Devlaeminck, R., De Schrijver, A., Hermy, M., 2005. Variation in throughfall deposition across a deciduous beech (*Fagus sylvatica* L.) forest edge in Flanders. Sci. Total Environ., 337, 1, 241–252. DOI: 10.1016/j.scitotenv.2004.07.005.

Díaz, M.F., Bigelow, S., Armesto, J.J., 2007. Alteration of the hydrologic cycle due to forest clearing and its consequences for rainforest succession. For. Ecol. Manage., 244, 1–3, 32–40. DOI: 10.1016/j.foreco.2007.03.030.

Dohnal, M., Černý, T., Votrubová, J., Tesař, M., 2014. Rainfall interception and spatial variability of throughfall in spruce stand. J. Hydrol. Hydromech, 62, 4, 277–284. DOI: 10.2478/johh-2014-0037.

Ebrahimpour, K.J., Nemati, M., Samariha, A., 2011. Study of product of the wood in forests in North of Iran at ten years period. J. Basic. Appl. Sci. Res., 1, 9, 1255–1261.

Forti, M.C., Neal, C., 1992. Spatial variability of throughfall chemistry in a tropical rainforest (Central Amazonia, Brazil). Sci. Total Environ., 120, 3, 245–259.

Frot, E., van Wesemael, B., Vandenschrick, G., Souchez, R., Benet, A.S., 2007. Origin and type of rainfall for recharge of a karstic aquifer in the western Mediterranean: A case study from the Sierra de Gador-Campo de Dalias (southeast Spain). Hydrol. Process., 21, 3, 359–368. DOI: 10.1002/hyp.6238.

Gabarrón-Galeote, M., Martínez-Murillo, J., Quesada, M., Ruiz-Sinoga, J., 2013. Seasonal changes in the soil hydrological and erosive response depending on aspect, vegetation type and soil water repellency in different Mediterranean microenvironments. Solid. Earth., 4, 2, 497–509. DOI: 10.5194/se-4-497-2013.

García-Fayos, P., Bochet, E., Cerdà, A., 2010. Seed removal susceptibility through soil erosion shapes vegetation composition. Plant. Soil., 334, 1–2, 289–297. DOI: 10.1007/s11104-010-0382-6.

Gay, T.E., Van Stan, J.T., Moore, L.D., Lewis, E.S., Reichard, J.S., 2015. Throughfall alterations by degree of *Tillandsia usneoides* cover in a southeastern US *Quercus virginiana* forest. Can. J. For. Res., 45, 12, 1688–1698. DOI: 10.1139/cjfr-2015-0233.

Germer, S., Elsenbeer, H., Moraes, J., 2006. Throughfall and temporal trends of rainfall redistribution in an open tropical rainforest, south-western Amazonia (Rondônia, Brazil). Hydrol. Earth Syst. Sci., 10, 3, 383–393. DOI: 10.5194/hess-10-383-2006.

Getis, A., Ord, J.K., 1992. The analysis of spatial associataion by use of distance statistics. Geogr. Anal., 24, 189–206. DOI: 10.1111/j.1538-4632.1992.tb00261.x.

Gurav, M., D, S.K.M., Kushalappa, C.G., Vaast, P., 2012. Throughfall and interception loss in relation to different canopy levels of coffee agroforestry systems. Int. J. Environ. Sci. Technol., 1, 3. DOI: 10.1109/CHUSER.2012.6504289.

Guswa, A.J., Spence, C.M., 2012. Effect of throughfall variability on recharge: application to hemlock and deciduous forests in western Massachusetts. Ecohydrology, 5, 5, 563–574. DOI: 0.1002/eco.281.

Herold, M., Couclelis, H., Clarke, K.C., 2005. The role of spatial metrics in the analysis and modeling of urban land use change. Comput. Environ. Urban Syst., 29, 4, 369–399. DOI: 10.1016/j.

Hinko-Najera, N., Fest, B., Livesley, S.J., Arndt, S.K., 2015. Reduced throughfall decreases autotrophic respiration, but not heterotrophic respiration in a dry temperate broadleaved evergreen forest. Agr. Forest. Meteorol., 200, 66–77. DOI: 10.1016/j.agrformet.2014.09.013.

Holder, C.D., 2003. Fog precipitation in the Sierra de las Minas biosphere reserve, Guatemala. Hydrol. Process., 17, 10, 2001–2010. DOI: 10.1002/hyp.1224.

Holder, C.D., 2004. Rainfall interception and fog precipitation in a tropical montane cloud forest of Guatemala. For. Ecol.

Manage., 190, 2, 373–384. DOI: 10.1016/j.foreco.2003.11.004.
Holko, L., Škvarenina, J., Kostka, Z., Frič, M., Staroň, J., 2009. Impact of spruce forest on rainfall interception and seasonal snow cover evolution in the Western Tatra Mountains, Slovakia. Biologia, 64, 3, 594–599. DOI: 10.2478/s11756-009-0087-6.
Hopp, L., McDonnell, J.J., 2011. Examining the role of throughfall patterns on subsurface stormflow generation. J. Hydrol., 409, 1–2, 460–471. DOI: 10.1016/j.jhydrol.2011.08.044.
Hosseini Ghaleh Bahmani, S.M., Attarod, P., Bayramzadeh, V., Ahmadi, M.T., Radmehr, A., 2012. Throughfall, stemflow, and rainfall interception in a natural pure forest of chestnut-leaved oak (*Quercus castaneifolia* C.A. Mey.) in the Caspian forest of Iran. Ann. For. Res., 55, 2, 197–206. DOI: 10.15287/afr.2012.60.
Hosseini, M., Ghafouri, M., Tabatabaei, M.R., Ebrahimi, N.G., Zare Garizi, A., 2016. Estimation of hydrologic budget for Gharasou Watershed, Iran. Ecopersia, 4, 3, 1455–1469.
Huber, A., Iroumé, A., 2001. Variability of annual rainfall partitioning for different sites and forest covers in Chile. J. Hydrol., 248, 1–4, 78–92. DOI: 10.1016/S0022-1694(01)00394-8.
Keesstra, S., Bruijnzeel, L., Van Huissteden, J., 2009. Meso-scale catchment sediment budgets: combining field surveys and modeling in the Dragonja catchment, southwest Slovenia. Earth. Surf. Poc. Land., 34, 11, 1547–1561. DOI: 10.1002/esp.1846.
Keesstra, S., Kondrlova, E., Czajka, A., Seeger, M., Maroulis, J., 2012. Assessing riparian zone impacts on water and sediment movement: a new approach. Neth. J. Geosci., 91, 1–2, 245–255. DOI: 10.1016/j.cosust.2012.10.007.
Keim, R.F., Skaugset, A.E., Weiler, M., 2005. Temporal persistence of spatial patterns in throughfall. J. Hydrol., 314, 263–274. DOI: 10.1016/j.jhydrol.2005.03.021.
Lal, R., 1997. Deforestation effects on soil degradation and rehabilitation in western Nigeria. IV. Hydrology and water quality. Land Degrad. Dev., 8, 2, 95–126, DOI: 10.1002.
Llorens, P., Domingo, F., 2007. Rainfall partitioning by vegetation under Mediterranean conditions. A review of studies in Europe. J. Hydrol., 335, 1–2, 37–54. DOI: 10.1016/j.jhydrol.2006.10.032.
Lloyd, C.R., 1988. Spatial variability of throughfall and stemflow measurements in Amazonian rainforest. Agr. Forest. Meteorol., 42, 1, 63–73.
Loescher, H.W., Powers, J.S., Oberbauer, S.F., 2002. Spatial variation of throughfall volume in an old-growth tropical wet forest, Costa Rica. J. Trop. Ecol., 18, 03, 397–407. DOI: 10.1017/S0266467402002274.
Marin, C.T., Bouten, W., Sevink, J., 2000. Gross rainfall and its partitioning into throughfall, stemflow and evaporation of intercepted water in four forest ecosystems in western Amazonia. J. Hydrol., 237, 1–2, 40–57. DOI: 10.1016/S0022-1694(00)00301-2.
Mitchell, M., Robarge, W.P., Bruck, R.I., Cowling, E.B., 1986. Throughfall and Stemflow Measurements during the Summer of 1986: A Preliminary Report.
Molina, A.J., Campo, A.D., 2012. The effects of experimental thinning on throughfall and stemflow: A contribution towards hydrology-oriented silviculture in Aleppo pine plantations. For. Ecol. Manage., 269, 206–213. DOI: 10.1016/j.foreco.2011.12.037.
Nanko, K., Hotta, N., Suzuki, M., 2006. Evaluating the influence of canopy species and meteorological factors on throughfall drop size distribution. J. Hydrol., 329, 3–4, 422–431. DOI: 10.1016/j.jhydrol.2006.02.036.
Nasiri, M., Zare, N., Jalilvand, H., 2012. Investigation of the effective factors on rate of stemflow for tree species in Hyrcanian forests. Egypt. J. Bio., 14, 1, 37–44. DOI: 10.4314/ejb.v14i1.4.
Novara, A., Gristina, L., Guaitoli, F., Santoro, A., Cerdà, A., 2013. Managing soil nitrate with cover crops and buffer strips in Sicilian vineyards. Solid. Earth., 4, 2, 255–262. DOI: 10.5194/se-4-255-2013, 2013.
Onozawa, Y., Chiwa, M., Komatsu, H., Otsuki, K., 2009. Rainfall interception in a moso bamboo (*Phyllostachys pubescens*) forest. J. For. Res., 14, 2, 111–116. DOI: 10.1007/s10310-008-0108-2.
Park, A., Cameron, J.L., 2008. The influence of canopy traits on throughfall and stemflow in five tropical trees growing in a Panamanian plantation. For. Ecol. Manage., 255, 5–6, 1915–1925. DOI: 10.1016/j.foreco.2007.12.025.
Pereira, P., Cerdà, A., Úbeda, X., Mataix-Solera, J., Martin, D., Jordán, A., Burguet, M., 2013. Spatial models for monitoring the spatio-temporal evolution of ashes after fire–a case study of a burnt grassland in Lithuania. Solid. Earth., 4, 1, 153–165. DOI: 10.5194/se-4-153-2013.
Pérez-Suárez, M., Fenn, M.E., Cetina-Alcala, V.M., Aldrete, A., 2008. The effects of canopy cover on throughfall and soil chemistry in two forest sites in the México City air basin. Atmosfera, 21, 1, 83–100. DOI: 10.1007/978-0-387-22520-3_15.
Pypker, T.G., Bond, B.J., Link, T.E., Marks, D., Unsworth, M.H., 2005. The importance of canopy structure in controlling the interception loss of rainfall: Examples from a young and an old-growth Douglas-fir forest. Agr. Forest. Meteorol., 130, 1–2, 113–129. DOI: 10.1016/j.agrformet.2005.03.003.
Rahmani, R., Sadoddin, A., Ghorbani, S., 2011. Measuring and modelling precipitation components in an Oriental beech stand of the Hyrcanian region, Iran. J. Hydrol., 404, 3, 294–303. DOI: 10.1016/j.jhydrol.2011.04.036.
Ritter, E., Dalsgaard, L., Einhorn, K.S., 2005. Light, temperature and soil moisture regimes following gap formation in a semi-natural beech-dominated forest in Denmark. For. Ecol. Manage., 206, 1, 15–33. DOI: 10.1016/j.foreco.2004.08.011.
Roberts, J., Rosier, P., 2005. The impact of broadleaved woodland on water resources in lowland UK: III. The results from Black Wood and Bridgets Farm compared with those from other woodland and grassland sites. Hydrol. Earth Syst. Sci., 9, 6, 614–620. DOI: 10.5194/hess-9-614-2005.
Sadeghi, S., Gholami, L., Sharifi, E., Khaledi Darvishan, A., Homaee, M., 2015. Scale effect on runoff and soil loss control using rice straw mulch under laboratory conditions. Solid. Earth., 6, 1, 1–8. DOI: 10.5194/se-6-1-2015.
Sadeghi, S.H.R., Mizuyama, T., Miyata, S., Gomi, T., Kosugi, K., Mizugaki, S., Onda, Y., 2007. Is MUSLE apt to small steeply reforested watershed? J. Forest Res., 12, 270–277. DOI: 10.1007/s10310-007-0017-9.
Sadeghi, S.H.R., Moatamednia, M., Behzadfar, M., 2011. Spatial and temporal variations in the rainfall erosivity factor in Iran. J.Agricul. Sci. Technol., 13, 451–464.
Sadeghi, S.H.R., Mizuyama, T., 2007. Applicability of Modified Universal Soil Loss Equation for prediction of sediment yield in Khanmirza watershed, Iran, Hydrol. Sci. J., 52, 5, 1068–1075. DOI:10.1623/hysj.52.5.1068.
Sadeghi, S.H.R., Mizuyama, T., Miyata, S., Gomi, T., Kosugi, K., Fukushima, T., Mizugaki, S., Onda, Y., 2008.

Determinant factors of sediment graphs and rating loops in a reforested watershed. J. Hydrol., 356, 271–282. DOI: 10.1016/j.jhydrol.2008.04.005.

Sadeghi, S.H.R., Vangah, B.G., Safaeeian, N.A., 2007. Comparison between effects of open grazing and manual harvesting of cultivated summer rangelands of northern Iran on infiltration, runoff and sediment yield. Land. Degrad. Dev., 18, 6, 608–620. DOI: 10.1002/ldr.799.

Sadeghi, S.H.R., Saeidi, P., 2010. Reliability of sediment rating curves for a deciduous forest watershed in Iran. Hydrol.Sci. J., 55, 5, 821–831. DOI: 10.1080/02626667.2010.489797.

Shachnovich, Y., Berliner, P.R., Bar, P., 2008. Rainfall interception and spatial distribution of throughfall in a pine forest planted in an arid zone. J. Hydrol., 349, 1–2, 168–177. DOI: 10.1016/j.jhydrol.2007.10.051.

Staelens, J., De Schrijver, A., Verheyen, K., 2007. Seasonal variation in throughfall and stemflow chemistry beneath a European beech (*Fagus sylvatica*) tree in relation to canopy phenology. Can. J. For. Res., 37, 8, 1359–1372. DOI: 10.1139/X07-003.

Staelens, J., De Schrijver, A., Verheyen, K., Verhoest, N.E.C., 2006. Spatial variability and temporal stability of throughfall water under a dominant beech (*Fagus sylvatica* L.) tree in relationship to canopy cover. J. Hydrol., 330, 3–4, 651–662. DOI: 10.1016/j.jhydrol.2006.04.032.

Tcherepanov, E., Zlotnik, V., Henebry, G., 2005. Using Landsat thermal imagery and GIS for identification of groundwater discharge into shallow groundwater-dominated lakes. Int. J. Remote. Sens., 26, 17, 3649–3661. DOI: 10.1080/01431160500177315.

Van Stan, J.T., Levia, D.F., Inamdar, S.P., Lepori-Bui, M., Mitchell, M.J., 2012. The effects of phenoseason and storm characteristics on throughfall solute washoff and leaching dynamics from a temperate deciduous forest canopy. Sci. Total Environ., 430, 48–58. DOI: 10.1016/j.scitotenv.2012.04.060.

Vattani, A., 2011. k-means requires exponentially many iterations even in the plane. Discrete. Comput. Geom., 45, 4, 596–616. DOI: 10.1007/s00454-011-9340-1.

Vega, J.A., Fernández, C., Fonturbel, T., 2005. Throughfall, runoff and soil erosion after prescribed burning in gorse shrubland in Galicia (NW Spain). Land Degrad. Dev., 16, 1, 37–51. DOI: 10.1002/ldr.643.

Vernimmen, R.R.E., Bruijnzeel, L.A., Romdoni, a., Proctor, J., 2007. Rainfall interception in three contrasting lowland rain forest types in Central Kalimantan, Indonesia. J. Hydrol., 340, 3–4, 217–232. DOI: 10.1016/j.jhydrol.2007.04.009.

Wuyts, K., De Schrijver, A., Staelens, J., Gielis, M., Geudens, G., Verheyen, K., 2008. Patterns of throughfall deposition along a transect in forest edges of silver birch and Corsican pine. Can. J. For. Res., 38, 3, 449–461. DOI: 0.1139/X07-181.

Xiao, Q., McPherson, E.G., Ustin, S.L., Grismer, M.E., Simpson, J.R., 2000. Winter rainfall interception by two mature open-grown trees in Davis, California. Hydrol. Process., 14, 4, 763–784. DOI: 10.1002/(SICI)1099-1085(200003)14:43.3.CO;2-Z.

Xu, X., Guan, H., Deng, Z., 2014. Isotopic composition of throughfall in pine plantation and native eucalyptus forest in South Australia. J. Hydrol., 514, 150–157. DOI: 10.1016/j.jhydrol.2014.03.068.

Yousefi, S., Moradi, H.R., Boll, J., Schönbrodt-Stitt, S., 2016. Effects of road construction on soil degradation and nutrient transport in Caspian Hyrcanian mixed forests. Geoderma, 284, 103–112. DOI: 10.1016/j.geoderma.2016.09.002.

Zhang, G., Zeng, G.-M., Huang, G.-H., Jiang, Y.-M., Yao, J.-M., Du, C.-Y., Jiang, R., Zhang, C., 2006. Deposition pattern of precipitation and throughfall in a subtropical evergreen forest in south-central China. J. For. Res., 11, 6, 389–396. DOI: 10.1007/s10310-006-0232-9.

Zhang, Q., Xu, C.-Y., Zhang, Z., Chen, Y.D., Liu, C.-L., 2009. Spatial and temporal variability of precipitation over China, 1951–2005. Theor. Appl. Climatol., 95, 1–2, 53–68. DOI: 10.1007/s00704-007-0375-4.

Ziegler, A.D., Negishi, J.N., Sidle, R.C., Gomi, T., Noguchi, S., Nik, A.R., 2007. Persistence of road runoff generation in a logged catchment in Peninsular Malaysia. Earth. Surf. Proc. Land., 32, 13, 1947–1970. DOI: 10.1002/esp.1508.

Zimmermann, A., Zimmermann, B., 2014. Agricultural and forest meteorology requirements for throughfall monitoring: The roles of temporal scale and canopy complexity. Agr. Forest. Meteorol., 189–190, 125–139. DOI: 10.1016/j.agrformet.2014.01.014.

Zimmermann, B., Zehe, E., Hartmann, N.K., Elsenbeer, H., 2008. Analyzing spatial data: An assessment of assumptions, new methods, and uncertainty using soil hydraulic data. Water Resour. Res., 44, 10, 1–18. DOI: 10.1029/2007WR006604.

Zirlewagen, D., von Wilpert, K., 2001. Modeling water and ion fluxes in a highly structured, mixed-species stand. For. Ecol. Manage., 143, 1–3, 27–37. DOI: 10.1016/S0378-1127(00)00522-3.

Received 13 October 2016
Accepted 24 January 2017

J. Hydrol. Hydromech., 66, 2018, 1, 107–120
DOI: 10.1515/johh-2017-0028

Use of conventional flow resistance equations and a model for the Nikuradse roughness in vegetated flows at high submergence

Paola Gualtieri*, Sergio De Felice, Vittorio Pasquino, Guelfo Pulci Doria †

University of Naples Federico II, Department of Civil, Architectural and Environmental Engineering, Via Claudio 21 80125 Napoli, Italy.
sdefelic@unina.it; vittorio.pasquino@unina.it
* Corresponding author. E-mail: paola.gualtieri@unina.it
† Deceased

Abstract: This study examines the problem of flow resistance due to rigid vegetation in open channel flow. The reliability of the conventional flow resistance equations (i.e. Keulegan, Manning and Chézy-Bazin) for vegetated flows at high submergence, i.e. $h/k > 5$, (where h = flow depth and k = vegetation height) is assessed. Several modern flow resistance equations based on a two-layer approach are examined, showing that they transform into the conventional equations at high submergences. To compare the conventional flow resistance equations at high submergences, an experimental methodology is proposed and applied to the experimental data reported in the literature and collected for this study. The results demonstrate the reliability of the Keulegan equation in predicting the flow resistance. Based on the obtained results, a model to evaluate the Nikuradse equivalent sand-grain roughness, k_N, starting from the vegetation height and density, is proposed and tested.

Keywords: Open channel flows; Vegetated flows; Rigid vegetation; Flow resistance; Roughness coefficients; Nikuradse equivalent sand-grain roughness.

INTRODUCTION

In the past, vegetation on riverbeds was considered to be an unwanted source of flow resistance, and for this reason, it was commonly removed. Currently, the preservation of vegetation is relevant for the ecology of water systems (Arthington et al., 2010; Poff et al., 1997) and, in this context, it is important to understand and characterise vegetated flows.

The effects of vegetation on flow, primarily dependent on the vegetation characteristics, such as its height, stiffness and density, are known (Stott, 2010) to include the following:

- decrease in water velocity and an increase in water levels (i.e., a reduction of the flow discharge capacity);
- deposition of suspended sediments; an increase or decrease in local erosion;
- influence on flood propagation;
- interference with the use of the water for conveyance, navigation and swimming.

Recently, the effects of vegetation on the flow resistance, turbulence characteristics, sediment transport and aquatic interfaces in open channel flows were examined in experimental and numerical studies (Marion et al., 2014; Nepf, 2012; Vargas-Luna et al., 2015), also using physics-based methods, such as the Kolmogorov vortex cascade (Gioia and Bombardelli, 2002; Huthoff et al., 2007; Konings et al., 2012) and the genetic programming (Babovic, 2000; Babovic et al., 2001; Baptist et al., 2007).

This study examines the problem of characterising flow resistance due to fully submerged, rigid vegetation and focuses particularly on submergence, i.e., the ratio between the flow depth h (m) and the vegetation height k (m), (Nepf and Vivoni, 2000) higher than 5. This condition, which is typical in river systems with extreme discharge conditions and extensive floodplains (Augustijn et al., 2008; Harris et al., 2003), has been less frequently studied. Previous studies (Augustijn et al., 2008) found that the equations proposed and tested for medium submergences are not sufficiently accurate for high submergences. Some authors (Augustijn, 2008; Huthoff, 2009, 2012; Huthoff et al., 2007; Lopez and Garcia, 1997, 2001) have also suggested that conventional flow resistance equations of Keulegan, Manning, Chézy-Bazin, could be used for high submergences.

Based on these considerations, the purposes of this study include the following: i) to assess the suitability of the conventional flow resistance equations for highly submerged, vegetated flows; ii) to choose the best equation among the three considered conventional equations; iii) to propose a model for the evaluation of the roughness height starting from the geometric characteristics of the vegetation and then show its good agreement with the experimental data.

FLOW RESISTANCE IN OPEN CHANNEL FLOW

For open channel flows, the Darcy-Weisbach, Manning and Chézy equations are the most commonly used flow resistance equations, which are described as follows, respectively:

$$V = \sqrt{\frac{8g}{f}}; \quad V = \frac{K_n}{n} R^{2/3} S^{1/2}; \quad V = C\sqrt{RS} \tag{1}$$

where V is the mean cross-sectional velocity (ms^{-1}), f is the Darcy-Weisbach friction factor, n is the Manning roughness coefficient ($m^{1/6}$), C is the Chézy resistance factor ($m^{1/2}s^{-1}$), R is the hydraulic radius of the flow cross-section (m), g is the gravitational acceleration (ms^{-2}), S is the energy slope and K_n ($m^{1/2}s^{-1}$) is a conversion factor (Yen, 1992, 2002). Comparing Equations (1) the following equivalencies are obtained:

$$\sqrt{\frac{f}{8g}} = \frac{n}{K_n R^{1/6}} = \frac{1}{C} \tag{2}$$

Hereafter, a brief examination of each equation is presented, neglecting the viscosity and Reynolds number effects, due to the usually large Reynolds number in open channel flows.

Keulegan equation, the friction factor *f* and the Nikuradse equivalent sand-grain roughness k_N

The following expression is known as the Keulegan equation:

$$V = K_\Phi \log\left(K_\rho \frac{R}{k_N} \right) \sqrt{RS} \tag{3}$$

where $K_\rho = 12.2$, $K_\Phi = 18.0$ m$^{1/2}$s^{-1} (Chow, 1988), and k_N (m) is the Nikuradse equivalent sand-grain roughness. Merging the Darcy-Weisbach equation and the Colebrook-White equation (Colebrook, 1939), the following is obtained (Yen, 2002):

$$V = -K_1 \sqrt{8g} \log\left(\frac{k_N}{K_2 R} \right) \sqrt{RS} \tag{4}$$

Consequently, Eqs. (3) and (4) are equivalent when $K_\Phi = K_1 (8g)^{1/2}$ and $K_\rho = K_2$. According to Yen (2002), $K_1 = 2$ and, for wide, rectangular channels $K_2 = 12.32$, (Marchi, 1961a, 1961b).

Manning equation, the roughness coefficient *n* and the Strickler roughness height k_S

Strickler (1923) proposed the following relationship between the Manning roughness coefficient n (m$^{1/6}$) and the Strickler roughness height k_S (m) (Chow, 1988):

$$n = K_n \Phi_S k_S^{1/6} \tag{5}$$

where $\Phi_S = 0.0400$ m$^{-1/2}$s (Huthoff et al., 2007). Merging the second equation in (1) and Eq. (5), it is possible to obtain:

$$V = \frac{R^{2/3} S^{1/2}}{\Phi_S k_S^{1/6}} \tag{6}$$

A theoretical derivation of the Manning equation was given by Gioia and Bombardelli (2002).

Chézy equation, the resistance factor *C*, the Bazin roughness coefficient *B* and the Chézy-Bazin roughness height k_B

In Chézy equation the resistance factor C can be evaluated via Bazin's formula (Bazin, 1865):

$$C = \frac{B_0}{1 + B/\sqrt{R}} \tag{7}$$

where $B_0 = 87$ m$^{1/2}$s^{-1}and B is a roughness coefficient. For vegetated beds, it could be useful to define a Chézy-Bazin roughness size, k_B (m) via the following equation:

$$B = \Phi_B k_B^{1/2} \tag{8}$$

where $\Phi_B = 4.00$ m$^{1/2}$s makes k_B of the same order as k_N and k_S for the same channel roughness. Merging the third equation in (1), Eqs. (7) and (8), it is possible to obtain:

$$V = \frac{B_0 R^{1/2} S^{1/2}}{1 + \dfrac{\Phi_B k_B^{1/2}}{R^{1/2}}} \tag{9}$$

Comparisons of k_N, k_S and k_B

To compare k_N, k_S and k_B, the following reasoning is developed.

After replacing f with the first equation in (1) and Eq. (3), and C, n and B with Eqs. (7), (5) and (8), respectively, Eq. (2) becomes the following:

$$\frac{1}{K_\Phi \log\left(K_\rho \dfrac{R}{k_N} \right)} = \frac{\Phi_S k_S^{1/6}}{R^{1/6}} = \frac{1 + \Phi_B k_B^{1/2} / R^{1/2}}{B_0} \tag{10}$$

Eq. (10) can then be rendered non-dimensional, as shown by:

$$\frac{1}{K_\Phi \log\left(K_\rho \dfrac{R}{k_N} \right)} = \frac{\Phi_S \left(k_S / k_N \right)^{1/6}}{\left(\dfrac{R}{k_N} \right)^{1/6}} = \frac{1 + \Phi_B \dfrac{\left(k_B / k_N \right)^{1/2}}{\left(R / k_N \right)^{1/2}}}{B_0} \tag{11}$$

which shows that k_S/k_N and k_B/k_N depend only on R/k_N:

$$\frac{k_S}{k_N} = \frac{R}{k_N} \left[\frac{1}{\Phi_S K_\Phi \log\left(K_\rho \dfrac{R}{k_N} \right)} \right]^6 \tag{12}$$

$$\frac{k_B}{k_N} = \frac{R}{k_N} \left[\frac{B_0}{\Phi_B K_\Phi \log\left(K_\rho \dfrac{R}{k_N} \right)} - 1 \right]^2 \tag{13}$$

In Fig. 1, Eqs. (12) and (13) are represented.

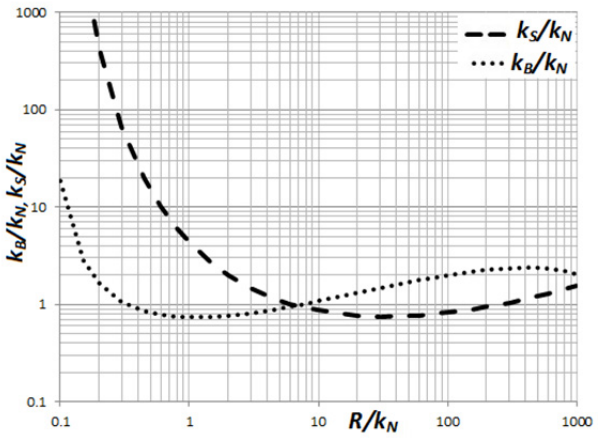

Fig. 1. Relationship among k_S/k_N, k_B/k_N and R/k_N.

Moreover choosing k_B or k_S as the scales it is possible to obtain k_N/k_B and k_S/k_B, and k_N/k_S (Chow, 1988; Sturm, 2010) and k_B/k_S as functions of R/k_N (Figs. 2, 3).

Generally k_S values are larger than the k_N and k_B, which are more similar to each other due to the different assumption for the velocity distribution, namely, the power law for k_S (Gioia and Bombardelli, 2002) and the logarithmic law for k_N and k_B (Baptist et al., 2007). The values of k_N, k_S and k_B are found to be different for R/k_N in the range of 0.1–1 but are only marginally different for R/k_N in the range of 1–1000. This observation is

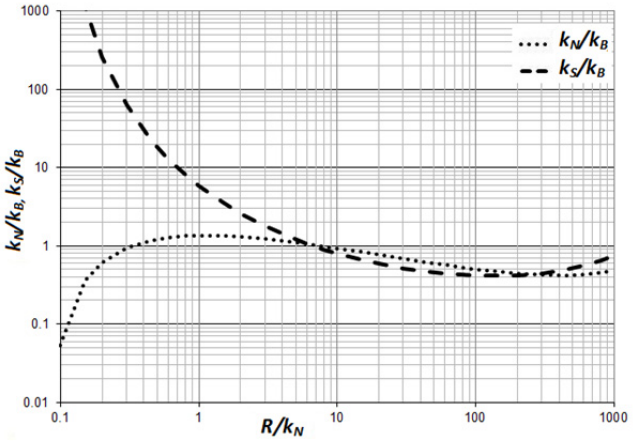

Fig. 2. Relationship among k_N/k_B, k_S/k_B and R/k_N.

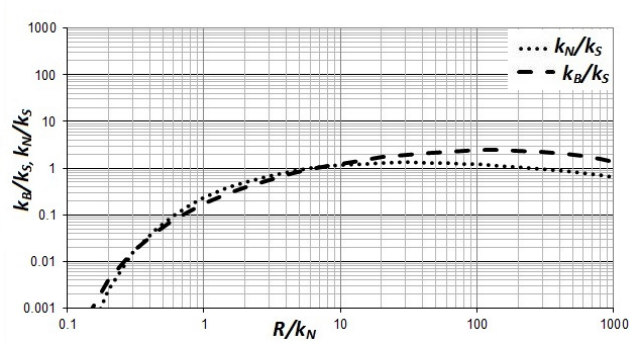

Fig. 3. Relationship among k_N/k_S, k_B/k_S and R/k_N.

important for the purpose of this study: for rough riverbeds without vegetation, R/k_N remains in the range of 1–1000 (Chow, 1988), while for vegetated beds, as will be shown, R/k_N remains in the range of 0.35–6.02. Due to Eq. (4), the lowest physically acceptable value for R/k_N is 1/12.32 = 0.0812.

Hereafter, Eqs. (12) and (13) are used. The Keulegan, Manning and Chézy-Bazin equations state that k_N, k_S and k_B are relative to the wall roughness and are independent of the flow characteristics; consequently, while the left sides of Eqs. (12) and (13) are independent of the flow characteristics, the right sides are dependent on them due to R. Therefore, if in a certain range of flow conditions (i.e., R values) one among the Keulegan, Manning and Chézy-Bazin equations yields a reliable evaluation of the flow resistance, the other two cannot, and thus, only one of the three equations may be considered valid within that range of flow conditions.

FLOW RESISTANCE IN VEGETATED FLOWS

One of the effects of vegetation is an increase in flow resistance, which is strongly influenced by the type of vegetation and the submergence. Vegetation may be modelled as either rigid, using wooden or metallic cylinders or stiff natural plants, or flexible, using plastic strips or flexible natural plants or grass. Vegetation may have different densities and can be wholly or partially submerged. Rigid vegetation allows for simple physics-based modelling and can be considered as a starting point to study the effects of flexible vegetation. In this study, vegetation modelled by rigid, equally spaced and completely submerged cylindrical elements is considered. Following the common assumptions of recent studies of vegetated flows, the two-dimensional approach (i.e., the hypothesis of a wide, rectangular channel) is assumed.

Brief review of flow resistance in vegetated flows

Conventional flow resistance equations are not valid for vegetated flows. One of the purposes of this study is to assess their use at high submergence. Firstly, a brief review of the flow resistance equations in vegetated flows is given. Most research is based on a two-layer approach (Fig. 4), which separately describes the velocity distribution in the vegetation layer and in the surface layer (Klopstra et al., 1997; Tsujimoto and Kitamura, 1990; Tsujimoto et al., 1992). The two distributions are matched at the separation surface, the mean cross-sectional velocity is obtained, and the flow resistance is evaluated.

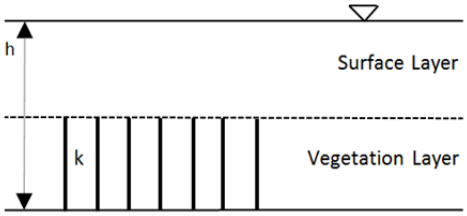

Fig. 4. Two-layer model.

For the vegetation layer, most authors consider the velocity to be constant, assuming a value obtained from the drag for a single element, as described in fluid mechanics. For the surface layer, some authors have assumed a logarithmic law, while others have used the Manning equation or another equation. This approach provides simple but sufficiently accurate flow resistance equations (Huthoff and Augustijn, 2006; Huthoff et al., 2007; Stone and Shen, 2002; Van Velzen et al., 2003). Starting from those equations, neglecting the bottom shear stresses (Nepf and Ghisalberti, 2008) and extracting the velocity, Galema (2009) obtained the following expressions:

a) Stone and Shen (2002), matching at the separation surface by assuming the ratio between the mean velocity in the channel and the velocity in the vegetation layer to be equal to $\sqrt{h/k}$, obtained the following expression:

$$V = \sqrt{\frac{2g}{C_D m D}}\sqrt{S}\left(1 - D\sqrt{m}\right)\sqrt{\left(\frac{h}{k} - \frac{1}{4}\pi m D^2\right)\frac{h}{k}} \tag{14}$$

where h is the flow depth (m), C_D is the drag coefficient of the cylindrical element, D is the diameter (m), k is the height (m) and m is the number of elements per unit area (m^{-2});

b) Van Velzen et al. (2003) assumed the logarithmic law in the surface layer and the resulting expression was:

$$V = \sqrt{\frac{2g}{C_D m D}}\sqrt{S} + K_\Phi \left(h - k\right)^{3/2}\frac{\sqrt{S}}{h}\log\frac{12\left(h - k\right)}{1.6k^{0.7}} \tag{15}$$

c) Huthoff and Augustijn (2006) and Huthoff et al. (2007) assumed in the surface layer the Manning equation, via Gioia and Bombardelli's (2002) approach, obtaining the following expression:

$$V = \sqrt{\frac{2g}{C_D m D}}\sqrt{S}\left[\sqrt{\frac{k}{h}} + \frac{h - k}{h}\left(\frac{h - k}{1/\sqrt{m} - D}\right)^{2/3}\right] \tag{16}$$

d) Keijzer and Babovic (2002), Babovic (2009) and Baptist et al. (2007) proposed a model based on genetic programming, obtaining the following expression:

$$V = \left(\sqrt{\frac{2g}{C_D mDk}} + \frac{\sqrt{g}}{\kappa} \ln\left(\frac{h}{k}\right) \right) \sqrt{hS} \tag{17}$$

where κ is the von Kármán constant.

e) Yang and Choi (2010) obtained the following expression by assuming a logarithmic law for the surface layer:

$$V = \left(\sqrt{\frac{2g}{C_D mDk}} + C_u \frac{\sqrt{g}}{\kappa} \left[\ln\left(\frac{h}{k}\right) - \frac{h-k}{h} \right] \right) \sqrt{hS} \tag{18}$$

where C_u is a parameter whose value is equal to 1 or 2 depending on the value of mD, which is less or more than 5, respectively;

f) Cheng (2011) defined the hydraulic radius as the ratio between the fluid-occupied volume and the total wetted surface area of the cylinders, obtaining the following expression:

$$V = \left[\begin{array}{l} \sqrt{\frac{\pi(1-\lambda_C)^3 D}{2C_D \lambda_C k}} \left(\frac{k}{h}\right)^{3/2} + \\ +4.54 \left(\frac{h-k}{D} \frac{1-\lambda_C}{\lambda_C} \right)^{1/16} \left(\frac{h-k}{h} \right)^{3/2} \end{array} \right] \sqrt{ghS} \tag{19}$$

where $\lambda_C = \pi m D^2/4$ is the fraction of the bed area occupied by the cylinders;

g) Konings et al. (2012), assumed Gioia and Bombardelli's (2002) approach and Huthoff et al. (2007), substituting k_S for n and making all terms non-dimensional, and obtained the following expression:

$$\begin{array}{l} \frac{(h-k)^2}{0.21h^2} \left(\frac{h}{0.85k} \right)^{1/3} \left(\frac{\sqrt{g}\Phi_S k_S^{1/6}}{h^{1/6}} \right)^2 + \\ +\sqrt{\frac{2}{C_D mDk}} \frac{\sqrt{g}\Phi_S k_S^{1/6}}{h^{1/6}} - 1 = 0 \end{array} \tag{20}$$

In the work of Sturm (2010), the methods of Kouwen (1992) were investigated to represent the resistance due to non-bending (i.e., rigid) and bending vegetation; the MEI method was thus proposed based on k_N.

Application of conventional flow resistance equations to vegetated flows at high submergence

Some authors have examined the use of conventional flow resistance for vegetated flows, in specific flow conditions.

Nepf and Vivoni (2000) observed that a terrestrial canopy model, which is analogous to flow over a rough boundary, occurs in aquatic canopies deeply submerged, (i.e. /k > 5).

Lopez and Garcia (1997, 2001) showed that the Manning roughness coefficient, exhibits a nearly constant value up to some threshold of vegetation density. Conversely, a linear increase is observed after this limit is exceeded. Those authors thus evaluated the flow resistance with the Manning equation, assuming constant the flow depth (i.e., the hydraulic radius) and the vegetation height and neglecting the submergence. However, the authors referred to two limiting conditions: very high vegetation or very low vegetation.

Another approach was proposed in (Huthoff, 2009, 2012; Huthoff et al., 2007) considering the Kolmogorov theory of turbulence (Gioia and Bombardelli, 2002). Those authors evaluated the flow resistance in the surface layer using the Manning equation, and obtained the following Strickler roughness height:

$$k_S \approx \frac{\theta^3}{0.04^6 g^3 s^2} \tag{21}$$

where θ (m) is the momentum thickness of the velocity distribution in the wakes of the cylinders and is evaluated by:

$$\theta = \frac{1}{2} C_D D \tag{22}$$

and s is the average distance between the cylinders (m).

Augustijn et al. (2008), compared the equations of Keulegan, Manning, Chézy-Bazin, De Bos and Bijkerk (1963), Van Velzen et al. (2003), Baptist et al. (2007) and Huthoff et al. (2007). The results demonstrated that on average, the Keulegan equation showed the best agreement. The models proposed by Van Velzen et al. (2003), Baptist et al. (2007) and Huthoff et al. (2007) performed as well as those proposed by Keulegan (1938) and De Bos and Bijkerk (1963) without the disadvantage of an empirical parameter that must be calibrated. Increasing the submergence, the Manning coefficient decreases and eventually reaches a constant value, for h/k > 5. However, when extrapolating at high submergence, the models showed a large uncertainty in evaluation of the flow resistance (Augustijn et al., 2008), showing that it is necessary to explore a wider range of flow conditions to identify the most suitable equation.

Modern flow resistance equations for vegetated flows at high submergence

In this section, Eqs. (14) – (20) are examined for high submergences (i.e., increasing h/k to infinity).

As described in (Stone and Shen, 2002), for high submergences, in Eq. (14), the minor term in the brackets under the root can be neglected with respect to the other term that is greater than 1 and increases with the submergence. Consequently, Eq. (14) results:

$$V = \sqrt{\frac{2g}{C_D mD}} \left(1 - D\sqrt{m}\right) \frac{\sqrt{h}}{k} \sqrt{hS} \tag{23}$$

This expression can be considered to be the Chézy equation, where the resistance factor C is:

$$C = \sqrt{\frac{2g}{C_D mD}} \left(1 - D\sqrt{m}\right) \frac{\sqrt{h}}{k} \tag{24}$$

Eq. (7), for high vegetation densities and therefore high values of B, results:

$$C = \frac{B_0 \sqrt{h}}{B} \tag{25}$$

A comparison of Eqs. (24) and (25) results in the following:

$$B = B_0 \sqrt{\frac{C_D mD}{2g}} \frac{k}{\left(1 - D\sqrt{m}\right)} \tag{26}$$

and finally from Eq. (8):

$$k_B = \left(\frac{B_0}{\Phi_B}\right)^2 \left(\frac{C_D m D}{2g}\right) \left[\frac{k}{\left(1 - D\sqrt{m}\right)}\right]^2 \quad (27)$$

Therefore, k_B depends only on the vegetation characteristics, such as C_D, D, k and m.

For high submergences, Eq. (15), neglecting the first term in the sum and the vegetation height with respect to the flow depth in the second term of the sum, results:

$$V = K_\Phi \sqrt{hS} \log \frac{12h}{1.6k^{0.7}} \quad (28)$$

Considering that 12≈12.32 (i.e., a wide rectangular channel), this expression is comparable to Keulegan equation, as shown below:

$$k_N = 1.6k^{0.7} \quad (29)$$

as suggested by the authors. Therefore, k_N depends only on k. For high submergences Eq. (16), neglecting both the first term in the square brackets and the vegetation height with respect to the flow depth, results:

$$V = \sqrt{\frac{2g}{C_D m D}} \left(\frac{1}{1/\sqrt{m} - D}\right)^{2/3} h^{2/3} \sqrt{S} \quad (30)$$

This equation is comparable to the Manning equation, when K_n is substituted, as shown below:

$$n = K_n \sqrt{\frac{C_D m D}{2g}} \left(1/\sqrt{m} - D\right)^{2/3} \quad (31)$$

and finally:

$$k_S = \frac{1}{\Phi_S^{\,6}} \left(\frac{C_D m D}{2g}\right)^3 \left(\frac{1 - D\sqrt{m}}{\sqrt{m}}\right)^4 \quad (32)$$

Therefore, k_S depends only on C_D, D, and m.

For high submergences, Eq. (17) neglecting the first term of the sum in parentheses, results:

$$V = \left(\frac{\sqrt{g}}{\kappa} \ln\left(\frac{h}{k}\right)\right) \sqrt{hS} = \left(1.016 K_\Phi \log\left(\frac{K_\rho h}{12.32k}\right)\right) \sqrt{hS} \quad (33)$$

substituting K_Φ and K_ρ for a wide, rectangular channel. This expression is also comparable to Keulegan equation, neglecting the factor 1.016 and considering:

$$k_N = 12.32k \quad (34)$$

as suggested by the authors. In this case, k_N depends only on k.

For high submergences, Eq. (18) is the same as Eq.(17), after eliminating the term $(h–k)/k$ with respect to $\ln(h/k)$ if the product mD is lower than 5 (i.e., $C_u = 1$), which results in Eq. (33).

If the product mD is higher than 5 (i.e., $C_u = 2$), the following equation holds:

$$V = \left(\frac{\sqrt{g}}{\kappa} 2\ln\left(\frac{h}{k}\right)\right) \sqrt{hS} = \left(2.032 K_\Phi \log\left(\frac{K_\rho h}{12.32k}\right)\right) \sqrt{hS} \quad (35)$$

The resulting equation can no longer be compared to Keulegan equation, due to the impossibility of considering K_Φ equal to unity.

For high submergences, Eq. (19) becomes:

$$V = \left[4.54 \left(\frac{h}{D} \frac{1 - \lambda_C}{\lambda_C}\right)^{1/16} \left(\frac{h - k}{h}\right)^{25/16}\right] \sqrt{ghS} \quad (36)$$

Therefore, it tends to approach neither the Nikuradse nor the Manning equations.

In Eq. (20), for high submergence, where the second term is generally small and decreases, the first term strongly increases. Consequently, Eq. (20) becomes:

$$\frac{1}{0.21} \left(\frac{1}{0.85}\right)^{1/3} \left(\frac{\sqrt{g} \Phi_S k_S^{1/6}}{k^{1/6}}\right)^2 - 1 = 0 \quad (37)$$

From this equation, k_S can be calculated by:

$$k_S = \frac{0.199}{g \Phi_S^{\,2}} k \quad (38)$$

which depends only on k.

Therefore, for high submergences, nearly all of the previous equations can be approximated by one of the three classic flow resistance equations, and thus, k_N, k_S or k_B are functions of the vegetation characteristics as k and/or C_D, D or m. The different dependences of k_N, k_S and k_B on the geometric parameters of the vegetation suggests that, in agreement with Augustijn et al. (2008), the modern flow resistance equations are only approximately reliable when evaluating the flow resistance of vegetated flows at high submergences.

Use of conventional flow resistance equations at high submergence

As a consequence of the conclusions of the previous two paragraphs, it could be interesting to investigate the possibility of using one of the conventional flow resistance equations (i.e., the Keulegan, Manning and Chézy-Bazin equations) at high submergence, evaluating k_N, k_S and k_B, and verify which of them, remaining constant for submergences higher than 5, can therefore be considered to be a reliable expression of the flow resistance. To verify this point, a methodology described in a following paragraph can be applied to experimental data, found in the literature and collected for this study.

EXPERIMENTAL MEASUREMENTS

Experimental data found in the literature

From the literature, a data set of twenty runs was selected. The experimental conditions of each run are summarised in Tables 1 and 2, where the following are reported: the flow rate Q, the velocity V, the uniform flow depth h_u, the Froude number Fr, the geometric characteristics of the cylindrical elements (i.e., height k, diameter D, m number of cylinders per unit area and the arrangement); the maximum submergence $(h/k)_{max}$,

Table 1. Experimental data from literature.

Authors	Arr.	Q ($m^{-3}s^{-1}$)	V(m/s)	h_u(m)	Fr	k (m)	D (m)	m(m^{-2})	λ	h/k	$h/k_N(2)$	$h/k_N(5)$	Run
Cheng (2011)	St.	0.004	0.097	0.130	0.086	0.10	0.007	2221	1.466	1.300	0.17	(0.35)	A1
		0.006	0.131	0.150	0.108	0.10	0.007	2221	1.466	1.500			
		0.008	0.155	0.170	0.120	0.10	0.007	2221	1.466	1.700			
		0.010	0.158	0.200	0.113	0.10	0.007	2221	1.466	2.000			
Cheng (2011)	St.	0.003	0.077	0.130	0.068	0.10	0.008	2221	1.800	1.300	0.19	(0.39)	A2
		0.005	0.102	0.150	0.084	0.10	0.008	2221	1.800	1.500			
		0.007	0.141	0.170	0.109	0.10	0.008	2221	1.800	1.700			
		0.011	0.190	0.200	0.136	0.10	0.008	2221	1.800	2.000			
Meijer and Van Velzen (1999)	Al.	1.04	0.175	1.98	0.040	1.50	0.008	256	3.072	1.320	0.21	(0.43)	A3
		1.39	0.212	2.19	0.046	1.50	0.008	256	3.072	1.460			
		1.72	0.244	2.35	0.051	1.50	0.008	256	3.072	1.567			
		1.91	0.255	2.5	0.051	1.50	0.008	256	3.072	1.667			
Meijer and Van Velzen (1999)	Al.	1.12	0.247	1.51	0.064	0.90	0.008	256	1.843	1.678	0.25	(0.52)	A4
		2.55	0.472	1.8	0.112	0.90	0.008	256	1.843	2.000			
		3.62	0.577	2.09	0.128	0.90	0.008	256	1.843	2.322			
		3.72	0.500	2.48	0.101	0.90	0.008	256	1.843	2.756			
Cheng (2011)	St.	0.008	0.169	0.150	0.139	0.10	0.003	2221	0.711	1.500	0.26	(0.54)	A5
		0.011	0.216	0.170	0.167	0.10	0.003	2221	0.711	1.700			
		0.015	0.253	0.200	0.181	0.10	0003	2221	0.711	2.000			
Cheng (2011)	St.	0.006	0.151	0.130	0.134	0.10	0.008	556	0.461	1.300	0.65	(0.55)	A6
		0.008	0.176	0.150	0.145	0.10	0.008	556	0.461	1.500			
		0.012	0.227	0.170	0.176	0.10	0.008	556	0.461	1.700			
		0.015	0.257	0.200	0.183	0.10	0.008	556	0.461	2.000			
Meijer and Van Velzen (1999)	Al.	1.795	0.298	2.01	0.067	1.50	0.008	64	0.768	1.34	0.27	(0.56)	A7
		2.245	0.342	2.19	0.074	1.50	0.008	64	0.768	1.460			
		2.640	0.381	2.31	0.080	1.50	0.008	64	0.768	1.540			
		3042	0.409	2.48	0.083	1.50	0.008	64	0.768	1.653			
Cheng (2011)	St.	0.006	0.159	0.130	0.141	0.10	0.007	556	0.367	1.300	0.28	(0.58)	A8
		0.010	0.213	0.150	0.176	0.10	0.007	556	0.367	1.500			
		0.012	0.241	0.170	0.187	0.10	0.007	556	0.367	1.700			
		0.016	0.268	0.200	0.192	0.10	0.007	556	0.367	2.000			
Yan (2008)	Al.	0.014	0.286	0.120	0.263	0.06	0.006	2000	0.720	2.000	0.40	0.63	A9
		0.023	0.307	0.180	0.231	0.06	0.006	2000	0.720	3.000			
		0.031	0.308	0.240	0.200	0.06	0.006	2000	0.720	4.000			
		0.038	0.300	0.300	0.175	0.06	0.006	2000	0.720	5.000			
Meijer and Van Velzen (1999)	Al.	1.75	0.384	1.51	0.100	0.90	0.008	64	0.461	1.678	0.37	(0.76)	A10
		3.53	0.498	1.78	0.158	0.90	0.008	64	0.461	1.978			
		4.72	0.613	2.06	0.170	0.90	0.008	64	0.461	2.289			
		4.77	0.760	2.47	0.131	0.90	0.008	64	0.461	2.74			

Fig. 5. Experimental flume.

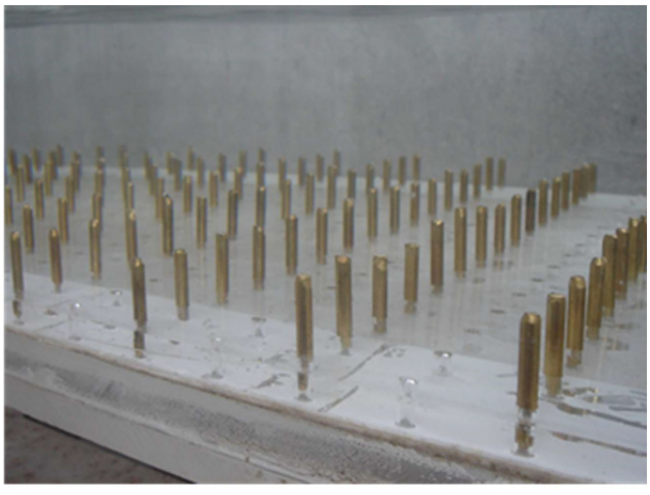

Fig. 6. Model of vegetation.

which reaches or exceeds 5 in only five cases. The number of flow depths, which varies from 4 to 8, except one case of 3; and the non-dimensional vegetation density λ, which ranges from 0.1306 to 3.072 and is evaluated as the product of k, D and m. Due to the relevance of the parameter h/k_N, as shown in Eqs. (12) and (13), $h/k_N = 2$ and $h/k_N = 5$, which are denoted respectively as $h/k_N(2)$ and $h/k_N(5)$, were evaluated and reported in Tables 1 and 2. In particular, each $h/k_N(5)$ value in brackets was obtained based on methodology that involves the experimental data collected for this study, which is described at the end of the following paragraph. The obtained $h/k_N(5)$ values range from 0.35 to 1.59.

Experimental data collected for this study

Experimental measurements were performed in a flume in the laboratory of the Department of Civil, Architectural and Environmental Engineering of the University of Naples Federico II, to extend the experimental conditions with respect to the data found in the literature. A channel with a variable slope was 8-m long and had a cross-section of 0.40 × 0.40 m^2 (Fig. 5).

Vegetation covered the entire channel bed and consisted of rigid cylinders with heights of k = 1.5 cm and diameters D = 0.4 cm that were set in two arrangements (i.e., aligned and staggered) with three non-dimensional densities λ (e.g., 0.024, 0.048 and 0.096) (Fig. 6).

Ten runs were performed, each with 5 to 10 different flow depths. To extend the experimental conditions with respect to the data found in the literature, vegetation densities were lower, varying from 0.096 to 0.024, and the submergences were higher, varying from 5 to 8.78. Information relative to the experimental data set is summarised in Table 3.

In Table 3, the values of $h/k_N(2)$ and $h/k_N(5)$ are reported, where the values of $h/k_N(5)$ are shown to vary from 1.60 to 6.02, thus extending the range of the data found in the literature.

To obtain the values of $h/k_N(5)$ shown in brackets in Tables 1 and 2, the following methodology was applied: 15 runs (i.e., 5 from the literature and 10 from this study) were selected, where it was possible to evaluate $h/k_N(5)$ directly from the experimental data. A mean value of 2.06 of the ratios between $h/k_N(5)$ and $h/k_N(2)$ was calculated and was used to extrapolate the values of $h/k_N(5)$ in brackets in Tables 1 and 2, starting from the corresponding $h/k_N(2)$ values.

Table 2. Experimental data from literature.

Authors	Arr.	Q ($m^{-3}s^{-1}$)	V(m/s)	h_u(m)	Fr	k (m)	D (m)	m(m^{-2})	λ	h/k	$h/k_N(2)$	$h/k_N(5)$	Run
Tsujimoto et al. (1992)	Al.	0.002	0.065	0.064	0.083	0.041	0.001	10000	0.410	1.551	0.39	(0.80)	A11
		0.005	0.140	0.066	0.174	0.041	0.001	10000	0.410	1.607			
		0.007	0.163	0.084	0.179	0.041	0.001	10000	0.410	2.054			
		0.009	0.201	0.085	0.220	0.041	0.001	10000	0.410	2.066			
		0.005	0.108	0.088	0.116	0.041	0.001	10000	0.410	2.154			
		0.009	0.182	0.094	0.189	0.041	0.001	10000	0.410	2.295			
		0.008	0.147	0.105	0.144	0.041	0.001	10000	0.410	2.571			
		0.011	0.199	0.106	0.195	0.041	0.001	10000	0.410	2.588			
Cheng (2011)	St.	0.010	0.254	0.130	0.225	0.10	0.003	556	0.178	1.300	0.395	(0.81)	A12
		0.013	0.284	0.150	0.234	0.10	0.003	556	0.178	1.500			
		0.016	0.316	0.170	0.244	0.10	0.003	556	0.178	1.700			
		0.021	0.342	0.200	0.244	0.10	0.003	556	0.178	2.000			
Tsujimoto et al. (1992)	Al.	0.003	0.124	0.057	0.165	0.046	0.002	2500	0.173	1.235	0.40	(0.82)	A13
		0.008	0.267	0.073	0.316	0.046	0.002	2500	0.173	1.580			
		0.005	0.179	0.074	0.211	0.046	0.002	2500	0.173	1.598			
		0.004	0.117	0.075	0.137	0.046	0.002	2500	0.173	1.628			
		0.012	0.331	0.090	0.353	0.046	0.002	2500	0.173	1.946			
		0.007	0.198	0.094	0.207	0.046	0.002	2500	0.173	2.035			
		0.005	0.133	0.095	0.137	0.046	0.002	2500	0.173	2.065			
Yan (2008)	Al.	0.015	0.290	0.120	0.267	0.06	0.006	1000	0.360	2.000	0.50	0.85	A14
		0.023	0.300	0.180	0.226	0.06	0.006	1000	0.360	3.000			
		0.030	0.300	0.240	0.195	0.06	0.006	1000	0.360	4.000			
		0.037	0.292	0.300	0.170	0.06	0.006	1000	0.360	5.000			
Meijer and Van Velzen (1999)	Al.	1.31	0.441	0.99	0.142	0.45	0.008	256	0.922	2.200	0.28	0.97	A15
		3.06	0.680	1.50	0.177	0.45	0.008	256	0.922	3.330			
		3.74	0.630	1.98	0.143	0.45	0.008	256	0.922	4.400			
		5.92	0.836	2.46	0.174	0.45	0.008	256	0.922	5.467			
Dunn et al. (1996)	St.	0.179	0.587	0.35	0.324	0.1175	0.006	172	0.128	2.851	0.55	(1.13)	A16
		0.088	0.422	0.229	0.282	0.1175	0.006	172	0.128	1.949			
		0.046	0.308	0.164	0.243	0.1175	0.006	172	0.128	1.396			
		0.178	0.709	0.276	0.431	0.1175	0.006	172	0.128	2.349			
		0.098	0.531	0.203	0.376	0.1175	0.006	172	0.128	1.728			
Lopez and Garcia (2001)	St.	0.046	0.308	0.164	0.243	0.12	0.006	170	0.131	1.367	0.56	(1.15)	A17
		0.098	0.531	0.203	0.376	0.12	0.006	170	0.131	1.692			
		0.088	0.422	0.229	0.282	0.12	0.006	170	0.131	1.908			
		0.178	0.709	0.276	0.431	0.12	0.006	170	0.131	2.300			
		0.179	0.587	0.335	0.324	0.12	0.006	170	0.131	2.792			
Yan (2008)	Al.	0.015	0.300	0.120	0.276	0.06	0.006	500	0.180	2.000	0.78	1.22	A18
		0.023	0.300	0.180	0.226	0.06	0.006	500	0.180	3.000			
		0.030	0.300	0.240	0.195	0.06	0.006	500	0.180	4.000			
		0.037	0.292	0.300	0.170	0.06	0.006	500	0.180	5.000			
Meijer and Van Velzen (1999)	Al.	1.983	0.661	1.00	0.211	0.45	0.008	64	0.230	2.222	0.64	1.37	A19
		2.808	0.624	1.50	0.163	0.45	0.008	64	0.230	3.333			
		5.73	0.955	2.00	0.216	0.45	0.008	64	0.230	4.444			
		6.57	0.883	2.48	0.179	0.45	0.008	64	0.230	5.511			
Nezu and Sanjou (2008)	Al.	0.0025	0.100	0.063	0.128	0.05	0.008	947	0.390	1.250	0.77	(1.59)	A20
		0.0030	0.100	0.075	0.117	0.05	0.008	947	0.390	1.500			
		0.0040	0.100	0.100	0.101	0.05	0.008	947	0.390	2.000			
		0.0050	0.100	0.125	0.090	0.05	0.008	947	0.390	2.500			
		0.0060	0.100	0.150	0.082	0.05	0.008	947	0.390	3.000			
		0.0080	0.100	0.200	0.071	0.05	0.008	947	0.390	4.000			

Table 3. Experimental data collected for this study.

Authors	Arr.	Q ($m^{-3}s^{-1}$)	V(m/s)	h_u(m)	Fr	k (m)	D (m)	m(m^{-2})	λ	h/k	$h/k_N(2)$	$h/k_N(5)$	Run
This Study	Al.	0.003	0.268	0026	0.534	0.015	0.004	1600	0.096	1.720	0.69	1.60	B1
		0.004	0.301	0.035	0.514	0.015	0.004	1600	0.096	2.333			
		0.005	0.343	0.039	0.553	0.015	0.004	1600	0.096	2.613			
		0.009	0.442	0.049	0.640	0.015	0.004	1600	0.096	3.233			
		0.014	0.555	0.064	0.702	0.015	0.004	1600	0.096	4.247			
		0.023	0.680	0.083	0.753	0.015	0.004	1600	0.096	5.540			
		0.027	0.751	0.091	0.795	0.015	0.004	1600	0.096	6.060			
		0.033	0.808	0.102	0.807	0.015	0.004	1600	0.096	6.807			
		0.045	0.924	0.122	0.846	0.015	0.004	1600	0.096	8.113			
		0.052	0.995	0.132	0.876	0.015	0.004	1600	0.096	8.780			
This Study	Al.	0.004	0.416	0.023	0.876	0.015	0.004	1600	0.096	1.533	0.72	1.77	B2
		0.008	0.550	0.034	0.950	0.015	0.004	1600	0.096	2.280			
		0.013	0.707	0.045	1.065	0.015	0.004	1600	0.096	2.993			
		0.019	0.854	0.055	1.159	0.015	0.004	1600	0.096	3.687			
		0.032	1.085	0.075	1.267	0.015	0.004	1600	0.096	4.980			
		0.052	1.342	0.098	1.372	0.015	0.004	1600	0.096	6.500			
This Study	St.	0.006	0.555	0.027	1.082	0.015	0.004	800	0.048	1.787	1.13	1.26	B3
		0.009	0.658	0.033	1.158	0.015	0.004	800	0.048	2.193			
		0.012	0.772	0.040	1.240	0.015	0.004	800	0.048	2.633			
		0.016	0.870	0.046	1.303	0.015	0.004	800	0.048	3.033			
		0.026	1.075	0.060	1.405	0.015	0.004	800	0.048	3.980			
		0.039	1.274	0.077	1.470	0.015	0.004	800	0.048	5.100			
		0.043	1.327	0.081	1.489	0.015	0.004	800	0.048	5.400			
		0.045	1.351	0.083	1.495	0.015	0.004	800	0.048	5.553			
		0.047	1.374	0.086	1.499	0.015	0.004	800	0.048	5.707			
		0.047	1.375	0.086	1.498	0.015	0.004	800	0.048	5.720			
This Study	Al.	0.005	0.389	0.030	0.715	0.015	0.004	800	0.048	2.013	1.480	2.270	B4
		0.007	0.462	0.040	0.742	0.015	0.004	800	0.048	2.633			
		0.010	0.511	0.048	0.748	0.015	0.004	800	0.048	3.167			
		0.019	0.677	0.069	0.825	0.015	0.004	800	0.048	4.570			
		0.030	0.824	0.090	0.879	0.015	0.004	800	0.048	5.973			
		0.043	0.961	0.111	0.921	0.015	0.004	800	0.048	7.397			
		0.052	1.046	0.124	0.949	0.015	0.004	800	0.048	8.267			
This Study	St.	0.006	0.510	0.030	0.943	0.015	0.004	800	0.048	1.987	1.22	1.60	B5
		0.008	0.572	0.035	0.979	0.015	0.004	800	0.048	2.320			
		0.010	0.640	0.041	1.015	0.015	0.004	800	0.048	2.700			
		0.013	0.715	0.047	1.058	0.015	0.004	800	0.048	3.100			
		0.021	0.878	0.060	1.142	0.015	0.004	800	0.048	4.013			
		0.023	0.915	0.064	1.156	0.015	0.004	800	0.048	4.260			
		0.034	1.083	0.080	1.226	0.015	0.004	800	0.048	5.307			
This Study	St.	0.005	0.397	0.033	0.698	0.015	0.004	800	0.048	2.193	1.09	2.83	B6
		0.008	0.467	0.040	0.743	0.015	0.004	800	0.048	2.687			
		0.011	0.551	0.050	0.788	0.015	0.004	800	0.048	3.327			
		0.017	0.674	0.064	0.852	0.015	0.004	800	0.048	4.253			
		0.025	0.775	0.079	0.880	0.015	0.004	800	0.048	5.273			
		0.025	0.783	0.079	0.887	0.015	0.004	800	0.048	5.293			
		0.028	0.823	0.085	0.900	0.015	0.004	800	0.048	5.687			
		0.029	0.830	0.086	0.903	0.015	0.004	800	0.048	5.747			
		0.039	0.947	0.103	0.942	0.015	0.004	800	0.048	6.880			
This Study	Al.	0.009	0.747	0.029	1.400	0.015	0.004	400	0.024	1.933	2.47	4.24	B7
		0.011	0.835	0.033	1.474	0.015	0.004	400	0.024	2.183			
		0.016	0.966	0.041	1.527	0.015	0.004	400	0.024	2.717			
		0.023	1.105	0.051	1.559	0.015	0.004	400	0.024	3.417			
		0.030	1.245	0.060	1.618	0.015	0.004	400	0.024	4.020			
		0.033	1.296	0.064	1.641	0.015	0.004	400	0.024	4.240			
		0.035	1.306	0.067	1.615	0.015	0.004	400	0.024	4.440			
		0.041	1.407	0.072	1.669	0.015	0.004	400	0.024	4.830			
		0.045	1.469	0.077	1.695	0.015	0.004	400	0.024	5.103			
		0.049	1.502	0.081	1.686	0.015	0.004	400	0.024	5.397			
This Study	St.	0.013	0.894	0.037	1.488	0.015	0.004	400	0.024	2.453	2.90	4.25	B8
		0.018	1.014	0.045	1.526	0.015	0.004	400	0.024	3.000			
		0.027	1.208	0.055	1.640	0.015	0.004	400	0.024	3.687			
		0.037	1.363	0.067	1.680	0.015	0.004	400	0.024	4.473			
		0.033	1.307	0.063	1.661	0.015	0.004	400	0.024	4.207			
		0.052	1.552	0.085	1.705	0.015	0.004	400	0.024	5.633			
This Study	Al.	0.007	0.502	0.033	0.883	0.015	0.004	400	0.024	2.193	2.66	5.93	B9
		0.010	0.596	0.041	0.939	0.015	0.004	400	0.024	2.733			
		0.014	0.704	0.051	0.992	0.015	0.004	400	0.024	3.420			
		0.022	0.826	0.065	1.033	0.015	0.004	400	0.024	4.347			
		0.033	0.978	0.084	1.076	0.015	0.004	400	0.024	5.620			
		0.033	0.964	0.084	1.059	0.015	0.004	400	0.024	5.627			
		0.045	1.103	0.102	1.103	0.015	0.004	400	0.024	6.793			
This Study	St.	0.007	0.502	0.033	0.883	0.015	0.004	400	0.024	2.193	2.5	6.02	B10
		0.010	0.594	0.041	0.936	0.015	0.004	400	0.024	2.740			
		0.015	0.703	0.052	0.987	0.015	0.004	400	0.024	3.440			
		0.022	0.825	0.065	1.030	0.015	0.004	400	0.024	4.353			
		0.033	0.977	0.083	1.081	0.015	0.004	400	0.024	5.553			

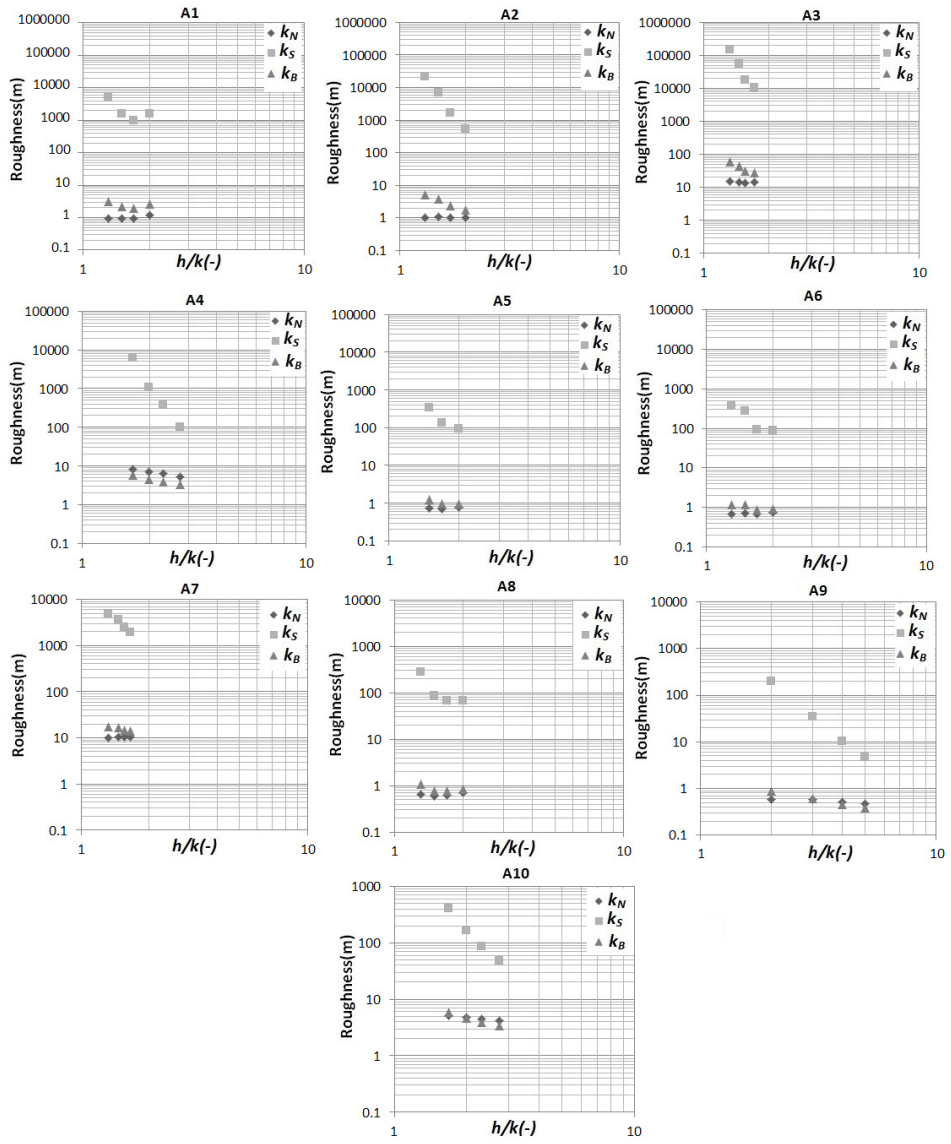

Fig. 7. Relationship among k_N, k_S and k_B with h/k using the experimental data found in the literature.

RESULTS AND DISCUSSION

Methodology for verifying the use of conventional flow resistance equations at high submergence

From Eqs. (3), (6) and (9), k_N, k_S and k_B were evaluated for experimental data in Tables 1, 2, 3. The results for each run are represented, respectively, in Figs. 7, 8, and 9. Each diagram is relative to a run: on the x-axis, which is shown in a log scale for better visualisation, the flow depth is scaled with the height of the cylinders; and on the y-axis, which is shown in a log scale due to the many decades involved, the roughness is represented. The results show that Eqs. (3), (6) and (9) tested for vegetated flows at low and medium submergences are not sufficiently accurate showing, in some cases, values of k_S, k_B and k_N without physical meaning, and this is all the more true the greater the density is. The values of k_N and k_B are similar, while the values of k_S are higher according to the comparison shown in Figs. 1, 2 and 3.

Comparison of the conventional flow resistance equations

In each diagram in Figs. 7, 8 and 9, k_N, k_S and k_B differ; however, especially at higher submergences (i.e., $h/k \geq 5$), the values show a general horizontal trend. The meaning of this trend is that the conventional flow resistance equations work better at higher submergence. It is thus necessary to determine which of the three roughnesses can be considered more reliable to evaluate the flow resistance in a vegetated flow.

To compare k_N, k_S and k_B, the following methodology was applied. In each diagram, for each series of experimental data, the mean gradient was evaluated through a regression line; in Fig. 10, the three mean gradients are +0.0012, –0.0124 and +0.0016. These mean gradients were then made non-dimensional using the mean values of the ordinate (i.e., roughness) of the points of the series; in Fig. 10, these mean values are 0.0271, 0.0688 and 0.0215, implying that the non-dimensional mean gradients are +0.0443, –0.1802 and +0.0746.

For each series, the non-dimensional mean gradients were attributed to the mean value of the abscissae (i.e., submergences) of the points of the series; in Fig. 10, the mean value for each of the three series was 3.38.

To compare the results of the diagrams, each non-dimensional mean gradient was normalised with the value it would attain at the submergence $h/k = 5$. These values were obtained by assuming that the non-dimensional mean gradient varies with the inverse of the submergence in each diagram;

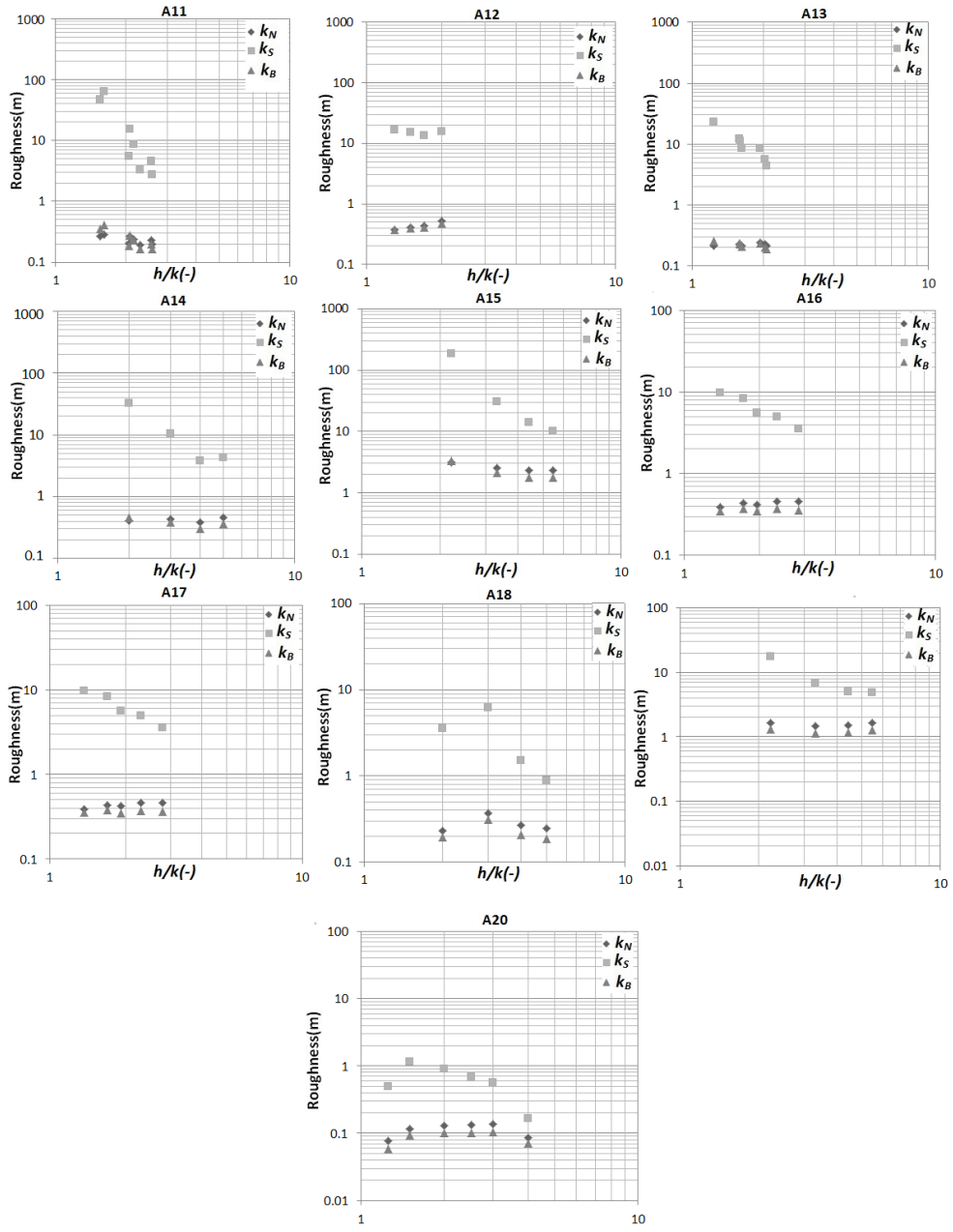

Fig. 8. Relationship among k_N, k_S and k_B with h/k using the experimental data found in the literature.

this is the simplest assumption that leads to a horizontal trend with increasing values of submergence. Consequently, for each series, the normalising factor is the ratio between the mean submergence and 5; in Fig. 10, this ratio is 3.38/5 = 0.677, which implies that the three non-dimensional normalised mean gradients are +0.0300, –0.1202 and 0.0505.

In Fig. 11, the obtained non-dimensional normalised mean gradients, which are hereafter called gradients, of each run in Tables 1, 2 and 3 are reported versus the corresponding value of $h/k_N(5)$. It is evident that: 1) as the value of $h/k_N(5)$ increases, the gradients relative to k_N, k_S and k_B tend to approach zero, indicating good reliability of the corresponding equations, increasing the submergence; and 2) the gradients relative to k_N show the best trend.

The reliability of using the conventional flow resistance equations for vegetated flows with $h/k = 5$ is demonstrated by the curves that approach 0. To better show the trends of the data removing random variations, 5-point moving averages were calculated (Fig. 12).

A band ±0.05 was fixed so that a point inside it corresponded to a roughness varying by no more than 5% for a submergence varying by one unit.

Comparing the curves with the band, it is shown that the gradients relative to k_N are always inside the band, irrespective of the value of $h/k_N(5)$, while the gradients relative to k_B are within the band only when $h/k_N(5) > 1$, and the gradients relative to k_S are within the band only when $h/k_N(5) > 3$. Consequently, remembering that $h/k_N(5)$ varies from 0.35 to 6.02, the previous results show that for $h/k \geq 5$, it is better to use the Keulegan equation rather than the Manning or Chézy-Bazin equations.

Model for the evaluation of the Nikuradse equivalent sand-grain roughness k_N

Starting from the conclusion of the previous paragraph, it is possible to select two groups of experimental runs from the literature and collected for this study, when $h/k \geq 5$. The first

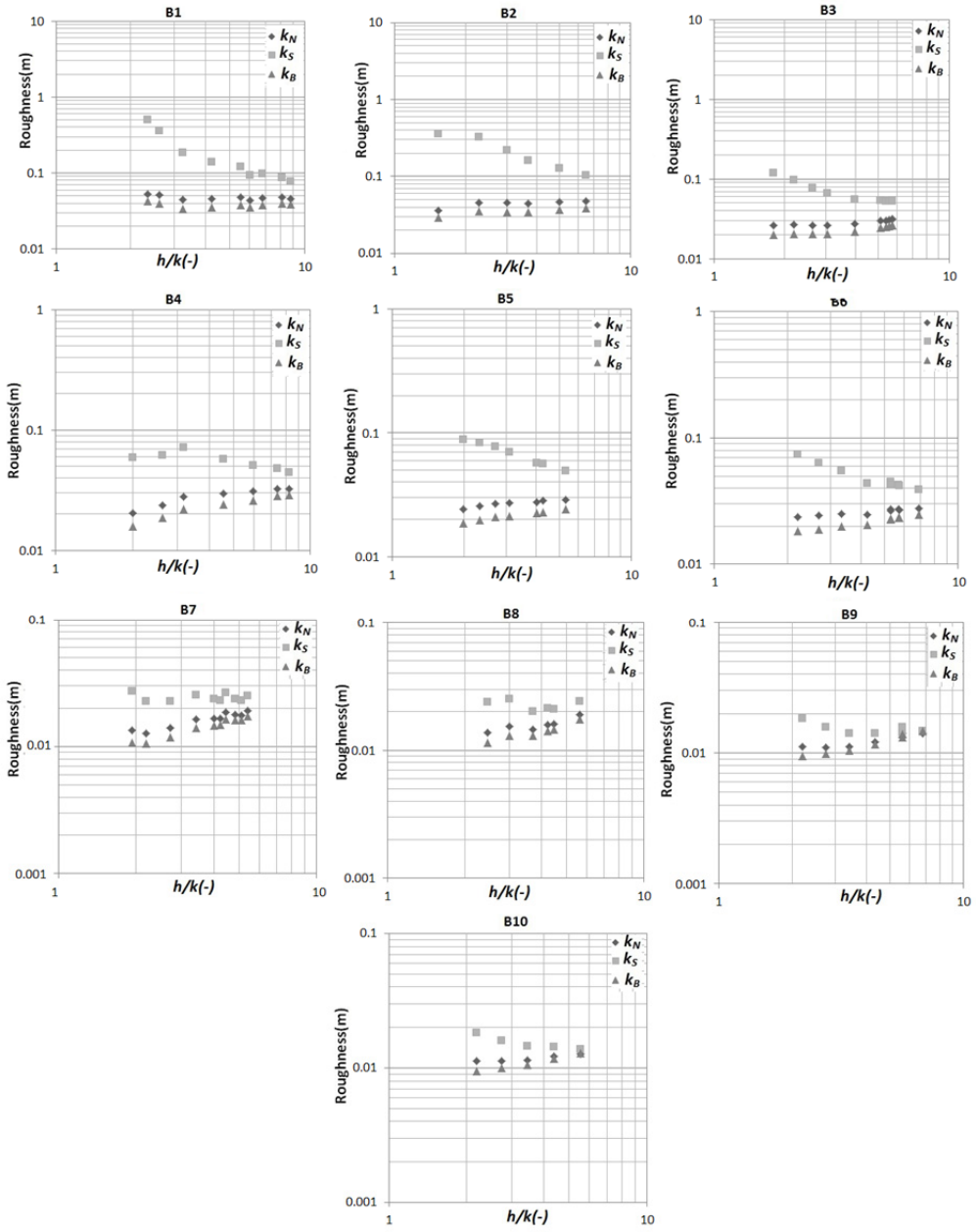

Fig. 9. Relationship of k_N, k_S and k_B with h/k for this study's experimental conditions.

group are 3 runs out of a total of 75 runs from the literature and the second group are 27 runs out of a total 90 runs collected for this study. In Fig. 13, the first group of 3 runs is represented by squares, and the second group of 27 runs is represented by rhombuses. In Fig. 13, the density is shown on the x-axis in a logarithmic scale, and the corresponding value of k_N/k when $h/k > 5$ is shown on the y-axis for each run.

Interpolating the points with a logarithmic curve, the graph shows a strong correlation ($R^2 = 0.93$) between these two quantities; thus, it is possible to state that:

$$\frac{k_N}{k} = 2.0116 \ln \lambda + 8.1916 \text{ or } k_N = k\left[2.0116 \ln \lambda + 8.1916\right] \quad (39)$$

Runs from the literature have densities greater than 0.1, while the runs collected for this study have densities lower than 0.1. The first group shows a spread larger than the second group, with respect to the regression line. This diversity does not depend on the parameter D/k, as suggested by the dimensional

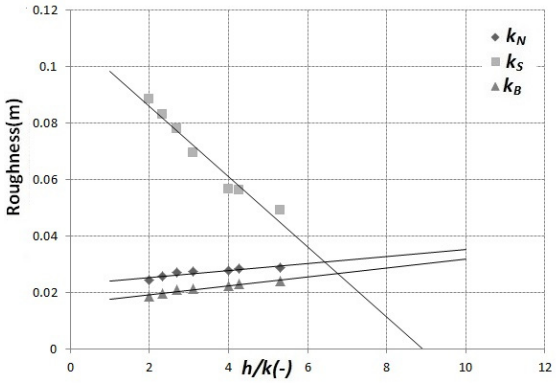

Fig. 10. Example of the regression lines for the experimental data.

considerations. Although the first group exhibits values of this parameter that are lower than the constant value of the second group, the members of the first group lie on both sides of the

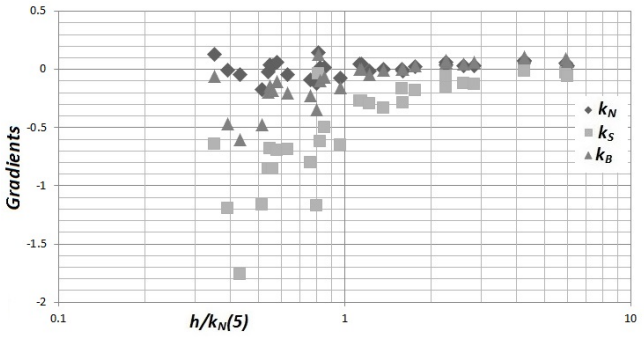

Fig. 11. Relationship of the gradients relative to k_N, k_S and k_B and $h/k_N(5)$.

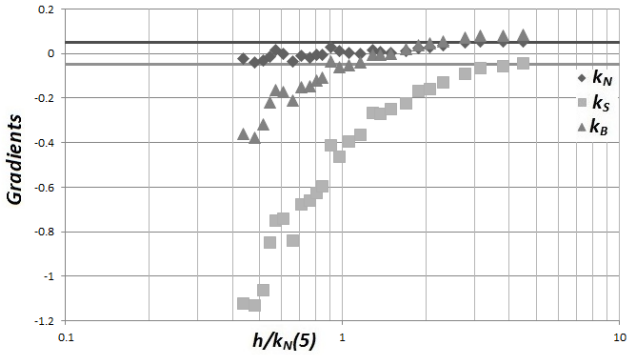

Fig. 12. Moving averages of the gradients relative to of k_N, k_S and k_B.

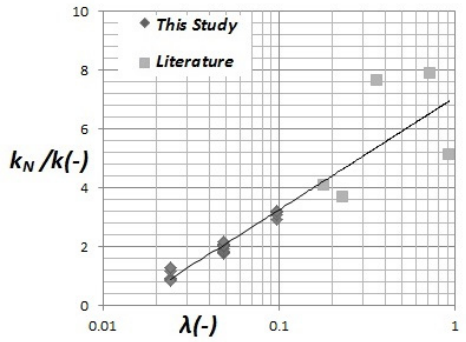

Fig. 13. Ratio of k_N/k versus the non-dimensional vegetation density λ.

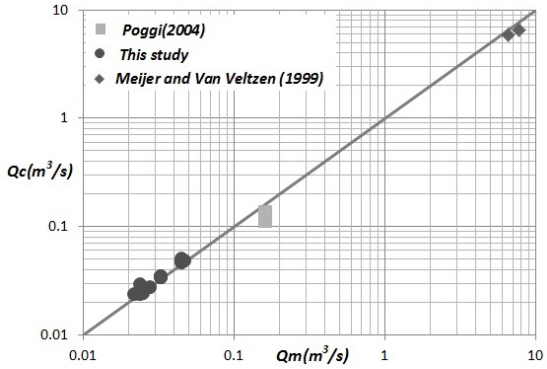

Fig. 14. Comparisons of measured (Q_m) and calculated (Q_c) flow rates.

logarithmic regression line, which does not depend on the parameter D/k. It is necessary to consider that the Nikuradse equivalent sand-grain roughness k_N, (as k_S and k_B,) is a sensitive parameter and that its influence on evaluating the flow rate is attenuated by the log in the Keulegan equation.

In the literature, comparisons are generally performed among the measured flow rates Q_m (m^3s^{-1}) and the calculated flow rates Q_c (m^3s^{-1}). The proposed model has been tested using new experimental data from literature and experimental measurements performed for the test (Table 4). The results are shown in Fig. 14. The range of flow rates that is generally present in the literature is represented. The flow rates considered in Fig. 14 range across three decades (i.e., 0.01–0.1 m^3/s, 0.1–1 m^3/s and 1–10 m^3/s). In Cheng (2011), there are four decades (i.e., 0.001–0.01 m^3/s, 0.01–0.1 m^3/s, 0.1–1 m^3/s and 1–10 m^3/s) and it is clear the lack of literature data in the third decade, which corresponds to the second in Fig. 14.

Measured and experimental data are in good agreement, considering the simplicity of the model, which allows for the evaluation of the Nikuradse equivalent sand-grain roughness k_N for high submergences, starting only from the non-dimensional vegetation density.

Table 4. Data to test the model.

Authors	Arr.	Q ($m^{-3}s^{-1}$)	V(m/s)	h_u(m)	Fr	k (m)	D (m)	m(m^{-2})	λ	h/k
Poggi (2004)	Al.	0.162	0.300	0.6	0.124	0.12	0.004	536	0.257	5.000
		0.162	0.300	0.6	0.124	0.12	0.004	1072	0.515	5.000
Meijer and Van Velzen (1999)	Al.	5.92	0.836	2.46	0.174	0.45	0.008	256	0.922	5.467
		6. 57	0.883	2.48	0.179	0.45	0.008	64	0.230	5.511
Current work	Al.	0.022	0.648	0.085	0.710	0.015	0.004	1600	0.096	5.660
		0.033	0.803	0.103	0.799	0.015	0.004	1600	0.096	6.853
		0.045	0.915	0.123	0.834	0.015	0.004	1600	0.096	8.193
		0.033	0.956	0.086	1.039	0.015	0.004	1600	0.096	5.753
		0.045	1.096	0.103	1.093	0.015	0.004	1600	0.096	6.840
		0.033	1.070	0.077	1.230	0.015	0.004	1600	0.096	5.140
		0.045	1.230	0.092	1.298	0.015	0.004	1600	0.096	6.100
		0.045	1.442	0.078	1.649	0.015	0.004	400	0.024	5.200
		0.033	0.967	0.085	1.057	0.015	0.004	400	0.024	5.687
		0.024	0.583	0.103	0.580	0.015	0.004	400	0.024	6.867
	Stag.	0.033	0.959	0.086	1.044	0.015	0.004	400	0.024	5.733
		0.045	1.082	0.104	1.071	0.015	0.004	400	0.024	6.933
		0.025	0.791	0.079	0.899	0.015	0.004	800	0.048	5.267
		0.028	0.824	0.085	0.902	0.015	0.004	800	0.048	5.667
		0.024	0.769	0.078	0.879	0.015	0.004	800	0.048	5.200
		0.047	1.366	0.086	1.487	0.015	0.004	800	0.048	5.733

Link between $h/k_N(5)$ and the non-dimensional vegetation density

Starting from Eq. (39), it is possible to directly link $h/k_N(5)$ with the non-dimensional vegetation density using the following equation:

$$\left[h/k_N(5)\right] = \frac{k}{k_N}\left[h/k(5)\right] = 5\frac{k}{k_N} = \frac{5}{2.0116\ln\lambda + 8.1916} \qquad (40)$$

Eq. (40) shows that as the non-dimensional density increases, the value of $h/k_N(5)$ decreases and vice versa.

Consequently, the results reported in the literature were confirmed: lower values of $h/k_N(5)$ (i.e., less than unity) correspond to higher vegetation densities, and higher values of $h/k_N(5)$ (i.e., more than unity) correspond to lower vegetation densities.

Limit and observations of previous results

A limitation of the previous results is described in this section. The above analysis was performed for values of $h/k_N(5)$ that did not exceed 6.02; in Fig. 12, due to the moving average, the maximum value is 4.48. Clearly, it is not possible to extrapolate these results for the highest values of $h/k_N(5)$, or, considering Eq. (18), for densities below 0.024.

This factor is not a significant limitation. Values of non-dimensional vegetation density lower than 0.024 (and consequently values of $h/k_N(5)$ higher than approximately 4–6) more typically correspond to rough beds than to vegetated beds (Nepf, 2012).

CONCLUSIONS

The flow resistance of vegetated flows cannot be described by conventional flow resistance equations such as the Keulegan, Manning or Chézy-Bazin equations. However, within some limitations, particularly in cases with high submergence (i.e., equal to 5 or more), these equations fit experimental data sufficiently well. These results are possible because bulk flow does not distinguish between a rough bed and a vegetated bed in high-submergence scenarios.

An analysis of the experimental data reported in the literature and collected for this study shows that the best equation to evaluate the flow resistance in vegetated flows for submergences of $h/k = 5$ or more is the Keulegan equation. For submergences equal or above 5, the Nikuradse equivalent sand-grain roughness k_N in the Keulegan equation can be determined using the logarithmic model proposed and tested in this study. These results support the reliability of using conventional flow resistance equations for vegetated flows at high submergence, as already explored in the literature, and, in addition, demonstrate the conventional equations that best fit different flow conditions (i.e., the Keulegan equation) and offer a model to simply evaluate the Nikuradse equivalent sand-grain roughness k_N when starting from the non-dimensional vegetation density.

REFERENCES

Arthington, A.H., Naiman, R.J., McClain, M.E., Nilsson, C., 2010. Preserving the biodiversity and ecological services of rivers: new challenges and research opportunities. Freshwater Biology, 55, 1–16.

Augustijn, D.C.M., Huthoff, F., van Velzen, E.H., 2008. Comparison of vegetation roughness descriptions. In: Proceedings of International Conferences on Fluvial Hydraulics (River Flow), Cezme, Izmir, Turkey, pp. 343–350.

Babovic, V., 2000. Data mining and knowledge discovery in sediment transport. Computer-Aided Civil and Infrastructure Engineering, 15, 5, 383–389. DOI: 10.1111/0885-9507.00202.

Babovic, V., Keijzer, M., Aquilera, D.R., Harrington, J., 2001. An evolutionary approach to knowledge induction: Genetic programming in hydraulic engineering. Proceedings of the World Water and Environmental Resources Congress, 111, 64–64.

Babovic, V., 2009. Introducing knowledge into learning based on genetic programming. Journal of Hydroinformatics, 11, 3–4, 181–193.

Baptist, M.J., Babovic, V., Rodriguez Uthurburu, J., Keuzer, M., Uittenbogaard, R.E., Mynett, A., Verwey, A., 2007. On inducing equations for vegetation resistance. J. Hydraul. Res., 45, 4, 435–450.

Bazin, H., 1865. Mémoires présentés par divers savants à l'Académie des Sciences, Paris, France, Vol. 19, 1–494.

Cheng, N.S., 2011. Representative roughness height of submerged vegetation. Water Resour. Res., 47, W08517.

Chow, V.T., 1988. Open Channel Hydraulics. Mc-Graw Hill, New York, NY, USA.

Colebrook, C.F., 1939. Turbulent flow in pipes, with particular reference to the transition between the smooth and rough pipe laws. J. Instn. Civ. Engrs. Eng., 11, 133–156.

De Bos, W.P., Bijkerk, C., 1963. A new monogram for the calculation of water courses. Cultuurtech Tijdschrift, 3, 149–155. (In Dutch.)

Dunn, C., Lopez, F., Garcia, M., 1996. Mean flow and turbulence in a laboratory channel with simulated vegetation. Hydrosystems Lab. Hydraulic Eng. Ser. 51, UIUL-ENG-96-2009, 148 pp., Univ. of Illinois at Urbana-Champaign, Urbana, Illinois, IL, USA.

Galema, A., 2009. Vegetation resistance: evaluation of vegetation resistance descriptors for flood management. MSc Thesis. University of Twente, Enschede, The Netherlands.

Gioia, G., Bombardelli, F.A., 2002. Scaling and similarity in rough channel flows. Phys. Rev. Lett., 88, 1, 14501–14504.

Harris, E.L., Babovic, V., Falconer, R.A., 2003. Velocity predictions in compound channels with vegetated floodplains using genetic programming. International Journal of River Basin Management, 1, 2, 117–123.

Huthoff, F., 2009. Estimating equivalent roughness lengths based on wake sizes. In: Proceedings of 33rd IAHR Congress, Vancouver, Canada (CD-ROM), pp. 1183–1190.

Huthoff, F., 2012. Theory for flow resistance caused by submerged roughness elements. J. Hydraul. Res., 50, 1, 10–17.

Huthoff, F., Augustijn, D.C.M., 2006. Hydraulic resistance of vegetation: predictions of average flow velocities based on a rigid-cylinders analogy. Civil Engineering & Management Report 2006R-001/WEM-003, University of Twente, Twente, The Netherlands.

Huthoff, F., Augustijn, D.C.M., Hulscher, S.J.M.H., 2007. Analytical solution of the depth-averaged flow velocity in case of submerged rigid cylindrical vegetation. Water Resour. Res., 43, W06413.

Keijzer, M., Babovic, V., 2002. Declarative and preferential bias in GP-based scientific discovery. Genetic Programming and Evolvable Machines, 3, 1, 41–79.

Keulegan, G.H., 1938. Laws of turbulent flow in open channels. Research paper RP1151, J. Res. Nat. Bur. Stand., 121, 6, 707–741.

Klopstra, D., Barneveld, H.J., Van Noortwijk, J.M., Van Velzen, E.H., 1997. Analytical model for hydraulic roughness of

submerged vegetation. In: Proceedings 27th IAHR Congress,San Francisco, CA, USA, pp. 775–780.
Konings, A.G., Katul, G.G., Thompson, S.E., 2012. A phenomenological model for the flow resistance over submerged vegetation. Water Resour. Res., 48, W02522.
Kouwen, N., 1992. Modern approach to design of grassed channels. J. Irrig. Drain. Eng., 118, 5, 733–743.
Lopez, F., Garcia, M., 1997. Open-channel flow through simulated vegetation: turbulence modeling and sediment transport. Wetlands Research Program Technical Report WRP-CP-10, Dept. of Civil Eng., Univ. of Illinois at Urbana-Champaign, Urbana, Illinois, IL, USA.
Lopez, F., Garcia, M., 2001. Mean flow and turbulence structure of open-channel flow through non-emergent vegetation. J. Hydraul. Eng., 127, 5, 392–402.
Marchi, E., 1961a. Il moto uniforme delle correnti liquide nei condotti chiusi ed aperti. L'Energia Elettrica, 38, 4, 289–301. (In Italian.)
Marchi, E., 1961b. Il moto uniforme delle correnti liquide nei condotti chiusi ed aperti. L'Energia Elettrica, 38, 5, 393–413. (In Italian.)
Marion, A., Nikora, V., Puijalon, S., Bouma, T., Koll, K., Ballio, F., Tait, S., Zaramella, M., Sukhodolov, A., O'Hare, M., Wharton, G., Aberle, J., Tregnaghi, M., Davies, P., Nepf, H., Parker, G., Statzner, B., 2014. Aquatic interfaces: a hydrodynamic and ecological perspective. J. Hydraul. Res., 52, 6, 744–758.
Meijer, D.G., Van Velzen, E.H., 1999. Prototype-scale flume experiments on hydraulic roughness of submerged vegetation. In: Proceedings of 28th IAHR Congress, Graz, Austria.
Nepf, H.M., 2012. Flow and transport in region with aquatic vegetation. Annu. Rev. Fluid Mech., 44, 123–142.
Nepf, H.M., 2012. Hydrodynamics of vegetated channels. J. Hydraul. Res., 50, 3, 262–279.
Nepf, H., Ghisalberti, M., 2008. Flow and transport in channels with submerged vegetation. ActaGeophysica, 56, 3, 753–777.
Nepf, H.M., Vivoni, E.R., 2000. Turbulence structures in depth-limited, vegetated flow. J. Geophys. Res., 105, C12, 28547–28557.
Nezu, I., Sanjou, M., 2008. Turbulence structure and coherent motion in vegetated canopy open-channel flows. J. Hydro-Environ. Res., 2, 62–90.
Poff, L.N., Allan, D.J., Bain, M.B., Karr, J.R., Prestegaard, K.L., Richter, B.D., Sparks, R.E., Stromberg, J.C., 1997. The natural flow regime: a paradigm for river conservation and restoration. BioScience, 47, 11, 769–784.
Poggi, D., Porporato, A., Ridolfi, L., Albertson, J.D., Katul, G.G., 2004. The effect of vegetation density on canopy sublayer turbulence. Boundary-Layer Meteorology, 111, 3, 565–587.
Sturm, T.W., 2001. Open Channel Hydraulics. Mc-Graw Hill, New York, NY, USA.
Sturm, T.W., 2010. Open Channel Hydraulics. 2nd Ed. Mc-Graw Hill, New York, NY, USA.
Stone, B.M., Shen, H.T., 2002. Hydraulic resistance of flow in channels with cylindrical roughness. J. Hydraul. Eng., 128, 5, 500–506.
Stott, T., 2010. Fluvial geomorphology. Progress in Physical Geography, 34, 221–245.
Strickler, A., 1923. Some contributions to the problem of velocity formula and roughness factors for rivers, canals, and closen conduits. Mitteilungen des eidgenössischen Amtes für Wasservirtschaft, Bern, Switzerland, no. 16. (In German.)
Tsujimoto, T., Kitamura, T., 1990. Velocity profile of flow in vegetated-bottom channels. KHL Progressive Report, Hydraulic Laboratory, Kanazawa University, Kanazawa City, Japan.
Tsujimoto, T., Shimizu, Y., Kitamura, T., Okada, T., 1992. Turbulent open-channel flow over bottom covered by rigid vegetation. J. Hydrosci. Hydraul. Eng., 10, 2, 13–25.
Van Velzen, E.H., Jesse, P., Cornelissen, P., Coops, H., 2003. Stromingsweerstand vegetatie in uiterwaarden. Handbook, Part 1 and 2, RIZA Reports 2003.028 and 2003.029, Arnhern, The Netherlands.
Vargas-Luna, A., Crosato, A., Uijttewaal, W.S.J., 2015. Effects of vegetation on flow and sediment transport: comparative analysis and validation of predicting models. Earth Surface and Landforms, 40, 157–176.
Yang, W., Choi, S.U., 2010. A two layer approach for depth-limited open-channel flows with submerged vegetation. J. Hydraul. Res., 48, 4, 466–475.
Yan, J., 2008. Experimental study of flow resistance and turbulence characteristics of open channel flow with vegetation. Ph.D. Thesis. Hohai University, Hohai, China.
Yen, B.C., 1992. Dimensionally homogeneous Manning's formula. J. Hydraul. Eng., 118, 9, 1326–1332.
Yen, B.C., 2002. Open channel flow resistance. J. Hydraul. Eng., 128, 1, 20–39.

NOMENCLATURE

B	Bazin roughness coefficient [$m^{1/2}$]
B_0	Correction factor [$m^{1/2}s^{-1}$]
C	Chezy resistance factor [$m^{1/2}s^{-1}$]
C_D	Drag coefficient
Cu	Dimensionless factor
D	Vegetation diameter [m]
f	Darcy-Weisbach friction factor
Fr	Froude number
g	Acceleration of gravity [m/s^2]
h	Flow depth [m]
h_u	Uniform flow depth [m]
k	Vegetation height [m]
k_B	Chezy-Bazin roughness height [m]
k_N	Nikuradse equivalent sand-grain roughness [m]
k_S	Strickler roughness height [m]
Kn	Conversion factor [$m^{1/2}s^{-1}$]
K_ρ	Dimensionless factor
K_Φ	Correction factor [$m^{1/2}s^{-1}$]
K_1	Dimensionless factor
K_2	Dimensionless factor
h/k	Submergence ratio
m	Vegetation elements per unit area [m^{-2}]
n	Manning roughness coefficient [$m^{1/6}$]
Q	Flow rate [m^3s^{-1}]
Q_c	Calculated flow rate [m^3s^{-1}]
Q_m	Measured flow rate [m^3s^{-1}]
R	Hydraulic radius [m]
s	Vegetation elements spacing [m]
S	Channel slope
S_H	Total head slope
λ	Non dimensional vegetation density
λ_C	Fraction of the bed area occupied by vegetation elements
Φ_B	Correction factor [$m^{1/2}s$]
Φ_S	Correction factor [$m^{-1/2}s$]

Received 27 July 2016
Accepted 14 March 2017

J. Hydrol. Hydromech., 66, 2018, 1, 121–128
DOI: 10.1515/johh-2017-0042

A combined CFD-experimental method for abrasive erosion testing of concrete

Gianandrea Vittorio Messa[1*], Renan De Lima Branco[2], José Gilberto Dalfré Filho[2], Stefano Malavasi[1]

[1] FLUIDLab group, Department of Civil and Environmental Engineering, Politecnico di Milano, Piazza Leonardo Da Vinci, 32, 20133 Milano, Italy.
[2] College of Civil Engineering, Architecture and Urbanism, University of Campinas, Av. Albert Einstein, 951, Campinas, SP, Brazil.
[*] Corresponding author. Tel.: +39 02 2399 6287. E-mail: gianandreavittorio.messa@polimi.it

Abstract: Serious damage may occur to concrete hydraulic structures, such as water galleries, spillways, and stilling basins, due to the abrasive erosion caused by the presence of solid particles in the flow. This underlines the importance of being capable in providing characterization of the concrete from the point of view of its vulnerability to abrasive erosion, in order to improve the design of the structure and the material selection. Nevertheless, the existing apparatus for concrete abrasive erosion testing are either far from allowing realistic simulation of the actual environment in which this phenomenon occurs, or show a large degree of complexity and cost. An alternative method has been developed with the aid of Computational Fluid Dynamics (CFD). CFD was first employed to verify the effectiveness of a new laboratory equipment. Afterwards, a parameter has been introduced which, by successful comparison against preliminary experiments, proved suitable to quantify the effect of the fluid dynamic conditions on the concrete abrasive erosion, thereby opening the way to CFD-based customization of the apparatus. In the future, the synergy of numerical and physical modelling will allow developing predictive models for concrete erosion, making it possible to reliably simulate real structures.

Keywords: Abrasive erosion; Computational fluid dynamics; Concrete; Experiments; Two-phase flow.

INTRODUCTION

The abrasive erosion of hydraulic concrete structures is the progressive disintegration of the material caused by water-transported solid, sand, gravel, ice, or debris (Graham, 1998). The irreversible nature of this damage, and the high costs related to this effect, makes the capability of correctly characterizing the concretes from the point of view of their resistance to abrasive erosion very important.

According to Liu et al. (2006), the mass loss caused by abrasive erosion in hydraulic concrete is a three-stage process. Initially, the pressure of water molecules causes a pre-abrasion peeling of the concrete surface. Afterwards, the impacts of the solids carried along with the water result in the removal of the mortar and the subsequent exposure of the coarse aggregates. Finally, the removal of the aggregates occurs due to scratching and shearing actions.

A number of test methods have been proposed by the ASTM committee to test the abrasion resistance of concrete. One out of them, referred to as "underwater method", is specifically intended to simulate the abrasive action of waterborne particle under water (ASTM C1138M, 2012). The apparatus, sketched in Fig. 1a, consists of a steel cylindrical tank filled with water at the bottom of which a concrete specimen is placed. An agitator with a specially designed paddle keeps the water and the abradant in rotary motion. The abradant consists of 70 steel grinding balls with nominal size ranging between 12.6 and 25.3 mm. This equipment was used by several authors to investigate the relative resistance of different concretes under an erosive action (e.g. Dalfré Filho et al., 2000; Horszczaruk, 2005, 2008, 2009; Kumar and Sharma, 2014; Mohebi et al., 2015; Yen et al., 2007). However, despite the attractive simplicity of the ASTM C1138M apparatus, its main problem is that it involves different erosion mechanisms than those encountered in practical applications.

Liu et al (2006, 2012) and Dandapat and Deb (2016) used a different setup, in which a concrete specimen is exposed, at a given inclination angle, to a slurry sand-water jet coming out from a nozzle (Fig. 1b). The large, rectangular nozzle and the inclination angle were defined in such a way to reproduce the water flow over a spillway. Moreover, the mass loss is due to normal impacts and shearing actions, further approaching the actual conditions. Nevertheless, the dimensions of the rig are considerable, having technical and economic implications.

The apparatus shown in Fig. 1c was developed by Horszczaruk (2000, 2004). It consists of a steel drum, partially filled with a mixture of aggregates and water. A rotating shaft with several concrete samples allows the interaction between concrete and abrasive mixture. The goal of better simulating the natural conditions in which concrete abrasion occurs was achieved, but, at the same time, the size of the rig and the difficulties in controlling the experimental conditions for such complex flow appear the key drawbacks of this solution.

The above discussion indicates that none of the available methods for concrete erosion testing is free from critical aspects, mainly residing in either difference from the actual working conditions (for the ASTM "underwater method") or excessive complexity of the setup (for the abrasive jet method and the rotating device). In the present work, an alternative testing strategy is proposed. This is not limited to the development of a new apparatus, designed with the aid of Computational Fluid Dynamics (CFD), which combines the earlier ones integrating the advantages from each of them. Actually, it involves a strong synergy between numerical and physical modelling, a concept which has already been explored in erosion studies (e.g. Clark, 2002; Gnanavelu et al., 2011; Mansouri et al., 2015). A parameter has been introduced which, at the present stage, represents only the effect of the fluid dynamic conditions on the effectiveness of the apparatus. This allows customization of the setup to optimize its performance for specific testing conditions.

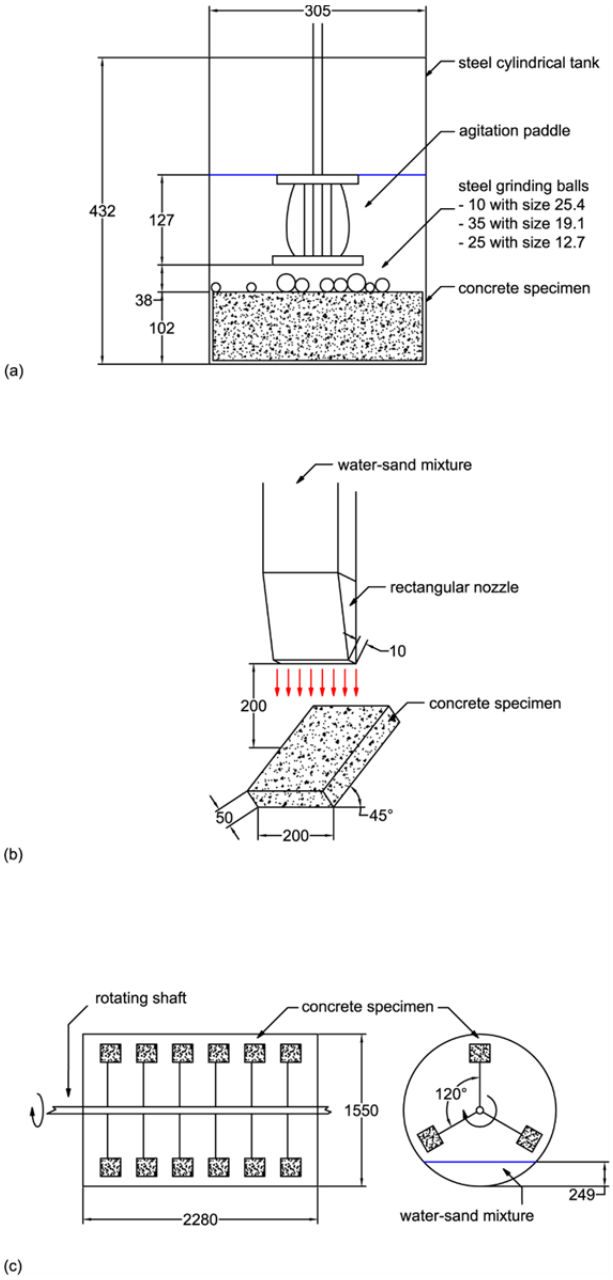

Fig. 1. Main details of three existing setups for underwater erosion testing: (a) the ASTM C1138M (2012) apparatus; (b) nozzle-specimen system used by Liu et al. (2006, 2012); (c) the device proposed by Horszczaruk (2000, 2004). Dimensions are in mm.

Laboratory experiments will be then performed on different concretes and, based on the acquired data, the proposed parameter will be made material-dependent and turned into a predictive erosion model. This will open the way to the reliable simulation of hydraulic structures, such as water galleries, spillways, and stilling basins. In addition, the laboratory apparatus may be also used as an alternative to the ASTM C1138M for comparing the resistance of various concrete formulations.

The remainder of the paper is divided in three sections, followed by the conclusions. In the first one, the proposed setup is described. In the second one, the CFD model used for simulating the liquid-solid flow in the system is illustrated, together with the followed computational methodology. In the third one, the effectiveness of the equipment is demonstrated, also by comparison to the outcomes of some preliminary tests performed in a prototype apparatus.

THE PROPOSED APPARATUS

The new device is a modification of the ASTM C1138M method in which the steel balls have been replaced by the smaller granular material encountered in actual environments. Moreover, the agitator has been changed with a Pitched Blade design and four lateral baffles have been introduced (Fig. 2), in order to create a downward flow with enhanced turbulence, which promotes the impingements of the particles against the concrete base. These modifications concur to make the testing conditions closer to those encountered by concrete hydraulic structures, in terms of involved materials and erosion mechanisms, without any increase in technical and economic burden.

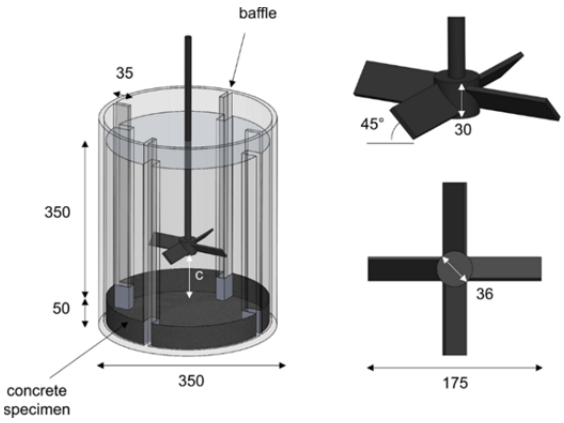

Fig. 2. The apparatus proposed in this study. Dimensions are in mm.

The dimensions reported in Fig. 2 and their ratios were defined based on analogy with the ASTM C1138M and the stirred tank used by Fokema et al. (1994). The tank diameter, T, is 350 mm, and it is equal to the still water depth above the specimen, which is located at the bottom and has a height equal to 50 mm. The width of the four, equally spaced, lateral baffles is 35 mm (T/10). The Pitched Blade impeller has angle of 45°, and diameter equal to 175 mm (T/2). As it will be clarified later, the rotational velocity of the impeller, Ω, and its clearance, c (that is, its distance from the concrete specimen) have significant influence on the development of the erosion phenomenon, and, therefore, they were the subject of specific analyses. In this paper, the abradant consists of 950 g of silica sand particles with density equal to 2650 kg/m^3, yielding a static solid volume fraction of 1%. In the laboratory experiments, the particle size ranges within 1.2 and 2.0 mm (the average being 1.5 mm), as determined by a sieve classification performed before the test. In the numerical simulations, the solid phase is modelled as monodispersed with size equal to 1.5 mm. The carrier fluid is water at 20°C with density and kinematic viscosity coefficient equal to 998.23 kg/m^3 and 1e-6 m^2/s, respectively.

METHODOLOGY

Governing equations

Even if the average abrasive content in the tank is low, the relatively high solid volume fraction occurring in certain regions makes it necessary to account for two- and four-way coupled interactions between the phases. Therefore, the liquid-particle flow was modelled based on the Euler-Euler approach, in which both phases are interpreted as interpenetrating continua. Particularly, use is made of the extension to dense flow of the IPSA model of Spalding (1980) which has been proposed by Messa and co-workers (2013, 2014, 2014a, 2014b, 2015).

The flow is assumed statistically steady and so the mass and momentum conservation equations for each phase are, respectively

$$\nabla\cdot\left(\alpha_q\rho_q\mathbf{U}_q\right)=\nabla\cdot\left(\rho_q\frac{\nu_t}{\sigma_\alpha}\nabla\alpha_q\right) \tag{1}$$

$$\begin{aligned}&\nabla\cdot\left(\alpha_q\rho_q\mathbf{U}_q\mathbf{U}_q\right)-\nabla\cdot\left(\alpha_q\rho_q\nu_q\nabla\mathbf{U}_q\right)-\nabla\cdot\left(\alpha_q\rho_q\nu_t\nabla\mathbf{U}_q\right)\\&-\nabla\cdot\left(\mathbf{U}_q\rho_q\frac{\nu_t}{\sigma_\alpha}\nabla\alpha_q\right)=-\alpha_q\nabla P+\alpha_q\rho_q\mathbf{g}+\mathbf{M}_q\end{aligned} \tag{2}$$

where the subscript q is a phase indicator parameter equal to f and p for the fluid and the particles, respectively. Moreover, α_q is the local average volume fraction, ρ_q is the density, $\mathbf{U}_k$ is the average velocity vector, σ_α is the turbulent Schmidt number for volume fractions, set equal to 0.7, ν_q is the kinematic viscosity coefficient, P is the average pressure, ν_t is the eddy viscosity, and $\mathbf{g}$ is the gravitational acceleration vector.

The viscosity of the solids is obtained from a friction, mixture-viscosity related parameter, μ_m, by assuming the following linear relationship:

$$\mu_m=\alpha_f\rho_f\nu_f+\alpha_p\rho_p\nu_p \tag{3}$$

and evaluating μ_m by means of the comprehensive formula proposed by Cheng and Law (2003):

$$\mu_m=\rho_f\nu_f\exp\left\{\frac{2.5}{\beta}\left[\frac{1}{\left(1-\alpha_p\right)^\beta-1}\right]\right\} \tag{4}$$

in which β is a material-dependent coefficient that, as suggested, was set to 3 in this paper.

The interfacial momentum transfer term $\mathbf{M}_{q=f,p}$ is given by:

$$\mathbf{M}_f=-\mathbf{M}_p=\frac{3}{4d_p}C_d\alpha_p\rho_f\left|\mathbf{U}_p-\mathbf{U}_f\right|\left(\mathbf{U}_p-\mathbf{U}_f\right) \tag{5}$$

where d_p is the particle size, and C_d is the drag coefficient, which is related to the μ_m-based particle Reynolds number, $\mathrm{Re}_p=\rho_f|\mathbf{U}_p-\mathbf{U}_f|d_p/\mu_m$, via the correlation of Shiller and Naumann (1935):

$$C_d=\max\left[\frac{24}{\mathrm{Re}_p}\left(1+0.15\,\mathrm{Re}_p^{0.687}\right),0.44\right] \tag{6}$$

The eddy viscosity, ν_t, was evaluated by an extension of the standard high-Reynolds form of the k-ε model of Launder and Spalding (1974) to two-phase flows, which is well documented in Messa et al. (2013, 2014, 2015).

Computational domain and boundary conditions

The computational domain is shown in Fig. 3, where it is evident that the geometrical symmetry of the system has been exploited by solving only over a quarter of the tank.

The boundary conditions are zero shear stress, cyclic, and solid walls. Particularly, zero shear stress has been imposed to both phases in correspondence to the upper boundary, in order to reproduce the free surface of the mixture, assumed flat. The two vertical, planar surfaces are attributed a cyclic condition to account for the effect of the remaining three quarters of the tank.

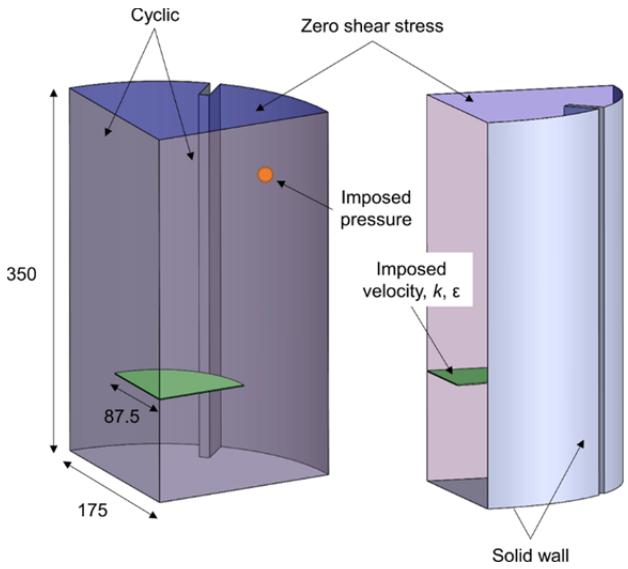

Fig. 3. Sketch of the computational domain and the imposed boundary conditions.

Finally, all other boundaries (i.e. the specimen, the tank wall, and the baffles) are modelled as solid walls. There, the liquid has zero velocity; the wall shear stress of this phase, and the turbulent kinetic energy and the dissipation rate in the near-wall cells are obtained from the equilibrium wall function of Launder and Spalding (1972) for smooth walls. Conversely, the zero wall shear stress condition has been applied to the solid phase.

In order to make the pressure distribution uniquely determined, the pressure was fixed in a cell of the computational domain. The average volume fraction in the tank was imposed as initialization step of the solution algorithm. Finally, the effect of the rotating impeller on the mean flow was modelled by imposing the velocity of both phases and the turbulent parameters on a surface with the shape of a quarter of a disk. Further details on this aspect are provided in Appendix A.

Computational methodology and consistency of the numerical solution

The commercial CFD code PHOENICS 2014 was employed for the numerical solution of the Euler-Euler model equations. Particularly, use was made of a recompiled version of the solver together with user-defined subroutines. The equations have been discretized using the finite volume method, and the calculations performed following the elliptic-staggered formulation, in which the scalar variables are evaluated at the cell centers and the velocity components at the cell faces. Central differencing is employed for the diffusion terms, while the convection terms are discretized using the hybrid differencing scheme of Spalding (1972). The finite-volume equations are solved by means of the IPSA algorithm of Spalding (1980). The calculation procedure is organized in a slab-by-slab manner, in which all the dependent variables are solved at the current slab before the solver routine moves to the next slab. The numerical solution procedure requires appropriate relaxation of the field variables to achieve convergence.

A cylindrical-polar structured mesh was used to discretize the domain. With the Euler-Euler model, the definition of the mesh is more delicate than in single-phase flow simulations, where the requirements are just grid-independence and consistency with the wall treatment approach. The averaging process at the basis of the flow equations implies that the cell size should be larger than the particle size in order to be physically

consistent. Trying to generalize the conclusions of Picardi et al. (2016) to a 3D domain, we adopted the criterion that Δr and Δz should be at least equal to $\sqrt{2}d_p$, whilst $\Delta\theta$ was defined in such a way to produce an average cell-area in the θ-r plane not lower than $2d_p^2$. The mesh below the impeller was the finest possible in compliance with the above constrains for d_p = 1.5 mm, namely $\Delta\theta$ = 0.0231 rad, $\Delta r = \Delta z$ = 2.12 mm. In order to reduce the computational burden of the simulations, the cells above the impeller were axially elongated in accordance to a 1.2 power law distribution, reaching a value of Δz equal to about 6 mm close to the upper surface. Specific tests were carried out to demonstrate that such a grid coarsening did not affect the erosion-related parameters introduced in the next section.

The PHOENICS solver was run until the sum of the absolute residual over the whole solution domain is less than 0.01% of reference quantities based on the total inflow of the variable in question. This is typically achieved in about 12000 iterations.

RESULTS

Effectiveness of the new apparatus

In order to produce wear mechanisms that are similar to those encountered in concrete hydraulic structures (Graham, 1998), the new apparatus should be able to create regions in which the sand particles impinge against the bottom. Numerical simulations allowed verifying that the Pitched blade impeller fits into this purpose, being capable in pushing the particles against the specimen and, afterwards, re-lifting them up close to the tank wall. In fact, the mean velocity field of the solid phase, depicted in Fig. 4, clearly shows the presence of an annular zone where particle impingements are likely to occur. In Fig. 4, the impeller clearance is c = 5.6 cm (equal to 0.16 tank diameters, T) and its rotational speed is 600 rpm, but qualitatively similar solutions are obtained in all the simulations.

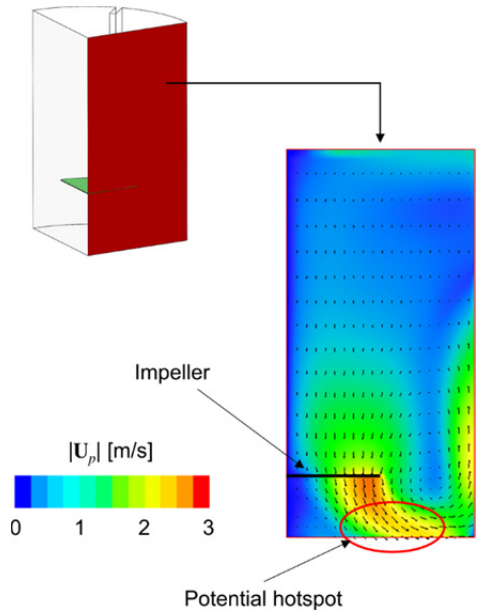

Fig. 4. Mean velocity field of the solid phase for a typical simulation.

Definition of a new erosion-related function

Usually, numerical investigations concerning solid particle erosion involve dilute flows, and they predict the loss of material by simulating the fluid-particle flow using an Eulerian-Lagrangian two-phase model, in which a Lagrangian equation of motion is solved for a number of computational particles, followed by the application of a single-particle erosion model to each particle-wall impingement (Parsi et al., 2014).

Nevertheless, this approach is precluded in this study for a couple of reasons. First, it is not clear how to couple the Euler-Euler fluid-dynamic solution with a single-particle erosion model. Second, it would be hard to guarantee the reliability of the wear estimates since they are strongly affected by the erosion model (Messa and Malavasi, 2017), which includes material-dependent constants obtained by fitting experimental data.

It is worth remarking that the numerical approach is here aimed at attaining rough estimation of how the fluid dynamic of the system affects the effectiveness of the apparatus, in order to create a tool that can be used in future experiment's design. Based on this consideration, we introduced a function, ϕ, which can be regarded as an indicator of erosion in an Euler-Euler framework. This parameter may be used for comparing different operating conditions of the setup (e.g. in terms of type of impeller, clearance, and rotational speed), but it does not allow any quantitative prediction of mass loss, as it does not account for the characteristics of the target material. As already mentioned, turning ϕ into an erosion prediction model will be demanded to a later stage of this research project. The function ϕ is defined on a discretized plane parallel to the surface of the specimen (Fig. 5), as follows

$$\phi = -\min(\dot{m}_{adv,z}, 0)\left|\mathbf{U}_p\right|^2 \frac{2\theta_p}{\pi} \tag{7}$$

where θ_p is the inclination angle of the mean solid phase velocity vector, and $\dot{m}_{adv,z}$ is the advective flux per unit area of the solid phase along direction z. All quantities above are interpolated at the centroid of each element of the plane, and the last two variables are calculated as

$$\theta_p = \arctan\frac{W_p}{\sqrt{U_p^2 + V_p^2}} \tag{8}$$

$$\dot{m}_{adv,z} = \rho_p \alpha_p W_p \tag{9}$$

where U_p, V_p, and W_p are the components of the mean solid phase velocity along directions θ, r, and z, respectively.

The values of ϕ are different from zero only in those elements where the advective solid mass flux is directed downwards, thereby assuming that the others do not contribute to the erosion process. Moreover, the function is directly proportional to the flux of kinetic energy, and linearly increases with the inclination angle, θ_p. By analogy with single-particle erosion models, ϕ was regarded as an indicator of the penetration rate, (i.e., the speed at which the scar depth increases) and, therefore, the integral of ϕ over the surface, referred to as Φ, relates to the erosion rate, i.e. the velocity at which mass loss occurs. The monotonically increasing trend of erosion versus the inclination angle is typical of brittle materials (Parsi et al., 2014) and, in the absence of specific data for concrete other than the experiments of Liu et al. (2012), as a first step a linear approximation was assumed.

An issue arises from the fact that ϕ is zero over the surface of the specimen, since $\dot{m}_{adv,z}$ is zero there. Therefore, this function has been evaluated at a certain distance from the lower boundary, referred to as δ in Fig. 5. This approach introduces an arbitrary parameter in the computational model but specific sensitivity analyses showed that, generally, the relative effect of

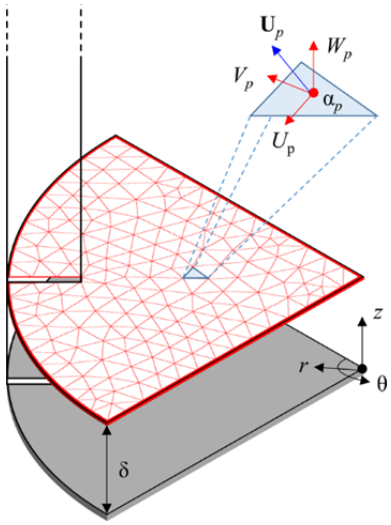

Fig. 5. Reference plane for evaluation of ϕ.

the fluid dynamics of the system on ϕ is only moderately affected by δ when this parameter varies between 10 and 30 mm. The results shown hereafter refer to δ = 20 mm.

A typical ϕ distribution is depicted in Fig. 6 for c/T = 0.16 and Ω = 600 rpm, showing consistency with the solid phase velocity vectors of Fig. 4. The similarity between the ring shape of the function and that of the scar on the top of the specimen will be made evident in the next section, giving strength to the assumption that ϕ is related to the penetration rate.

A sensitivity analysis was performed to investigate the effect of the impeller clearance and the impeller rotational speed on the expected development of the erosion process. The ratio between the impeller clearance and the tank diameter, c/T, was varied in the range 0.16 ÷ 0.29, and Ω increased from 500 to 700 rpm. Researches by Zwietering (1958), Mak (1992), and Jirout and Rieger (2011) suggest that, in all cases, the rotational speed is enough to avoid particle accumulation. The effects of the above parameters on the predicted wear scar are shown in Figs. 7(a) and (b), making reference to the profile of ϕ along the line midway between two baffles. The simulation suggest that c/T and ϕ differently affect the erosion shape due to their effect on the fluid dynamics of the two-phase system. Particularly, the lifting the impeller upwards causes a decrease in the penetration rate accompanied by an increase in the inner radius of the scar ring. Conversely, a variation in the impeller speed results in a change in the velocity at which erosion occurs, but it is unlikely to produce a change in the shape of the scar.

The considerable influence of c/T and ϕ on the erosion of the specimen is confirmed by the values of the integral of ϕ, reported in Table 1 for all flow conditions.

Table 1. Values of Φ for different flow conditions.

c/T [–]	Ω [rpm]	Φ [kg·m^2/s^3]
0.16	600	2.72
0.22	600	1.90
0.29	600	0.91
0.16	500	1.75
0.16	700	4.08

Comparison against experiments

Prototypes of the apparatus were set up in accordance with the dimensions reported in Fig. 2, and the first experimental tests were performed in the Laboratory of Hydraulics and Fluid

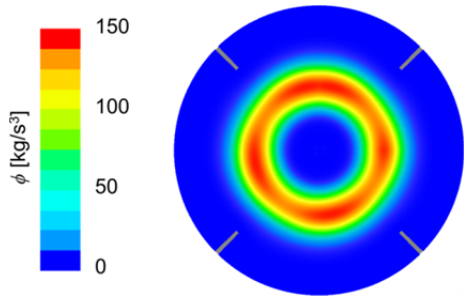

Fig. 6. Distribution of ϕ for c/T = 0.16 and Ω = 600 rpm.

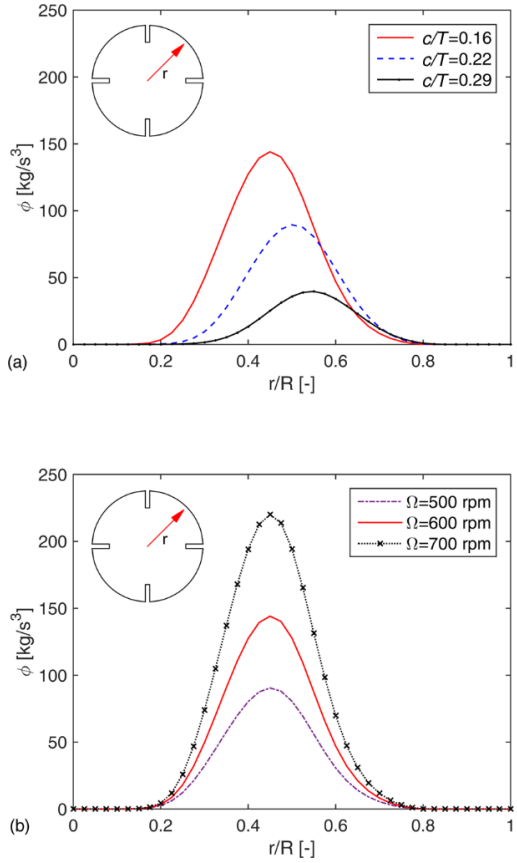

Fig. 7. Radial profile of ϕ along the line midway between two baffles: (a) effect of c/T for Ω = 600 rpm; (b) effect of Ω for c/T = 0.1.

Mechanics of the University of Campinas (Fig. 8). The tank and the baffles are made of acrylic Plexiglass to allow visual inspection of the test. The thickness of the tank wall is 5 mm. The Pitched Blade impeller is kept into rotation by a 4-pole motor with nominal power of 370 W, driven by a frequency inverter that allows varying the rotating speed up to 1800 rpm.

The specimens for the erosion tests were cylinders, which have been accurately re-shaped to fit into the baffled tank. The Brazilian Standard NBR 5738 (2003) was followed for their preparation. For the resistance compressive strength and elasticity modulus at 28 days, cylindrical samples of 10 mm diameter and 200 mm height were molded. It is again underlined that the objective of these preliminary experiments is the verification of the effectiveness of the apparatus and the above simulation methodology, whilst the use of the setup for characterizing con-

Fig. 8. The experimental setup at the University of Campinas.

cretes to be employed in practical applications is demanded to a later stage. Therefore, the mixture had an extremely high water-to-cement ratio, thus very low compressive resistance, to accelerate the erosion process and enhance the influence of the fluid-dynamic parameters of the system. The samples have the cement-sand-rock composition of 1-6.47-5.29 and w/c ratio of 1.47. As already mentioned, the carrier fluid is water, and the abradant consists of silica sand with size in the range 1.19 ÷ 2.00 mm, the average being 1.5 mm (which is the value of d_p considered in the numerical simulations).

The experimental methodology is as follows. Firstly, the concrete sample is weighted using a balance (Toledo, model PRIX III Fit, range 0.050–15.000 kg, accuracy of 0.005 kg) and its initial mass is recorded. Secondly, the sample is positioned at the bottom of the tank, and the gap between the specimen and the tank wall is filled with sealant material. Thirdly, clean water is poured into the tank up to a static level of 350 mm above the specimen. 0. 950 kg of abradant was added to produce a static solid volume fraction equal to 1%. Fourthly, after positioning the impeller-shaft motor assembly at the desired clearance, the motor is turned on and the rotational velocity is adjusted. Every 6 hours, the mass of the specimen was measured and the relative mass decrement, $\Delta M/ M_0$, calculated. Each time, the abrasive mixture was renewed, in order to reduce as much as possible not only the self-enhancements of the erosion process due to the contribution of detached concrete pieces, but also the spurious effects due to particle degradation.

The experiments were made for two different impeller clearances, namely c = 56 mm (c/T = 0.16) and c = 100 mm (c/T = 0.29), at constant impeller speed of 600 rpm. The overall testing time was 96 hours for the high clearance case, whilst it was reduced to 24 hours for the low clearance one due to the higher velocity at which erosion occurred.

The verification of the effectiveness of the ϕ function was made in two steps. Firstly, visual comparison between the surface of the specimen at the end of the test (Fig. 9) and the predicted ϕ distribution (Fig. 6) gave strength to the hypothesis that ϕ can be related to the penetration rate, and, consequently, to the erosion depth at a certain time instant.

Secondly, attention was focused on the erosion rate. As already noticed, in the numerical simulations this parameter is expected to be related to Φ, i.e. the integral of ϕ. In the experiments, the erosion rate can be estimated from the temporal evolution of the relative mass decrement, shown in Fig. 10.

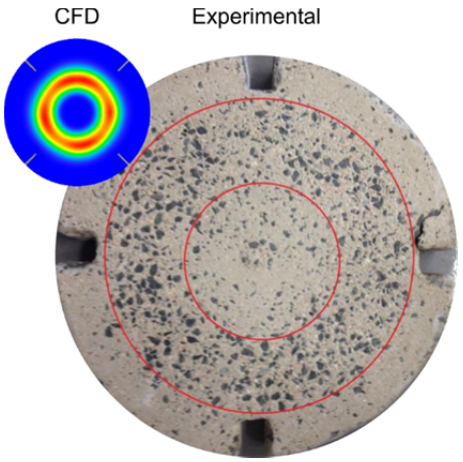

Fig. 9. Surface of the specimen after 24 hours for the low clearance case (c/T = 0.16). The image also shows the corresponding ϕ distribution, already depicted in Fig. 6.

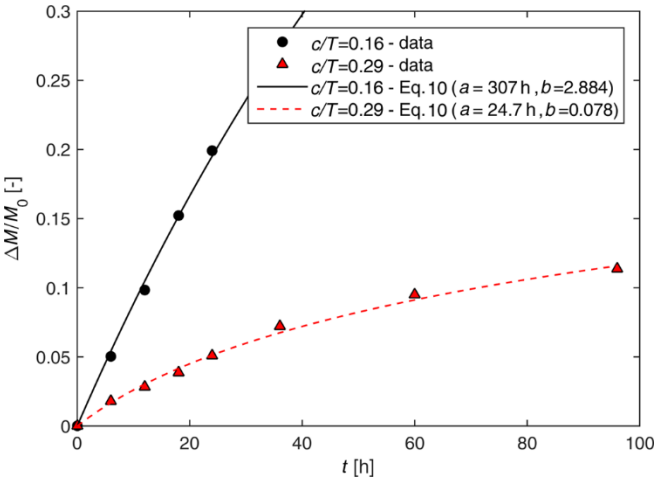

Fig. 10. Time history of the relative mass decrement: experimental data and fitting lines.

Following Horszczaruk (2005), the course of erosion is represented by the following expression:

$$\frac{\Delta M}{M_0} = 1 - \left(1 + \frac{t}{a}\right)^{-b} \tag{10}$$

The numerical coefficients, a and b, have been determined for both tests using interpolation methods, and the corresponding curves are shown in Fig. 10 as well. The evidence indicates that erosion occurs faster for the low clearance case, but the erosion rate, i.e. the derivative of the curves, decreases with time. This behavior is well known in the literature (Horszczaruk, 2004), and it may be caused by different factors, including the inhomogeneous structure of the concrete, the changes in the surface of the specimen due to erosion. The size and the shape degradation may also come into play (Cooke, 1996; Clark, 2002), as this effect may not be fully eliminated by renewing the slurry in the tank every 6 hours.

Since the steady-state Eulerian-Eulerian model employed is not capable in handling such dynamic effects, the comparison against the simulations is made between Φ and the experimentally estimated erosion rate at t = 0, when the surface of the specimen is still flat and homogeneous. This quantity, referred

to as $\dot{E}_{r0,\exp}$, is equal to:

$$\dot{E}_{r0,\exp} = \left.\frac{d(\Delta M)}{dt}\right|_{t=0} = \left.\frac{d\left\{M_0\left[1-\left(1+t/a\right)^{-b}\right]\right\}}{dt}\right|_{t=0} = M_0 b\left(1+\frac{t}{a}\right)^{-b-1}\left.\frac{1}{a}\right|_{t=0} = M_0\frac{b}{a} \quad (11)$$

The results, summarized in Table 2, indicate that the rate of variation of Φ with c/T deviates about 6.5% from that of $\dot{E}_{r0,\exp,}$ thereby confirming the suitability of ϕ for attaining rough estimation of the effect of the fluid dynamic parameters on the erosion of the specimens.

Table 2. Values of Φ, obtained by CFD, and $\dot{E}_{r0,\exp}$, inferred from experiments.

	CFD	Experimental
c/T [–]	Φ [kg·m^2/s^3]	$\dot{E}_{r0,\exp}$ [g/h]
0.16	2.72	94.0
0.29	0.91	33.5
Ratio	2.99	2.81

CONCLUSIONS

A new strategy has been proposed for testing the abrasive erosion of concrete, which involves a strong synergy between numerical simulations and laboratory experiments. As part of this method, a new apparatus has been designed. The equipment is a modified version of the ASTM "underwater method", the differences being the insertion of four lateral baffles in the tank, the change of the impeller with a Pitched Blade one, and the use of sand particles instead of steel balls as abradant (Fig. 2). These changes allow activating erosion mechanisms which are closer to those encountered in concrete hydraulic structures, without the need of resorting to complex and expensive setups.

Computational Fluid Dynamics has been employed for the design of the setup. Particularly, the water-sand flow has been simulated in a steady-state by an Euler-Euler model previously developed by two of the authors, and the effect of the rotation of the impeller has been modelled by imposing proper values of mean velocity and turbulence parameters. The effectiveness of the designed equipment was inferred from inspection of the mean velocity field of the solid phase (Fig. 4).

Afterwards, a parameter has been identified to estimate the effect of the fluid dynamics of the system on the erosion of the concrete specimen. A sensitivity analysis allowed establishing the influence on the position of the impeller and its rotational speed on the shape of the erosion scar and the rapidity at which mass removal occurs (Fig. 7 and Table 1). Finally, the succesful comparison against experimental data performed in a prototype apparatus (Figs. 9 and 10) gave strength to the possibility of referring to the proposed parameter for customizing the setup in function of the peculiarities of the experiments.

The next step of this research will consist in the development of specifically-calibrated erosion models for the materials of interests. This will open the way to reliable simulation of concrete hydraulic structures by means of CFD.

Acknowledgements. The authors would like to acknowledge Professor Elzbieta Horszczaruk for kindly providing one of her papers.

REFERENCES

ASTM C1138M-12, 2012. Standard Test Method for Abrasion Resistance of Concrete (Underwater Method). ASTM International, West Conshohocken, PA.

Cheng, N.S., Law, A.W.K., 2003. Exponential formula for computing effective viscosity. Powder Technol., 129, 156–160.

Clark, H. McI, 2002. Particle velocity and size effects in laboratory slurry erosion measurements OR... do you know what your particles are doing? Tribol. Int., 35, 617–624.

Cooke, R., 1996. Pipeline material evaluation for the Mina Grande hydrohoist system. In: Proc. 13th Int. Conf. on Hydrotransport, Johannesburg, South Africa, pp. 455–477.

Dalfré Filho, J.G., Genovez, A.I.B., Paulon, W.A., 2000. Wear in hydraulic structures and concrete resistance to water-solid mixture. Ingeniería Estructural, 8, 20, 18–22. (In Portuguese.)

Dandapat, R., Deb, A., 2016. A probability based model for the erosive wear of concrete by sediment bearing water. Wear, 350–351, 165–181.

Fokema, M.D., Kresta, S.M., Wood, P.E., 1994. Importance of using the correct impeller boundary conditions for CFD simulations of stirred tanks. Can. J. Chem. Eng., 72, 177–183.

Gnanavelu, A., Kapur, N., Neville, A., Flores, J.F., Ghorbani, N., 2011. A numerical investigation of a geometry independent integrated method to predict erosion rates in slurry erosion. Wear, 271, 712–719.

Graham, J.R., 1998. Erosion of concrete in hydraulic structures. Reported by ACI Committee 210, ACI manual practice, Part 1.

Horszczaruk, E.K., 2000. Abrasion-erosion of concrete. Arch. Civ. Eng., 46, 585–609.

Horszczaruk, E.K., 2004. The model of abrasive wear of concrete in hydraulic structures. Wear, 256, 787–796.

Horszczaruk, E.K., 2005. Abrasion resistance of high-strength concrete in hydraulic structures. Wear, 259, 62–69.

Horszczaruk, E.K, 2008. Mathematical model of abrasive wear of high performance concrete. Wear, 264, 113–118.

Horszczaruk, E.K., 2009. Hydro-abrasive erosion of high performance fiber-reinforced concrete. Wear, 267, 1–4, 110–115.

Jirout, T., Rieger, F., 2011. Impeller design for mixing of suspensions. Chem. Eng. Res. Des., 89, 1144–1151.

Kumar, R.G.B., Sharma, U.K., 2014. Abrasion resistance of concrete containing marginal aggregates. Construction and Building Materials, 66, 712–722.

Launder, B.E., Spalding, D.B., 1972. Mathematical Models of Turbulence. Academic Press, London.

Launder, B.E., Spalding, D.B., 1974. The numerical computation of turbulent flows. Comput. Meth. Appl. Mech. Eng., 3, 269–289.

Liu, Y.W, Yen, T., Hsu, T.H., 2006. Abrasion erosion of concrete by water-borne sand. Cem. Concr. Res., 36, 1814–1820.

Liu, Y.W, Cho, S.W., Hsu, T.H., 2012. Impact abrasion of hydraulic structures concrete. J. Mar. Sci. Tech.-Japan, 20, 3, 253–258.

Mak, A.T.C., 1992. Solid-liquid mixing in mechanically-agitated vessels. PhD Thesis. University College, London UK.

Mansouri, A., Arabnejad, H., Shirazi, S.A., McLaury, B.S., 2015. A combined CFD/experimental methodology for erosion prediction. Wear, 332–333, 1090–1097.

Messa, G.V., Malavasi, S., 2014a. Computational investigation of liquid-solid slurry flow through an expansion in a rectangular duct. J. Hydrol. Hydromech., 62, 234–240.

Messa, G.V., Malavasi, S., 2014b. Numerical prediction of particle distribution of solid-liquid slurries in straight pipies and bends. Eng. Appl. Comput. Fluid Mech., 8, 3, 356–372.

Messa, G.V., Malavasi, S., 2015. Improvements in the numerical prediction of fully-suspended slurry flow in horizontal pipes. Powder Technol., 270, 358–367.

Messa, G.V., Malavasi, S., 2017. The effect of sub-models and parameterizations in the simulation of abrasive jet impingement tests. Wear, 370–371, 59–72.

Messa, G.V., Malin, M., Malavasi S., 2013. Numerical prediction of pressure gradient of slurry flows in horizontal pipes. In: Proc. ASME Pressure Vessels and Piping PVP2013 Conf. (Paris, France). Paper No. PVP2013-97460.

Messa, G.V., Malin, M., Malavasi S., 2014. Numerical prediction of fully-suspended slurry flow in horizontal pipes. Powder Technol., 256, 61–70.
Mohebi, R., Behfarnia, K., Shojaei, M., 2015. Abrasion resistance of alkali-activated slag concrete designed by Taguchi method. Constr. Build. Mater., 98, 792–798.
NBR 5738, 2003. Moulding and cure of concrete cylindrical and prismatic test pieces. ABNT-Brazilian Association for Technical Standards, Rio de Janeiro, Brazil.
Parsi, M., Najmi, K., Najafifard, F., Hassani, S., McLaury, B.S., Shirazi, S.A., 2014. A comprehensive review of solid particle erosion modeling for oil and gas wells and pipelines applications. J. Nat. Gas Sci. Eng., 21, 850–873.
Picardi, R., Zhao, L., Battaglia, F., 2016. On the ideal grid resolution for two-dimensional eulerian modeling of gas–liquid flows. ASME J. Fluids Eng., 138, No. 114503.
Shiller, L., Naumann, A., 1935. A drag coefficient correlation. Z. Ver. Dtsch. Ing., 77, 318–320.
Spalding, D.B., 1972. A novel finite-difference formulation for differential expresions involving both first and second derivatives. Int. J. Numer. Methods Eng., 4, 551–559.
Spalding, D.B., 1980. Numerical computation of multi-phase fluid flow and heat transfer. In: Taylor, C., Morgan, K. (Eds.): Recent Advances in Numerical Methods in Fluids. Pineridge Press Limited, Swansea.
Yen, T.Y., Hsu, T.H., Liu, Y.W., Chen, S.H., 2007. Influence of class F fly ash on the abrasion–erosion resistance of high-strength concrete. Constr. Build. Mater., 21, 2007, 458–463.
Zwietering, T.N., 1958. Suspending of solid particles in liquid by agitators. Chem. Eng. Sci., 8, 244–253.

Received 13 March 2017
Accepted 15 August 2017

SUPPLEMENTARY MATERIAL
Appendix A: impeller model

As is it a common practice in stirred tank simulations, the effect of the rotating impeller on the mean flow was modelled by fixing the velocities of both phases, the turbulent kinetic energy, and the dissipation rate in a fluid region located in correspondence of the impeller (green coloured in Fig. 3).

These variables are assumed axi-symmetrically distributed. Their radial profiles are obtained by interpolating the data reported by Fokema et al. (1994) for a relative clearance of 0.5. In order to allow extension to different blade diameters, hub diameters, and impeller rotational velocities, the interpolation curves are shown in Fig. 1A in dimensionless form, making reference to the following variables, U_{imp}/V_{tip}, V_{imp}/V_{tip}, W_{imp}/V_{tip}, k_{imp}/V^2_{tip}, $\varepsilon_{imp}/V^3_{tip}$. In the above, U_{imp}, V_{imp}, W_{imp} are the induced mean velocity components along the azimuthal, radial, and axial direction, respectively, k_{imp} and ε_{imp} are the induced turbulent kinetic energy and dissipation rate, R_{imp} is the radius of the impeller, and the tip velocity, V_{tip}, and the dimensionless radial coordinate, ζ, are given by:

$$V_{tip} = 2\pi\Omega R_{imp} \tag{A1}$$

$$\zeta = \frac{r - R_{hub}}{R_{imp} - R_{hub}} \tag{A2}$$

where R_{hub} is the radius of the hub. The equations corresponding to the profiles shown in Fig. 1A are reported below:

$$\frac{U_{imp}}{V_{tip}} = 0.313 \cdot \frac{r}{R_{imp}} \tag{A3}$$

$$\frac{V_{imp}}{V_{tip}} = 0.262\zeta^3 - 0.572\zeta^2 + 0.349\zeta \tag{A4}$$

$$\frac{W_{imp}}{V_{tip}} = 2.3997\zeta^4 - 4.0526\zeta^3 + 2.6984\zeta^2 - 1.2961\zeta \tag{A5}$$

$$\frac{k}{V^2_{tip}} = 0.2991\zeta^3 - 0.3605\zeta^2 + 0.1564\zeta \tag{A6}$$

$$\frac{\varepsilon}{V^3_{tip}} = 5.1254\zeta^3 - 5.547\zeta^2 + 1.7241\zeta \tag{A7}$$

In order to account for the obstacle produced by the hub, V_{imp}, W_{imp}, k_{imp}, and ε_{imp} were set to a null value for $\zeta < 0$ ($r < R_{hub}$).

The mean velocity profiles reported above have been applied to both the fluid and the solids, thereby assuming absence of slip between the phases in the impeller region.

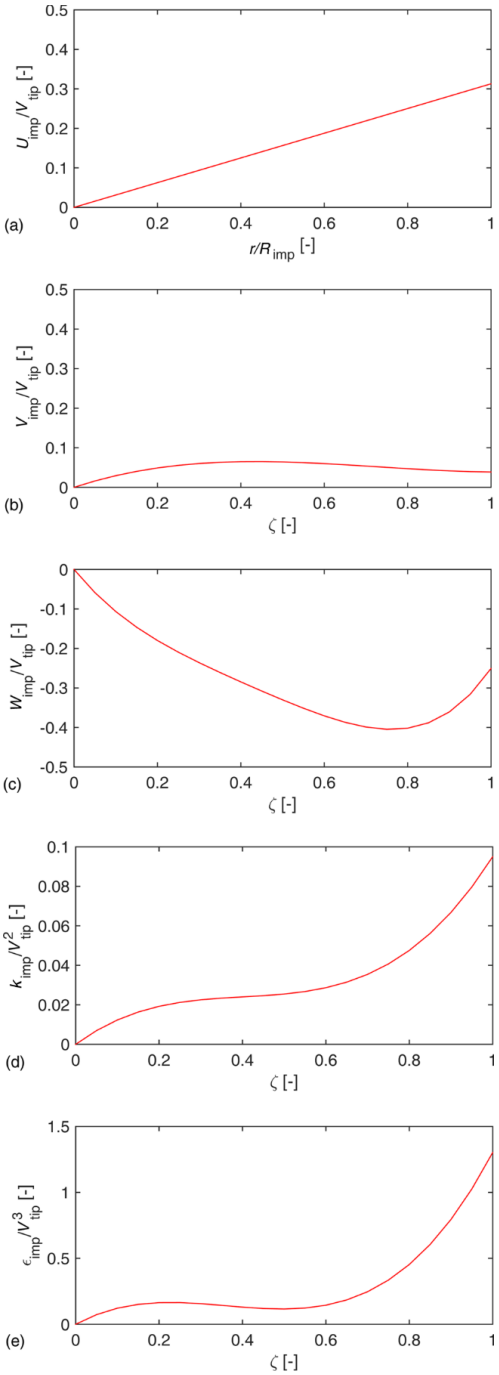

Fig. 1A. Radial profiles of the mean velocity and turbulent parameters imposed in the impeller region.